Zebrafish disease models to study the pathogenesis of inherited manganese transporter defects and provide a route for drug discovery

Dr Karin Tuschl

University College London

PhD Supervisors: Dr Philippa Mills & Prof Stephen Wilson

A thesis submitted for the degree of

Doctor of Philosophy

University College London

August 2016

Declaration

I, Karin Tuschl, confirm that the work presented in this thesis is my own. Where information has been derived from other sources, I confirm that this has been indicated in the thesis. Part of the work of this thesis has been published in the following articles for which copyright clearance has been obtained (see **Appendix**):

- Tuschl K, *et al.* Manganese and the brain. Int Rev Neurobiol. 2013. 110:277-312.
- Tuschl K, *et al.* Mutations in *SLC39A14* disrupt manganese homeostasis and cause childhood-onset parkinsonism-dystonia. Nat Comms. 2016. 7:11601.

I confirm that these publications were written by me and may therefore partly overlap with my thesis.

Abstract

Although manganese is required as an essential trace element excessive amounts are neurotoxic and lead to manganism, an extrapyramidal movement disorder associated with deposition of manganese in the basal ganglia. Recently, we have identified the first inborn error of manganese metabolism caused by mutations in *SLC30A10*, encoding a manganese transporter facilitating biliary manganese excretion. Treatment is limited to chelation therapy with intravenous disodium calcium edetate which is burdensome due to its route of administration and associated with high socioeconomic costs.

Whole exome sequencing in patients with inherited hypermanganesaemia and early-onset parkinsonism-dystonia but absent *SLC30A10* mutations identified *SLC39A14* as a novel disease gene associated with manganese dyshomeostasis. Zebrafish loss-of-function mutants for *slc30a10* (*slc30a10*^{U800}) and *slc39a14* (*slc39a14*^{U801}) were generated using TALEN and CRISPR/Cas9 genome editing technologies in order to model these Mn transporter defects *in vivo*. Both mutants demonstrate prominent manganese accumulation during larval development. Adult *slc39a14*^{U801} mutants show significantly increased brain manganese levels similar to the human phenotype. During larval stages *slc39a14*^{U801} mutants display increased sensitivity to manganese toxicity, reduced locomotor activity and visual impairment upon manganese exposure. This phenotype is accompanied by a reduction of tyrosine hydroxylase positive cells in the ventral diencephalon suggesting an involvement of dopaminergic circuits. RNA sequencing further identified genes involved in neurotransmitter release and signalling, phototransduction, circadian clock, and hypoxia inducible factor (HIF) signalling to be affected by manganese dyshomeostasis.

In summary, *slc30a10*^{U800} and *slc39A14*^{U801} zebrafish mutants provide disease models of inherited manganese transporter defects that allow the study of disease mechanisms to identify novel therapeutic targets with the view to improve clinical treatment strategies.

Acknowledgements

I would like to express my deep gratitude to my primary supervisor and long term mentor Dr Philippa Mills who has guided and taught me for over 10 years and has always been there for me both as an excellent academic supervisor and as a close friend. Furthermore, I would like to thank my secondary supervisor Prof Steve Wilson, who has been extremely supportive and uplifting whenever my moral seemed to plummet, for giving me the unique opportunity to learn in his laboratory. Eternal thanks go to Dr Leonardo Valdivia who has spent a huge amount of time teaching me everything about zebrafish and helping with experiments, and has tolerated my neverending interruptions of his work with senseless questions. I would like to thank Prof Peter Clayton who, for many years, has been an extremely motivating and unceasingly supportive mentor. I would also like to thank Prof Paul Gissen who has sold zebrafish to me so well that I am now hooked on this stripy animal. A big thank you goes to my colleagues in both the Translational Omics Group at the Institute of Child Health and the Department of Cell and Developmental Biology for their readiness to help and making each day in the lab a fun day.

I would like to thank Prof Olaf Bodamer and Dr Christina Hung at the University of Miami for their generous collaboration. I would also like to thank Dr John Spencer, Dr Rupert Purchase and Dr Alaa Abdul-Sada for their interest in my work and their valuable guidance regarding metal chemistry. Thanks also go to Dr Kling Chong for his assistance with the interpretation of radiology images and Dr Tom Jacques for histopathological analysis. I would like to thank Dr Manju Kurian and Dr Esther Meyer for their efforts to publish our joint work.

I am indebted to the patients and their families who have taken part in this research and made this work possible. I am sincerely grateful to Action Medical Research for providing the funding for this project and for giving me this unique opportunity.

Finally, eternal thanks go to my family for their neverending support and belief in me, particularly to Tomi for enduring our fruitful research discussions and to Tobias for every minute of sleep that allowed me to write this thesis.

Table of Contents

Table of figures

List of tables

Abbreviations

AHD	acquired hepatocerebral degeneration
ALP	alkaline phosphatase
ALT	alanine aminotransferase
AST	aspartate transaminase
ATF	activating transcription factor
ATP	adenosine triphosphate
BCIP	5-bromo-4-chloro3-indolyl-phosphate, toluidine salt
BDNF	brain derived neurotrophic factor
bp	base pair
BSA	bovine serum albumin
B&W	bind and wash buffer
C. elegans	caenorhabditis elegans
Cd	cadmium
CDF	cation diffusion facilitator
CDG	congenital disorder of glycosylation
cDNA	complementary deoxyribonucleic acid
cGMP	cyclic guanosine monophosphate
CIP	calf intestinal alkaline phosphatase
CK	creatine kinase
CNG	cyclic nucleotide gated cation channel
CNS	central nervous system
Co	cobalt
CRISPR	clustered regularly interspaced short palindromic repeat
crRNA	CRISPR repeat-spacer array RNA
CSF	cerebrospinal fluid
CT	computed tomography
CTP	cytidine triphosphate
Cu	copper
CV	cresyl violet
DAPI	4',6-diamidino-2-phenylindole
DAT	dopamine transporter
del	deletion
DIG	digoxigenin

DMSA	dimercaptosuccinic acid
DMSO	dimethyl sulfoxide
DMT1	divalent metal transporter 1
DNA	deoxyribonucleic acid
dNTP	deoxyribonucleotide triphosphate
dpf	days post fertilisation
DSB	double strand break
dUTP	deoxyuridine-triphosphate
D2R	D2 dopamine receptor
EB	elution buffer
EDTA	ethylendiaminetetraacetic acid
ef1α	elongation factor 1 alpha
EGFP	enhanced green fluorescent protein
eIf2α	eukaryotic initiation factor 2 alpha
EPO	erythropoietin
EPRS	glutamyl-prolyl-tRNA synthetase
ER	endoplasmic reticulum
ERK	extracellular signal-regulated kinases
ExoI	exonuclease I
E. coli	*escherichia coli*
Fe	iron
Fpn	ferroportin
FRET	fluorescent resonance energy transfer
Fw	forward
GABA	gamma aminobutyric acid
GAP	GTPase activating protein
GCAP	guanylcyclase activating protein
gDNA	genomic DNA
GDP	guanosine diphosphate
Ge	germanium
GFP	green fluorescent protein
GGT	gamma-glutamyltransferase
GLAST	glutamate:aspartate transporter
Glu R	glutamate receptor
GRK	G-protein coupled receptor kinase

gRNA	guide RNA
GRP 78	glucose regulated protein 78
GTP	guanosine triphosphate
h	hour
Hb	haemoglobin
H&E	haematoxylin and eosin
HEK	human embryonic kidney
HIF	hypoxia inducible factor
hpf	hours post fertilisation
HPRT	hypoxanthine-guanine phosphoribosyltransferase
HR	homologous recombination
HRE	hypoxia responsible element
HRMA	high resolution melting analysis
HSP	heat shock protein
Hyb+	hybridisation mix
H_2O_2	hydrogen peroxide
ICP-MS	inductively coupled plasma – mass spectrometry
IL	interleukin
ins	insertion
IRE1	inositol-requiring kinase 1
IVC	inferior vena cava
kb	kilobase
KO	knock-out
LB	Luria Bertani
LC_{50}	median lethal concentration
LDH	lactate dehydrogenase
LFB	luxol fast blue
LZT	LIV subfamily of ZIP transporters
MAPK	mitogen-activated protein kinases
MEK	mitogen-activated protein kinase kinase
min	minute
MMT	methylcyclopentadienyl manganese tricarbonyl
Mn	manganese
MPT	mitochondrial permeability transition
MRI	magnetic resonance imaging

mRNA	messenger RNA
MQ	milli Q
MRS	magnetic resonance spectroscopy
MS-222	tricaine methanesulfonate
$Na_2CaEDTA$	disodium calcium edetate
NBIA	neurodegeneration with brain iron accumulation
NBT	4-nitro blue tetrazolium chloride
NCBI	National Center for Biotechnology Information
NEB	New England Biolabs
NHEJ	non-homologous end joining
Ni	nickel
nls	nuclear localisation signal
NMDA	N-methyl-D-aspartate
NO	nitric oxide
NTC	non-template control
NTP	nucleotide triphosphate
$OH^{\cdot}$	hydroxyl radical
OKR	optokinetic response
OMIM	Online Mendelian Inheritance in Man
O_2-	superoxide radical
PAM	protospacer adjacent motif
PASA	para-aminosalicylic acid
PBS	phosphate buffered saline
pBSK-	pBlueScript SK-
PBST	PBS / Tween-20
PBSTr	PBS / Triton-X100
PCR	polymerase chain reaction
PD	Parkinson’s disease
PDE	phosphodiesterase
PERK	PKR-like eukaryotic initiation factor 2a kinase
PET	positron emission tomography
PFA	paraformaldehyde
PHD	prolyl hydroxylase
PI3K	phosphoinositide 3-kinase
PK	protein kinase

PKC	protein kinase C
PLC	phospholipase C
PMCA	plasma membrane calcium ATPase
PNK	polynucleotide kinase
PTP	permeability transition pore
PTU	1-phenyl 2-thiourea
qPCR	quantitative PCR
RACE	rapid amplification of cDNA ends
RE	restriction enzyme
RFP	red fluorescent protein
RLM	RNA Ligase Mediated
RNA	ribonucleic acid
ROS	reactive oxygen species
RT	room temperature
RT-PCR	reverse transcription PCR
Rv	reverse
RVD	repeat variable di-residue
SAP	Shrimp alkaline phosphatase
s.d.	standard deviation
Se	selenium
sec	second
s.e.m.	standard error of the mean
SERCA	sarco/endoplasmic reticulum calcium ATPase
SLC	solute carrier
SNAP	synaptosomal associated protein
SNP	single nucleotide polymorphism
SO Ca^{2+}	store operated Ca^{2+} channel
SPCA	secretory pathway calcium ATPase
SPECT	single photon emission computed tomography
ss	somite stage
SSC	saline-sodium citrate buffer
SV	synaptic vesicle
SV40	simian virus 40
Syt	synaptotagmin
S1P	site-1 protease

S2P	site-2 protease
TAE	tris base, acetic acid and EDTA
TALEN	transcription activator-like effector nuclease
Taq	thermus aquaticus
TAP	tobacco acid pyrophosphatase
TdT	terminal deoxynucleotidyl transferase
TE	tris – EDTA
Tf	transferrin
TfR	transferrin receptor
TH	tyrosine hydroxylase
TIBC	total iron binding capacity
TMD	transmembrane domaine
TNF-α	tumor necrosis factor α
tracrRNA	transactivating crRNA
TSAP	thermosensitive shrimp alkaline phosphatase
TUNEL	terminal deoxynucleotidyl transferase dUTP nick end labelling
U	unit
UPR	unfolded protein response
UTR	untranslated region
VR Ca^{2+}	voltage Regulated Ca^{2+} Channel
vHL	von Hippel Lindau protein
UTP	uridine triphosphate
WES	whole exome sequencing
WGA	wheat germ agglutinin
WT	wild-type
XBP	X-box binding protein
zf	zebrafish
ZFIN	Zebrafish Information Network
ZFN	zinc finger nucleases
ZIP	Zrt, Irt-like protein
Zn	Zinc
Zrt	Zinc regulated transporter

Chapter 1. Introduction

1.1 Manganese and its role in disease processes

Manganese (Mn) is an essential trace element that is pivotal for normal cell function and metabolism. As such, Mn is involved in amino acid, lipid, protein and carbohydrate metabolism as well as protein glycosylation, immune function, regulation of blood sugar, production of cell energy, reproduction, digestion, bone growth and blood clotting[1-3].

Our diet is the major source of Mn which is present ubiquitously in a variety of foods. The gut tightly controls the body Mn load by limiting the absorption of ingested Mn from the intestine. Following Mn absorption, any excess Mn present in the portal circulation is promptly excreted into the bile by the liver, the key regulator of Mn elimination. A significant fraction of biliary excreted Mn undergoes enterohepatic circulation[3]. Increased dietary exposure to Mn induces homeostatic adaptation and leads to reduced gastrointestinal Mn absorption and increased biliary excretion of Mn[4-7]. Mn absorption is also affected by several dietary factors such as the presence of other trace elements[8]. Particularly important is its interaction with iron (Fe)[9]. High intake of Fe reduces blood Mn levels while Fe deficiency anaemia enhances intestinal Mn absorption[6,10,11].

Nutritional Mn deficiency has not been described in humans. This has been attributed to its ubiquitous presence in the diet. However, experimental models of Mn deficiency have suggested that low levels of Mn cause poor bone growth, skeletal abnormalities, ataxia and abnormal glucose tolerance[12]. Furthermore, erythematous skin changes and altered mood have been observed in subjects on experimental low Mn diets[13,14]. Mutations in *SLC39A8* have recently been associated with an inherited Mn depletion syndrome causing cerebellar atrophy, hypotonia, epilepsy, strabismus, developmental delay, short stature and skeletal dysplasia[15,16]. Biochemically, this disorder is accompanied by dysglycosylation resembling a type II congenital disorder of glycosylation (CDG) due to dysfunction of Mn dependent enzymes such as the beta 1,4 glycosyltransferase involved in galactosylation of glycoproteins[16]. Treatment with daily galactose to improve the impaired galactosylation completely normalises the

hypoglycosylated transferrin pattern. Early dietary galactose treatment in combination with manganese supplementation may therefore be an effective treatment strategy[16].

While an essential trace metal, excessive amounts of Mn are neurotoxic and cause a movement disorder known as “manganism”. Mn accumulates in the basal ganglia and causes distinct neurotoxic effects. The first description of Mn neurotoxicity was published by Couper in 1837 describing a case series of five Mn ore crushers who suffered from parkinsonian symptoms including tremor in the extremities, gait disturbance and whispering speech[17]. Rodier further described Mn poisoning in 151 workers of Moroccan mines a century later[18]. Manganism has since been extensively characterised; this parkinsonian syndrome can be divided into three overlapping stages: An initial stage of emotional and cognitive disturbances with impaired fine motor coordination, followed by a second stage with worsening psychotic behaviour, slurred speech, clumsiness and mask-like facies. During the final stage, patients develop disabling limb rigidity, dystonia, impairment of balance and a characteristic cock-walk gait[19,20]. While some symptoms overlap with idiopathic Parkinson’s disease such as bradykinesia, there are a number of dissimilarities including (a) less frequent resting tremor, (b) more frequent dystonia, (c) a particular propensity to fall backward, (d) failure to achieve a sustained therapeutic response to levodopa, and (e) failure to show a reduction in fluorodopa uptake by positron emission tomography (PET)[21,22].

Excessive Mn accumulation in the brain can occur either through Mn overexposure or through impaired hepatobiliary excretion. The predominant route of exposure in occupational settings is the inhalation of Mn laden dust during mining, welding, smelting or battery manufacturing. Individuals living near ferroalloy industries or in areas with high use of methylcyclopentadienyl Mn tricarbonyl (MMT), a gasoline fuel additive, are at risk of airborne Mn exposure and accumulate increased levels of Mn. Whether inhaled Mn is directly taken up via the olfactory or trigeminal nerve, transported across the pulmonary epithelium or ingested following mucociliary clearance from the lungs has still to be elucidated[3,23-25]. Excessive dietary exposure to Mn can lead to increased absorption and accumulation of Mn in the brain and has been described in communities receiving drinking water with a high Mn content[26,27]. High doses of Mn in parenteral nutrition that bypass gut and liver control mechanisms can also lead to Mn neurotoxicity[28-30]. Similarly, cases of Mn poisoning have been observed in intravenous methcathinone drug-addicts who use potassium permanganate as the

oxidant in the synthesis of the drug[31-34]. Mn accumulation in end stage liver disease occurs due to impaired hepatic function that leads to insufficient biliary excretion of Mn and subsequent accumulation of Mn in the basal ganglia, a condition described as acquired hepatocerebral degeneration (AHD)[35].

Mn toxicity also plays a role in the pathogenesis of other neurodegenerative disorders such as Parkinson's disease[36,37]. Several early-onset parkinsonism genes including *PARK2 (Parkin)*, and *PARK9 (ATP13A2)* are associated with Mn dyshomeostasis. Affected patients share common neuropathological features of Mn neurotoxicity, including oxidative stress and mitochondrial dysfunction, impaired autophagy, and altered alpha-synuclein aggregation. Indeed, Parkin and ATP13A2 are postulated to protect dopaminergic cells from Mn toxicity[38-40]. Furthermore, polymorphisms in *ATP13A2* are associated with increased susceptibility to Mn toxicity[41]. Alpha-synuclein is also suggested to act as an intracellular Mn store[42], and Mn exposure promotes alpha-synuclein oligomerization and enhances cellular toxicity[43-45].

Recently, our group has identified the first inherited Mn overload syndrome caused by loss-of-function mutations in the Mn transporter gene *SLC30A10*[46]. SLC30A10 is localised at the plasma membrane and facilitates export of Mn from the cell in brain and liver[47]. Mutations in *SLC30A10* lead to accumulation of Mn in liver and brain associated with an extrapyramidal movement disorder and chronic liver disease that may progress to cirrhosis[46,48-50].

1.2 Inherited hypermanganesaemia with dystonia-parkinsonism caused by mutations in *SLC30A10*

Our work and that of others have shown that recessive loss-of-function mutations in *SLC30A10* cause a movement disorder and chronic liver disease reminiscent of Wilson's disease[46,48-50]. As with acquired causes of hypermanganesaemia, the magnetic resonance imaging (MRI) is pathognomonic for Mn accumulation with T1 weighted hyperintensity of the basal ganglia and white matter[51,52]. Further characteristics include haematological abnormalities such as polycythaemia and abnormal Fe indices. While liver toxicity appears to be a major contributor to the mortality of this disease, liver disease has not been reported in cases of chronic

environmental manganism. In animal models, however, Mn has been shown to promote intrahepatic cholestasis and induce hepatocellular necrosis[53,54]. Furthermore, acute Mn poisoning has been reported to cause fatal hepatic failure in humans and dogs[55,56]. Depending on the time of disease onset, two distinct phenotypes caused by mutations in *SLC30A10* can be distinguished; a childhood-onset form with predominant dystonia and an adult-onset form with predominant parkinsonism[48,57].

1.2.1 Clinical phenotype

The majority of affected individuals with SLC30A10 deficiency present with gait disturbance within the first ten years of life. Motor symptoms include dystonia causing a characteristic high stepping gait ("cock-walk"), painful limb spasms and fine motor impairment as well as dysarthria, truncal ataxia, bradykinesia and retropulsion[46,48]. Fewer cases develop spastic paraparesis and typical pyramidal tract signs[58,59]. Motor impairment is progressive and many patients experience loss of ambulation. Some individuals show signs of motor neuropathy with distal weakness and areflexia[58]. Intellect appears normal and affected individuals attend mainstream schools.

To date, a single sibship with adult-onset parkinsonism has been described. Two brothers presented at the age of 47 and 57 years with progressive gait disturbance and bradykinesia. Neurological examination revealed hypomimia, monotone speech, mild rigidity, global bradykinesia, wide-based gait with freezing and starting hesitation, and moderate postural instability without evidence of tremor, dystonia, or cerebellar and pyramidal disturbances. Treatment attempts with L-dopa and dopamine agonists, as used in idiopathic Parkinson's disease, were unsuccessful[48].

In both childhood and adult-onset forms, neurological symptoms are accompanied by polycythaemia, defined by an abnormally increased haemoglobin (Hb) level, that can precede the manifestation of the movement disorder. Hb values often exceed 20 g/dL; however, individuals remain asymptomatic without evidence of ischaemic complications. Polycythaemia is thought to occur due to increased erythropoietin (EPO) gene expression that regulates erythropoiesis[50]. Transition metals such as Mn, cobalt (Co) and nickel (Ni) are known to activate DNA binding of hypoxia inducible factor (HIF) to *EPO*[60,61]. HIF is a heterodimeric transcription factor that mediates the transcription of O_2-regulated genes in response to hypoxia. It consists of an O_2

sensitive alpha subunit (HIFα) and a constitutively expressed beta subunit (HIFβ). Three alpha subunits exist, HIF-1α, HIF-2α and HIF-3α. While HIF-1α and HIF-2α function as transcriptional activators of hypoxia dependent genes, the role of HIF-3α is less understood and may have opposing effects[62]. During normoxia the HIFα subunit forms a complex with von Hippel-Lindau protein (vHL) which is subsequently ubiquitinated and degraded in proteasomes. Binding of vHL is facilitated by the action of O_2 dependent prolylhydroxylases (PHD) that convert proline to hydroxyproline. Three PHD enzymes exist, PHD-1 (EGLN2), PHD-2 (EGLN1) and PHD-3 (EGLN3).[63] During hypoxia and exposure to transition metals the vHL-HIFα complex does not form and HIF can induce EPO gene expression[60,61,64] (**Figure 1.1**).

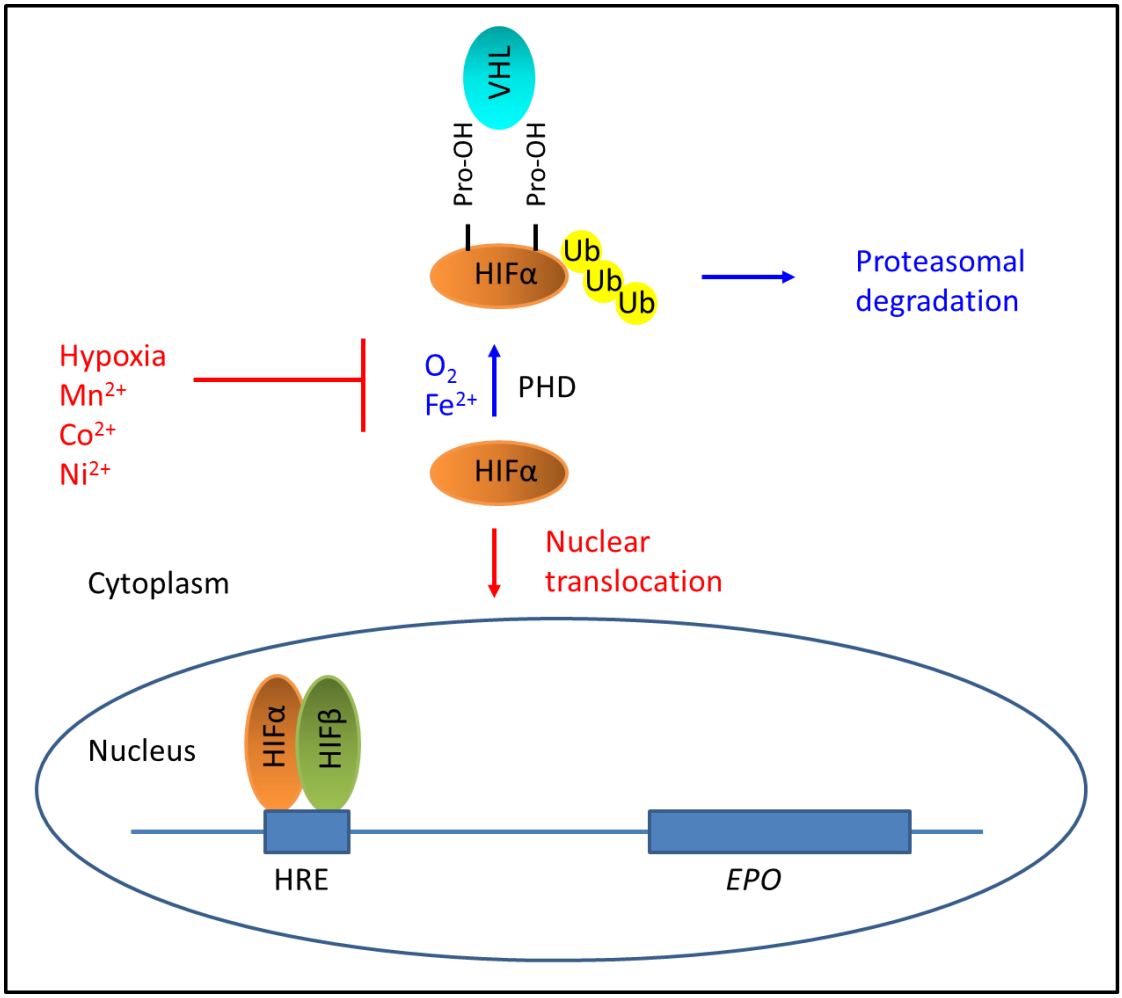

Figure 1.1 Mn induces erythropoietin gene expression.

Schematic demonstrating the effects of divalent metals such as Mn^{2+}, Co^{2+} and Ni^{2+} on the transcription of EPO. Under physiological conditions HIFα is hydroxylated by O_2 and Fe^{2+} dependent prolyl-4-hydroxylases (PHD) with subsequent ubiquitination by the VHL-E3-ubiquitin ligase complex that targets HIFα for proteasomal degradation. Hypoxia and the presence of high concentrations of divalent metals including Mn^{2+} prevents prolylhydroxylation leading to stabilisation of HIFα, nuclear translocation and HIFα/β dimerisation. HIFα/β heterodimers bind to the hypoxia-responsible element (HRE) upstream of the EPO gene leading to increased EPO transcription. Adapted from Haase et al.[62].

Given the interdependency of Mn and Fe transport[11], it is not surprising that abnormal Fe indices are a feature of this disorder. Hallmarks of inherited hypermanganesaemia are low serum ferritin and Fe levels and elevated total iron binding capacity (TIBC)[46].

Hepatic involvement is variable in this disorder. While some patients die of cirrhosis associated complications in adolescence / early adulthood, others survive into late adulthood without liver disease. Hence, liver disease is not pathognomonic for this disease but when present should further suggest the diagnosis. To date, the majority of identified individuals have some evidence of hepatic involvement including hepatomegaly, raised liver transaminases and unconjugated hyperbilirubinaemia[46]. However, pure neurological phenotypes presenting with dystonia alone can occur. Furthermore, marked intrafamilial phenotypic variability has been observed. Within one family, two siblings have survived into late adulthood with an isolated movement disorder while their sister died of liver failure at the age of 46 years with minimal neurological symptoms[48,58]. Factors determining an individual's susceptibility for liver disease progression have yet to be identified and are likely to involve genetic and environmental aspects.

1.2.2 Diagnosis

Diagnosis of inherited hypermanganesaemia is suggested by the typical clinical findings, biochemical characteristics and MRI brain appearances. While whole blood Mn levels are not usually part of the diagnostic work-up of dystonia or parkinsonism, the association of an extrapyramidal movement disorder, chronic liver disease and polycythaemia together with T1 hyperintensity of the basal ganglia should prompt determination of whole blood Mn levels. In the majority of affected individuals reported to date whole blood Mn levels are elevated above 1,000 nmol/L (reference range <320 nmol/L), hence, whole blood Mn seems to be a reliable disease marker. However, blood Mn levels are affected by chelation therapy and Fe treatment and should be interpreted together with other disease parameters[57].

Brain MRI appearances are pathognomonic for the disease and are similar to those seen in acquired cases of hypermanganesaemia. Mn accumulation in the basal ganglia causes T1 hyperintensities affecting the globus pallidus, putamen, caudate, subthalamic and dentate nuclei while the thalamus and ventral pons are spared. When

the disease is extensive, white matter and anterior pituitary involvement can also be observed. T2-weighted images may show changes, however, to a much lesser extent and are often reported as normal[46,48] (**Figure 1.2**). Improvement of blood Mn levels during can lead to normalisation of the MRI brain appearances following months of treatment[51].

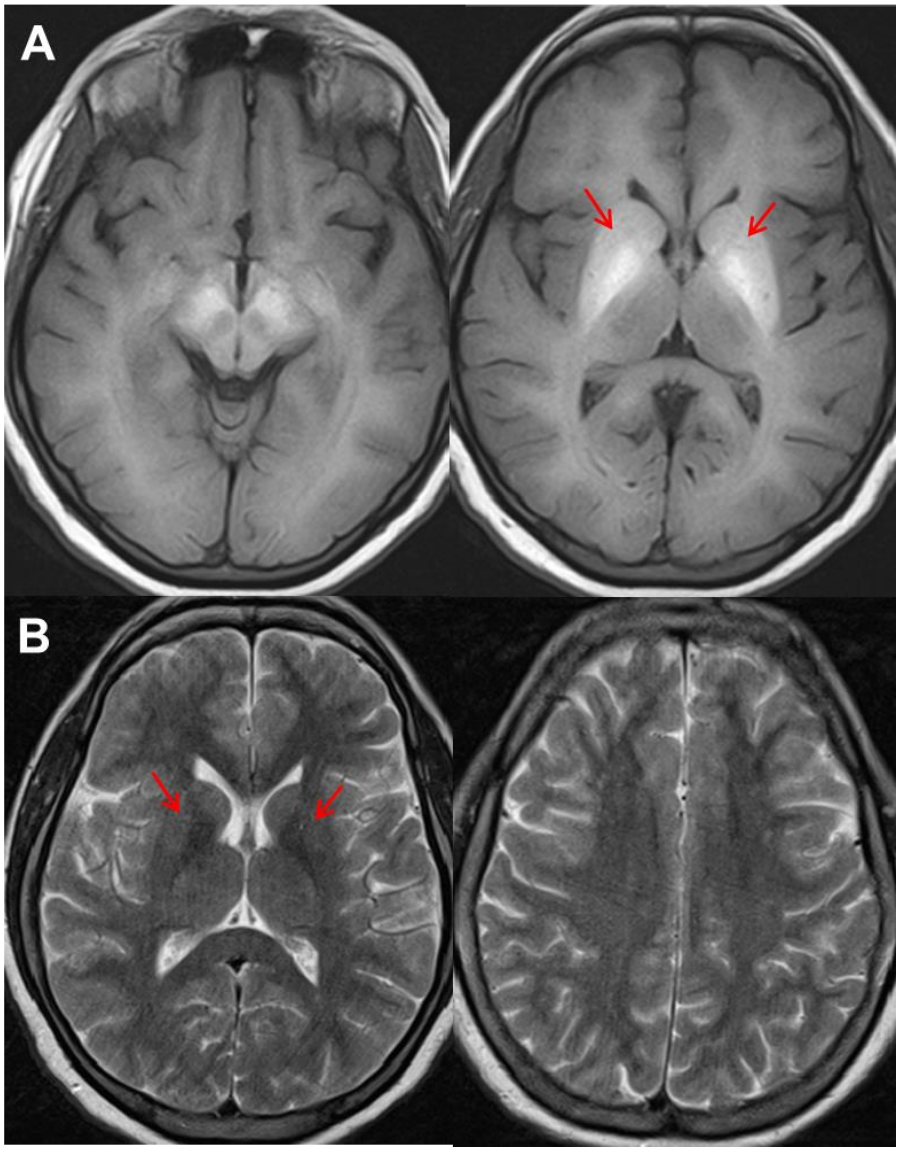

Figure 1.2 Representative MRI brain scan of a patient with SLC30A10 deficiency. *(**A**) Transaxial T1-weighted images: Abnormally high signal return from all white matter as well as more prominent signal return from the putamen and globus pallidus bilaterally (red arrows). (**B**) Transaxial T2-weighted images: Abnormally low signal returned from the globus pallidus (red arrows) in the same distribution as the regions of highest signal returned on T1-weighted images. From Tuschl et al.[46].*

Liver ultrasound and MRI can be helpful to assess liver involvement and severity of cirrhosis. Liver MRI in a patient with SLC30A10 deficiency shows marked hyperintensity due to the deposition of Mn (**Figure 1.3**).

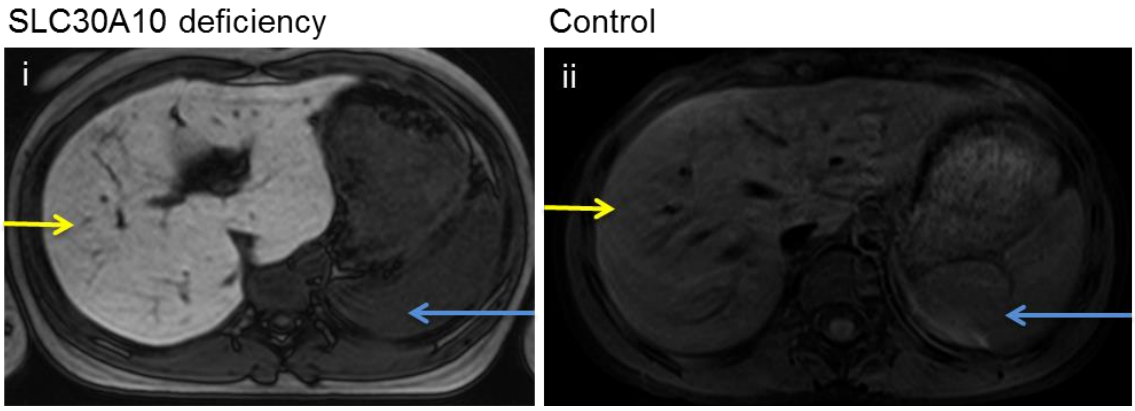

Figure 1.3 Hepatic Mn deposition causes marked hyperintensity of the liver on T1-weighted imaging.

*Transverse abdominal T1-weighted MR images of an individual with (**i**) SLC30A10 deficiency compared to (**ii**) a healthy control subject. Signal intensity of the liver (yellow arrow) is compared to that of the spleen (blue arrow). From Tuschl et al.*[65]

Liver biopsies performed in individuals with progressive liver disease has confirmed accumulation of Mn. Histologically, various degrees of liver fibrosis, steatosis and cirrhosis have been reported[46,48]. Rhodanine staining for Mn is positive and the liver Mn level is above the normal range of 1-2 µg Mn / g wet weight[50] (**Figure 1.4**).

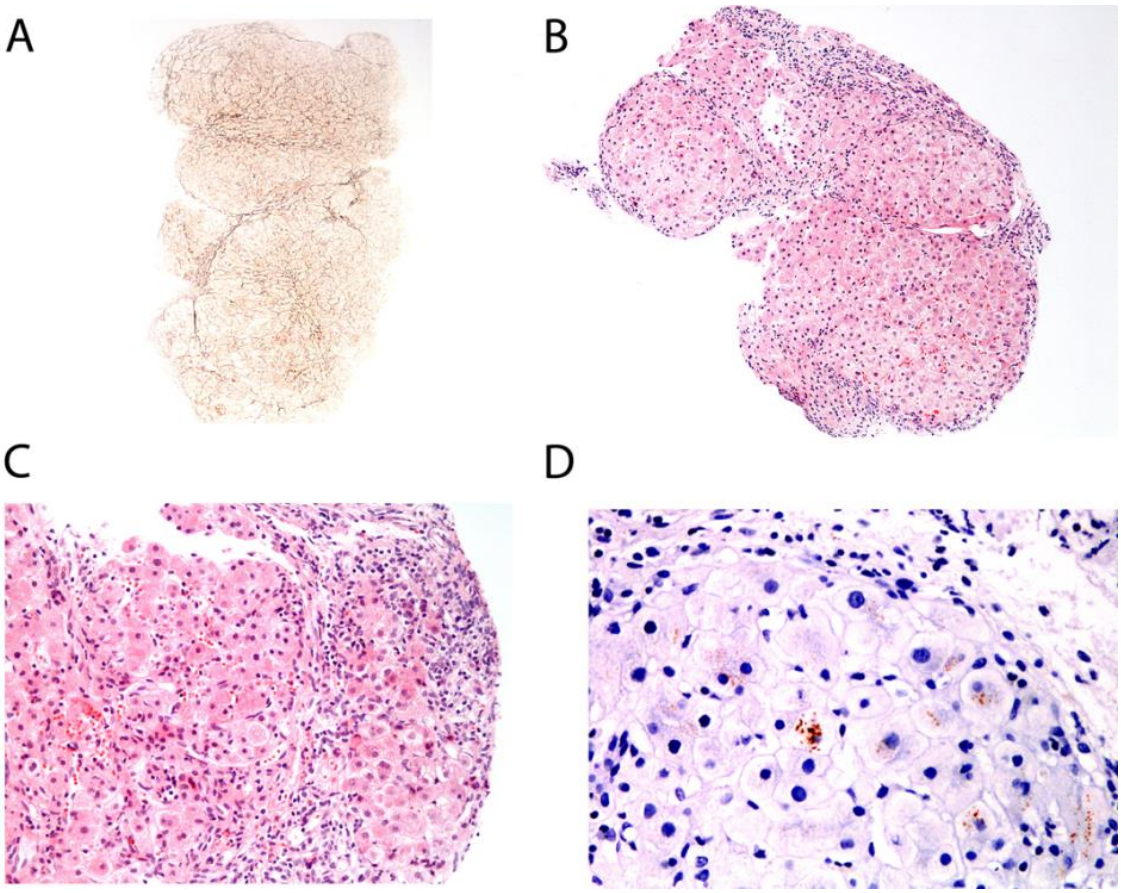

Figure 1.4 Liver histology of a patient with SLC30A10 deficiency.

*(**A**) Reticulin stain x40 (visualising collagen fibres), (**B**) Haematoxylin and eosin stain x100 (H&E) (nucleus and cytoplasm staining), and (**C**) H&E x200 of a fragmented liver biopsy shows bridging fibrosis and cirrhosis. (**D**) Rhodanine stain x400 shows scanty granular positive staining for copper (Cu) and/or Mn. From Tuschl et al.[50].*

Mutation analysis of *SLC30A10* confirms the diagnosis. To date, 13 different mutations in *SLC30A10* have been described in 13 families[46,48,49] (**Figure 1.5**). The mutation found in the sibship with adult-onset parkinsonism affects the terminal 3' end of the coding sequence resulting in a protein that is truncated by only the last 49 amino acids (family M in Figure 1.5). It is possible that this mutant allele produces a protein with residual function causing a milder phenotype[46,48].

Family	Exon	Mutation	
A	3-4	g.1qdel218.057.426_218.158.564bp	
B	1	c.266T>C	p.Leu89Pro
C	1	c.292_402del	p.Val98_Phe134del
D	1	c.314_322del	p.Ala105_Pro107del
E	1	c.460C>T	p.Gln154*
F	1	c.492delC	p.Gly165Alafs*27
G	1	c.496_553del	p.Ala166Glnfs*7
H	1	c.500T>C, 507delG	p.Phe167Ser, Pro170Leufs*22
I	1	c.585del	p.Thr196Profs*17
J	3	c.765_767del	p.Val256del
K	3	c.922C>T	p.Gln308*
L	4	c.1046T>C	p.Leu349Pro
M	4	c.1235delA	p.Gln412Argfs*26

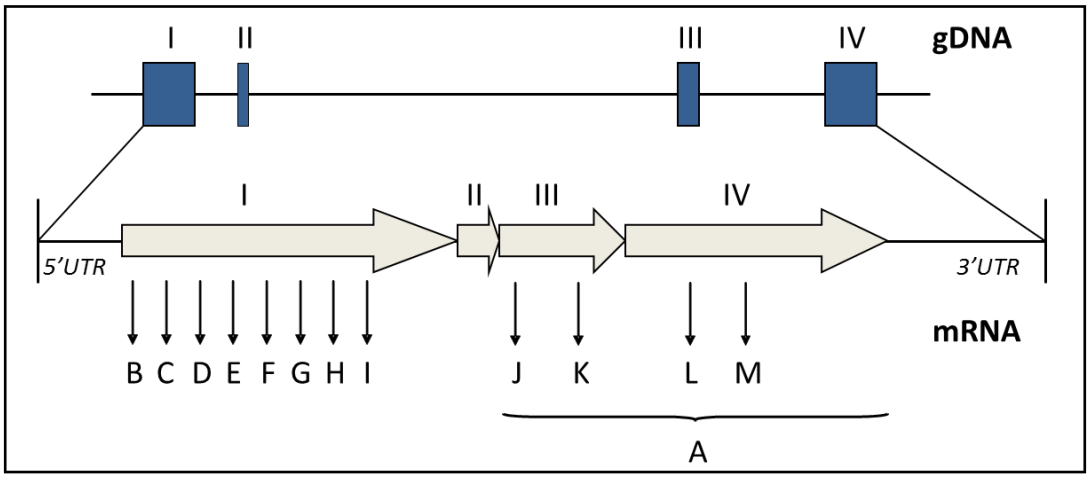

Figure 1.5 Reported mutations in *SLC30A10* identified in families affected by inherited hypermanganesaemia with dystonia-parkinsonism.

Table showing the SLC30A10 mutations identified to date. Family A-D and I-L are from Tuschl et al.[46], Family E-H and M from Quadri et al.[48,49]. Genomic structure of the exons (blue boxes) and introns (black line) of SLC30A10. Positions of identified mutations are displayed below (not drawn to scale). The large deletion spanning exon 3 and 4 in family A is indicated by a bracket.

1.2.3 Treatment

Chelation therapy with intravenous disodium calcium edetate ($Na_2CaEDTA$) has proven effective in childhood and adult-onset forms of *SLC30A10* related parkinsonism-dystonia[46,48]. Response to an initial five-day course of twice-daily disodium calcium edetate at 20 mg/kg/dose (maximum 2 g/day) markedly increased urinary Mn excretion suggesting effective chelation of Mn[50]. $Na_2CaEDTA$ is given intravenously because of poor enteral absorption. Long-term treatment with monthly five-day courses of $Na_2CaEDTA$ (20 mg/kg/dose twice daily) led to significant reduction of whole blood Mn levels, normalisation of Hb and Fe indices, and improvement of MRI brain appearances. Biochemical changes were accompanied by clinical recovery with normalisation of gait, increased mobility, improved fine motor movements and halt of liver disease progression[48,51]. $Na_2CaEDTA$ has the potential to cause nephrotoxicity and can impair the homeostasis of other heavy metals such as copper (Cu) and zinc (Zn)[66]. However, in cases of inherited hypermanganesaemia it has proved an effective and safe chelator with minimal adverse effects. Nephrotoxicity was not observed even during long term treatment. A mild decrease in blood Zn levels was corrected using low dose Zn supplementation. Other heavy metal concentrations remained stable. While on treatment, monitoring of serum electrolytes including calcium, phosphate and magnesium, renal and liver function, full blood count, and serum concentrations of trace metals such as Zn, Cu, and selenium (Se) is recommended[57].

In cases of inherited hypermanganesaemia Fe indices are suggestive of Fe depletion, hence, optimisation of Fe intake was attempted in order to lower intestinal Mn uptake. Indeed, Fe supplementation alone and in addition to chelation therapy effectively lowered blood Mn and further reduced the body Mn load[50,67]. This is attributed to the interdependency of Fe and Mn levels in states of deficiency as mentioned above[11].

Other chelation agents including D-Penicillamine and para-aminosalicylic acid (PASA) have been used with little effect[50,68]. A single individual has been treated with dimercaptosuccinic acid (DMSA) and Fe leading to a marked improvement of neurological symptoms (data from personal communication). Whether this effect is due to the chelating action of DMSA or Fe supplementation itself is debatable.
In cases of end stage liver disease liver transplantation should be considered. However, to date transplantation has not been attempted in individuals with inherited hypermanganesaemia, hence, no data on the outcome is available.

Although SLC30A10 transporter deficiency responds well to chelation therapy with $Na_2CaEDTA$, the treatment is burdensome due to the requirement for intravenous administration and monthly hospital admissions associated with high socioeconomic costs. Moreover, repeated or long-term vascular access carries the risk of infections and is associated with considerable discomfort. Therefore, the identification of an effective oral chelation agent would be favourable that will allow uncomplicated treatment of any patient affected with SLC30A10 deficiency.

1.3 Mn transport and homeostasis

The recent identification of inherited Mn transportopathies caused by loss-of-function mutations in *SLC30A10* and *SLC39A8* has contributed hugely to our understanding how Mn homeostasis is regulated in humans[15,16,46,48,49]. The mechanisms of Mn homeostasis and Mn transport have been the subject of many studies, however, the exact routes of Mn transfer across the cell remain controversial. Numerous transporters have the ability to transport Mn *in vitro* including SLC39A8 and SLC39A14, DMT1, transferrin/transferrin receptor, calcium channels, Mn citrate shuttle, SLC30A10, ferroportin, secretory pathway and sarco-endoplasmic reticulum Ca^{2+} ATPases and ATP13A2 (**Figure 1.6**).

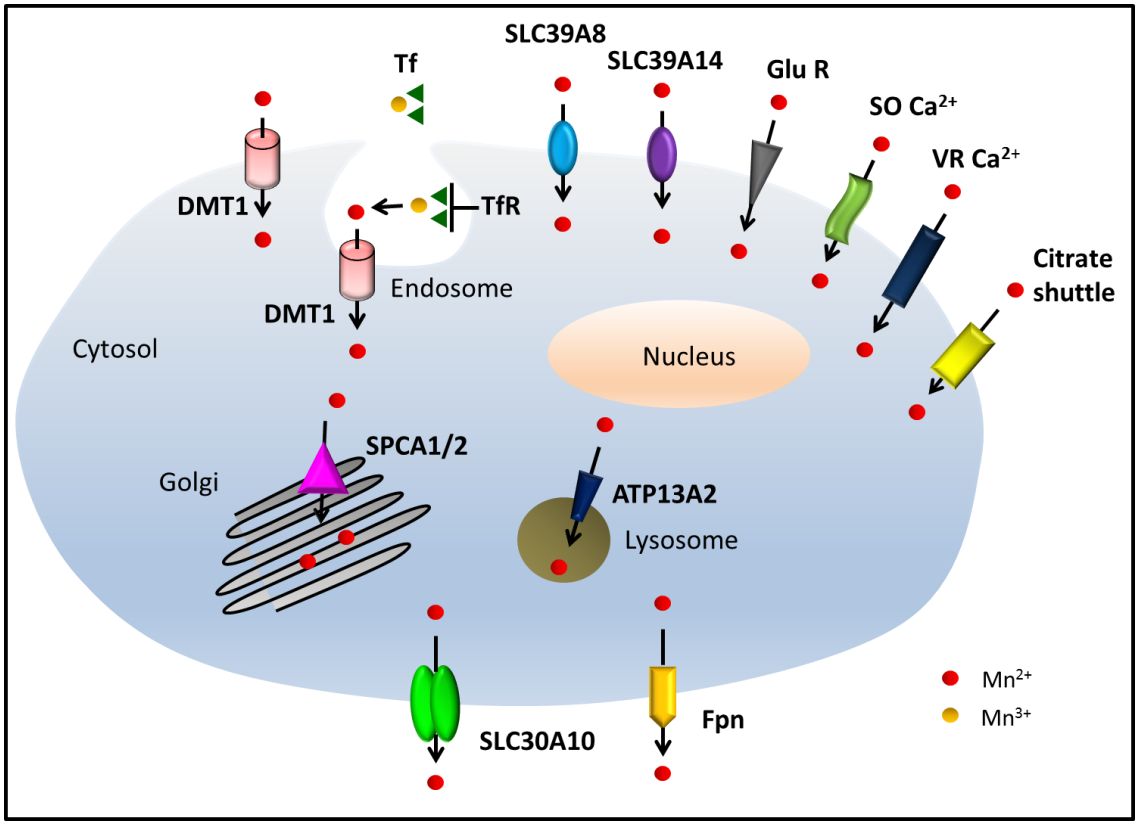

Figure 1.6 Transporters potentially involved in Mn trafficking across the cell.
DMT1; Divalent metal transporter 1. Tf; Transferrin. TfR; Transferrin receptor. Glu R; Glutamate receptor. SO Ca^{2+}; Store operated Ca^{2+} channel. VR Ca^{2+}; Voltage Regulated Ca^{2+} Channel. Fpn; Ferroportin.

1.3.1 Mn uptake

Current literature suggests the following transporters to play a role in Mn uptake:

1.3.1.1 SLC39A8 and SLC39A14

SLC39A8 and SLC39A14, also known as Zrt, Irt-like protein 8 and 14 (ZIP8 and 14) are both members of the solute carrier-39 family and transport divalent metals. They are expressed in tissues involved in the regulation of Mn homeostasis including duodenum, liver, brain, lungs and kidney. *In vitro* studies have shown that they are capable of transfering Mn, Fe, Zn and cadmium (Cd) into the cell. ZIP8 and ZIP14 are Mn^{2+}/HCO_3^- symporters that use a HCO_3^- gradient across the plasma membrane as the driving force for Mn uptake[69-72]. Given that both transporters are localised on apical surfaces of brain capillaries and transport Mn^{2+} with high affinity it is plausible that they facilitate Mn uptake into the brain[70,73,74]. Studies on the function of ZIP8 and ZIP14 have shown that they also play a role in the absorption of Mn in the liver and the proximal tubule in the kidney[69,70]. The recent discovery that mutations in *SLC39A8* cause a deficiency syndrome with low Mn blood levels suggests that this transporter is a major facilitator of Mn uptake into the organism[15,16].

1.3.1.2 Divalent Metal Transporter 1

Divalent Metal Transporter 1 (DMT1) transports both Mn and Fe, and also a range of other cations, and acts as H^+ - symporter that transports one H^+ and one divalent cation in the same direction[75]. It is ubiquitously present in human tissues with high levels of DMT1 found in the duodenum and the brain. DMT1 is thought to contribute to absorption of Mn into the enterocyte in the proximal small bowel. DMT1 expression is regulated by Fe status leading to increased DMT1 expression at the enterocyte membrane during Fe deficiency[76]. Consequently, in Fe deficiency, Mn absorption across the intestine is increased with subsequent Mn accumulation in the brain. Conversely, diets high in Mn lead to decreased plasma Fe levels with an increase in transferrin (Tf) and total iron binding capacity[11,77]. Mutations in *SLC11A2*, the gene encoding DMT1, in the microcytic (mk) mice and Belgrade (b/b) rats affect both Mn and Fe transport across the intestine and result in severe microcytic anaemia[78-80].

Additionally, DMT1 has been suggested to transfer divalent Mn^{2+} at the blood brain barrier. However, there is contradictory data as to whether DMT1 is actually expressed in capillary endothelial cells[78,81]. Furthermore, it has been shown that Mn^{2+} uptake requires a neutral pH which is not consistent with the acidic pH optimum required for DMT1 facilitated uptake[82]. On the other hand, highest expression levels of DMT1 in the brain are found in the dopamine rich areas of the basal ganglia, the brain regions most affected by Mn toxicity[83]. In addition, DMT1 expression is induced upon Mn exposure which is associated with increased dopaminergic neurotoxicity[84]. Furthermore, DMT1 is involved in the endosomal uptake of Mn via the transferrin receptor (TfR)[85].

1.3.1.3 Transferrin/Transferrin Receptor

Mn^{3+} has a high affinity for transferrin (Tf) and in the blood around 20% of total Mn is bound to Tf as Mn^{3+}. Binding of the Tf-Mn^{3+} complex to the Tf receptor (TfR) at the plasma membrane causes internalisation of the Tf-TfR complex into endosomal vesicles. The endosomal V-ATPase facilitates acidification of the vesicle and leads to release of the metal, followed by conversion of Mn^{3+} to Mn^{2+} and activation of endosomal DMT1 with subsequent uptake of Mn into the cytosol[86,87]. Tf and DMT1 co-localise at the endosomal membrane at the blood brain barrier supporting the theory of Tf dependent uptake of Mn[85].

1.3.1.4 Ca^{2+} channels

The relative contribution of Ca^{2+} channels to Mn transport into the brain has still to be determined. Evidence suggests that both voltage-regulated and store-operated Ca^{2+} channels mediate brain Mn influx[88,89]. The ionotropic glutamate receptor channel is yet another candidate proposed to facilitate Mn uptake into the brain[90].

1.3.1.5 Mn citrate shuttle

Mn citrate represents the major non-protein bound species of Mn to enter the brain at the blood brain barrier. The influx transfer coefficient for Mn citrate was shown to be greater than that of Mn^{2+} alone and Tf-Mn^{3+} [91].

1.3.2 Mn export

The following transporters have been shown to facilitate Mn export:

1.3.2.1 SLC30A10

Recently, we have identified SLC30A10 as a key player in the regulation of Mn homeostasis[46,48]. Recognised as the disease causing gene in an inherited Mn overload syndrome, it is thought to mediate Mn export at the cell membrane[47]. SLC30A10 belongs to the cation diffusion facilitator (CDF) family of divalent metal ion transporters[92]. They share the same structure of six TMDs with cytosolic N and C termini and a conserved cation efflux domain at the C terminus (**Figure 1.7**).

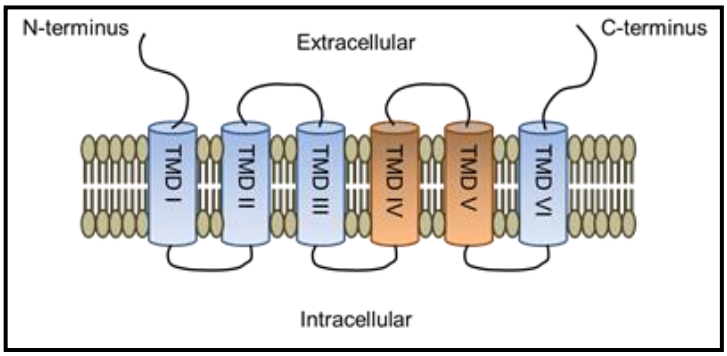

Figure 1.7 SLC30A10 protein structure.
Schematic of SLC30A10 showing its six TMDs (orange and blue cylinders) interlinked by intracellular and extracellular loops. TMD I, II, III and VI are postulated by the transmembrane protein topology prediction tool MemSatSVM (http://bioinf. cs.ucl.ac.uk/psipred/?memsatsvm=1) to form a pore.

Sequence homology with transporters from the same family has suggested a role of SLC30A10 in Zn transport[93]. However, our recent work examining its function in the Mn sensitive yeast strain Δ*pmr1* has confirmed its ability to transport Mn and protect cells from Mn toxicity. *pmr1* (plasma membrane ATPase-related) encodes a P-type Ca^{2+} /Mn^{2+} ATPase located at the Golgi membrane that is involved in the transport of Mn^{2+} from the cytosol into the Golgi. Deletion of *pmr1* leads to accumulation of Mn in the cytosol and increased sensitivity of cells to high concentrations of Mn[94]. Transformation

of Δ*pmr1* yeast with human *SLC30A10* rescues growth under high Mn concentration while mutations in *SLC30A10* abolish the effect[46] (**Figure 1.8**).

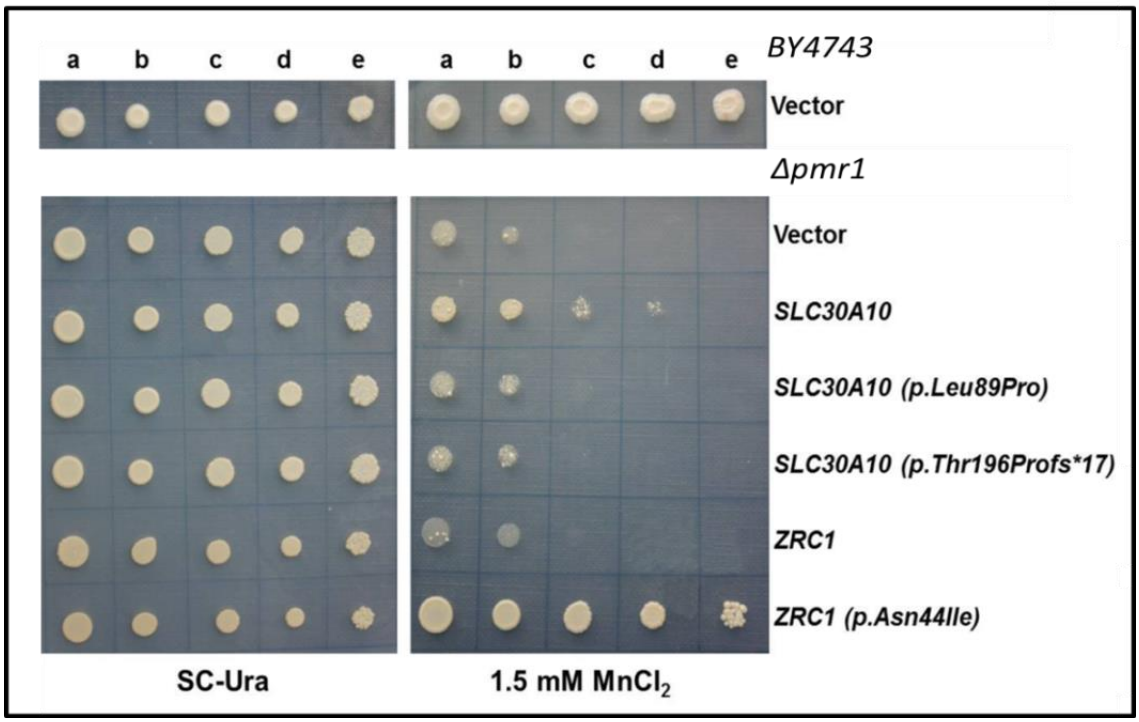

Figure 1.8 Human SLC30A10 protects Δpmr1 yeast from Mn toxicity.
*Image showing yeast strains grown on media without (left) and with 1.5mM $MnCl_2$ (right) supplementation. Each strain was spotted at a density of 10^5, 5 x 10^4, 10^4, 5 x 10^3 and 10^3 cells (a–e). While wild-type BY4743 cells grow normal on either medium, the Δpmr1 strain shows growth inhibition upon $MnCl_2$ exposure. Human SLC30A10 rescues growth of Δpmr1 on Mn supplemented medium while the missense mutation (Leu89Pro) or nonsense mutation (Thr196Profs*17) abolish the effect. ZRC1 (yeast orthologue to SLC30A1 and SLC30A10 with metal affinity to Zn only), and ZRC1 (Asn44Ile) (mutation altering metal specificity from Zn to Mn and Fe)[94] were used as negative and positive controls, respectively. Taken from Tuschl et al.[46].*

The alteration in the metal binding affinity of the transporter was attributed to evolutionary changes of the amino acid sequence of the protein[46]. Studies in yeast have shown that a single amino acid change in ZRC1 (Asn44Ile), the yeast orthologue of SLC30A1 and SLC30A10, alters the metal specificity of the transporter. While ZRC1 has affinity to Zn, the Asn44Ile mutation changes its affinity from Zn to Mn and Fe[94]. In

the SLC30A10 protein, the key structures required for Zn binding such as a histidine rich region in the cytosolic loop between TMD IV and V and a conserved HxxxD motif in TMD II are altered. The HxxxD motif in TMD II is replaced by an asparagine while the histidine rich region is replaced by sequences rich in arginines, lysines and serines. An absence of the histidine rich region has also been observed in another plant Mn transporter called ShCDF8. ShCDF8 shares a conserved cytosolic cysteine residue at TMD IV with SLC30A10 that is absent in other Zn specific transporters of the CDF family[48].

Studies investigating the subcellular localisation of SLC30A10 in human neuroblastoma SH-SY5Y cells have shown it localises to the Golgi. High extracellular Zn concentrations cause the redistribution of SLC30A10 to the plasma membrane[95]. More recently, Leyva-Illades and co-workers showed that SLC30A10 localises to the cell membrane in HeLa cells and *C. elegans* where it functions as a Mn efflux transporter and protects against Mn toxicity[47]. Mutations in *SLC30A10* affect the intracellular trafficking of the transporter from the endoplasmic reticulum to the cell membrane and impair its efflux function[47]. *SLC30A10* is highly expressed in the small intestine, liver and brain tissues consistent with Mn accumulation seen in these tissues in humans with *SLC30A10* mutations[95]. High concentrations of Mn lead to increased *SLC30A10* transcription and protein expression in HepG2 hepatocellular carcinoma cells consistent with a role of SLC30A10 in the detoxification of Mn from the cytoplasm[48].

1.3.2.2 Ferroportin

Efflux of Mn from the enterocyte is believed to occur via Ferroportin (Fpn). Once absorbed into the portal circulation, the majority of Mn (approximately 80%), becomes bound to β-globulin and albumin as bivalent Mn^{2+}. Some is oxidised to Mn^{3+} by ceruloplasmin and bound to transferrin as trivalent Mn^{3+} [96]. The cytoplasmic Fe exporter ferroportin has been shown to act as an effective mediator of Mn efflux. Ferroportin is highly expressed at the plasma membrane of all relevant Fe exporting cells such as enterocytes, hepatocytes and macrophages, and is also present in neurons and oligodendrocytes. Mn exposure significantly increases ferroportin expression with subsequent reduction of total cell Mn and attenuated Mn toxicity[97,98]. Patients with mutations in the ferroportin gene *SLC40A1* develop haemochromatosis

type 4 with Fe overload within the reticuloendothelial system[99]. However, the effect on Mn homeostasis has not been studied in humans. Ferroportin deficient flatiron (ffe) mice show reduced blood, hepatic and bile Mn levels. Furthermore, expression of wild-type Fpn reverses Mn-induced cytotoxicity in dopaminergic SH-SY5Y cells and human embryonic kidney (HEK293) cells while mutant protein fails to confer protection[100]. Hepcidin, a peptide hormone produced by the liver, plays a pivotal role in systemic Fe homeostasis by regulating the activity of ferroportin. High Fe levels and inflammation increase hepcidin expression followed by internalisation and degradation of the hepcidin-ferroportin complex[101]. Recently, Mn has also been shown to induce hepcidin expression in hepatocytes providing a further link between Mn and Fe homeostasis[102].

1.3.2.3 SPCA and SERCA

The Secretory Pathway Ca^{2+}/Mn^{2+}ATPases SPCA1 and SPCA2 localised at the Golgi provide an alternative route of cytosolic Mn detoxification. Both pumps have high affinity for Ca^{2+} and Mn^{2+} ions and sequester these ions into the Golgi. Overexpression of *SPCA1* facilitates Mn accumulation in the Golgi and increases cell viability[103]. While *SPCA1* is ubiquitously expressed, *SPCA2* has a more restricted expression pattern limited to the gastrointestinal tract, brain and testes. Monoallelic mutations in *SPCA1* are known to cause Hailey-Hailey disease, a blistering skin disorder, while biallelic sequence changes with complete loss of function are thought to be incompatible with life[104,105]. Mice exposed to high levels of Mn accumulate this metal in areas of the brain that show high expression of *SPCA1* further supporting a role of SPCA1 in Mn detoxification[106]. Similarly, SPCA1 has been shown to facilitate Mn detoxification in the liver by sequestering Mn into the Golgi and early endosomes[107].

The sarco/endoplasmic reticulum Ca^{2+} ATPases (SERCA) have also been suggested to transport both Ca^{2+} and Mn^{2+}, however, Mn^{2+} is only a weak competitor of Ca^{2+} for the transport sites[108-110].

1.3.2.4 ATP13A2

The discovery of *ATP13A2* (PARK9) as the gene affected in a rare form of juvenile-onset Parkinson's disease, also known as Kufor-Rakeb Syndrome, has provided an additional insight into Mn trafficking. *ATP13A2* encodes a P5-type cation-transporting

ATPase located at the lysosome that protects cells from Mn-induced toxicity. Overexpression of *ATP13A2* leads to decreased levels of intracellular Mn. Expression of *ATP13A2* is found to be highest in the substantia nigra, the region of dopaminergic neuron loss in Parkinson's disease. Exposure to excess Mn further induces *ATP13A2* gene expression followed by sequestration of Mn into the lysosome[38,40,111,112].

1.4 Mechanisms of Mn toxicity

While it has long been recognised that Mn causes neurotoxicity the exact mechanisms leading to neurodegeneration and neuronal dysfunction have not been identified. Mn has been shown to affect dopamine, gamma aminobutyric acid (GABA) and glutamate neurotransmitter signalling, induce oxidative stress and mitochondrial dysfunction, and affect autophagy and apoptosis[22,113].

1.4.1 Mn and its effect on dopamine neurotransmission

Mn neurotoxicity causes an extrapyramidal motor disorder that resembles idiopathic Parkinson's disease. However, it remains debatable whether manganism and Parkinson's disease share common cellular mechanisms[114]. The hallmark of Parkinson's disease is the degeneration of the nigrostriatal dopaminergic neurons in the substantia nigra pars compacta that innervate the caudate and putamen. This is consistent with a loss of dopamine transporter (DAT) levels and reduced dopa decarboxylase activity in the substantia nigra in single-photon emission computed tomography (SPECT) and PET studies of Parkinson's disease patients[114,115]. In contrast, the most significant effects of Mn toxicity occur in the striatum while synthesis of dopamine and DAT levels in the substantia nigra are preserved in most cases[22,116,117] (**Figure 1.9**).

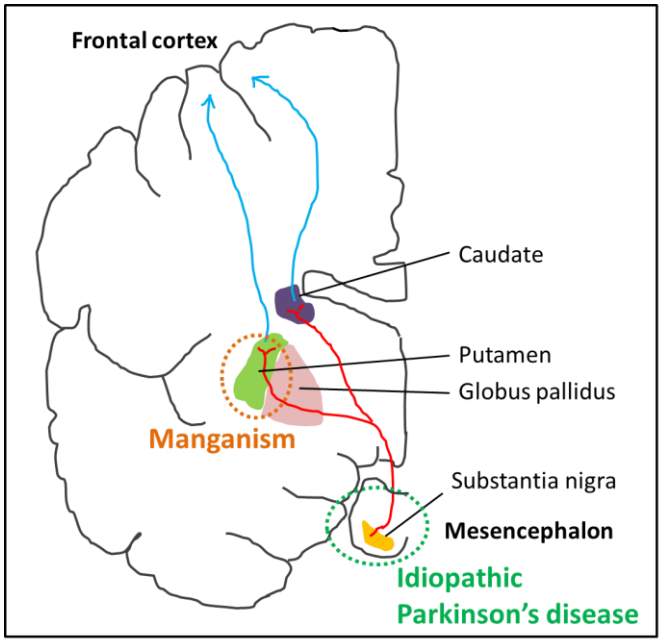

Figure 1.9 Basal ganglia pathways affected in manganism and idiopathic Parkinson's disease.
Red: nigrostriatal dopaminergic neurons. Striatum = Caudate + Putamen. Blue: projections to the cortex.

While some studies have described a loss of dopaminergic neurons within the substantia nigra upon Mn exposure[118], the majority of studies report intact pre-synaptic dopaminergic neurons[22,119]. Given the overlapping clinical symptoms between manganism and Parkinson's disease, it is likely that dopamine neurotransmission is affected in both conditions. However, the disturbance most probably occurs at different points within the complex neuronal pathways in the basal ganglia[120]. PET studies in patients with manganism showed that nigrostriatal neurons are not degenerated[121]. Indeed, recent studies have confirmed that chronic Mn exposure significantly impacts on amphetamine-induced dopamine release in the striatum while the neurons in the substantia nigra remain intact. Furthermore, a significant decrease in DAT levels in the striatum was observed in Mn exposed primates and rats[119,122]. Mn was also found to decrease dopamine uptake and dopamine efflux in DAT transfected HEK293 cells by promoting redistribution of DAT from the cell surface to the internal compartment of the cell[120]. Other studies showed that expression of postsynaptic D2-dopamine receptors (D2R) is down-regulated in the basal ganglia and the midbrain following Mn exposure[84,123,124]. In Parkinson's disease on the other hand the level of postsynaptic D2Rs is either unaffected or increased. Overall, there is increasing evidence that Mn neurotoxicity causes abnormal dopaminergic signalling while dopamine neuron integrity within the substantia nigra remains preserved[119]. This is consistent with the fact that in patients with mutations in *SLC30A10*, Mn toxicity is reversible to some degree with removal of Mn by chelation therapy[50].

Intrastriatal Mn injections in the rat brain have been found to cause dopaminergic neuron loss[125]. Studies in *C. elegans* have shown that Mn has the ability to induce dopaminergic specific neurodegeneration. This neurotoxicity is dependent on the presence of extracellular dopamine and requires functional dopamine reuptake via DAT[126]. It was concluded that dopamine is required for Mn toxicity to occur and that Mn and dopamine work together synergistically resulting in selective dopaminergic neurotoxicity. Mn was suggested to mediate oxidation of extracellular dopamine which, after uptake via DAT, causes oxidative injury and degeneration of dopaminergic neurons[127].

1.4.2 Effects of Mn on Glutamine, Glutamate and γ-Aminobutyric acid (GABA) signalling

Glutamine is an important precursor in the brain for the synthesis of both the excitatory neurotransmitter glutamate and the inhibitory neurotransmitter γ-aminobutyric acid (GABA), and plays a critical role in neuron-glia interactions[128]. Glutamate and GABA neurons both project widely within the basal ganglia and are involved in the regulation of motor coordination. Astrocytes facilitate the regulation of glutamate-glutamine cycling between astrocytes and neurons and have in fact been shown to accumulate Mn to a much higher extent than neurons[129-132]. Mn exposure impairs astrocytic glutamine transport by reducing the expression of specific glutamine transporters with subsequent decrease in glutamine uptake[128]. Mn is thought to promote ubiquitination and degradation of the transporter protein by a mechanism involving the protein kinase C (PKC) signalling pathway[133]. In addition, the uptake of glutamate via the astrocytic glutamate:aspartate transporter (GLAST) is affected by Mn, leading to increased extracellular glutamate levels and neuronal excitability[134]. This is consistent with the finding of N-methyl-D-aspartate (NMDA) excitotoxic lesions following the local intrastriatal injection of $MnCl_2$ into rat striatum[125]. Glutamate further augments Mn induced toxicity as both Mn and glutamate toxicity affect Ca^{2+} accumulation in the mitochondria promoting cell death[135].

Upon Mn exposure, extracellular GABA concentrations are increased due to altered expression levels of GABA transporters and receptors causing reduced uptake of GABA[136,137]. The authors suggest that the increased extracellular levels of GABA in the striatum affect the activity of the GABA projections to the substantia nigra, thus facilitating increased inhibition and impaired striatal dopamine release via the nigrostriatal pathway. Consistent with these findings, magnetic resonance spectroscopy (MRS) studies in Mn exposed workers confirmed raised levels of GABA in the thalamus and adjacent brain regions[138].

1.4.3 Effects of Mn on oxidative stress and mitochondrial dysfunction

Exposure to high levels of Mn has been shown to be involved in the production of reactive oxygen species (ROS) and enhanced oxidative stress. The most common ROS include the superoxide radical (O_2^-), hydrogen peroxide (H_2O_2) and hydroxyl radical ($OH^\cdot$) leading to damage of nucleic acids, proteins and phospholipids[139-141]. Within the cell, Mn preferentially concentrates in the mitochondria via the Ca^{2+} uniporter[142]. Long term Mn exposure increases oxidative stress markers including p38 mitogen-activated protein kinase (MAPK) phosphorylation and caspase activity in the striatum[143]. Furthermore, intracellular levels and activation of antioxidants such as glutathione and catalase are augmented following Mn exposure[144-146]. Consistent with a role of Mn in the production of oxidative stress, treatment of Mn exposed cells with antioxidants attenuates Mn toxicity[143,147,148]. The basal ganglia are areas in the brain with high oxidative activity promoting oxidation from Mn^{2+} to Mn^{3+}, the species with a greater pro-oxidant potential, augmenting the auto-oxidation of dopamine[149]. Dopamine auto-oxidation leads to the formation of quinones that are cytotoxic[150]. The main species of Mn in the mitochondria is Mn^{2+} bound to ATP[130]. Mn^{2+} is thought to directly interfere with oxidative phosphorylation causing ROS production[142]. However, the exact pathways that lead to Mn induced production of ROS are still unknown. It is suggested that the first step in ROS generation is the production of O_2^- that can be converted to H_2O_2 by the Mn and Cu/Zn superoxide dismutase in the mitochondria and cytoplasm, respectively. H_2O_2 can be further converted to $OH^\cdot$ in the presence of Mn or other transition metals[139,151].

Recent work demonstrates that Mn exposure in rats leads to decreased complex I activity that can be prevented by treatment with Edaravone, a radical scavenger, further suggesting that ROS overproduction leads to oxidative stress and mitochondrial dysfunction[152]. Mn^{2+} also interferes with Ca^{2+} homeostasis within the mitochondria by occupying Ca^{2+} binding sites. Together with the generation of oxidative stress this leads to the induction of a process named mitochondrial permeability transition (MPT). Opening of a permeability transition pore (PTP) mediates increased solubility of the mitochondrial membrane for ions and protons causing rapid swelling and ultrastructural changes associated with loss of the mitochondrial inner membrane potential, impaired oxidative phosphorylation and ATP synthesis thereby inducing apoptosis and contributing to neurodegeneration[130,131,139].

1.4.4 Role of Mn in neuroinflammation

Whilst Mn can affect neurons directly through oxidative damage and mitochondrial dysfunction, Mn has also been shown to enhance neurotoxicity by activation of glial cells and subsequent release of inflammatory cytokines and non-neuronal ROS. Mn has the ability to induce the release of interleukin (IL) -1β, IL-6 and tumor necrosis factor α (TNF-α) from microglial cells[153]. Mn induced neuronal injury has been shown to require the presence of astrocytes confirming the crucial role of astrocytes in Mn neurotoxicity. This is further supported by the significantly higher levels of Mn accumulating in astrocytes during Mn exposure compared with neurons[132]. In addition, Mn has been shown to alter astrocyte morphology and lead to Alzheimer type II astrocytosis in the globus pallidus[154]. This is associated with increased production of nitric oxide (NO) and increased expression of NO synthase in astrocytes[155]. Mn potentiates cytokine-induced expression of NO synthase and production of NO in astrocytes via activation of soluble guanylate cyclase leading to extracellular signal-regulated kinases (ERK) – dependent enhancement of NF-kappaB signalling[156]. Overall, inflammation of glial cells within the basal ganglia with subsequent neurotoxic injury seems to be an important mechanism of Mn toxicity.

1.5 Zebrafish as a disease model

Given the complexities of the mechanisms involved in Mn toxicity and homeostasis, a simpler *in vivo* model may facilitate the study of Mn metabolism and the effects of Mn accumulation. Zebrafish have been shown to be an excellent vertebrate model organism for monogenetic human disease[157-159].

Over the past decades, the zebrafish has become a powerful vertebrate model for the study of neurodegenerative and metabolic human diseases. Several inherited metabolic disorders have been successfully modelled in zebrafish including aromatic L-amino acid decarboxylase deficiency, maple syrup urine disease, multiple acyl-CoA dehydrogenase deficiency, late infantile neuronal ceroid lipofuscinosis, Niemann Pick disease type C and congenital disorder of glycosylation caused by phosphomannose isomerase deficiency[160-165]. Zebrafish have also proven a valuable tool in the study of neurodegenerative disorders with later disease onset including amyotrophic lateral sclerosis and Alzheimer's disease[166-168]. In addition, zebrafish have been used to analyse the effects of environmental metal toxins and the function of metal transporters such as DMT1 as well as having provided an ideal experimental tool to uncover novel mechanisms of trace metal homeostasis [169,170]. Indeed, trace mineral transporter systems are highly conserved across vertebrate organisms including zebrafish making them a powerful model to study metal metabolism[171].

Zebrafish offer several advantages over other animal models including i) transparency and *ex utero* development of embryos allowing non-invasive observation and live imaging; ii) large numbers of eggs and embryos available for manipulation and high-throughput screening; iii) low costs of maintenance, iv) the availability of transgenic lines expressing fluorescent proteins allowing visualisation of different cell types and the study of organ morphology *in vivo*, v) available tools for precise genome modification including transcription activator-like effector nucleases (TALENs), clustered regularly interspaced short palindromic repeats (CRISPR) / Cas9 system and zinc finger nucleases (ZFN)[157,172]. Furthermore, many pharmacological targets in zebrafish have been shown to be highly similar to those in humans. This together with the large number of embryos available per experiment makes zebrafish an ideal model for drug discovery[172-174]. Zebrafish embryos are permeable to low molecular weight chemical compounds, and therefore drugs and small molecules can simply be added to

the water for drug testing and toxicological studies including studies of metal toxicity[174,175].

The zebrafish genome is now fully sequenced and shares a considerable degree of homology with the human genome confirming the suitability of zebrafish for genetic studies; it has been estimated that 70% of human genes have at least one zebrafish orthologue[176]. In particular, advances in genome editing methods such as TALENs and CRISPR/Cas9 system are now allowing us to uncover the role of disease causing genes and their involvement in disease processes in a cost and time efficient manner. These approaches have been shown to be highly efficient in generating powerful gene knockout models and more recently even gene knock-in animals[168,177-182].

1.5.1 Transcription activator-like effector nucleases (TALENs)

Transcription activator-like effectors (TALEs) are specific DNA binding proteins found in X*anthomonas* bacteria that allow the modulation of host gene expression. TALE proteins consist of a varying number of 34-amino-acid repeats (LTPDQVVAIAS**XX**GGKQALETVQRLLPVLCQDHG) that mediate binding to a specific DNA target sequence (**Figure 1.10**). The residues at positions 12 and 13 (XX) in each 34 amino-acid repeat, the 'repeat-variable di-residue' (RVD), bind to a specific base of the target DNA. When the RVD consists of an asparagine and isoleucine (NI) it recognises the nucleotide 'A', a histidine and aspartic acid (HD) the 'C', an asparagine and glycine (NG) the 'T' and two asparagines (NN) the 'G'. Therefore, a specific sequence of RVDs determines the target nucleotide sequence. Such a TALE repeat array can be *de novo* synthesised and fused to a FokI nuclease at the C-terminus which creates a transcription activator-like effector nuclease (TALEN)[179,181,183-188]. A pair of TALENs binding opposing DNA strands across a spacer region of 14 to 18 bases will cause the dimerisation of the FokI nuclease and result in a double strand break (DSB) of the target DNA. DSBs are repaired primarily by non-homologous end joining (NHEJ) which is error prone and often results in small insertions or deletions (indels) thereby causing gene disruption, or by homologous recombination (HR) which can be utilised for the insertion and replacement of DNA sequences when a template DNA is presented simultaneously[184,189]. TALENs have been successfully used in zebrafish to generate heritable gene mutations that are passed efficiently through the germline[179-181,183,186].

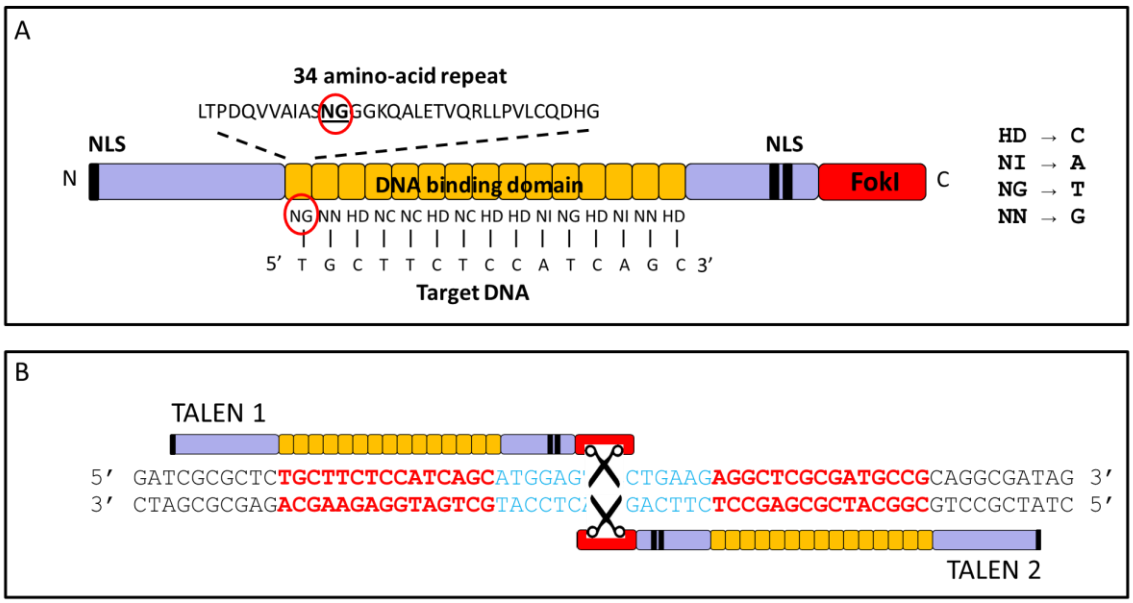

Figure 1.10 TALEN structure.

*(**a**) Schematic diagram of a single TALEN arm. The TAL effector (blue) is fused to a FokI nuclease (red) and contains a sequence of 34 amino-acid repeats (orange) that determines the target DNA sequence. Each 34 amino-acid repeat contains a repeat-variable di-residues (RVD) at position 12 and 13 (red circle). The four RVDs HD, NI, NG and NN within the repeat sequence specifically bind to one of the four nucleotides C, A, T and G, respectively. NLS, nuclear localisation signal. (**b**) Two monomeric TALENs bind to the target DNA sequence (red) allowing the dimerization of FokI in the spacer region (blue) and subsequent DNA cleavage. Adapted from Cermak et al.*[184]

1.5.2 CRISPR/Cas9 genome editing

The clustered regularly-interspaced short palindromic repeats (CRISPR)/Cas system is a bacterial immune system facilitating acquired resistance to invading viruses and plasmids. Foreign DNA fragments, also called “spacers”, are integrated into the bacterial CRISPR locus with subsequent transcription into CRISPR repeat-spacer arrays (crRNAs) that are annealed to a transactivating crRNA (tracrRNA) that facilitates sequence specific cleavage of foreign DNA through the Cas9 nuclease. The Cas9 nuclease only successfully binds to the target sequence if it is followed by a protospacer adjacent motif (PAM) sequence (-NGG-)[185,190]. A single engineered guide RNA (gRNA) can be synthesised *in vitro* that contains a genome specific sequence followed by the sequence of the crRNA and tracrRNA (**Figure 1.11**). Injection of the

gRNA together with an mRNA encoding the Cas9 nuclease into a zebrafish embryo leads to double strand DNA breaks that are subsequently repaired by NHEJ or HR which can be utilised for site specific genome editing[177-179,191].

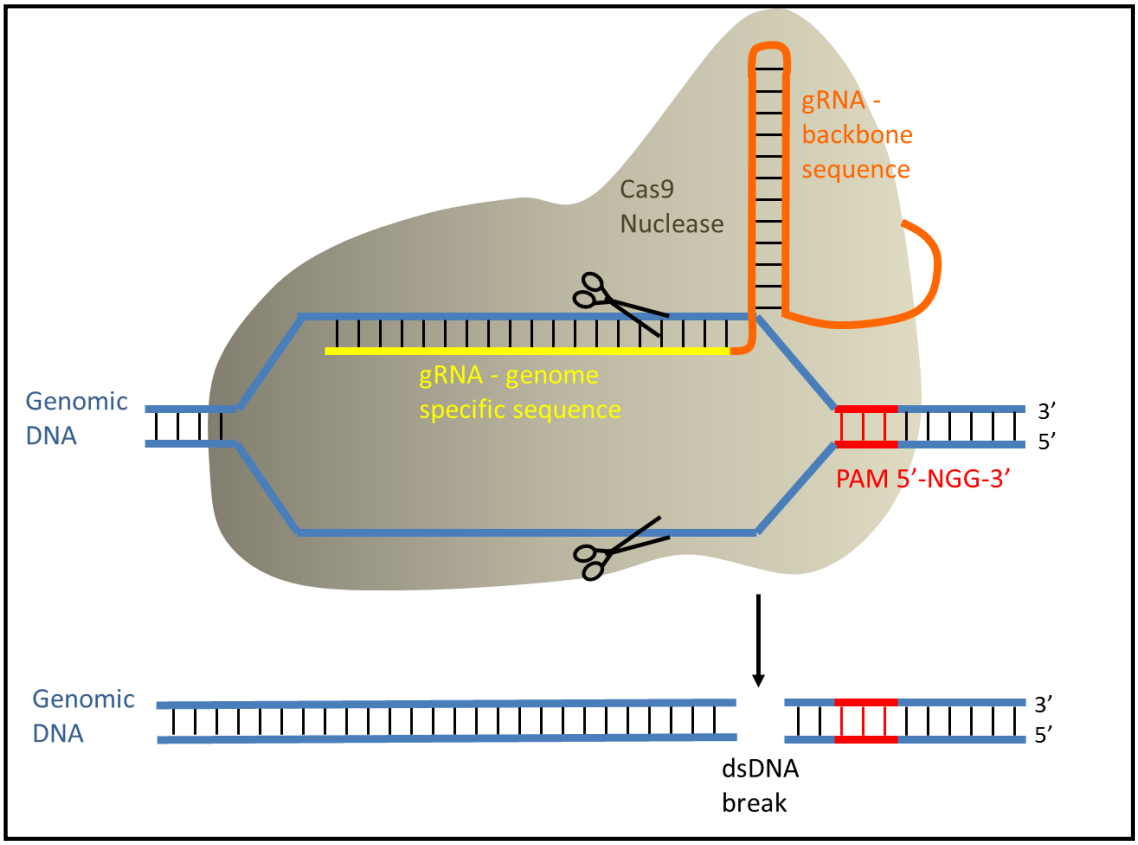

Figure 1.11 Mechanism of gRNA/Cas9 DNA cleavage.

The gRNA consists of a sequence complementary to a specific genomic locus and a backbone sequence containing the crRNA and tracrRNA, and allows recognition of genome specific sequences that are adjacent to a PAM sequence (5'-NGG-3'). Subsequently, the Cas9 nuclease site-specifically cleaves dsDNA.

1.6 Aims and scope of this thesis

As discussed in this Chapter, there is increasing evidence that Mn plays an important role as a neurotoxin both in environmental exposure and in inherited dystonia-parkinsonism. Mn toxicity seems to affect the balance of several neurotransmitters in the basal ganglia, cause neuroinflammation and oxidative stress[192]. However, to what extent each of these pathways contributes to Mn neurotoxicity remains unknown. We have made an important contribution towards a better understanding of Mn homeostasis by the discovery of SLC30A10 as a crucial Mn transporter[46]. Nevertheless, further research is required to elucidate the mechanisms of Mn toxicity and transport and subsequently translate these findings into potential treatments and biomarkers for Mn related neurodegenerative disorders. In this thesis I attempt to shed more light on these unanswered questions.

This thesis aims to

- delineate the phenotypic and genotypic spectrum of inherited Mn transporter defects in any new patients presenting with the clinical characteristics of inherited hypermanganesaemia.
- develop disease models of inherited Mn transportopathies to elucidate disease mechanisms. Because zebrafish are an excellent model in which to study neurodegenerative disorders and amenable to genetic modification as described above in **Section 1.5** they were used to generate loss-of-function mutants of Mn transporter genes.
- assess the phenotype of Mn transportopathy zebrafish mutants to elucidate the pathological processes underlying Mn associated neurotoxicity.

Ultimately, this thesis aims to provide new insights into the pathogenesis of Mn related disease with the view to identify novel therapeutic targets and compounds with disease-modifying potential.

Chapter 2. Materials & Methods

2.1 Reagents

Unless otherwise stated general laboratory chemicals were purchased from Sigma-Aldrich. Protocols for standard laboratory solutions are listed in **Appendix 9.2**.

2.2 Subjects

Patients sharing a neurological phenotype characteristic of Mn deposition in the basal ganglia associated with typical MRI brain appearances were analysed in this study. Informed consent for DNA storage and genetic analyses was obtained from all subjects or parents. The research protocol was approved by the West London Research Ethics Committee (10/H0711/51).

2.3 Molecular biology

2.3.1 Genomic DNA extraction

DNA extraction from human blood samples (1 mL) was performed using the Gentra Puregene Blood Kit (Qiagen) according to the manufacturer's instructions in a final volume of 50 µL DNA hydration solution. DNA concentration was determined using a NanoDrop 2000C spectrometer (ThermoScientific). A 260/280 ratio ≥1.8 was accepted as pure for DNA.

For DNA extraction from zebrafish embryos, larvae and fin clips the HotSHOT method was used[193]. In brief, samples were incubated in 25 µL (for embryos) or 50 µL (for larvae and fin clips) base solution (1.25 M KOH and 10 mM EDTA) at 95°C for 30 minutes followed by addition of 25 or 50 µL neutralisation solution (2M Tris HCl). 1 µL of this mix was used for downstream applications such as PCR without further quantification.

2.3.2 PCR and Sanger sequencing

Standard PCR was performed using recombinant *Taq* polymerase (Invitrogen) according to the manufacturer's instructions with the addition of betaine, a PCR enhancing agent:

10 x PCR buffer	2.5 µL
50 mM $MgCl_2$	0.75 µL
10 mM dNTP Mix (Promega)	0.5 µL
10 µM forward primer	1.25 µL
10 µM reverse primer	1.25 µL
5 M betaine	2.5 µL
MQ H_2O	17.5 µL
Template DNA (50 ng/µL)	1 µL
Taq polymerase	0.25 µL
Total volume	25 µL

Thermocycling conditions:

Initial denaturation		95°C	5 min
35 cycles	Denaturation	95°C	30 sec
	Annealing	[a]°C	30 sec
	Extension	72°C	[b] sec
Final extension		72°C	5 min

[a] specific annealing temperature

[b] 30 sec per 500 bp

For PCR amplification requiring a proof reading DNA polymerase the Q5 High-Fidelity DNA polymerase (New England Biolabs, NEB) was used according to the manufacturer's recommendations:

5 x Q5 reaction buffer	5 µL
5X Q5 High GC Enhancer	5 µL
10 mM dNTP Mix (Promega)	0.5 µL
10 µM forward primer	1.25 µL
10 µM reverse primer	1.25 µL
MQ H_2O	10.75 µL
Template DNA	1 µL
Q5 High-Fidelity DNA polymerase	0.25 µL
Total volume	25 µL

Thermocycling conditions:

Initial denaturation		98°C	30 sec
35 cycles	Denaturation	98°C	10 sec
	Annealing	[a]°C	30 sec
	Extension	72°C	[b] sec
Final extension		72°C	2 min

[a] specific annealing temperature

[b] 15 sec per 500 bp

PCR products were run on a 1-2% agarose gel (depending on the product size) prepared in 1 x Tris base, acetic acid and EDTA buffer (TAE, **Appendix 9.2**) with 1 µL ethidium bromide (10 mg/mL) per 50 mL gel solution at 100-120 volts in 1 x TAE. Amplicon sizes were determined by comparison to standard DNA markers (100 bp or 1 kb ladder, Promega). DNA bands were visualised by ultraviolet illumination.

For direct sequencing, PCR products were cleaned up using ExoSap:

PCR product	10 µL
SAP buffer	0.25 µL
Shrimp Alkaline Phosphatase (Affymetrix)	1 µL
Exonuclease I (NEB)	0.5 µL
Total volume	12 µL

The reactions were incubated at 37°C for 15 min followed by an inactivation step of 80°C for 15 min.

Sanger sequencing was performed using a commercial provider service (SourceBioScience). Alternatively, the BigDye Terminator v1.1 Cycle Sequencing Kit (Applied Biosystems) was used according to the following protocol:

DNA template	3 µL
5 µM primer	1 µL
5 x BigDye sequencing buffer	1.5 µL
BigDye reaction mix v1.1	0.5 µL
Total volume	6 µL

Thermocycling conditions:

Initial denaturation		95°C	2 min
35 cycles	Denaturation	95°C	20 sec
	Annealing	50°C	10 sec
	Extension	60°C	3 min

Subsequently, the DNA was precipitated in a 96 well plate by adding 2 µL 3M sodium acetate (pH 5.2) and 50 µL 100% ethanol to each sample. Following 20 min incubation at room temperature the plate was centrifuged for 40 min at >10,000 x g, the supernatant discarded, the samples washed in 50 µL 70% ethanol and centrifuged for 10 min at >10,000 x g. The supernatant was discarded and the plate centrifuged upside down on tissue paper for 1 min at 1,000 x g. The precipitated DNA was resuspended in 10 µL of 0.1 x TE buffer.

Sequencing was performed on an ABI 3730 DNA Analyzer (Applied Biosystems) and the data analysed using Sequencher 5.2.4 software (Genecodes).

Population frequencies of identified sequence changes were obtained from the dbSNP[194] (http://www.ncbi.nlm.nih.gov/SNP/), 1000 Genomes (http://www.1000 genomes.org/) and ExAc (http://exac.broadinstitute.org/) databases. The ExPASy translate tool was used to predict the translation of a given nucleotide sequence to that of a protein (http://web.expasy.org/translate/). Amino acid alignments were generated using ClustalW2 (http://www.ebi.ac.uk/Tools/msa/clustalw2/) or UniProt software (http://www.uniprot.org/). To predict transporter protein structures, the MEMSAT3 & MEMSAT-SVM membrane helix prediction tool were used (http://bioinf.

cs.ucl.ac.uk/psipred/). The Basic Local Alignment Search Tool (BLAST, www.ncbi.nlm.nih.gov/BLAST/) was used to identify specific genomic sequences. PolyPeakParser software[195] (http://yosttools.genetics.utah.edu/ PolyPeakParser/) was used to separate the chromatogram data of CRISPR induced indel mutations identified in the F1 fish.

Primers used for PCR and sequencing of human *SLC30A10* and *SLC39A14* are listed in **Table 2.1** and **2.2**.

Primer	Sequence (5' → 3')	Predicted amplicon size (bp)	Annealing temp. (°C)
hSLC30A10_5UTRFw	AAGAGAGACATCGGCTCGTG	360	62
hSLC30A10_5UTRRv	GTGAGCACCAGCATGAAGAG		
hSLC30A10_Exon1Fw1	ACAATCTGGGAGGCGGGTA	497	62
hSLC30A10_Exon1Rv1	GACCAACAGCCCCAGGAC		
hSLC30A10_Exon1Fw2	CTTCAGCGCCACCTACGG	498	62
hSLC30A10_Exon1Rv2	GTGGGAGGAGGAAGGAAGG		
hSLC30A10_Exon2Fw	TACTGTTCTGAGCTGTGGGT	480	62
hSLC30A10_Exon2Rv	CCTCAGGATCAATGCAGTGA		
hSLC30A10_Exon3Fw	CCTGCAGGTCAGAATCTTCC	554	62
hSLC30A10_Exon3Rv	GCTTGTCCTTTGGCCTGA		
hSLC30A10_Exon4Fw1	GCAGCCATTTTGGTGAGAAT	391	62
hSLC30A10_Exon4Rv1	CAACACAGCTGCTTAGCACA		
hSLC30A10_Exon4Fw2	TCCACAATGTGACCATCCAG	474	62
hSLC30A10_Exon4Rv2	AACAGCCAACCCCTAGTGAA		
hSLC30A10_3UTRFw	GTGGGCCCTCTCTAGACACA	546	62
hSLC30A10_3UTRRv	TGATCTCACCTGAGCATTAGC		

Table 2.1 Primer sequences and annealing temperatures for PCR and sequencing of human *SLC30A10*.

Primers were designed to amplify all coding exons and intron/exon boundaries of transcript NM_018713.

Primer	Sequence (5' → 3')	Predicted amplicon size (bp)	Annealing temp. (°C)
hSLC39A14_Exon2Fw	TCAAGAAGGAGCAGAGAAGCA	480	60
hSLC39A14_Exon2Rv	AGACAGGGAACCCTGAGAGG		
hSLC39A14_Exon3Fw	TCCTCTGGGAAGGCTGAGTA	371	62
hSLC39A14_Exon3Rv	CATTCAGTGAGGAGCAGCAG		
hSLC39A14_Exon4aFw	GAGTGTCCCCACCCTCAGT	298	60
hSLC39A14_Exon4aRv	GTAGGGGAGGAGGGGATTG		
hSLC39A14_Exon4bFw	GGCATGTGCCTTCTCTCC	300	60
hSLC39A14_Exon4bRv	CCTTCTATCCAAACGGAGGTC		
hSLC39A14_Exon5Fw	AGGGGGATCAGTAAAGATGCT	242	60
hSLC39A14_Exon5Rv	TGTTTGAGATGGGTGTTTTCC		
hSLC39A14_Exon6Fw	AGCAGGTGCTCAATCAGGTT	328	60
hSLC39A14_Exon6Rv	ACCATGTGCCCTCAAGGTAA		
hSLC39A14_Exon7Fw	GGCTTACCTTGAGGGCACAT	377	60
hSLC39A14_Exon7Rv	GCACTGTGAAGACAGGGAGA		
hSLC39A14_Exon8Fw	CCATGCCCATCTTACTCTTCC	299	60
hSLC39A14_Exon8Rv	ACCTAACATCCATCCCCTTAG		
hSLC39A14_Exon9aFw	TTGCCCTGGACTTACAAGATG	297	60
hSLC39A14_Exon9aRv	GTGGTGCATTGTGGATGGT		
hSLC39A14_Exon9bFw	CGGCCATGTTTATGTTTTTG	299	60
hSLC39A14_Exon9bRv	CATCATGCAGTTAGGAAATACCA		

Table 2.2 Primer sequences and annealing temperatures for PCR and sequencing of human *SLC39A14*.

Primers were designed to amplify all coding exons and intron/exon boundaries of transcripts NM_001128431.2, NM_015359.4 and NM_001135154.1.

Primers used for PCR with subsequent restriction enzyme digestion (**Section 2.3.5**), and TOPO TA cloning for sequencing (**Section 2.3.9**) of TALEN or CRISPR target regions are listed in **Table 2.3**.

Primer	Sequence (5' → 3')	Predicted amplicon size (bp)	Annealing temp. (°C)
zfSLC30A10_Exon1Fw	TCCGGGCGCTTCTCCTTC	459	60
zfSLC30A10_Exon1Rv	CAGGGAGTGTGTTTCCCGC		
zfSLC30A10_Exon3Fw	CCTGCATGTGCTGAATGACG	214	60
zfSLC30A10_Exon3Rv	GTCCTCGGGGCTCATCTG		
zfSLC39A14_Exon5Fw	AACCCCAAACATCTGAACAGT	330	55
zfSLC39A14_Exon5Rv	ACCGGAACAGACCATCAGTT		
zfSLC30A10_Del1_3Fw	TCGGACTCCTTCAACATGCT	~230	56
zfSLC30A10_Del1_3Rv	CAGGTCCTCGGGGCTCAT		
zfSLC39A14_Del5_8Fw	AACCCCAAACATCTGAACAGT	~300	56
zfSLC39A14_Del5_8Rv	TCAGCATGACGTCTCTTACCA		
zfSLC39A14_Del5_9Fw	AACCCCAAACATCTGAACAGT	~280	56
zfSLC39A14_Del5_9Rv	ATCCAAGCTGTATCTGTCCAG		

Table 2.3 Primer sequences and annealing temperatures for PCR and sequencing of TALEN/CRISPR target regions.

The last three primer pairs amplify the region around the deletions generated by double injection of TALENs/CRISPRs. ~, approximate (amplicon size depends on size of deletion).

2.3.3 Whole exome sequencing (WES)

WES was performed in generous collaboration with Prof Olaf Bodamer at the University of Miami.

Library construction and capture hybridisation were performed using the SureSelect XT Human All Exon V5 Kit (Agilent Technologies) according to the manufacturer's protocol. Samples were barcoded post-capture to allow for multiplexing of four samples per HiSeq2000 lane. Cluster generation took place on the Illumina cBot according to the manufacturer's recommendations. Sequencing occurred on the Illumina HiSeq2000 using the reagents provided in the Illumina TruSeq PE Cluster Kit v3 and the TruSeq SBS Kit-HS (200 cycle) kit. 82 million pass filter paired-end reads per sample were generated for an average read depth of 79% at 20 x. Variants were called based on dbSNP139[194] and annotation based on SeattleSeq Annotation 137 version 8.01. Filtering was performed using the in-house developed software GEMapp[196].

2.3.4 DNA purification

Where purified DNA was required for downstream applications such as cloning or *in vitro* transcription, samples were either purified using the QIAquick or MinElute PCR purification kit (Qiagen) or extracted from an agarose gel using the QIAquick Gel Extraction kit (Qiagen) according to the manufacturer's protocol. Final elution was done in 30 µL H_2O (10 µL for MinElute columns).

2.3.5 Restriction enzyme digestion

Restriction enzymes purchased from NEB or Promega were used according to the manufacturer's recommendations. Typically, 10 units of enzyme were used per 1 µg plasmidic DNA or PCR reaction and incubated at the specified temperature for a minimum of 2 hours. Acetylated bovine serum albumin (BSA) was added to Promega enzyme reactions at a final concentration of 0.1 µg/µL. Complete digestion was verified against undigested plasmid DNA or PCR product on a 1-2% agarose gel depending on the size of the expected products. Digested plasmid DNA was purified using the QIAquick or MinElute PCR purification kit (**Section 2.3.4**).

2.3.6 Total RNA isolation, reverse transcription and RT-PCR

Total RNA extraction from human tissues or pools of zebrafish embryos/larvae was performed using the TRIzol protocol (Life Technologies). In brief, 1 mL TRIzol was added to 100 mg tissue or 500 µL TRIzol to 30 embryos/larvae. Tissues were homogenized using a glass homogeniser; zebrafish embryos/larvae were taken through a 27 gauge needle until the lysate looked uniform. After incubation for 5 min at room temperature 100 µL chloroform was added, the solution mixed vigorously and centrifuged at 12,000 x g for 15 min at 4°C to allow the separation of the sample into a clear upper aqueous phase containing the RNA, a white interphase containing the DNA and a red lower organic layer containing the proteins. The RNA was precipitated from 200 µL of the aqueous phase by mixing with 170 µL isopropyl alcohol, incubation for 10 min at room temperature and subsequent centrifugation at 12,000 x g for 10 min at 4°C. The supernatant was discarded and the RNA pellet washed with 1 mL 75% ethanol. After centrifugation at 7,500 x g for 5 min at 4°C the supernatant was discarded and the RNA pellet rehydrated in 20 µL of RNase free H_2O. To avoid genomic DNA contamination, samples were treated with DNase I (NEB) at 37°C for 15 min according to the following protocol:

Total RNA	20 µL
10 x DNase buffer	10 µL
RNase free H_2O	68 µL
DNase	2 µL
Total volume	100 µL

The RNA was purified using the RNeasy Mini Kit according to the manufacturer's protocol. RNA was eluted in 30 µL RNase free H_2O. The RNA concentration was quantified by measuring the absorbance of the solution at 260/280 on a NanoDrop 2000C spectrophotometer (Thermo Scientific). 260/280 and 260/230 ratios of 2-2.2 and ≥2.0, respectively, assessing possible contamination with protein and organic solvents such as phenol, were accepted as pure for RNA.

For reverse transcription the SuperScript III reverse transcriptase (Invitrogen) was used. 1 µg total RNA was mixed with 1 µL oligo$(dT)_{20}$ primers (50 µM), 1 µL dNTP mix and RNase free H_2O to a final volume of 13 µL. After a 5 min incubation at 65°C to

denature the RNA secondary structure and a 1 min incubation on ice to let the primers anneal the following reagents were added:

5X First-Strand Buffer	4 µl
0.1 M DTT	1 µl
RNaseOUT Recombinant RNase Inhibitor	1 µl
SuperScript III RT	1 µl
Total volume	20 µL

The reaction was incubated at 50°C for 60 min to facilitate extension. Finally, the enzymes were inactivated at 70°C for 15 min.

The resulting cDNA was diluted 1:5 with nuclease free H_2O and 1 µl used for RT-PCR amplification. Additionally, a human cDNA panel from heart, brain, lung, liver, kidney and pancreas was purchased from Clontech. Fetal cDNA from placenta, skin, brain, heart, kidney, intestine and liver were kindly provided by the BabyBioBank at UCL Institute of Child Health, London, UK.

Primers used for RT-PCR are listed in **Table 2.4**.

Primer	Sequence (5' → 3')	Predicted amplicon size (bp) cDNA/gDNA	Annealing temp. (°C)
zfSLC30A10_RT_5UTRFw	CGAGGAGAACCACAGGTGATCT	1361/	60
zfSLC30A10_RT_3UTRRv	ACAGCACACACTCCTGCATT	4488	
zfSLC30A10_Iso2Fw	GTGTGTAGAGCCGCTGGTGT	209/	60
zfSLC30A10_Exon3Rv	CGGCCACACATAGAACAGAG	396	
hSLC39A14_RT_Exon4aFw	GACCGTCATCTCCCTCTGCT	139/	64
hSLC39A14_RT_Exon5Rv	CCAAACACCACTGCAGACTTGG	2773	
hSLC39A14_RT_Exon3Fw	CGGAGAACCAGGAAAACGAGG	109/	64
hSLC39A14_RT_Exon4bRv	GAGGCCAGGTTAATCAGTGAG	1558	
hSLC39A14_RT_Exon6Fw	GTGCTTCCTTCACTGTGTCA	165/	58
hSLC39A14_RT_Exon7Rv	CGTTGAGCAGGATGACAAAG	1475	
zfSLC39A14_RT_Exon3Fw	CCCTAGACCCACTGAAGCTG	240/	58
zfSLC39A14_RT_Exon5Rv	GCGGACTTGGGCACATAATA	>22kb	
hHPRT_Fw	CCACGAAAGTGTTGGATATAAGC	205/	58
hHPRT_Rv	GGCGATGTCAATAGGACTCCAGA	1721	

Table 2.4 Primer sequences for RT-PCR.

Primers were designed to span an intron/exon boundary. HPRT, hypoxanthine-guanine phosphoribosyltransferase.

2.3.7 Quantitative real time PCR (qRT-PCR)

qRT-PCR was performed using GoTaq qPCR Master Mix (Promega) according to the following protocol:

cDNA (diluted 1:5)	2 µL
10 µM forward primer	1 µL
10 µM reverse primer	1 µL
Nuclease free H_2O	6 µL
GoTaq qPCR Master Mix	10 µL
Total volume	20 µL

All samples were run in triplicates. For each primer pair a non-template control (NTC) sample was included containing H_2O instead of template DNA to exclude DNA contamination of the reagents. qRT-PCR was carried out on a CFX96 Touch Real-Time PCR Detection System (BioRad) with the following thermocycling conditions:

Initial denaturation		94°C 2 min
40 cycles	Denaturation	94°C 15 sec
	Annealing	60°C 30 sec
	Extension	72°C 30 sec

Primers were designed to span at least one intron/exon boundary to allow detection of genomic DNA contamination. The amplification efficiency (E) for each primer pair was calculated by standard curve analysis in Microsoft Excel using 1:5 serial dilutions over five samples (1:1, 1:5, 1:25, 1:125, 1:625) according to the following formula:

E (%) = (10^(-1/slope)-1)*100

Only primer pairs with R^2 values >0.99 and amplification efficiencies between 90% and 110% were used (**Table 2.5**).

Relative quantification of gene expression was determined using the $2^{-\Delta\Delta Ct}$ method[197], with elongation factor 1α (*ef1α*) as a reference gene. Statistical analysis was performed using Student's two tailed *t* test on individual ΔCt values.

Amplicon	Primer	Sequence (5' → 3')	Predicted amplicon size (bp)	E (%)
slc39a14 transcript 1	Fw	CCTTTTACAAGCGGTTGCTGC	133	97.6
	Rv	GCGGACTTGGGCACATAATA		
slc39a14 transcript 2	Fw	CGCGGTTCATGCGCAGAGTT	136	97.8
	Rv	GCGGACTTGGGCACATAATA		
slc39a14 all transcripts	Fw	CCCTAGACCCACTGAAGCTG	240	101.5
	Rv	GCGGACTTGGGCACATAATA		
ef1α	Fw	GTACTTCTCAGGCTGACTGTG	136	98.2
	Rv	ACGATCAGCTGTTTCACTCC		
DMT1	Fw	TTCCCAGCAAACAACGAGAC	101	106.9
	Rv	CCCACAGCCCAGATGTAGAG		
slc39a8	Fw	GCCTGCCCTTACACTTCTTC	104	109.4
	Rv	GCAGCCAAGTTAATCACCGT		
tfr1a	QuantiTect Primer Assay (Qiagen, QT02189621)			
tfr1b	QuantiTect Primer Assay (Qiagen, QT02196558)			

Table 2.5 Primers used for qRT-PCR.

E, amplification efficiency.

2.3.8 Conventional molecular cloning

For conventional cloning into pBSK or pCS2+ plasmids, inserts were PCR amplified using phosphorylated primers and the product ligated into a linearised, dephosphorylated vector. Primers were phosphorylated using T4 polynucleotide kinase (PNK) (Promega) according to the following protocol:

100 µM primer	5 µL
10 x T4 PNK buffer	4 µL
10 mM ATP	4 µL
MQ H_2O	25 µL
T4 PNK (10 units/ µL)	2 µL
Total volume	40 µL

The reaction was incubated at 37°C for 30 min. 2 µL of each primer was used for PCR with Q5 High-Fidelity DNA polymerase (NEB) (**Section 2.3.2**). The product was gel purified using the QIAquick Gel Extraction kit (Qiagen) (**Section 2.3.4**). Simultaneous vector dephosphorylation and blunt linearisation was performed using the thermosensitive alkaline phosphatase (TSAP) (Promega) and EcoRV (for pBSK-) and StuI (for pCS2+), respectively:

Vector (1 µg/ µL)	1 µL
10 x restriction enzyme buffer	2 µL
Acetylated BSA (10 µg/µL)	0.2 µL
EcoRV/StuI	1.5 µL
TSAP	1 µL
MQ H_2O	14.3 µL
Total volume	20 µL

Samples were incubated at 37°C for 15 min followed by heat inactivation of the enzymes at 74°C for 15 min. Complete digestion was confirmed on a 1% agarose gel and the linearised vector purified using the QIAquick PCR purification kit (Qiagen) (**Section 2.3.4**).

Ligation of the phosphorylated PCR amplicon into the dephosphorylated vector was performed according to the following calculation using a ratio of 3:1 insert to vector:

$$\frac{\text{vector (ng)} \times \text{insert (kb)}}{\text{vector (kb)}} \times \frac{3}{1} = \text{ng insert}$$

Typically, 50 ng vector was used for ligation with the Quick T4 DNA ligase (NEB):

vector + insert + MQ H2O	10 µL
2 x Quick ligation buffer	10 µL
Quick T4 DNA ligase	1 µL
Total volume	20 µL

The reaction was incubated for 5 min at room temperature and kept on ice until transformation of XL10-Gold ultracompetent *E. coli* cells (prepared by the Biosciences Molecular Biology Unit, UCL).

2.3.9 TOPO TA cloning for sequencing

Taq polymerase amplified PCR products were cloned into the pCRII-TOPO TA vector (Invitrogen) according to the manufacturer's protocol:

Gel purified PCR product	4 µL
Salt Solution supplied by manufacturer	1 µL
pCRII-TOPO TA vector	1 µL
Total volume	6 µL

The reaction was incubated at room temperature for 30 min and kept on ice until transformation of One Shot TOP10 Competent *E. coli* cells (Invitrogen) (**Section 2.3.11**). Plasmid mini-preparations (**Section 2.3.13**) were sequenced using generic M13 primers (**Section 2.3.22**).

2.3.10 In-Fusion cloning

To generate C-terminally enhanced green fluorescent protein (EGFP) tagged constructs of human SLC39A14 the In-Fusion HD Cloning Kit (Clontech) was used. In brief, pCS2+ constructs of human *SLC39A14* transcript 1 or 2 were PCR amplified using a gene specific reverse primer just upstream of the stop codon and a vector specific forward primer upstream of the simian virus 40 (SV40) polyA site to generate a linearised vector containing the open reading frame of *SLC39A14* transcript 1 and 2. Similarly, the EGFP sequence together with a 5' flexible linker (GGTGGATCAGGAGGTGGCGGAAGTGGTGGAGGGAGCTCAGGA) was PCR amplified using primers with 15 bp overhangs homologous to the pCS2+ constructs (**Table 2.6**).

Primer	Sequence (5' → 3')
InfFw_pCS2_hSLC39A14	GCCTCTCGAGCCTCTAGAACT
InfRv_pCS2_hSLC39A14	CCCAATCTGGATCTGTCCTGA
InfFW_EGFP	CAGATCCAGATTGGGGGTGGATCAGGAGGTGGC
InfRV_EGFP	AGAGGCTCGAGAGGCTTACTTGTACAGCTCGTCCATGC

Table 2.6 Primer used for In-Fusion cloning.

Primers used to amplify and linearise the vector constructs were positioned to eliminate the stop codon (grey). The primers amplifying the EGFP sequence with a 5' linker contain 15 bp overhangs (underlined) complementary to the ends of the linearised vector.

PCR was performed using CloneAmp HiFi PCR Premix (Clontech) according to the following protocol:

2 x CloneAmp HiFi PCR Premix	12.5 µL
10 µM forward primer	2.5 µL
10 µM reverse primer	2.5 µL
Plasmid DNA	1 µL
MQ H_2O	6.5 µL
Total volume	25 µL

Thermocycling conditions:

35 cycles	98°C	10 sec
	55°C	15 sec
	72°C	1 min

The PCR products were purified using the QIAquick PCR purification kit (**Section 2.3.4**).

Ligation was performed according to the following protocol:

5 x In-Fusion HD Enzyme Premix	2 µL
Linearised vector	x µL (50-200 ng)
Purified PCR fragment	x µL (10-200 ng)
dH2O	x µL
Total volume	10 µL

The reaction was incubated at 50°C for 15 min and kept on ice until transformation of Stellar Competent *E. coli* cells (Clontech).

2.3.11 Transformation of competent *E. coli* cells

Competent cells (25 µL) were thawed on ice, mixed gently with 2 µL of the cloning reaction and incubated on ice for 30 min. For transformation the cells were heat-shocked at 42°C for

- 30 sec: One Shot TOP10 Competent *E. coli* cells (Invitrogen)
  XL10-Gold ultracompetent *E. coli* cells
- 45 sec: Stellar Competent *E. coli* cells (Clontech)

and immediately incubated on ice for 1-2 min. 250 µL S.O.C medium (Invitrogen) was added followed by incubation and shaking at 220 rpm at 37°C for 1 hour. 50 to 100 µL of cells were plated on Luria Bertani (LB) agar (**Appendix 8.1**) containing the appropriate antibiotic and incubated overnight at 37°C.

2.3.12 Colony PCR

To screen for positive bacterial colonies containing the correct size insert, single colonies were picked with a pipette tip and resuspended in 50 µL MQ H_2O. PCR was performed using 4 µL resuspended colony and *Taq* polymerase (**Section 2.3.2**), and gel verified. 20 µL of a resuspended positive colony was cultured in 3-5 mL LB broth at 37°C containing the appropriate antibiotic with shaking at 220 rpm for 12-16 hours followed by plasmid preparation the next day.

2.3.13 Plasmid preparation

Plasmidic DNA was isolated using the QIAprep Spin Miniprep Kit (Qiagen) according to the manufacturer's recommendations. DNA was eluted in 30 µL MQ H_2O with an average yield of 200-300 ng/µL. If required, plasmid midi- and maxi- preparations were prepared by the Biosciences Molecular Biology Unit, UCL.

2.3.14 *In vitro* transcription of capped RNA

mRNA for injection into zebrafish embryos was prepared using the mMESSAGE mMACHINE Kit (Ambion) according to the manufacturer's recommendations and 1µg of linearised and purified plasmid DNA (**Section 2.3.5**):

Nuclease-free Water	X (adjust to final volume of 20 µL)
2 x NTP/CAP	10 µL
10 x Reaction Buffer	2 µL
Linear template DNA (1 µg)	X µL
Enzyme mix	2 µL
Total volume	20 µL

Reactions were incubated at 37°C for a minimum of 2 hours followed by addition of 1 µL TURBO DNase and incubation at 37°C for 15 min to digest the template DNA.

For plasmids that did not contain a SV40 polyA sequence polyA tailing was performed using the polyA tailing kit (Ambion) according to the manufacturer's protocol:

mMESSAGE mMACHINE reaction	20 µL
Nuclease-free Water	36 µL
5X E-PAP Buffer	20 µL
25 mM MnCl2	10 µL
10 mM ATP	10 µL (0.5 µL kept as minus enzyme control to run on agarose gel)
E-PAP enzyme	4 µL
Total volume	100 µL

Reactions were incubated at 37°C for 1 hour and purified using the RNeasy Mini Kit (Qiagen). RNA samples were analysed on a 1% agarose gel to exclude contamination with DNA and ensure that the polyA tail had attached (linearised plasmid DNA and the minus enzyme control RNA were run as controls). RNA concentration was determined on a NanoDrop 2000C spectrophotometer (Thermo Scientific). 260/280 and 260/230 ratios ≥2.0 were accepted as pure for RNA.

2.3.15 Probe synthesis for *in situ* hybridisation

To generate digoxigenin (DIG) labelled RNA probes linearised plasmids containing the desired insert and promoter sequence or PCR amplified linear DNA with the correct promoter overhangs were used as templates for *in vitro* transcription according to Thisse and Thisse 2008[198] (**Table 2.7**).

Probe	Orientation	Plasmid & insert	RE	Primers used for PCR	P	Size (bp)
slc30a10	antisense	pBSK-, *slc30a10* 5'→3'	NruI	−	T3	1109
	sense		BglII		T7	1099
slc30a10	antisense	−	−	Fw AATTAACCCTCACTAAAGGG CCTGCATGTGCTGAATGACG	T7	706
	sense	−	−	Rv TAATACGACTCACTATAGGG ACAGCACACACTCCTGCATT	T3	706
***slc30a10* transcript 2**	antisense	−	−	Fw CGTGTTTGGGTCACGAGTAA Rv TAATACGACTCACTATAGGG GCGCTCCATCTTTCTCAGTC	T7	719
slc39a14	antisense	pBSK-, *slc39a14* 5'→Exon 8B	HindIII	−	T3	970
	sense		EcoRI		T7	970
slc39a14	antisense	−	−	Fw AATTAACCCTCACTAAAGGG TCTCTGTGTTCACTGGTCGG	T7	940
	sense	−	−	Rv TAATACGACTCACTATAGGG TGGTGAGTACAAGCATTATGGC	T3	940

Table 2.7 DNA templates and primers used for *in vitro* transcription to generate *in situ* hybridisation probes.

RE, restriction enzyme. P, promoter. Primers contain RNA polymerase promoter sequences (underlined).

For each gene two probes spanning a different part of the transcript were designed. *In vitro* transcription was performed using T3/T7 RNA polymerase (Promega) according to the manufacturer's recommendations:

Linearised plasmidic DNA (2 µg)	X µL
5X Transcription buffer	4 µL
0.1 M DTT	2 µL
DIG-RNA labelling mix (Roche)	2 µL
RNAse inhibitor	1 µL
MQ Water	adjust to final volume of 20 µL
RNA polymerase	1.5 µL
Total volume	20 µL

The reactions were incubated at 37°C for a minimum of 2 hours. To digest the template DNA 1 µL RNase free DNase (Promega) was added followed by incubation at 37°C for 20 min. The probes were purified and quantified as described in **Section 2.3.14**.

2.3.16 5' and 3' rapid amplification of cDNA ends (RACE)

To verify the sequences of *slc39a14* transcripts in zebrafish the FirstChoice RLM (RNA Ligase Mediated) – RACE Kit (Ambion) was used according to the manufacturer's protocol.

In brief, total RNA was extracted from zebrafish larvae at 5 days post fertilisation (dpf) (**Section 2.3.6**). For 5' RACE total RNA was treated with Calf Intestinal Alkaline Phosphatase (CIP) to remove free 5'-phosphates from molecules such as ribosomal RNA, fragmented mRNA, tRNA, and contaminating genomic DNA (the cap structure found on intact 5' ends of mRNA is not affected by CIP):

Total RNA (10 µg)	X µL
10 x CIP buffer	2 µL
CIP	2 µL
Nuclease free H_2O	X µL
Total volume	20 µL

The reaction was incubated at 37°C for 1 hour. To terminate the CIP reaction the RNA was purified using phenol:chloroform extraction:

Reaction	20 µL
Ammonium acetate	15 µL
Nuclease free H_2O	115 µL
Acid phenol:chloroform	150 µL
Total volume	200 µL

Following centrifugation at >10,000 x g for 5 min the aqueous (top) phase was transferred to a new tube. 150 µL chloroform were added to the aqueous phase and after centrifugation for another 5 min again transferred to a new tube. RNA was precipitated by addition of 150 µL isopropranol, incubation on ice for 10 min and centrifugation at >10,000 x g for 20 min. The pellet was washed in 500 µL cold 70% ethanol and air dried after centrifugation for 5 min. RNA was resuspended in 11 µL nuclease free H_2O.

The RNA was then treated with Tobacco Acid Pyrophosphatase (TAP) to remove the cap structure from full-length mRNA, leaving a 5'-monophosphate:

RNA treated with CIP	5 µL
10X TAP buffer	1 µL
TAP	2 µL
Nuclease free H_2O	2 µL
Total volume	10 µL

The reaction was incubated at 37°C for 1 hour.

A 45 base RNA adapter oligonucleotide was ligated to the RNA population using T4 RNA ligase. The adapter cannot ligate to dephosphorylated RNA because these molecules lack the 5'-phosphate necessary for ligation:

CIP/TAP-treated RNA	2 µL
5' RACE Adapter	1 µL
10X RNA Ligase Buffer	1 µL
T4 RNA Ligase (2.5 U/µL)	2 µL
Nuclease free H_2O	4 µL
Total volume	10 µL

The reaction was incubated at 37°C for 1 hour. Subsequent to this, random-primed reverse transcription was performed according to the following protocol and the reaction incubated at 42°C for 1 hour:

Ligated RNA	2 µL
dNTP Mix	4 µL
Random Decamers	2 µL
10 x RT Buffer	2 µL
RNase Inhibitor	1 µL
M-MLV Reverse Transcriptase	1 µL
Nuclease free water	8 µL
Total volume	20 µL

For 3’ RACE cDNA was synthesized from total RNA using the supplied 3' RACE adapter and the reaction was incubated at 42°C for 1 hour:

Total RNA (1 µg)	2 µL
dNTP Mix	4 µL
3' RACE adapter	2 µL
10 x RT Buffer	2 µL
RNase Inhibitor	1 µL
M-MLV Reverse Transcriptase	1 µL
Nuclease free Water	8 µL
Total volume	20 µL

Nested PCR then amplified the 5' and 3' ends using the 5' RACE and 3' RACE combined with gene specific outer and inner primers (**Figure 2.1, Table 2.8**). PCR was performed using Q5 High-Fidelity DNA polymerase (**Section 2.3.2**). For the inner PCR primers were phosphorylated to allow cloning into pBSK- as described above (**Section 2.3.8**). The PCR products were run on a 1% agarose gel and all visualised bands gel purified for subsequent cloning and sequencing.

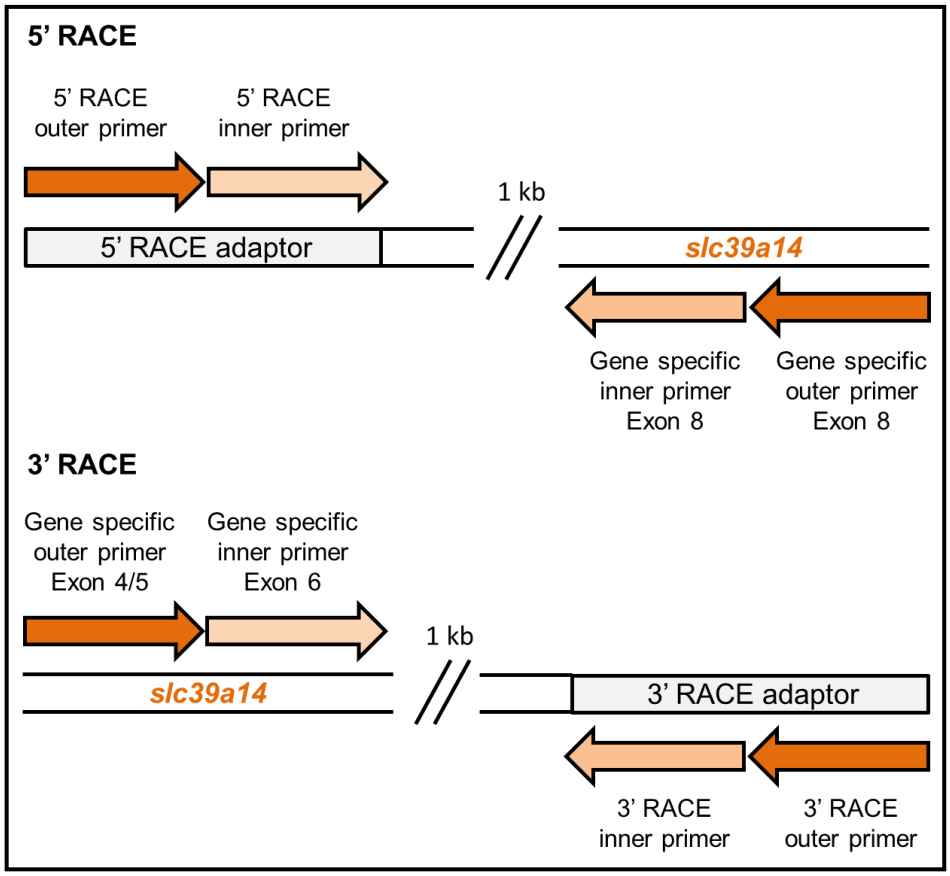

Figure 2.1 Primer positions for 5' and 3' RACE.

Outer primers are highlighted in orange, inner primers in salmon.

	Sequence (5' → 3')
5' RACE zfslc39a14 outer	CCAGCGCAATGTAGAGGAAC
5' RACE zfslc39a14 inner	GCAGGATCACAAAATCACCCA
3' RACE zfslc39a14 outer	ACTAATCCCAGAGGCCTTCG
3' RACE zfslc39a14 inner	CATGGGCACAGTCACTTTCC

Table 2.8 *slc39a14* gene specific primers used for 5' and 3' RACE.

2.3.17 TALEN mRNA design and synthesis

The FLASH TALEN library was obtained from the Joung laboratory and the TALEN arrays assembled according to the published protocol[187,188]. The library consists of 376 plasmids that encode one (α and β), two (βγ, βγ* and δε*), three (βγδ) or four (βγδε) TAL effector repeats consisting of all possible combinations of the NI, NN, HD or NG repeat variable di-residues (RVDs) (**Figure 2.2**).

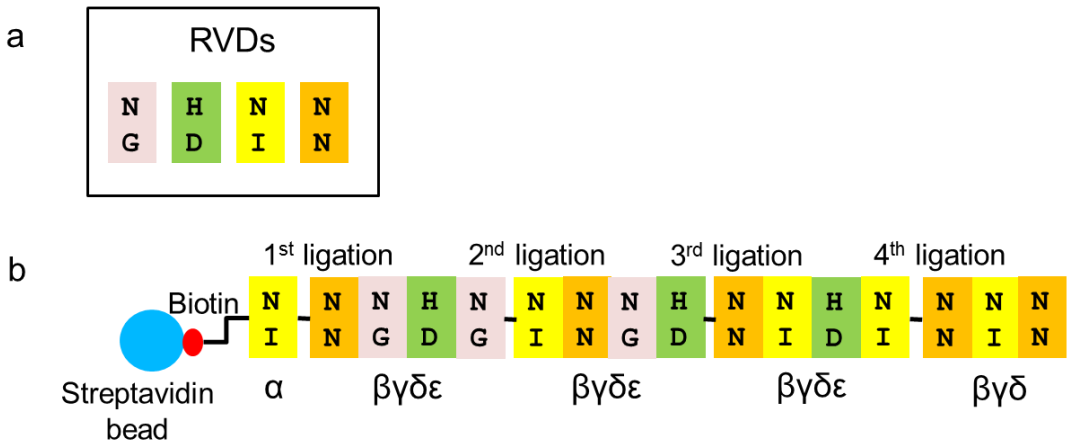

Figure 2.2 Overview of the FLASH assembly method.
*(**a**) Plasmids encode the four possible RVDs. (**b**) Ligation steps of the FLASH assembly method: The biotinylated (red) single TAL effector repeat (α unit) is bound to the streptavidin coated magnetic bead (blue). Additional DNA fragments encoding three or four TAL effector repeats are ligated until the full length of the TALEN array is assembled.*

Two TALEN arms targeting a conserved region within the first exon of zebrafish *slc30a10* were designed using the Zifit software (http://zifit.partners.org/ZiFiT/). The spacer region was chosen to contain a restriction enzyme site for EarI to facilitate screening of induced mutations by restriction enzyme digest (**Figure 2.3**).

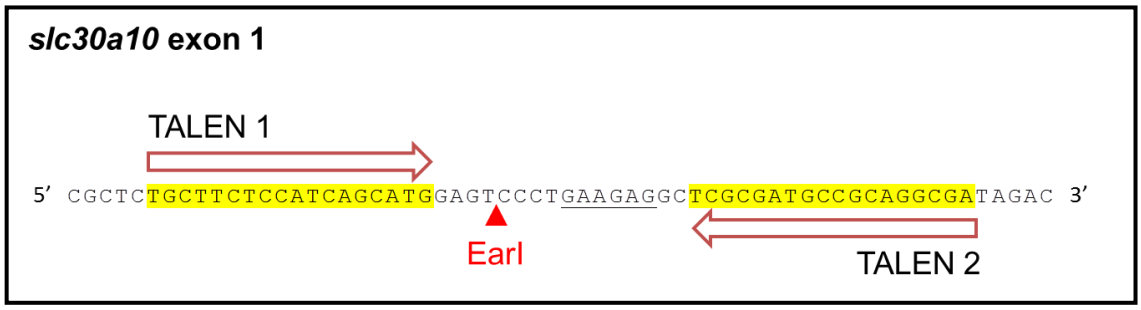

Figure 2.3 TALEN binding sites and EarI recognition and cut site.
Schematic showing the genomic sequence of part of exon 1 of zebrafish slc30a10 with each TALEN binding site highlighted in yellow and the two TALEN arrays marked by a red arrow. The EarI recognition site is underlined, the cut site marked with a red triangle.

The TALEN arrays were assembled according to the protocol in **Appendix 9.3**. In summary, the four 130 bp α-unit DNA fragments were amplified from each α-unit plasmid using the Herculase II Fusion DNA polymerase (Agilent) and oJS2581 and oJS2582 primers (**Table 2.9**). The resulting 5' biotinylated PCR products were digested with BsaI-HF (NEB) to generate four base-pair overhangs. To generate the DNA fragments encoding the βγδε (extension fragment) and βγδ (termination fragment) repeats, each of these plasmids was digested with BbsI followed by serial restriction digests of XbaI, BamHI-HF and SalI-HF (all NEB) to cleave the plasmid backbone and avoid interference with subsequent ligations. The four TALEN expression vectors encoding one of four possible RVDs were linearised with BsmBI (NEB).

All steps of the FLASH assembly were performed in a 96 well plate with the use of a SPRIplate 96-ring magnet (Beckman Coulter Genomics) and a DynaMag-96 side magnet (Life Technologies). The magnets facilitate mixing and washing of the bead bound fragments. The biotinylated α unit fragments were ligated to the first βγδε fragments using Quick T4 DNA ligase and bound to Dynabeads MyOne C1 streptavidin-coated magnetic beads (Life Technologies). The bead bound α-βγδε fragments were digested with BsaI-HF (NEB) to prepare the 3' end of the DNA fragments for the subsequent ligation step. By repeating the digestion and ligation steps, each extension and termination fragment is ligated to assemble the complete DNA fragment encoding the TALE repeat array (**Figure 2.2**). Each ligation and BsaIHF

digestion step was followed by a wash in 1X B&W (bind and wash) buffer and a wash in 1X bovine serum albumin (BSA).

Final digestion with BbsI (NEB) released the full length fragments. The purified DNA fragments were ligated into one of four BsmBI (NEB) digested TALEN expression vectors encoding one of four possible RVDs using Quick T4 DNA ligase. Ligation products were transformed into chemically competent XL-10 Gold *E. coli* cells and clones grown on LB Agar plates containing Ampicillin at 37°C overnight.

Bacterial colonies of each TALEN arm were selected and screened by colony PCR using primers oSQT34 and oSQT35 (**Table 2.9, Section 2.3.12**). Clones showing a correct size band of 2168 bp were cultured in LB medium containing Ampicillin at 37°C overnight. Following plasmid mini-preparation (**Section 2.3.13**) the inserts were sequenced using primers oSQT1, oSQT3 and oJS2980 (**Table 2.9**).

Plasmids containing the correct DNA sequence were linearised with PmeI (NEB) (**Section 2.3.5**) and capped mRNA was synthesised using the mMESSAGE mMACHINE T7 and polyA tailing kit (**Section 2.3.14**).

Primer	**Sequence 5' → 3'**
oJS2581	Biotin–TCTAGAGAAGACAAGAACCTGACC
oJS2582	GGATCCGGTCTCTTAAGGCCGTGG
oSQT34	GACGGTGGCTGTCAAATACCAAGATATG
oSQT35	TCTCCTCCAGTTCACTTTTGACTAGTTGGG
oSQT1	AGTAACAGCGGTAGAGGCAG
oSQT3	ATTGGGCTACGATGGACTCC
oJS2980	TTAATTCAATATATTCATGAGGCAC

Table 2.9 Primers used for PCR and sequence verification of the TALEN arrays.

2.3.18 Generation of CRISPR gRNAs and Cas9 nuclease mRNA

The CRISPR design tool (http://crispr.mit.edu/) was used to identify a 20 nucleotide target sequence that is followed by a PAM sequence (5'-NGG-3') in the genomic sequence of the desired gene. Oligonucleotides with compatible overhangs (**Table 2.10**) for cloning into the DR274 vector (Addgene) were annealed according to the following protocol[177,178]:

Oligonucleotide 1 (100 µM)	1 µL
Oligonucleotide 2 (100 µM)	1 µL
10 x annealing buffer	5 µL
MQ H_2O	43 µL
Total volume	50 µL

10 x annealing buffer:	1M Tris, pH 8.0	400 µL
	1M $MgCl_2$	200 µL
	5M NaCl	100 µL
	0.5M EDTA, pH 8.0	20 µL
	MQ H_2O	280 µL
	Total volume	1 mL

The reaction mix was incubated at:

95°C	5 min
95°C → 25°C	decrease by 1°C every 30 sec
4°C	Hold

Target	Oligonucleotide 1 (5' → 3')	Oligonucleotide 2 (5' → 3')
slc30a10 exon 3	TAGG**TTTCTTTGAGCAGCGGCG**	AAAC**CGCCGCTGCTCAAAGAAA**
slc39a14 exon 5	TAGG**CCTTCGGGTTTGACCCCA**	AAAC**TGGGGTCAAACCCGAAGG**
slc39a14 exon 8	TAGG**GCATGGGCTTTGGCATCC**	AAAC**GGATGCCAAAGCCCATGC**
slc39a14 exon 9	TAGG**TCAGTCGTGAGGAAGAGG**	AAAC**CCTCTTCCTCACGACTGA**

Table 2.10 Oligonucleotide sequences used to generate DNA templates for CRISPR gRNAs.

The target sequence is highlighted in bold. The overhangs required for directional cloning are underlined.

The DR274 vector (Addgene) that harbours a T7 promoter sequence positioned upstream of a sequence encoding the gRNA backbone was linearised using BSAI-HF (NEB) (**Section 2.3.5**). Following purification with the QIAquick PCR purification kit (**Section 2.3.4**) the annealed oligonucleotides were ligated into the DR274 vector according to the following protocol:

Linearised DR274 vector (5 ng/µL)	1 µL
Annealed oligonucleotides	3 µL
2 x Quick ligation buffer (NEB)	5 µL
Quick T4 DNA ligase (NEB)	1 µL
Total volume	10 µL

The reaction was incubated at room temperature for 15 min and kept on ice until transformation of XL10-Gold ultracompetent *E. coli* cells (**Section 2.3.11**). Clones were screened by colony PCR using M13 forward primer and oligo 1 primers (**Section 2.3.12**), and plasmid mini-preparations (**Section 2.3.13**) from positive clones sequence verified. A DR274 plasmid containing the correct insert was digested with DraI (**Section 2.3.5**) and the gRNA generated by *in vitro* transcription using the HiScribe T7 High Yield RNA Synthesis Kit (NEB) according to the following protocol:

Nuclease free water	X µl
10X Reaction Buffer	1.5 µl
ATP (100 mM)	1.5 µl
GTP (100 mM)	1.5 µl
UTP (100 mM)	1.5 µl
CTP (100 mM)	1.5 µl
Template DNA (1 µg)	X µl
T7 RNA polymerase Mix	1.5 µl
Total reaction volume	20 µl

The reaction was incubated at 37°C overnight prior to DNase I (NEB) digestion to remove the template DNA:

In vitro transcription reaction	20 µl
Nuclease free H_2O	70 µl
10 x DNase buffer	10 µl
DNase I	2 µl
Total volume	100 µl

The digestion reaction was incubated at 37°C for 15 min followed by purification using the RNeasy MiniKit (Qiagen).

To generate the Cas9 nuclease mRNA the pT3TS-nCas9n plasmid (Addgene) was used[191]. The plasmid was linearised with XbaI (NEB) (**Section 2.3.5**) and capped mRNA generated with the mMessage mMachine T3 Transcription Kit (Ambion) followed by polyadenylation with the polyA tailing kit (both Ambion) (**Section 2.3.14**). The synthesised mRNA was purified using the RNeasy MiniKit (Qiagen).

2.3.19 High resolution melting analysis (HRMA)

To screen for TALEN/CRISPR induced mutations HRMA was set up on a CFX96 Touch Real-Time PCR Detection System (BioRad)[181]. HRMA allows the identification of variations in dsDNA sequences through detection of small differences in melting (dissociation) curves following PCR using a fluorescent dsDNA binding dye on a real-time PCR machine.
PCR Primers were designed to generate short amplicons of less than 120 bp in order to achieve optimal discrimination of mutant and wild-type sequence (**Table 2.11**).

TALEN/CRISPR	Forward primer (5' → 3')	Reverse primer (5' → 3')	Size (bp)
slc30a10 exon 1	TGCTTCTCCATCAGCATGGAG	GTCTATCGCCTGCGGCATCGCG	57
slc30a10 exon 3	ATCATCATCCTGTCCTCCGC	GTCCTCGGGGCTCATCTG	75
slc39a14 exon 5	CCCTGTATGTAGGCCTTCGG	CCAAACACGACTGCGGACTTGG	82
slc39a14 exon 8	TAACTTCCTGTCAGCCTGCT	TGTAGAGGAACATGCCACCG	113
slc39a14 exon 9	GTTTGTCCATATCTCTGCAGTTT	GCATTCTGGAGGGCGAAAG	106

Table 2.11 Primers used for HRMA.

The predicted amplicon size is given in the last column.

Genomic DNA extracted from zebrafish embryos/fin clips (**Section 2.3.1**) was PCR amplified according to the following protocol:

2 x Precision Melt Supermix (Biorad)	5 µl
Primermix (2 µM each primer)	1 µl
Genomic DNA	1 µl
MQ H_2O	3 µl
Total volume	10 µl

Thermocycling conditions:

Initial denaturation		95°C	2 min
40 cycles	Denaturation	95°C	10 sec
	Annealing	60°C	30 sec
	Extension	72°C	30 sec

HRMA:

Heteroduplex formation	95°C	30 sec
	60°C	1 min
High resolution melting	65 → 95°C: increase by 0.2°C /10 sec	

A minimum of 4 wild-type samples and a non-template control was run for each primer pair. Data was analysed with BioRad Precision Melt Analysis software and the melt curve from TALEN/CRISPR injected zebrafish compared to un-injected wild-types.
HRM analysis software identifies the areas of stable pre- and post-melt fluorescence intensity of the melting curves and normalises them to relative values between 1.0 and 0 to detect subtle differences in the melting profile, generating “normalised melt curves”. The data are plotted as “difference curves” to visually magnify differences between the melt profiles of different genotypes.

2.3.20 KASP genotyping

For rapid genotyping of the generated mutant lines KASP assays were used (LGC Genomics)[199]. In this approach, allelic discrimination is achieved through competitive annealing of two allele-specific forward primers, each containing a unique tail sequence that corresponds with a distinctly labelled fluorescent resonance energy

transfer (FRET) cassette; HEX for the mutant allele, FAM for the wild-type allele. The reverse primer is common to both alleles (**Table 2.12**). The KASP Mastermix contains the two universal FRET cassettes (FAM and HEX), the ROX passive reference dye, Taq polymerase, free nucleotides and $MgCl_2$ in an optimised buffer solution.

Mutant	**Wildtype allele (FAM, 5'→ 3')**	**Mutant allele (HEX, 5' → 3')**	**Common primer (5' → 3')**
slc30a10^{U800}	GCTTCTCCATCAGC ATGGAGT	GCTTCTCCATCA GCATGGAGG	CGTYGTCTATCGCC TGCGGCAT
slc39a14^{U801}	GGCACATAATAATC CTCCATGGG	GGGCACATAATA ATCCTCCATGGT	CCCTGTATGTAGGC CTTCGGGTT

Table 2.12 KASP primers used for genotyping of mutant lines.

PCR amplification was performed according to the following protocol:

2 x KASP mastermix	3.89 µl
KASP assay	0.11 µl
MQ H_2O	3 µl
DNA	1 µl
Total volume	8 µl

Thermocycling conditions:

Initial denaturation		94°C	15 min
10 cycles	{	94°C	20 sec
	{	61°C → 55.6°C	60 sec, decrease by 0.6°C per cycle
26 cycles	{	94°C	20 sec
	{	55°C	60 sec

Fluorescence was quantified on a CFX96 Touch Real-Time PCR Detection System (Biorad) at 37°C for 1 min and the allelic discrimination plot generated using Biorad CFX Manager Software.

2.3.21 Yeast complementation studies

Yeast complementation studies were performed using Gateway cloning (Invitrogen) as described previously[46].

The full length coding sequence of zebrafish *slc30a10* was amplified using the I.M.A.G.E. *slc30a10* cDNA clone (Source BioScience, IRBOp991B11105D) as a template, Platinum Pfx DNA Polymerase (Invitrogen) and *att*B site introducing primers (**Table 2.13**) according to the following protocol:

10X Pfx Amplification Buffer	5 µl
10 mM dNTP mixture (Promega)	1.5 µl
50 mM MgSO4	1 µl
Forward primer (10 µM)	1.5 µl
Reverse primer (10 µM)	1.5 µl
Template DNA	1 µl
MQ H_2O	38.1 µl
Platinum Pfx DNA polymerase	0.4 µl
Total volume	50 µl

Thermocycling conditions:

Initial denaturation		94°C	5 min
35 cycles:	Denaturation	94°C	15 sec
	Annealing	55 °C	30 sec
	Extension	68 °C	90 sec

The amplicon was gel purified using the QIAquick Gel Extraction Kit (**Section 2.3.4**).

	Sequence 5' → 3'
*zf slc30a10 att*B1	GGGGACAAGTTTGTACAAAAAAGCAGGCTTC**GAAGGAGATA**GAA AAATGGGCCGCTACAGCGGGAAGACC
*zf slc30a10 att*B2	GGGGACCACTTTGTACAAGAAAGCTGGGTTCTAGAGTTTGGAGC TGTGTGTGCA

Table 2.13 Primers used to generate an attB PCR product of zebrafish *slc30a10*. *The attB1 and 2 sequences are marked in grey, the Shine Dalgarno sequence (ribosomal binding site in prokaryotic mRNA to initiate protein synthesis) in bold and the yeast consensus sequence is underlined. The start and stop codon are highlighted in yellow and green, respectively.*

Subsequent to this a *slc30a10* entry clone was generated by performing a BP recombination reaction that was incubated at 25°C for 1 hour:

attB-PCR product (40 ng)	1 µL
pDONR vector (150 ng/µl)	1 µL
TE Buffer (**Appendix 9.2**)	6 µL
BP Clonase II enzyme	2 µL
Total volume	10 µL

This was followed by addition of 1 µL Proteinase K and incubation at 37°C for 10 min. One Shot TOP10 Competent *E. coli* cells were transformed with 1 µL of the BP recombination reaction (**Section 2.3.11**).

An entry clone with the correct insert sequence was used to perform the LR recombination reaction:

Entry clone (50-150 ng)	1 µL
Destination vector (150 ng/µL) (pYesDEST52)	1 µL
TE Buffer, pH 8.0	6 µL
LR Clonase II enzyme	2 µL
Total volume	10 µL

The reaction was incubated at 25°C for 1 hour followed by addition of 1 µL Proteinase K and incubation at 37°C for 10 min. One Shot TOP10 Competent *E. coli* cells were transformed with 1 µL of the LR recombination reaction (**Section 2.3.11**). An expression clone with the correct insert sequence was used for transformation of competent yeast cells.

Wild type *BY4743 saccharomyces cerevisiae* (*Mat a/α his3Δ1/ his3Δ1 leu2Δ0/ leu2Δ0 lys2Δ0/+ met15Δ0/+ ura3Δ0/ ura3Δ0*) and *Δpmr1::KanMX* strains in the *BY4743* background were obtained from Open Biosystems. Yeast strains transformed with empty pYesDEST52 vector, human *SLC30A10*, *ZRC1* and *ZRC1* (N44I) had been prepared previously[7]. All yeast strains were streaked out on SC-Ura medium (0.67% yeast nitrogen base without amino acids, 2% glucose and 0.13% amino acid drop-out mixture without Uracil) and incubated at 30°C for 2 days. Competent *Δpmr1::KanMX* cells (50 µL) were transformed with 1 µg of zebrafish *slc30a10* vector DNA by adding 500 µL of Solution III (S.c. EasyComp Transformation Kit, Invitrogen) and incubating at 30°C for 1 hour. Expression clones were selected on SC-Ura medium containing 2% glucose at 30°C for 2 days.

Strains were inoculated in SC-Ura induction medium containing 2% galactose and 1% raffinose. High Mn Agar plates were prepared by adding $MnCl_2$ to the medium at a concentration of 2 mM (1 M stock in H_2O). 10^5, 5 x 10^4, 2.5 x 10^4, 10^4 and 7.5 x 10^3 cells of each strain were spotted onto SC-Ura plates supplemented with or without 2 mM $MnCl_2$ and incubated at 30°C for six days.

2.3.22 Vectors and constructs used

Table 2.14 lists the vectors used and constructs generated in this thesis. **Table 2.15** lists the sequences of generic primers that were used to sequence the vector inserts.

Vector	Insert	Ab	Primers	Promoter	Other
pBSK-	−	Amp	M13F, M13R	T7, T3	−
	zfslc30a10 5'→3'				cloned from cDNA (3 dpf)
	zfslc39a14 5' → Exon 8 (5'RACE)				cloned from cDNA (5 dpf)
	zfslc39a14 Exon 6 → 3' (3'RACE)				cloned from cDNA (5 dpf)
pCS2+	−	Amp	SP6, M13R	SP6, T3, CMV	SV40 polyA
	hSLC39A14 Iso1				cloned from fetal liver cDNA
	hSLC39A14 Iso2				
	hSLC39A14 Iso1-EGFP				
	hSLC39A14 Iso2-EGFP				
pME18S-FL3	*zfslc30a10* cDNA NM_001128234.1	Amp	pME18S F/R	SV40	IMAGE clone, SV40 polyA IRBOp991B11105D
pCRII-TOPO TA	−	Amp/ Kan	M13F, M13R	SP6, T7	−
DR274	gRNA backbone	Kan	M13F	T7	−
pT3TS-nCas9n	Cas9	Amp	M13F, M13R	T3	−
pDONR221	−	Kan	M13F, M13R	−	Gateway, attP1/2
	hSLC30A10				Entry clone
	zfslc30a10				Entry clone
	zrc1				Entry clone
	zrc1 N44I				Entry clone

pYes dest52	−	Amp	GAL1, CYC1	T7,GAL1	Gateway, attR1/2, *URA3*
	hSLC30A10				Expression clone
	zfslc30a10				Expression clone
	zrc1				Expression clone
	zrc1 N44I				Expression clone

Table 2.14 Vectors and constructs used.

For each vector the antibiotic resistance (Ab), sequencing primers and promoters are given, followed by a list of generated constructs with the specific insert. Amp, ampicillin; Kan, kanamycin. For TALEN plasmids see ***Section 2.3.17****. Iso, isoform. dpf, days post fertilisation.*

Generic sequencing primers	Sequence 5’ → 3’
M13Fw	GTAAAACGACGGCCAGT
M13Rv	AACAGCTATGACCATG
SP6	ATTTAGGTGACACTATAG
GAL1	AATATACCTCTATACTTTAACGTC
CYC1	GCGTGAATGTAAGCGTGAC
pME18SF	CTTCT GCTCT AAAAG CTGCG
pME18SR	CGACCTGCAGCTCGAGCACA

Table 2.15 Generic sequencing primers used to sequence the vector inserts.

2.4 Embryology

2.4.1 Zebrafish husbandry

The wild-type zebrafish strains AB and Tuebingen were used for all experiments. Zebrafish were kept on a 14 hour light, 10 hour dark cycle in reverse osmosis water supplemented with sodium bicarbonate and sea salt (Tropic Marin) that was maintained with the following parameters: pH 7 to 8, conductivity 425 µS, temperature 28.5°C, ammonia 0 ppm, nitrite 0 ppm, nitrate 0 to 5 ppm, exchange rate of 10% per day. Embryos were obtained by natural spawning and staging was performed according to standard criteria[200]. Up to five dpf, embryos were kept in petri-dishes (50 embryos per dish) containing fishwater supplemented with methylene blue (2 mL of 0.1% methylene blue in 1 L of system-water) to reduce the growth of bacteria or fungus. For *in situ* hybridisation experiments, 1-phenyl 2-thiourea (PTU, **Appendix 9.2**), an inhibitor of tyrosinase, was added at 24 hours post fertilisation (hpf) at a final concentration of 0.003% to block melanogenesis. Anaesthesia was performed using tricaine methanesulfonate (MS-222, **Appendix 9.2**) at a concentration of 50 µg/mL in fishwater.

2.4.2 Injection procedure

Embryos at the 1 cell stage were aligned against a glass slide in a petri dish. RNA injections were performed into the yolk at a volume of approximately 1-2 nl using a borosilicate glass capillary needle (Clarke) attached to a Picospritzer III injector (Science Products) (**Figure 2.4**). The final injection concentration was procedure specific and is as detailed in **Table 2.16.** ,

RNA	Concentration per embryo
TALEN mRNA (each)	100 - 200 pg
CRISPR gRNA	50 -100 pg
Cas9 nuclease mRNA	150 - 300 pg
slc39a14-EGFP mRNA (Iso1/2)	50 - 100 pg
membrane mCherry mRNA	50 pg

Table 2.16 RNA concentrations used for injection of zebrafish embryos.

For $Na_2CaEDTA$ cardiac injections, larvae between 2 and 4 dpf anaesthetised in fishwater with MS-222 were mounted on their left side (**Figure 2.4**) in 1.5% low melting point agarose (made up in fishwater with MS-222) in a petri dish with a 1.5% agarose coating. Anaesthetised larvae were directly injected into the heart with 1 nl at the required concentration using a borosilicate glass capillary needle attached to the Picospritzer III injector. Following injection, larvae were carefully removed from the agarose using Tungsten needles and transferred back to fishwater without MS-222. This procedure was repeated daily between 2 and 4 dpf.

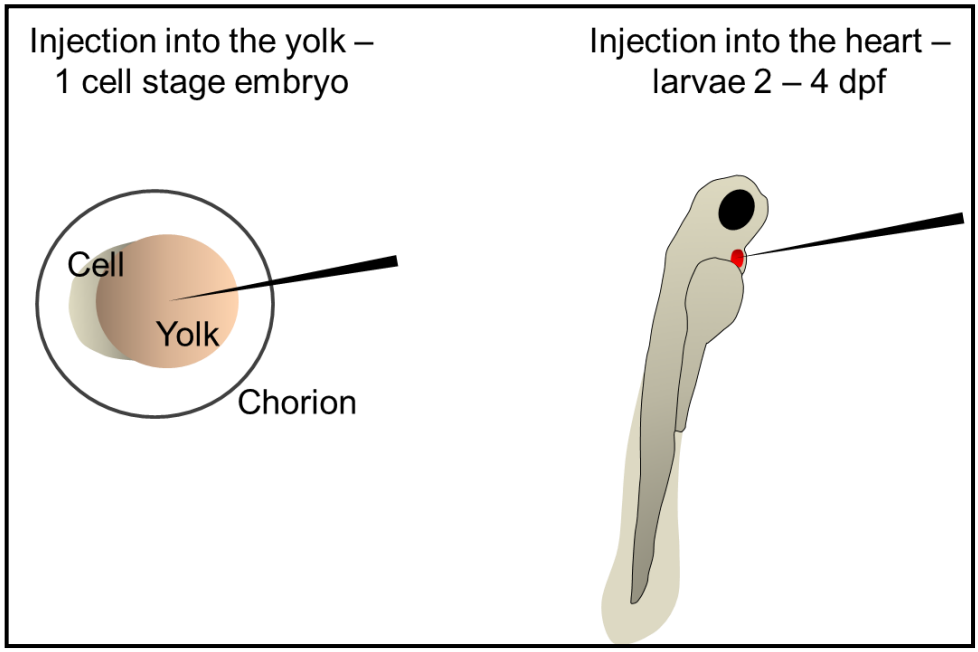

Figure 2.4 Zebrafish embryo and larval injection.

Schematic showing the injection position within the yolk of 1 cell stage embryos (left) and the heart of zebrafish larvae (right).

2.4.3 Generation of stable mutant lines using TALEN or CRISPR genome editing

Following injection of TALEN mRNA or CRISPR gRNA/Cas9 mRNA and confirmation of successful mutagenesis, injected embryos were raised to adulthood. Adult F0 fish were outcrossed to a wild-type strain (AB or Tuebingen) and embryos screened for mutations. Embryos from founder fish (F0) that transmitted mutations to their progeny were raised to adulthood (F1) and fin-clipped to identify specific mutations by cloning and sequencing (**Section 2.3.9**). A heterozygous carrier fish harbouring a frameshift

mutation was picked to generate a stable mutant line by outcrossing to a wild-type fish. The resulting F2 generation was fin-clipped to identify heterozygous carrier fish using the KASP assay (**Section 2.3.20**) and the progeny of an incross raised to adulthood (**Figure 2.5**).

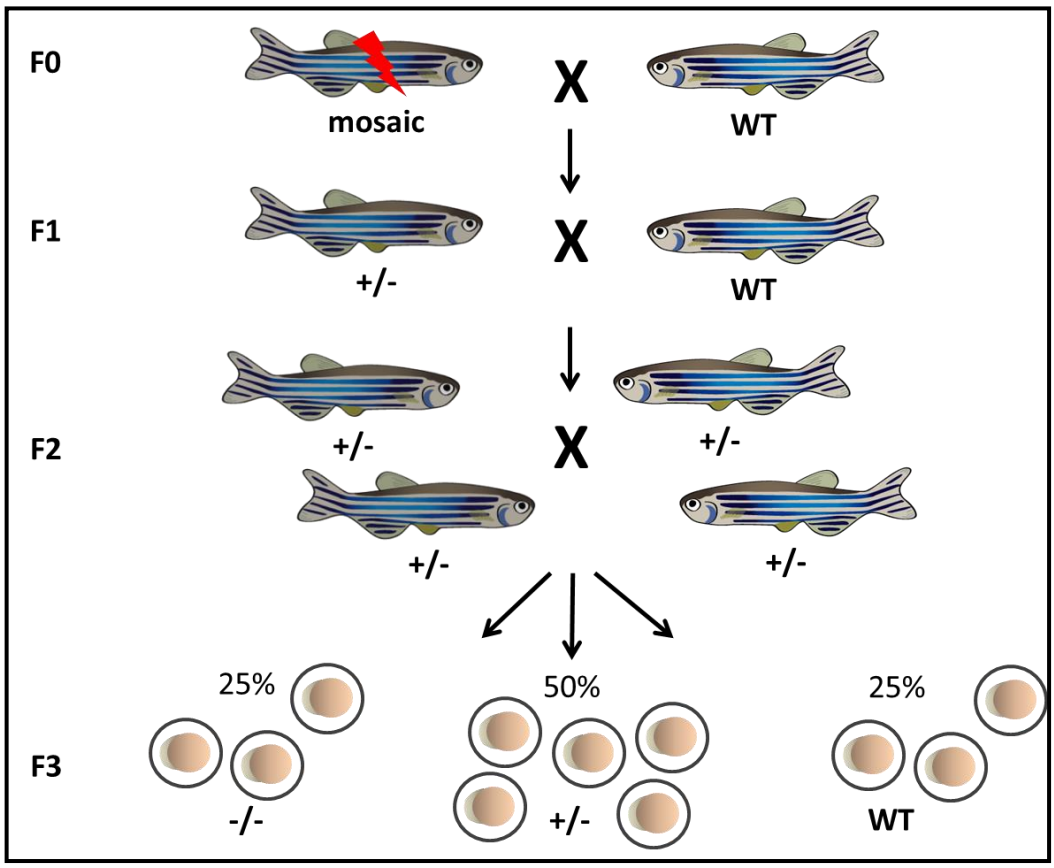

Figure 2.5 Generation of a stable mutant line.

TALEN or CRISPR injected F0 fish are mosaic for mutations in somatic and germ cells (indicated by a red bolt). If germline mutagenesis has occurred mutations are transmitted to the F1 generation. A F1 heterozygous carrier fish (+/-) harbouring a desired mutation is then outcrossed to a wild-type (WT) fish generating heterozygous F2 fish with identical mutations. Incross of the F2 generation produces homozygous mutant embryos that can be used for subsequent experiments.

Unless otherwise stated, maternal-zygotic mutants from an incross of homozygous adult mutants were used for experiments in this thesis. This ensures that loss-of-gene function is not rescued through maternal transcripts. The progeny of adult wild-type siblings was used as wild-type control animals.

2.4.4 Environmental Mn exposure

Zebrafish treatments with $MnCl_2$ were performed by adding $MnCl_2$ directly to the fishwater. To determine the median lethal concentration (LC_{50}) 20 wild-type and *slc39a14*^{U801} mutant zebrafish larvae were placed in each well of a six well plate containing 10 mL of fishwater. $MnCl_2$ was added at various concentrations from 2 dpf and lethality was assessed until 5 dpf. The LC_{50} was calculated by Probit Analysis using the IBM SPSS Statistics package version 21.

2.4.5 Whole mount *in situ* hybridisation

Whole mount *in situ* hybridisation was performed according to standard protocols[198]. Embryos/larvae were fixed at the required time points in 4% paraformaldehyde (PFA, **Appendix 9.2**) at 4°C overnight. They were subsequently stored in 100% methanol at -20°C for a minimum of 24 hours before whole mount *in situ* hybridisation. Embryos were gradually rehydrated by replacing the 100% methanol with 5 min washes of i) 75% methanol / 25% PBST [Phosphate buffered saline (PBS) / 0.1% Tween-20], ii) 50% methanol / 50% PBST, iii) 25% methanol / 75% PBST and iv) 100% PBST (4 x 5 min). Embryos older than 2 somite stage (ss) were permeabilised by treatment with protein kinase (PK, 10 mg/mL, 1000 x stock solution). Length of time of permeabilisation and concentration of PK was dependent on the embryo/larval developmental stage as detailed below:

2-10ss	in and out 1x PK
10-15ss	1 min 1x PK
16-26ss	2 min 1x PK
24hpf	10 min 1x PK
30hpf	20 min 1x PK
36-48hpf	35 min 1x PK
2.5dpf	35 min 1.5x PK
3dpf	35 min 2x PK
4dpf	35 min 3x PK
5dpf	35 min 4x PK

Following PK digestion, embryos were refixed in 4% PFA (20 min) and washed in PBST (5 x 5 min). Prehybridisation was performed in hybridisation mix (Hyb^+, **Appendix 9.2**) at 70°C for 2 hours followed by probe hybridisation at a concentration of 50-100 ng/µL in Hyb+ at 70°C overnight.

Hyb+ was gradually changed to 0.2x saline-sodium citrate buffer (SSC, **Appendix 9.2**) through a series of 15 minute washes at 70°C: i) 75% Hyb- (**Appendix 9.2**) / 25% 2x SSC, ii) 50% Hyb- / 50% 2x SSC, iii) 25% Hyb- / 75% 2x SSC, iv) 2x SSC; followed by 2 x 30 min washes in 0.2x SSC. The 0.2X SSC was then replaced with PBST through a series of 10 minute washes at room temperature: i) 75% 0.2xSSC / 25% PBST, ii) 50% 0.2xSSC / 50% PBST, iii) 25% 0.2xSSC / 75% PBST, iv) 100% PBST. Embryos were subsequently incubated in blocking solution (MABlock, **Appendix 9.2**) at room temperature for several hours followed by incubation in polyclonal anti-digoxigenin-alkaline phosphatase (AP) antibody (Roche) at a concentration of 1:2,000 in blocking solution at 4°C overnight.

Following washes in PBST (6 x 15 min) and staining buffer (3 x 5 min) the embryos were developed by incubation in 4-nitro blue tetrazolium chloride (NBT, 1 µL/mL staining buffer) (Roche) and 5-bromo-4-chloro-3-indolyl-phosphate, toluidine-salt (BCIP, 3.5 µL/mL) (Roche). Development was assessed under the microscope and once strong staining had occurred embryos were washed in stop solution (**Appendix 9.2**) followed by fixation in 4% PFA for 30 min. For long-term storage embryos were placed in 100% methanol and stored at -20°C.

Prior to imaging, embryos were taken to 80% glycerol and mounted in a droplet of 80% glycerol on a hanging drop microscope slide (Fisher Scientific). Images were taken on a Nikon Eclipse E1000 microscope using the Openlab 4.0.2 software package.

2.4.6 Sectioning of whole mount *in situ* hybridisation samples

Embryos/larvae were embedded using the JB-4 embedding kit (Sigma-Aldrich) according to the manufacturer's recommendations. Embryos were left to overstain for at least 24 hours. After fixation in 4% PFA for 2 hours and 3 washes in PBST the embryos were washed in MQ H_2O in glass dishes (3 x 10 min). The samples were dehydrated through washes of i) 30% ethanol / 70% H_2O, ii) 50% ethanol / 50% H_2O,

iii) 70% ethanol / 30% H_2O, iv) 95% ethanol / 5% H_2O and v) 100% ethanol. The embryos were incubated in a 1:1 mix of activated Solution A (0.36 g benzoyl peroxide in 25 mL of Solution A) and 100% ethanol for 1 hour at room temperature followed by incubation in 100% activated Solution A at 4°C overnight on a shaker. The embryos were then mounted in embedding moulds filled with 175 µl of plastic resin (40 µL of Solution B to 960 µL of activated solution A). The samples were dried in a plastic container with a constant flow of nitrogen gas for 15 min. Once the samples had hardened the following day they were mounted on microtome blocks using cold-curing resin (Technovit, 500 µL liquid were added to powder filling a 1.5 mL microcentrifuge tube to the 1 mL mark).

Samples were sectioned at 10 µm thickness using a Leica Jung RM2055 microtome. Sections were placed in a drop of distilled water on a multispot microscope slide and airdried on a hotplate. Finally, the sections were counterstained with 0.002% neutral red solution and imaged using a Nikon Eclipse E1000 microscope and the Openlab 4.0.2 software package.

2.4.7 Immunofluorescence and confocal imaging

Embryos / larvae fixed in 4% PFA and stored in 100% methanol were rehydrated using PBS + 0.5% Triton-X100 (PBSTr), permeabilised with PK and postfixed as described above (**Section 2.4.5**). Dissected brains from 5 dpf larvae were permeabilised using 1 x PK for 15 min. The samples were then incubated in blocking solution [10% normal goat serum, 1% dimethylsulfoxide (DMSO), 0.5% Triton X-100 in PBS] for a minimum of 1 hour at room temperature followed by overnight incubation in primary antibody in blocking solution at the required concentration at 4°C. The next day, the samples were washed for 6 x 30 min in PBSTr followed by incubation in secondary antibody at a concentration of 1:200 in PBSTr and 6 x 30 min washes in PBSTr. For nuclear staining 4',6-diamidino-2-phenylindole (DAPI, 10 mg/mL) was added to one of the PBSTr washes at a concentration of 1:1000. For zebrafish brains, toto-3 iodide was used as a nuclear stain at a concentration of 1:5000. The toto-3 iodide was added directly to the secondary antibody and incubated at room temperature overnight. Samples were kept in PBS and mounted in 1.5 % low melting point agarose in PBS. Alternatively, zebrafish brains were taken through a dilution series of glycerol/PBS to 80% glycerol/PBS and mounted in 1% agarose in 80% glycerol/PBS. Images were obtained

either on a Leica TCS SPE or SP8vis confocal microscope using a 25x 0.95 water-immersion/dipping objective or a 40x glycerol immersion objective. Z-stacks were acquired in 1 µm intervals and maximum-intensity projections generated with Fiji software.

Primary Antibody	Isotype	Company	Catalogue number	Concentration
GFP	Chicken polyclonal	Abcam	Ab13970	1:500
RFP	Rabbit polyclonal	MBL	PM005	1:1000
Tyrosine Hydroxylase	Mouse IgG1	Millipore	MAB318	1:1000
Secondary Antibody	Isotype	Company	Catalogue number	Concentration
Chicken Alexa Fluor 488	Goat IgG	Life Technologies	A-11039	1:200
Rabbit Alexa Fluor 568	Goat IgG	Life Technologies	A-11011	1:200
Mouse Alexa Fluor 568	Goat IgG	Life Technologies	A-11031	1:200

Table 2.17 Primary and secondary antibodies used for immunofluorescence.
GFP, green fluorescent protein; RFP, red fluorescent protein.

2.4.8 Apoptosis analysis

The TUNEL (Terminal deoxynucleotidyl transferase dUTP Nick End Labelling) assay was used to examine apoptosis in Mn exposed wild-type and mutant *slc39a14*^{U801} brains at 5 dpf. One of the hallmarks of apoptosis is the endonucleolytic fragmentation of DNA from 180 to 200 bp[201]. The DNA strand breaks are detected by enzymatic labelling of the DNA ends using terminal deoxynucleotidyl transferase (TdT) and digoxigenin labelled nucleotides.

In brief, PFA fixed zebrafish brains in 100% methanol were rehydrated and permeabilised as described (**Sections 2.4.5 and 2.4.7**). Following washes in PBSTr,

the samples were incubated at -20°C in pre-chilled ethanol:acetone (2:1) for 10 min followed by 3 x 5 min washes in PBSTr. After 1 hour incubation in Apoptag equilibration buffer (Millipore) the samples were incubated in 35 µL of TdT enzyme mix [24 µL reaction buffer, 12 µL TdT enzyme (both Millipore), 1 µL 10% Triton-X100] at 37°C overnight. This was followed by four washes in PBSTr and incubation in blocking solution for more than two hours at room temperature. Subsequently, the samples were incubated with polyclonal Anti-Digoxigenin-AP antibody (Roche) at a concentration of 1:2,000 in blocking solution at 4°C overnight and the samples developed as described for whole mount *in situ* hybridisation (**Section 2.4.5**).

2.4.9 Locomotor behaviour analysis

The behavioural assay was conducted as described previously[202] (**Figure 2.6**). In brief, zebrafish embryos and larvae were raised in a 14h:10h light:dark cycle. Single larvae were transferred to each well of a flat-bottom, clear polystyrene 96 well plate (Whatman) in 650 µL fish water at 4 dpf. The 96-well plate was maintained at a constant temperature (28.5°C) and exposed to a 14h:10h white light:dark schedule with constant infrared illumination within a custom-modified Zebrabox (Viewpoint LifeSciences). Fish water was refilled daily to maintain appropriate water levels. The locomotor behaviour of zebrafish larvae was tracked from 4 to 7 or 8 dpf using an automated video tracking system (Viewpoint LifeSciences). Larval movement was recorded using Videotrack Quantization mode. The following Videotrack detection parameters were empirically defined for each Zebrabox to ensure clean detection of larval movement with minimal noise: a detection threshold to distinguish the dark larvae from the white background (pixels darker than this threshold that change were detected as movement) and a freeze threshold (change of pixel number required to constitute movement rather than random pixel noise). Data was collected for each individual larva as total seconds spent moving per minute. A custom-designed Matlab code (kindly provided by Dr Jason Rihel, Department of Cell and Develomental Biology, UCL) was used to extract the following data:

- Total activity: measured for each day and night as average activity per 10 min.
- Total sleep: sleep is defined as a continuous period of inactivity lasting at least one minute. Total sleep was measured for each day and night period given as average sleep per 10 min.

- Average waking activity: measures the average activity only during periods of waking activity (given as average activity per waking minute). This is calculated by dividing the total activity by the total active minutes (total time minus total sleep time).

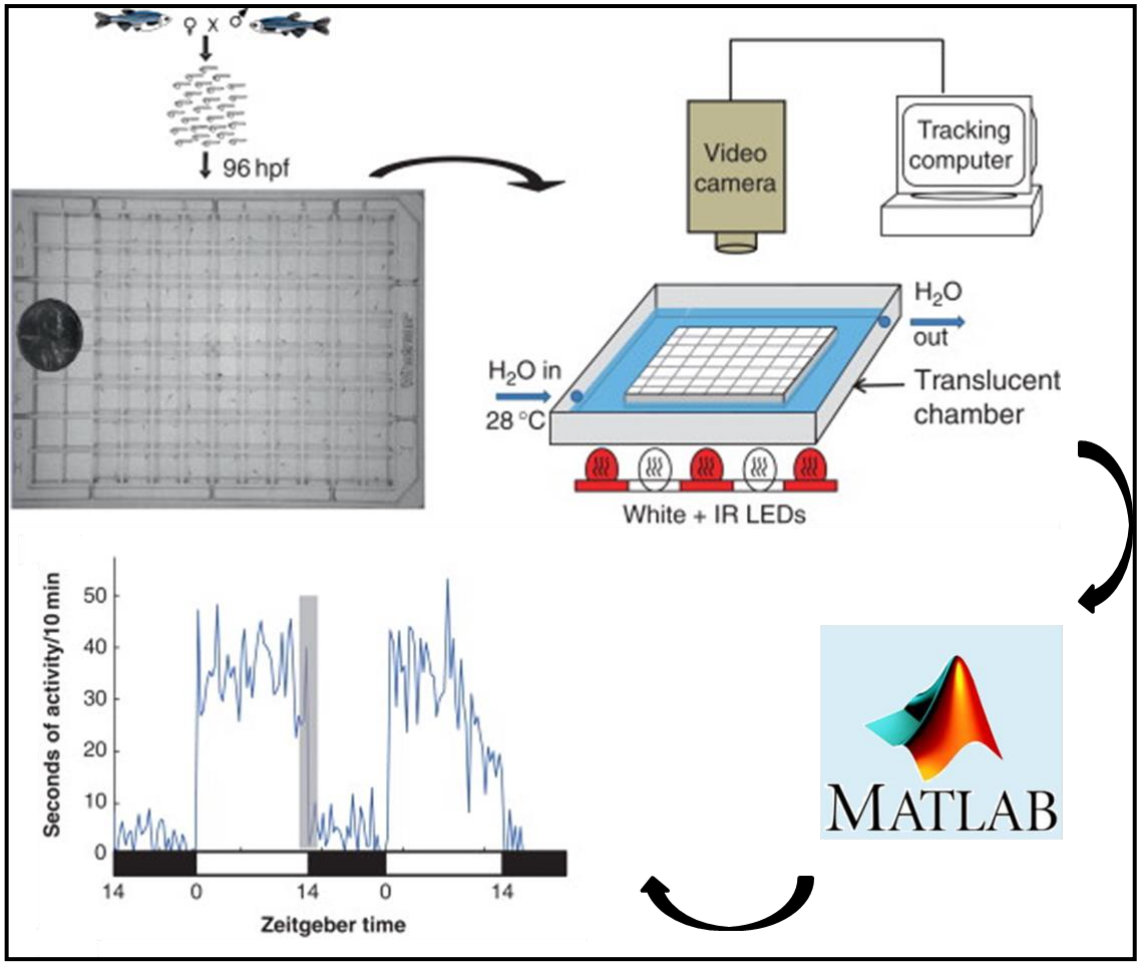

Figure 2.6 Locomotor behaviour analysis setup.

The movement of single larvae in a 96 well plate was continuously tracked and recorded between 4 and 7 dpf. A Matlab code was used to extract various activity and sleep parameters from the data collected from each larva (seconds of movement per minute). The data is plotted against the recorded time. The black and white bars indicate day and night periods, respectively.

Statistical analysis was performed using GraphPad Prism 5.0 Software. Mn exposure was achieved by adding $MnCl_2$ (50 µM) directly to the fish water. Results from

genotypically presorted larvae were confirmed by analysis of a heterozygous in-cross with subsequent genotyping.

2.4.10 Optokinetic response (OKR)

The OKR was examined using a custom-built rig to track horizontal eye movements in response to whole-field motion stimuli. Larvae at 4 dpf were immobilised in 1.5% agarose in a 35 mm petri dish and analysed at 5 dpf. The agarose surrounding the eyes was removed to allow normal eye movements. Sinusoidal gratings with spatial frequencies of 0.05, 0.1, 0.13 and 0.16 cycles/degree were presented on a cylindrical diffusive screen 25 mm from the centre of the fish's head. Gratings had a constant velocity of 10 degrees/second and changed direction and/or spatial frequency every 20 seconds. Eye movements were tracked under infrared illumination (720 nm) at 60 Hz using a Flea3 USB machine vision camera and custom-written software. A custom-designed Matlab code (kindly provided by Dr Isaac Bianco, Department of Cell and Developmental Biology, UCL) was used to determine the eye velocity (degrees per second).

2.5 Metal determination using inductively coupled plasma – mass spectrometry ICP-MS

2.5.1 Blood samples

50 µL of EDTA blood were added to 1.95 mL of 3% nitric acid (Fisher) and incubated at 85°C for four hours in 10 mL Falocn tubes. After centrifugation at >10,000 x g the supernatant was analysed by ICP-MS.

2.5.2 Zebrafish larvae

Ten larvae of the same genotype, anaesthetised with MS-222, were pooled and washed several times with dH_2O. Samples were digested in 1 mL 3% nitric acid in 0.5 mL Eppendorf tubes at 85°C overnight followed by a final 95°C incubation step for 2 hours.

2.5.3 Zebrafish tissues

Tissues (brain and abdominal viscera including intestine, liver, pancreas and spleen) dissected from adult zebrafish were digested in concentrated nitric acid at room temperature overnight and subsequent incubation at 95°C for 30 minutes. Samples were diluted with ICP-MS grade H_2O (Fluka) to a final nitric acid concentration of 3%. Samples from four zebrafish of the same genotype were combined to ensure metal concentrations exceeded the limit of detection.

2.5.4 Cell culture samples

Transiently transfected HEK293 cells or stable cell lines were incubated in culture medium containing 1 µM $MnCl_2$ for 15 and 30 minutes, respectively. Following 2 washes with ice-cold PBS, cells were harvested in 500 µl PBS using a cell scraper and transferred to a microcentrifuge tube. The cell pellets were washed once in 250 µl ICP-MS grade H_2O and lysed by repeated freeze-thawing using an ethanol dry ice and 37°C water bath. The protein concentration was determined using BCA reagent (Thermo Scientific) and the cell lysates digested in 3% nitric acid in a final volume of 1 mL. Digestion was carried out at 85°C overnight and 95°C for 2 hours the following day.

2.5.5 ICP-MS analysis

ICP-MS analysis was done in collaboration with Dr Alaa Abdul-Sada at the Department of Chemistry, Sussex University.

The metal ion isotopes Mn-55, Fe-56, Zn-66 and Cd-111 were measured by an Agilent 7500 Series ICP-MS, and germanium (Ge)-72 was used as internal standard. Calibration solutions were prepared for each element between 0 and 200 ng/mL. A blank sample was run for each analysed condition to correct for background contamination originating from the reagents used.

2.6 RNA sequencing

2.6.1 Preparation of larvae for RNA and DNA extraction

The progeny of an in-cross of *slc39a14*^{U801} +/- fish were raised under standard conditions. $MnCl_2$ at a concentration of 20 µM was added to the fishwater from 2 to 5 dpf. After 72 hours of exposure single larvae were collected in the wells of a 96 well plate, immediately frozen on dry ice and stored at -80°C. RNA and DNA extraction, and KASP genotyping were performed at the Wellcome Trust Sanger Institute according to local protocols.

2.6.2 RNA sequencing

A polyA enriched RNA sequencing method was used by Dr Elisabeth Busch-Nentwich at the Wellcome Trust Sanger Institute according to local protocols. The subsequent bioinformatic analysis mapped each identified transcript to the closest annotated gene and determined a p-value for each differentially expressed gene. Only differentially expressed genes with a p-value below 0.05 were considered statistically significant. Anatomical gene enrichment analysis using local bioinformatics analysis software was based on data from the Zebrafish Information Network (ZFIN; http://zfin.org/).
Inidividual differentially expressed genes were analysed for their link with Mn homeostasis using online databases such as ZFIN, Online Mendelian Inheritance in Man (OMIM;http://www.ncbi.nlm.nih.gov/omim) and Pubmed (http://www.ncbi.nlm.nih.gov/pubmed) to determine those that may play an important role in the pathophysiology of Mn toxicity and SLC39A14 deficiency.

2.7 Statistical analysis

Wherever possible, a minimum of three biological replicates were analysed in each experiment. Statistical analysis including student's *t*-test, one and two way ANOVA were performed using GraphPad Prism 5.0 Software or IBM SPSS Statistics package version 21. Probit regression analysis was done using IBM SPSS Statistics package version 21.

Chapter 3. Clinical phenotype and genetics of SLC30A10 deficiency

3.1 Introduction

SLC30A10 deficiency, the first ever identified inborn error of Mn metabolism, was only described recently[46,48]. SLC30A10 is a Mn exporter localised at the cell membrane of hepatocytes and neurons allowing the cellular detoxification of Mn[47,48]. Mutations in *SLC30A10* lead to impaired hepatic Mn excretion resulting in accumulation of Mn in the liver and brain[46,48]. Mn deposition in the brain causes distinct MRI brain features including T1 hyperintensity of the basal ganglia, the cerebral and cerebellar white matter and dorsal pons with sparing of the ventral pons[51]. The affinity of Mn to particular brain regions is shared by acquired and inherited forms of Mn overload, however, the mechanism behind this phenomenon is still unkown[51,203].

SLC30A10 deficiency affects children from as early as the first years of life with parkinsonism-dystonia but can also present in adulthood with parkinsonism resembling Parkinson's disease. Neurological symptoms are accompanied by haematological characteristics including polycythaemia and depleted iron stores, and a variable degree of liver disease[46,48-50]. The movement disorder is similar to the one seen in manganism due to chronic environmental Mn overexposure, however, manganism lacks the development of polycythaemia and cirrhosis[22]. Acute Mn overexposure on the other hand can cause liver failure due to acute hepatic necrosis[53-56].

To date, 22 patients from 13 families have been diagnosed with SLC30A10 deficiency, all carrying different homozygous sequence changes in *SLC30A10*, including missense, nonsense and frameshift mutations as well as deletions[46,48,49]. It is possible that a genotype-phenotype relationship exists; a single sibship with adult-onset parkinsonism has been described carrying a homozygous frameshift mutation in the last exon of *SLC30A10* that only removes the last 49 of the 485 amino acid protein[48]. Given the small number of patients identified to date it is likely that the full phenotypic spectrum of this disorder is yet unknown.

Treatment of SLC30A10 deficiency aims to reduce the body Mn load with chelation therapy and minimise gastrointestinal Mn abosorption by optimising iron levels[46,57]. The

only effective chelation agent used to date is disodium calcium edetate ($Na_2CaEDTA$). It is given intravenously as a five day course every four weeks thereby significantly adding to the disease burden, socioeconomic costs and complications associated with long-term vascular access[46,57].

This work aimed to add to our previously published work[46] on the phenotypic and genotypic spectrum of SLC30A10 deficiency by performing mutation analysis of *SLC30A10* in any new patients presenting with clinical characteristics of inherited hypermanganesaemia including dystonia-parkinsonism and typical MRI brain appearances of hyperintensity of the basal ganglia and white matter on T1-weighted images[46,48].

3.2 Case presentations

The clinical features of studied patients are detailed below (**Table 3.1**).

Subject	G	Origin	CS	Onset	D/P	PC	↑ LFTs	T1 HI	Blood Mn
N-II-1	F	Brazil	N*	7 y	Y	Y	Y	Y	9 µg/L (<2)
O-II-1	M	Yemen	N*	2 y	Y	Y	N	Y	4 µg/L (1.5-2.5)
O-II-2	M			3 y	Y	Y	N	Y	N/A
O-II-3	F			7 y	Y	Y	N	N/A	3.5 µg/L (1.5-2.5)
O-II-4	M			-[#]	N[#]	Y	N	N/A	N/A
P-II-2	F	Turkey	Y	1.5 y	Y	Y	Y	Y	3528 mol/L (<273)
Q-II-2	M	Guam	Y	2 y	Y	Y	Y	Y	25 µg/L (0-2)
R-II-1	M	Pakistan	Y	7 y	Y	Y	N	Y	1511 nmol/L (<320)
R-II-2	M			11 y	Y	Y	N	Y	14972 nmol/L (<320)
R-II-3	M			6 y	Y	Y	N	Y	539 nmol/L (<320)
S-II-2	M	Macedonia	N/A	1.5 y	Y	Y	Y	N/A	N/A
T-II-1	F	India	N/A	36 y	Y	N	N	Y	56 µg/L (4.2-16.5)
U-II-1	F	Australia	N/A	32 y	(Y)^	N	N	N	410 nmol/L (100-300)
V-II-1	M	Serbia	N	10 y	(Y)+	N	N	Y	16.4 µg/L (<16)
W-II-1	M	Portugal	N	13 y	Y	N	Y	Y	1001 nmol/L (187-209)
X-II-1	F	UK	N	14 y	N	N	Y	Y	263 nmol/L (73-210)
Y-II-1	F	Yemen	Y	7 m	Y	N	N	Y	N/A
Y-II-4	F			7 m	Y	N	N	Y	8101 nmol/L (<320)
Z-II-1	M	Spain	Y	10 m	Y	N	N	Y	965 nmol/L (<145.6)

Table 3.1 Clinical characteristics of individuals with suspected SLC30A10 deficiency.

*Individual families are numbered N to Z with each affected sibling listed. *Regions where cases of SLC30A10 deficiency have been diagnosed previously. #Currently only affected with asymptomatic polycythaemia. ^Isolated dystonic tremor of left hand. +Episodic bradykinesia. Laboratory reference ranges for blood Mn levels are given in parentheses. G, gender. CS, consanguinity. D/P, dystonia-parkinsonism. PC, polycythaemia. LFT, liver function tests. T1 HI, basal ganglia hyperintensity on T1 weighted MR imaging. F, female. M, male. N, no. Y, yes. N/A, not available.*

Family N

The family described originates from São Paulo, Brazil, the same geopgraphical region where two cases of inherited hypermanganesaemia have been identified previously[46]. The affected patient (N-II-1) is a girl born to non-consanguineous parents who presented at the age of seven years with progressive generalised dystonia, sardonic smile, “cock-walk” gait, cog-wheel sign in her upper extremities and mild chorea particularly in her toes and fingers[204]. Unlike recently reported cases of inherited hypermanganesaemia due to *SLC30A10* mutations, this affected girl has also shown progressive cognitive decline.

Polycythaemia with Hb values above 23 g/dL (reference range 11-16 g/dL) was detected, and whole blood Mn was raised at 9 ng/dL (reference range <2 ng/dL). Her liver enzymes were deranged; aspartate transaminase (AST) measured 63 U/L (reference range <32 U/L), alanine aminotransferase (ALT) 57 U/L (reference range <33 U/L), alkaline phosphatase (ALP) 594 U/L (reference range <300 U/L) and gamma-glutamyltransferase (GGT) 46 U/L (reference range <40 U/L). Liver biopsy showed a diffuse portal lymphocytic inflammatory infiltrate with parenchymal perivenular fibrosis, expansion of sinusoids and foci of necrosis. MRI brain was characteristic of Mn deposition with hyperintensity of the basal ganglia including the globus pallidus, putamen, caudate and dentate nucleus (**Figure 3.1**) on T1-weighted imaging. There was no history of environmental Mn exposure.

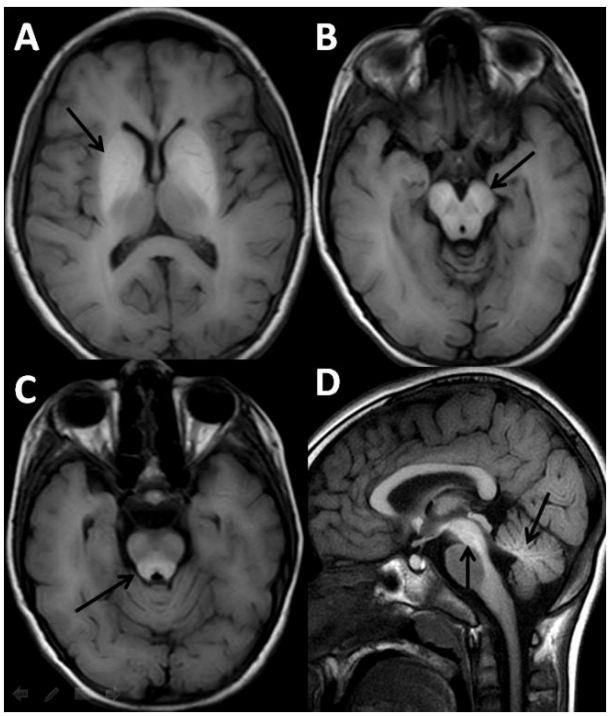

Figure 3.1 Neuroradiological appearances of individual N-II-I.
*Transverse T1 weighted MRI show bilateral hyperintense signal changes in the globus pallidus (**A**), midbrain (**B**) and pontine tegmentum (**C**). The sagittal image demonstrates T1 hyperintensity of the cerebellar dentate nuclei and the dorsal pons with sparing of the ventral pons (**D**). From Avelino et al.[204].*

Family O

The four affected children are from a non-consanguineous Arabic marriage with both parents originating from the same village in Yemen. A family with mutations in *SLC30A10* has been reported in this geographical region previously[46]; a degree of consanguinity within the family and with the previously described family cannot be excluded. Three of the four affected children presented at the age of two (O-II-1), three (O-II-2) and seven (O-II-3) years, respectively, with generalised dystonia and gait disturbance. Whole blood Mn levels were raised above 3.5 ng/dL (reference range 1.5 to 2.5 ng/dL). All affected siblings presented with polycythaemia, however, liver function tests were reported as normal. The MRI brain scan was consistent with Mn deposition in the basal ganglia. The youngest affected sibling has remained asymptomatic to date. The only abnormality found is significant polycythaemia.

Family P

The affected girl (P-II-2) was born as the second child to first cousin parents of Turkish ancestry. She presented at the age of one year and six months with difficulty walking. Neurological examination at the age of three years revealed generalized dystonia particularly prominent in the lower extremities. She was unable to stand and walk without support. Mild hyperbilirubinaemia (total bilirubin 1.8 mg/dL, reference range 0.2-1.2 mg/dL), polycythaemia (Hb 23.4 g/dL, reference range 9-16 g/dL), and liver dysfunction (AST 78 U/L, reference range 5-42 U/L; ALT 130 U/L, reference range 5-45 U/L) were detected. Whole blood Mn levels were raised (3528 nmol/L, reference range <273 nmol/L). T1 hyperintensities of the basal ganglia including the caudate and lentiform nuclei, and dentate nuclei were consistent with Mn deposition. Liver biopsy confirmed portal fibrosis. Her most recent neurological examination at the age of 7 years showed additional severe dysarthria and mild to moderate cognitive deficit.

Family Q

The affected boy (Q-II-2) was born at term to consanguineous parents in Guam. The maternal grandmother and the paternal grandfather are first cousins. He presented at the age of two years when he started running but had difficulties with balance. At four years of age his brain MRI confirmed T1 hyperintense signal return within the globus pallidus. He had elevated serum Cu levels, but normal coeruloplasmin. Neurological examination revealed dystonia in all four limbs, spasticity with mild left hemiparesis but no dysarthria/dysphagia. He reportedly is keeping up cognitively at school. Serum Mn

levels were raised at 25 µg/dL (reference range 0-2 µg/dL) and he was polycythaemic (Hb 17.7 g/dL, reference range 9-16 g/dL). While ferritin and Fe levels were normal he had a high TIBC of 508 µg/dL (reference range 228-428 µg/dL). Liver transaminases were raised (AST 98 U/L, reference range 5-42 U/L; ALT 89 U/L, reference range 5-45 U/L) and a liver ultrasound was suggestive of liver cirrhosis.

Family R

This large consanguineous family originates from Sind, Pakistan with three of twelve siblings affected with typical features of dystonia, polycythaemia and hypermanganesemia (R-II-1 to R-II-3)[205]. Affected siblings presented between 6 and 11 years with difficulty walking, four limb dystonia and slurred speech but absent liver disease. Hb ranged from 16.4 to 20.7 g/dL (reference range 13-16 g/dL), blood Mn levels were between 539 nmol/L and 14972 nmol/L (reference range <320 nmol/L). In individual R-II-2, ferritin was at the lower end of normal at 13.2 ng/mL (reference range 7-140 ng/mL) and erythropoietin was raised at 18.55 mU/mL (reference range 3.3-16.6). MR brain imaging showed the typical T1 hyperintense changes in the globus pallidus (**Figure 3.2**), dentate nuclei and white matter in sibling O-II-2. The two youngest affected siblings (R-II-1 and R-II-2) were commenced on chelation therapy with Na_2CaEDTA and Fe supplementation. Following five cycles of chelation, Mn levels reduced from 14972 to 1777 nmol/L in individual R-II-2 while they remained almost unchanged in individual R-II-1 (from 1511 to 1481 nmol/L). Polycythaemia in both siblings worsened with Hb levels of 21 and 23.6 g/dL, respectively. Given the risk of thrombotic events they were both treated with phlebotomy to reduce the haematocrit. Due to unavailability of Na_2CaEDTA both siblings' chelation therapy was changed to D-Penicillamine which led to further improvement of dystonia and stabilisation of Mn blood levels (from 1481 to 673 nmol/L in individual R-II-1 and from 1777 to 1092 nmol/L in individual R-II-2).

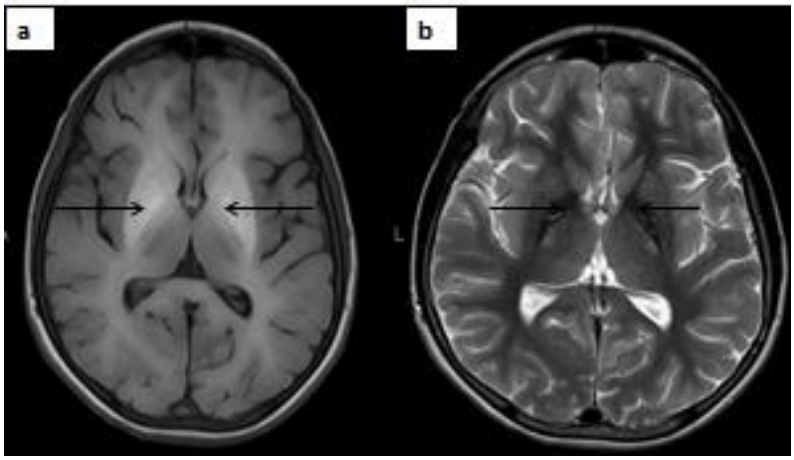

Figure 3.2 Neuroradiological appearances of individual R-II-2.

*(**a**) T1-weighted imaging. Arrows indicating bilateral hyperintense signals in the globus pallidus along with mild cystic changes in this region. (**b**) T2-weighted imaging shows hypointense signal return in the corresponding region. From Mukhtiar et al.[205].*

Family S

The affected boy (S-II-2) was born as the second child to healthy parents of Macedonian ancestry. After a normal initial development he presented at the age of one year and six months with hypotonia and abnormal posturing during a febrile illness. He was also noted to have abnormal liver function tests. Subsequent to this he developed torsion dystonia and pyramidal tract involvement and became wheelchair bound by the age of six years. A liver biopsy at the age of three years showed micronodular cirrhosis. Plasma Cu levels were slightly raised, however, liver stains for Cu and Fe were negative. Polycythaemia with Hb values between 17 and 20 g/dL were treated with repeated phlebotomies. Intellectual development has been normal. This patient is now in his early twenties and has advanced liver disease. He has experienced severe complications including oesophageal bleeding. Unfortunately, the result from blood Mn measurements and brain MRI are not available.

Family T

This lady (T-II-1) presented at the age of 37 years with anxiety disorder, hallucinations, insomnia and anaemia. Nine months into treatment with antidepressants and antipsychotics she developed slurred speech and generalised limb stiffness and dystonia. She was commenced on treatment for atypical parkinsonism including carbi/levodopa, trihexyphenidyl, tetrabenazene, clonazepam and baclofen with minimal

improvement of dystonia and dysarthria. Whole blood Mn levels were raised at 56 µg/L (reference range 4.2-16.5 µg/L). Polycythaemia is absent in this patient; her highest Hb level was 14.5 g/dL. Liver enzyme studies were normal, however, MRI of the liver was suggestive of early cirrhosis. Fe indices were indicative of Fe depletion (ferritin 6.9 ng/mL, reference range 10-291 ng/mL; Fe 23 µg/dL, reference range 50-170 µg/dL; TIBC 256 µg/dL, reference range 250-425 µg/dL). MRI brain imaging showed mild hyperintensity of bilateral globus pallidus, however, to a much lesser extent than previously observed in patients with SLC30A10 deficiency (**Figure 3.3**). T1 hyperintensity of the white matter was absent.

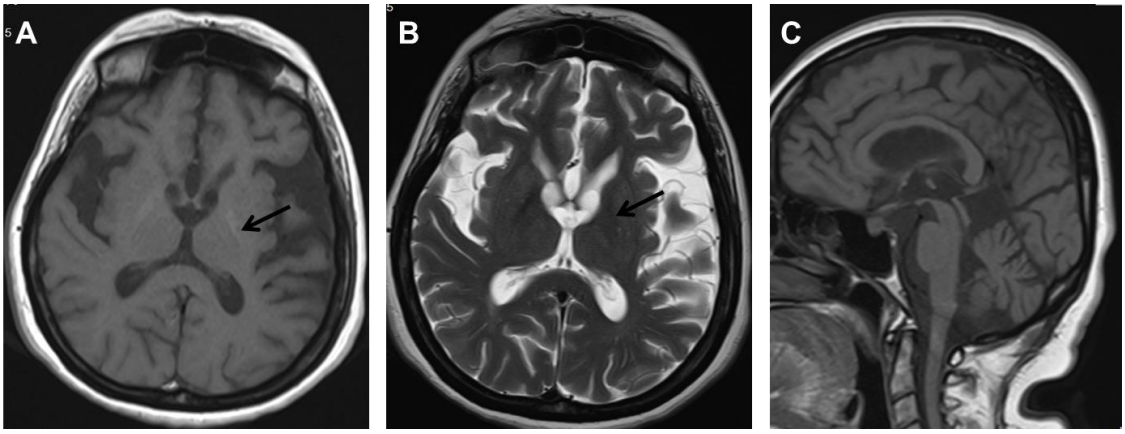

Figure 3.3 Neuroradiological appearances of individual T-II-I.

*Mild features consistent with Mn deposition are present on transverse T1 weighted MR images (**A**) with some T1 shortening in the globus pallidus which is accompanied by T2 hypointensity (**B**). The prominent T1 hyperintensity of the cerebral white matter and dorsal pons with sparing of the ventral pons normally observed in SLC30A10 deficiency is absent on sagittal imaging (**C**).*

Family U

This 33 year old lady (U-II-1) presented with a one year history of dystonic tremor of her left hand. MR brain imaging showed some signal reduction in the right basal ganglia on T2 weighted images. Hb and liver function tests were normal. Blood Mn levels were raised at 0.41 µmol/L (reference range 0.1-0.3 µmol/L).

Family V

The affected boy (V-II-1) was born at term as the only child to healthy, non-consanguineous Serbian parents. He presented at the age of ten years with attention problems at school. Following scoliosis surgery at the age of 16 years he developed auditory and visual hallucinations, stupor and bradykinesia that lasted for two to three days. These symptoms have recurred on several occasions over the following years. He is now 20 years old and between episodes shows mild to moderate cognitive decline, hallucinations, anxiety and mild dysarthria. Whole blood Mn level was at the upper limit of normal (16.4 µg/L, reference range <16.5 µg/L). MRI brain appearances were consistent with Mn deposition showing bilateral hyperintense signal changes of the globus pallidus on T1 weighted images (**Figure 3.4**). There was no polycythaemia (Hb 12.4 g/dL, reference range 9-16 g/dL) and liver function tests were normal. Liver ultrasound was suggestive of early liver cirrhosis.

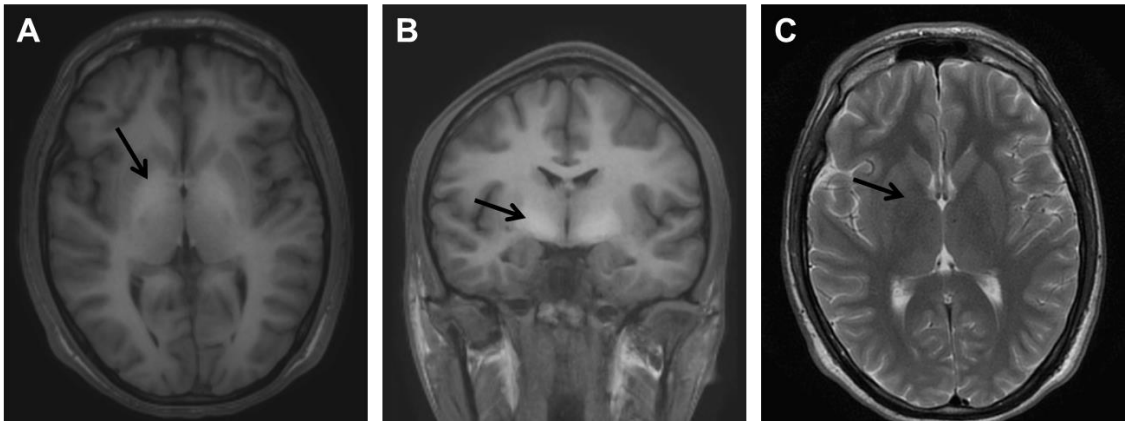

Figure 3.4 Neuroradiological appearances of individual V-II-I.

*Transverse (**A**) and coronal (**B**) T1 weighted MR images show bilateral hyperintense signal changes in the globus pallidus with corresponding hypointense changes on T2 (**C**) suggestive of Mn deposition.*

Family W

This affected boy (W-II-1) was born at term to healthy non-consanguineous parents of Portuguese ancestry. He presented at the age of 13 years with mild learning difficulty and attention deficit hyperactivity disorder. Three years later he was noted to have splenomegaly and mild palmar erythema. Liver enzyme tests including ALT, AST and lactate dehydrogenase (LDH) were deranged and a liver ultrasound was suggestive of

liver cirrhosis. The whole blood Mn level was raised at 1001 nmol/L (reference range 187-209). Polycythaemia was absent (highest Hb 13.6 g/dL, reference range 9-16 g/dL). Neurological examination revealed mild dystonia and dysdiadochokinesis in the left arm and a somewhat unsteady gait. Aside from mild hyperintense changes of bilateral globus pallidus on T1 weighted images the MRI brain did not show the characteristic changes usually observed in SLC30A10 deficiency (**Figure 3.5**).

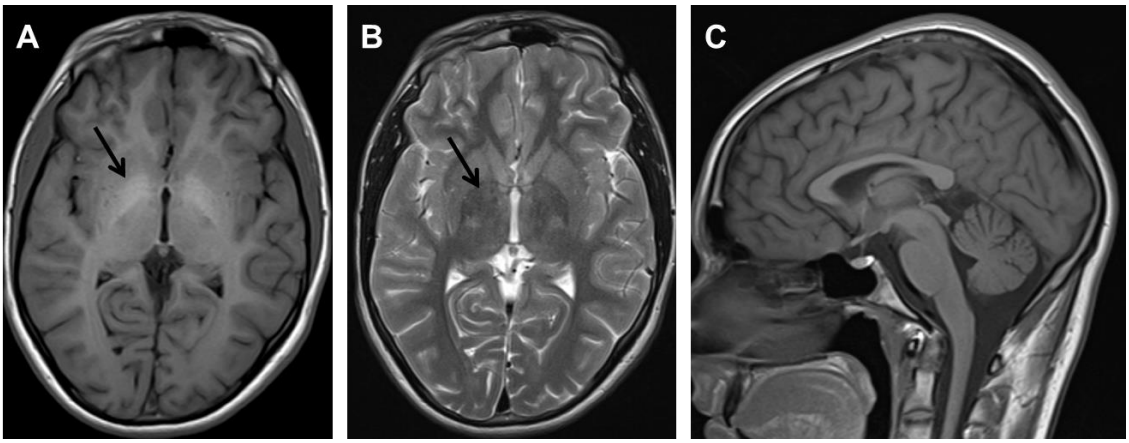

Figure 3.5 Neuroradiological appearances of individual W-II-I.

Some degree of Mn deposition is present in the globus pallidus on transverse imaging suggested by T1 hyperintensity (A) and T2 hypointensity (B). There is no white matter involvement (C).

Family X

The affected girl (X-II-1) was born at term to healthy non-consanguineous parents of British ancestry. She was diagnosed with auto-immune hepatitis and polyendocrinopathy with ovarian and adrenal involvement at the age of 14 years. She responded well to treatment with Azathioprine and her liver function tests normalised. Liver biopsy showed a mild degree of fibrosis. She had no neurological symptoms. MR brain imaging showed an abnormally high T1 signal in the globus pallidus, subthalamic nuclei and substantia nigra which could not be explained by the degree of liver disease. Whole blood Mn was mildly raised at 263 nmol/L (reference range 73-210 nmol/L). She was never polycythaemic (latest Hb 9.6 g/dL, reference range 9-16 g/dL).

Family Y

Family Y originate from Yemen. The parents are first cousins and have two affected and two unaffected daughters. One sister (Y-II-1) presented with generalised dystonia and dysphagia at the age of seven months and, unfortunately, passed away at the age of thirteen months. The cause of death is unknown. The second affected girl (Y-II-4) presented at the age of seven months with loss of motor milestones following a normal birth and normal initial psychomotor development. She became increasingly irritable and lethargic, and developed central hypotonia, generalised dystonia and dysphagia. She showed no pyramidal tract signs, and hearing and vision appeared normal. MRI brain showed extensive T1 hyperintensity of the globus pallidus, dentate nucleus and white matter which was accompanied by T2 hypointensity (**Figure 3.6**). Unfortunately, she was lost to follow up after her initial consultation and there is no further information available on her progress.

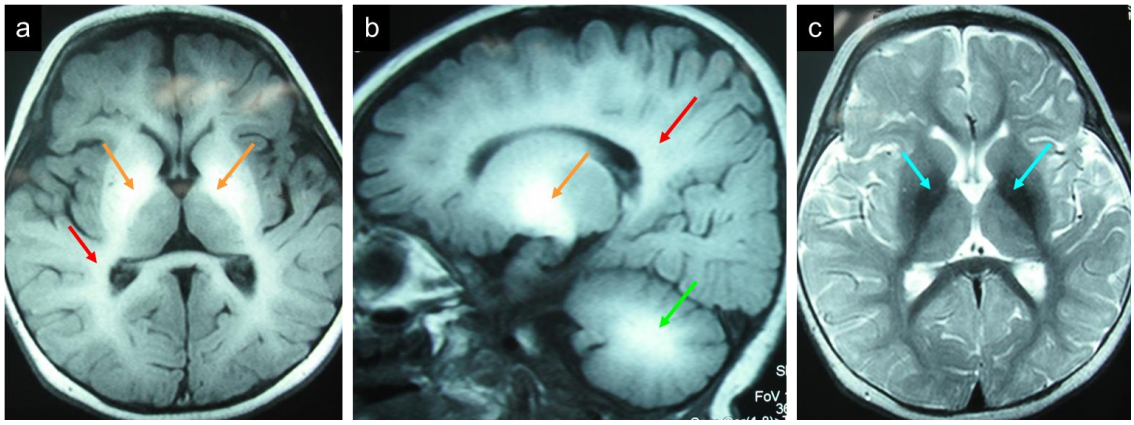

Figure 3.6 Neuroradiological appearances of individual Y-II-4.

(**a**) Transverse T1-weighted (**b**) Sagittal T1-weighted (**c**) Transverse T2-weighted MR brain imaging. There is marked hyperintensity of the globus pallidus (orange arrows in a and b), dentate nucleus (green arrow in b) and white matter (red arrows in a and b) on T1-weighted imaging with corresponding T2 hypointensity of the globus pallidus (turquoise arrows in c).

Family Z

The affected boy (Z-II-1) of Spanish ancestry was the only child of first cousin parents. He presented at the age of ten months with global developmental delay, macrocephaly, marked global hypotonia with normal reflexes, poor spontaneous movements and

some dystonic neck movements. He suffered from thermal dysregulation episodes and developed severe generalised dystonia unresponsive to drug treatment. At four years of age he died of septic shock following *E. coli* bronchopneumonia.

Hypermanganesemia was persistent with values four to twenty times that of normal. Neither parent had hypermanganesemia and environmental Mn exposure was ruled out. Mn deposition was visible on MR brain imaging with additional cerebral and cerebellar atrophy (**Figure 3.7**). He was found to have a slightly elevated creatine kinase (CK) with normal electromyography. Metabolic screening included plasma amino acids, urine organic acids, cerebrospinal fluid (CSF) neurotransmitter amine metabolites and transferrin isoelectric focusing, all of which was negative. The only metabolic abnormality found was an impairment of the mitochondrial respiratory chain with deficiencies of complex III and V in muscle. Molecular analysis for recessive mitochondrial DNA mutations was negative.

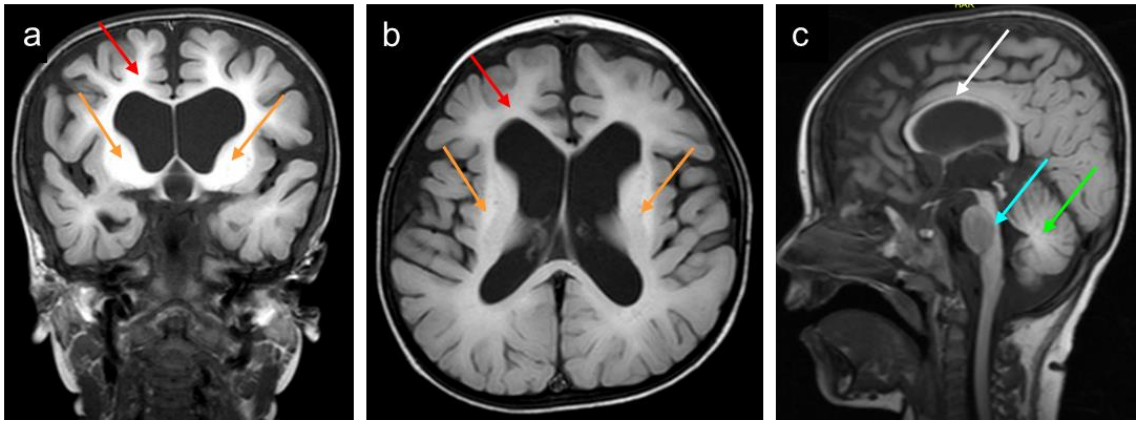

Figure 3.7 Neuroradiological appearances of Individual Z-II-1.

(**a**) Coronal T1-weighted (**b**) Transverse T1-weighted (**c**) Saggital T1-weighted MR brain imaging. There is marked hyperintensity of the globus pallidus (orange arrows in a and b), dentate nucleus (green arrow in c) and white matter (red arrows in a and b). Saggital imaging demonstrates hyperintensity of the dorsal pons with sparing of the ventral pons (turquoise arrow in c). Additionally, there is marked cerebral and cerebellar atrophy demonstrated by a thinning of the corpus callosum (white arrow in c) and widening of the extracerebral space and ventricles (a-c).

3.3 Novel mutations identified in *SLC30A10*

Sanger sequencing of the coding exons and intron/exon boundaries of *SLC30A10* in the above patients identified homozygous missense, nonsense or frameshift mutations in all individuals who presented with hypermanganesaemia and associated polycythaemia and typical MRI brain appearances that included white matter involvement (family N to S) (**Table 3.2, Section 2.3.2**).

Subject	Exon	cDNA change	Amino acid change	PC
N-II-1	3	922C>T	Gln308*	Y
O-II-1	1	266T>C	Leu89Pro	Y
O-II-2	1	266T>C	Leu89Pro	Y
O-II-3	1	266T>C	Leu89Pro	Y
O-II-4	1	266T>C	Leu89Pro	Y
P-II-2	4	1188dup	Leu397Thrfs*15	Y
Q-II-2	3	870_872del	Ile291del	Y
R-II-1	4	1006C>T	His336Tyr	Y
R-II-2	4	1006C>T	His336Tyr	Y
R-II-3	4	1006C>T	His336Tyr	Y
S-II-2	5'UTR→2	Deletion*		Y
T-II-1	No mutation identified			N
U-II-1	No mutation identified			N
V-II-1	No mutation identified			N
W-II-1	No mutation identified			N
X-II-1	No mutation identified			N
Y-II-2	No mutation identified			N
Z-II-1	No mutation identified			N

Table 3.2 *SLC30A10* mutations identified in individuals with clinical phenotypes suggestive of inherited hypermanganesaemia.

**Individual S-II-2 carries a homozygous deletion involving part of the 5'UTR, the first and second exon. PC, polycythaemia. Y, yes. N, no.*

Where polycythaemia or MRI features suggestive of Mn deposition were absent, no *SLC30A10* mutations were found (family T to Z) indicating that polycythaemia together with distinctive MRI brain features are diagnostic markers for this disease. Identified

mutations in family N and O have previously been observed in affected individuals from the same geographical region suggesting a possible founder effect[46]. It was possible to confirm segregation of the mutations detected in parental samples from all of the families except for patients Q-II-2 and S-II-2 for whom parental DNA was not available. Amino acid changes either affect highly conserved regions or cause significant truncation of the protein (**Figure 3.8**).

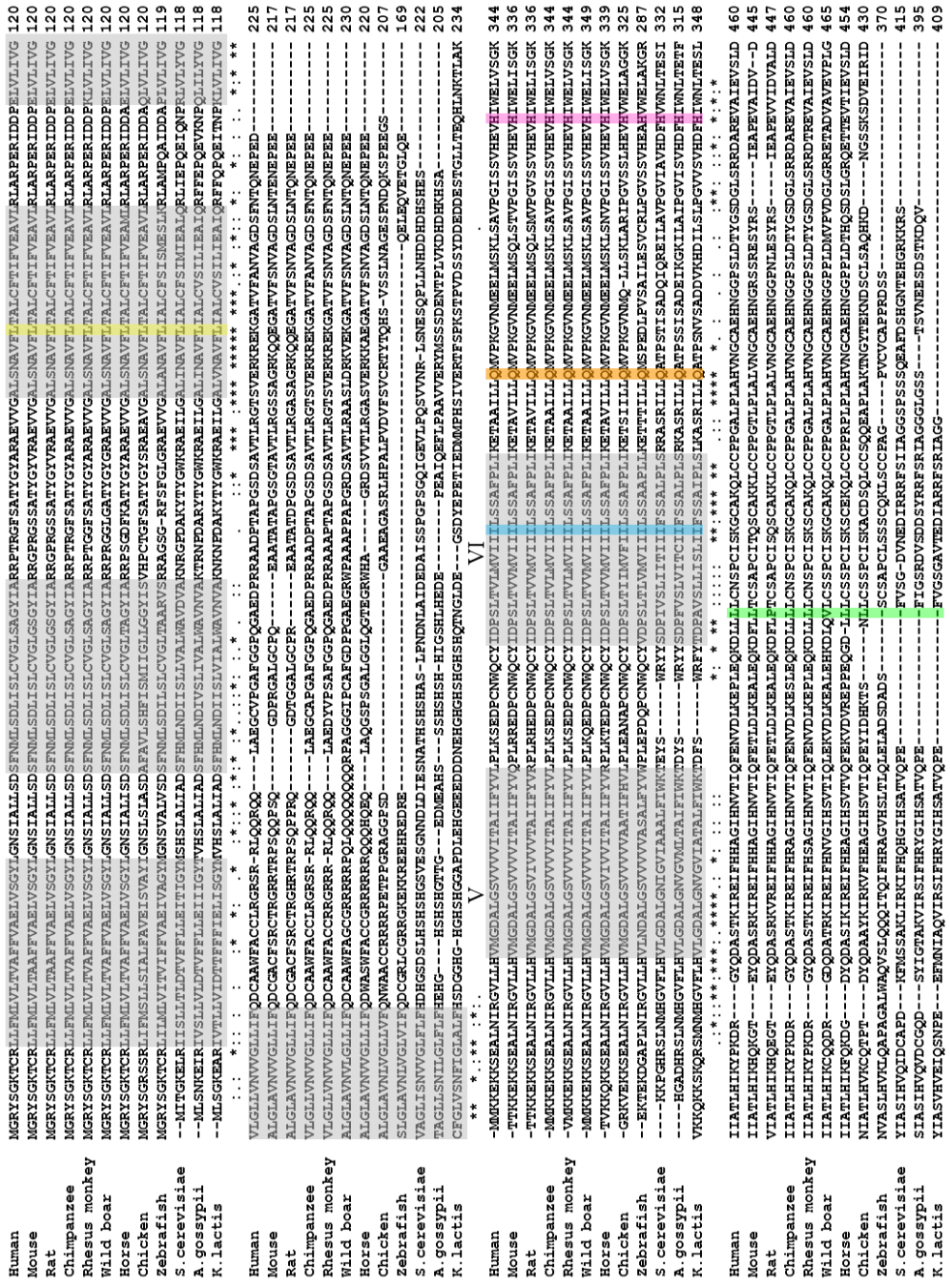

Figure 3.8 *SLC30A10* mutations affect evolutionary conserved protein domains.

Graph showing the evolutionary conservation data of SLC30A10 and positions of newly identified amino acid changes. TMDs are marked in grey. Positions with single, fully conserved residues are marked with an asterisk (*). Conservation between groups of strongly and weakly similar properties is indicated by a colon (;) and a period (.), respectively. Amino acid substitutions are marked in colour: p.Leu89Pro (yellow), p.Arg239Lys (red), p.Ile291del (blue), p.Gln308 (orange), p.His336Tyr (purple), Leu397Thrfs*15 (green).*

Individual S-II-2 appears to carry a homozygous deletion of part of the 5'UTR, the first and the second exon of *SLC30A10* which did not amplify by PCR (**Figure 3.9**). All of the other regions of *SLC30A10* amplified successfully and Sanger sequencing did not identify a mutation.

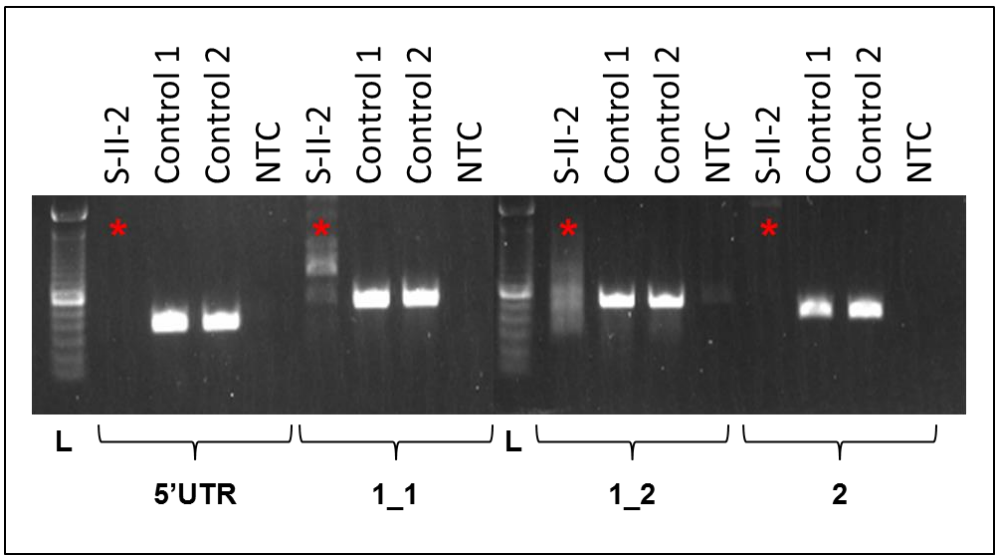

Figure 3.9 5'UTR, exon 1 and 2 of SLC30A10 do not amplify in subject S-II-2.
Gel electrophoresis image of the PCR amplicons of the 5'UTR, exon 1 and 2 of SL30A10 of individual S-II-2, control subject 1 and control subject 2. Exon 1 is covered by amplicon 1_1 and 1_2, respectively. For individual S-II-2 the bands of the correct size are absent for 5'UTR, exon 1 and 2 (marked by asterisks). L, 500 bp ladder. NTC, non template control.

In order to identify the exact position of the deletion, multiple loci around the suspected deletion within *SLC30A10* and its neighbouring gene *EPRS* encoding the glutamyl-prolyl-tRNA synthetase were PCR amplified from both patient and control DNA. The results suggest that the deleted genomic sequence lies within a 6100 bp spanning region (**Figures 3.10 and 3.11**). Primers within this region have been designed and tested, however, they failed to amplify control DNA. Also, an initial attempt to amplify the whole 6100 bp spanning region for subsequent cloning was unsuccessful. Additional work is required to further delineate the locus of the deletion, and amplify and sequence this region to define the exact position.

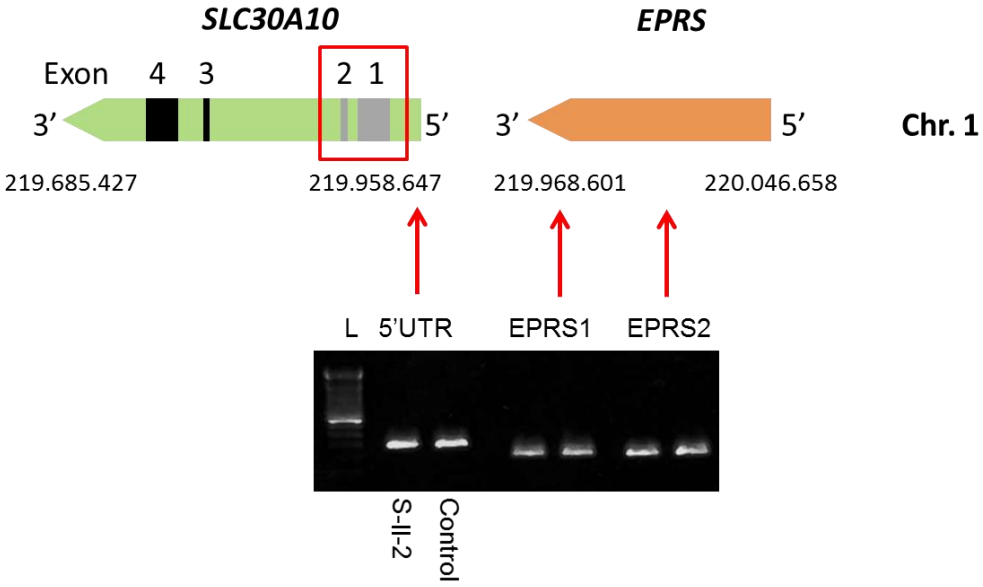

Figure 3.10 Location of the presumed deletion within *SLC30A10* in individual S-II-2.

Schematic of the chromosomal location of SLC30A10 and its neighbouring gene EPRS on chromosome 1 (not drawn to scale). Gel electrophoresis image below showing the amplicons from a region upstream in the 5'UTR of SLC30A10 and two regions within the neighbouring gene EPRS encoding the glutamyl-prolyl-tRNA synthetase (EPRS1, EPRS2). Given that exon 3 and 4 and loci upstream in the 5'UTR of SLC30A10 and EPRS are present in the patient DNA the deletion must span across part of the 5'UTR, exon 1 and 2 of SLC30A10 (indicated by a red box).

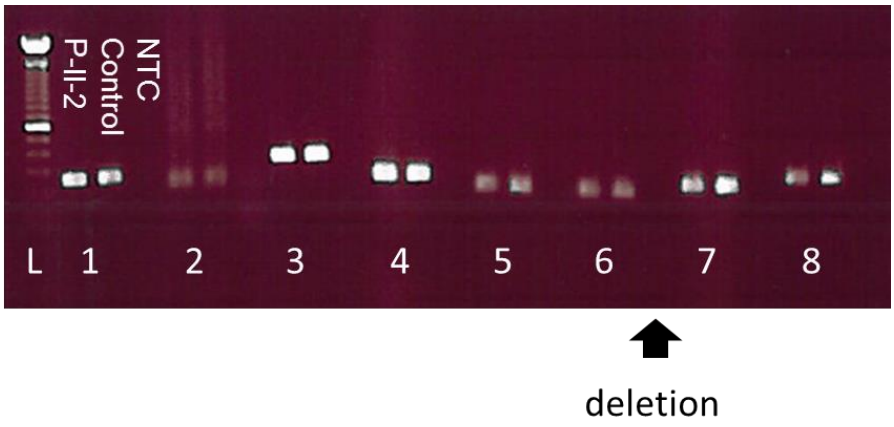

Primer pair	Genomic location
1	219.954.290 - 219.954.057
2	219.950.632 - 219.950.460
3	219.946.173 - 219.945.906
4	219.941.278 - 219.941.031
5	219.936.231 - 219.936.056
6	219.931.311 - **219.931.109**
Exon 1 & 2	**219.928.645 – 219.927.028**
7	**219.925.025** - 219.924.928
8	219.921.662 – 219.921.431

Figure 3.11 Individual S-II-2 carries a homozygous deletion within a region of 6100 bp around exon 1 and 2 of *SLC30A10*.

Gel electrophoresis image of PCR amplicons of loci neighbouring SLC30A10 exon 1 and 2. The positions of the amplicons are given in the table below. Amplification of these loci in individual S-II-2 suggest that the deletion (arrow) locates to a region between amplicon 6 and 7, genomic position 219.931.109 and 219.925.025 (marked in red).

3.4 Discussion

3.4.1 Further delineation of the clinical characteristics of SLC30A10 deficiency

Eleven individuals from six different families out of the 19 patients investigated were shown to have homozygous mutations in *SLC30A10*. Together with previously reported cases[46,48,49], a total of 36 patients from 19 families with SLC30A10 deficiency are now known.

All eleven subjects presented in early childhood between 1.5 and 11 years of age with a dystonic movement disorder and hypermanganesaemia. No case with adult-onset parkinsonism was identified. So far, the majority of patients with *SLC30A10* mutations manifest early-onset forms. Only one sibship with adult-onset parkinsonism has been reported in the literature so far[48]. Both subjects were initially diagnosed with Parkinson's disease, however, they failed to respond to treatment with Levodopa or Dopamine agonists. *SLC30A10* mutation screening of Parkinson's disease patients with poor response to drug treatment may identify further late-onset cases in the future. Review of the MRI brain appearances for changes associated with manganese deposition (discussed below) in such patients may highlight affected individuals.

Consistent with previous reports all individuals with *SLC30A10* mutations had significant polycythaemia[46,48,49]. Subject O-II-4 presented with polycythaemia prior to the manifestation of dystonia, hence, it is likely that polycythaemia precedes neurological disease. Mn is known to induce *EPO* gene expression[61,206] (discussed in **Sections 1.2.1 and 4.7**). Increased EPO levels were confirmed in affected siblings from family R and is consistent with previous reports[50]. Individuals with hypermanganesaemia and absent polycythaemia screened negative for mutations in *SLC30A10*. Polycythaemia is therefore an important diagnostic hallmark of this disorder. Polycythaemia in the context of a movement disorder should therefore prompt the analysis of whole blood Mn levels. It is possible that some cases of idiopathic polycythaemia with absent mutations in the common disease gene *JAK2*[207-209] may carry mutations in *SLC30A10* that cause a milder disease phenotype. It would therefore be interesting to perform *SLC30A10* mutation screening in a cohort of patients with polycythaemia rubra vera and no identified genetic cause.

The raised hepatic manganese concentrations in patients with SLC30A10 deficiency is the likely cause for the observed polycythaemia. Hepatic manganese content was measured in two subjects and shown to be elevated 2- and 9-fold, respectively[50,210]. Transition metals such as manganese, cobalt and nickel are known to induce HIF-1 activation[211]. Consistent with this observation erythropoietin levels have been found to be raised in several patients with SLC30A10 deficiency[46].

Another haematological feature of SLC30A10 deficiency is that of depleted Fe stores. Unfortunately, for most patients studied here this information is not available. However, where analysed they consistently show an increased TIBC and low ferritin. Iron deficiency may further contribute to HIF pathway activation and increased erythropoietin gene expression[212].

MRI brain appearances were similar to those previously described[46,48-51,58,204] and included hyperintensity on T1-weighted imaging of the globus pallidus and dentate nucleus, the cerebellar white matter and dorsal pons with sparing of the ventral pons. T1 signal changes were accompanied by hypointensity on T2-weighted imaging. These changes are characteristic of Mn deposition and occur because Mn, a paramagnetic metal, causes signal enhancement on T1 and attenuation on T2 weighted images[213,214]. MRI changes in inherited Mn transporter deficiencies are more pronounced than in acquired manganism where T2 images are often reported as normal[52,203,215]. The T1 hyperintensity of the pons with sparing of the ventral pons has only been observed in inherited Mn transporter defects caused by *SLC30A10* and *SLC39A14* mutations (described in **Chapter 4**)[46,48-51,65]. These MRI brain changes appear to be pathognomonic for inherited Mn transportopathies. Indeed, individuals studied who did not share the typical MRI changes were found to be negative for mutations in *SLC30A10*.

As previously observed, liver involvement is variable[46,48,50,57]. While individuals from four families showed raised liver enzymes those from two families did not have signs of liver disease. Liver involvement ranged from mild transaminitis in the majority of patients to severe liver disease in individual S-II-2 who experienced severe complications including oesophageal bleeding. It is still unknown what factors make an individual more susceptible to liver disease and why some patients remain unaffected.

From the newly identified indiviudals with SLC30A10 mutations described above only those from one family have received treatment with $Na_2CaEDTA$ according to standard protocols[57]. The high costs and requirement for hospitalisation remain the main obstacle for initiation of treatment. Two affected individuals from family R showed a good response to chelation therapy with $Na_2CaEDTA$ leading to improvement of Mn levels and mobility. However, due to financial constraints $Na_2CaEDTA$ had to be stopped and was replaced with oral D-Penicillamine. Mn levels and neurological symptoms are reported to have improved further[205]. There is evidence that D-Penicillamine mobilises Mn with increased urinary excretion of Mn evident in patients with SLC30A10 deficiency, however, to a lesser degree than that is observed with $Na_2CaEDTA$[51]. A positive response to D-Penicillamine has been observed in a patient with SLC30A10 deficiency previously (F-II-1 in Tuschl *et al.*, 2012[46]). This patient was also found to have an increased 24 hour urinary Cu excretion presumably due to a heterozygous mutation in *ATP7B*, the gene affected in Wilson's disease[216] (data from personal communication). Several patients with SLC30A10 deficiency have shown mildly raised Cu levels[50,210]. It is therefore plausible that D-Penicillamine may reduce both Mn and Cu levels in this disorder with subsequent improvement of clinical symptoms. Other reports in the literature suggest that para-aminosalicylic acid (PASA) may be an efficacious chelator with Mn binding capacity[217-219]. An individual with manganism showed an improvement of neurological symptoms following repeated courses of intravenous application[218]. Unlike $Na_2CaEDTA$, para-aminosalicylic acid is absorbed in the gastrointestinal tract, hence, oral administration is possible. Therefore, para-aminosalicylic is a promising candidate for testing its Mn chelation ability *in vivo*. In addition, dimercaptosuccinic acid has been suggested as a Mn chelator, however, there is considerable uncertainty about its efficacy[220,221]. In a single individual with SLC30A10 deficiency dimercaptosuccinic acid led to an imrovement of blood Mn levels. However, this patient was simultaneously treated with iron supplementation which may solely contribute to the change of blood Mn level observed (data from personal communication).

Post-mortem studies of a patient with SLC30A10 deficiency showed substantial neurodegenerative changes of the basal ganglia including neuronal loss, astrocytosis, myelin loss and spongiosis[210]. However, reversibility of neurological symptoms in response to $Na_2CaEDTA$ implies that in addition to neuronal death, Mn toxicity must cause circuit dysfunction by interference with some unknown aspects of neuronal

function (as discussed in **Section 6.5.2**). Furthermore, SLC30A10 plays a role in signal transduction by increasing the phosphorylation of mitogen-activated protein kinase (MEK) and ERK1 and 2 involved in the regulation of transcription and translation[222]. Hence, *SLC30A10* mutations might directly impair signalling pathways.

In summary, SLC30A10 deficiency causes hypermanganesaemia associated with polycythaemia and Mn deposition in the brain causing a parkinsonian movement disorder. While these features are pathognomonic for SLC30A10 deficiency liver disease is variable and does not occur in every patient. Polycythaemia is an important diagnostic feature and should point towards a diagnosis in the presence of a parkinsonian movement disorder. At present, $Na_2CaEDTA$ remains the only proven efficacious chelation agent able to reverse neurological symptoms.

3.4.2 Expansion of the genetic spectrum of SLC30A10 deficiency

SLC30A10 mutations described in **Section 3.3** include two known changes; a homozygous nonsense mutation in exon 3 in patient N-II-1 (Gln308*) and a missense mutation in exon 1 in patients O-II-1 to O-II-4 (Leu89Pro). These mutations have previously been observed in affected individuals from the same geographical region suggesting a possible founder effect. Four novel mutations were identified in family P to S including a homozygous frameshift mutation in exon 4 (Leu397Thrfs*15), an in-frame deletion in exon 3 (Ile291del), a missense change in exon 4 (His336Tyr) and a large deletion affecting the 5'UTR to exon 2 that will require further delineation. These changes have not been reported in the population previously. Wherever possible segregation of these changes within the families were confirmed. Given the unique clinical phenotype of hypermanganesaemia associated with dystonia, polycythaemia and cirrhosis we can be confident that these mutations are disease causing.

Including the mutations identified here, there are now a total of 17 homozygous mutations in patients with SLC30A10 deficiency known to date[46,48,49]. Mutations have been identified in all of the four exons of *SLC30A10* and encompass a range of missense, nonsense, frameshift and deletion mutations. Some of the deletions span several exons as in the case of individual S-II-2 reported here. The mutation identified in the sibship with adult-onset parkinsonism reported by Quadri *et al.* remains the one situated closest to the end of the protein sequence[48]. Therefore, it is possible that part

of the function of this mutated protein (Val425Ile) is maintained leading to manifestation of the disease in later life. This would suggest a genotype-phenotype relation to some degree. These two patients remain the only ones who have presented with adult-onset parkinsonism. Despite its rarity, SLC30A10 deficiency is an important differential diagnosis in adult patients with parkinsonism poorly responsive to L-Dopa treatment. The features of cerebral Mn deposition on MRI are not well known and blood Mn levels are not part of routine blood tests, hence, it is likely that some cases of SLC3010 deficiency are missed.

Rather surprisingly, no compound heterozygous mutations have been identified to date. This may be due to incomplete penetrance of mutations in the compound heterozygous state as observed for other autosomal recessive disorders such as trichothiodystrophy or familial Mediterranean fever caused by mutations in the *Xpd* and *MEVF* gene, respectively [223,224]. Amelioration of disease symptoms or later disease onset are observed. At the same time, compound mutations can be associated with more severe disease phenotypes as seen in long QT syndrome[225]. Compound heterozygous mutations may therefore be embryonic lethal due to deleterious effect on gene function.

Given its role in Mn transport it is not surprising that non-coding polymorphisms in *SLC30A10* have been reported to be associated with increased Mn blood levels and increased sway velocity in cohorts with environmental Mn exposure[226,227]. Neurological function is affected independent of blood Mn concentrations suggesting that blood Mn levels may not reflect the degree of Mn deposition in the brain[227]. This is consistent with observations in patients with SLC30A10 deficiency whose blood Mn levels do not necessarily correlate with the degree of neurological impairment[46,57].

In conclusion, only homozygous recessive mutations in *SLC30A10* have been identified in patients with hereditary hypermanganesaemia with dystonia, polycythaemia and cirrhosis to date. Non-coding polymorphisms are associated with altered Mn blood levels and neurological function.

Chapter 4. Identification of a new Mn transporter defect - SLC39A14 deficiency

4.1 Introduction

Affected individuals from family Y and Z who had screened negative for *SLC30A10* mutations shared a severe clinical phenotype with disease onset in infancy. Marked Mn deposition was evident on MR brain imaging and blood Mn levels were significantly raised (**Section 3.2**). They had an isolated neurological phenotype with rapidly progressive parkinsonism-dystonia without evidence of liver disease, polycythaemia or altered iron parameters. Given that the affected children had a similar clinical phenotype and were from consanguineous marriages it was possible that they shared a novel autosomal recessively inherited disorder of Mn metabolism, hence, they were investigated further using whole exome sequencing.

4.2 Whole exome sequencing identifies *SLC39A14* as a novel disease gene

Whole exome sequencing of patient Y-II-4 and Z-II-1 including bionformatical analysis was completed by Prof Olaf Bodamer at the University of Miami (**Section 2.3.3**). The data was filtered for Mn associated genes using the locally developed software GEMapp[196]. For individual Y-II-4 homozygous sequence changes were found in five Mn related genes (*ITSN2*, *DNAJC27*, *NRXN1*, *ETS2* and *SLC39A14*), for individual Z-II-1 in three Mn related genes (*MEX3D*, *ANO6* and *SLC39A14*). As only *SLC39A14* was shared by both patients it appeared to be a strong candidate gene. Subject Y-II-4 was found to have a nonsense mutation (E105X) in *SLC39A14* predicted to truncate the protein by 387 amino acids while subject Z-II-1 was identified to have a missense change (G383R) affecting the highly conserved metal binding domain EEXPHEXGD. Both mutations were confirmed by Sanger sequencing (**Section 2.3.2**).

Subsequently, a homozygous frameshift mutation in *SLC39A14* (S160Cfs*5) was also found in a third patient, C-II-2, with hypermanganesaemia and parkinsonism-dystonia but absent mutations in *SLC30A10* (for clinical details see **Section 4.4**) using Sanger sequencing (**Section 2.3.2**). The S160Cfs*5 mutation, caused by a two base pair

deletion within exon 4A, is predicted to solely affect isoform 2. The clinical phenotype of this subject, however, is similar to that of the other two patients.

Further five individuals from two families (family A and B, clinical details in **Section 4.4**) were identified by Dr Manju Kurian, UCL Institute of Child Health, to have mutations in *SLC39A14*. Subsequently, work in this thesis is based on all five families thanks to the kind collaboration and provision of samples by Dr Manju Kurian. The mutations identified include two homozygous missense changes, F98V in family A and N469K in family B, affecting highly conserved amino acid residues.

SLC39A14 mutations of all investigated patients are listed in **Table 4.1** and **Figure 4.1**. Where DNA of parents was available the segregation of the mutations within the family was verified (**Figure 4.1**).

Subject	Exon	cDNA change	Amino acid change	Isoform
Y-II-1[a]	[a]	[a]	[a]	[a]
Y-II-4	3	313G>T	Glu105*	1-3
Z-II-1	7	1147G>A	Gly383Arg	1-3
A-II-1	3	292T>G	Phe98Val	1-3
A-II-2	3	292T>G	Phe98Val	1-3
B-II-2	9A	1407C>G	Asn469Lys	1-3
B-II-3	9A	1407C>G	Asn469Lys	1-3
B-II-4	9A	1407C>G	Asn469Lys	1-3
C-II-2	4A	477_478del	Ser160Cysfs*5	2

Table 4.1 List of *SLC39A14* mutations in individuals with hypermanganesaemia and early-onset dystonia-parkinsonism.

Nucleotide and amino acid changes refer to transcript 2 (NM_015359.4) and protein isoform 2 (NP_056174.2) and are listed together with the exon and isoform affected. [a]*DNA of this subject was not available for mutation testing; the clinical phenotype was similar to her sibling suggesting that they were both affected by the same disorder.*

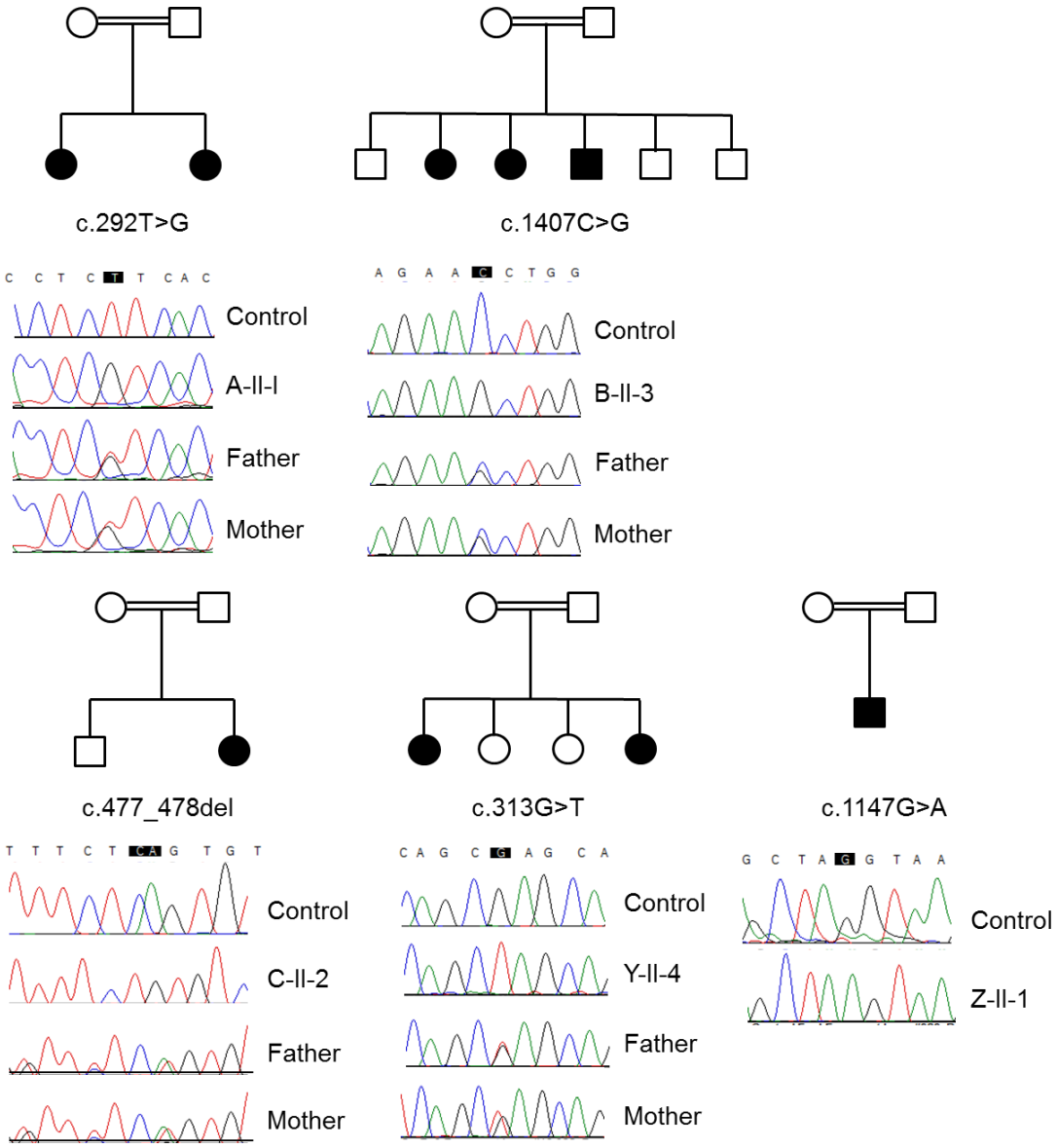

Figure 4.1 Pedigrees and sequence chromatograms of affected individuals with homozygous mutations in *SLC39A14*.

Affected individuals are indicated by black shading. Squares represent males, circles females, and a double line a consanguineous union. Mutated bases are boxed in black. For each family, the top chromatogram shows the wild-type SLC39A14 sequence and the chromatogram below the homozygous SLC39A14 mutation identified in the affected individuals. Parental studies for families A-C and Y demonstrate that both parents are heterozygous carriers of the identified mutation.

All identified changes are novel variants that have not been reported in the literature previously including the dbSNP, 1000 Genomes Project and ExAc databases (**Section 2.3.2**). They affect highly conserved domains of the protein or are predicted to lead to significant truncation of the protein (**Figure 4.2**).

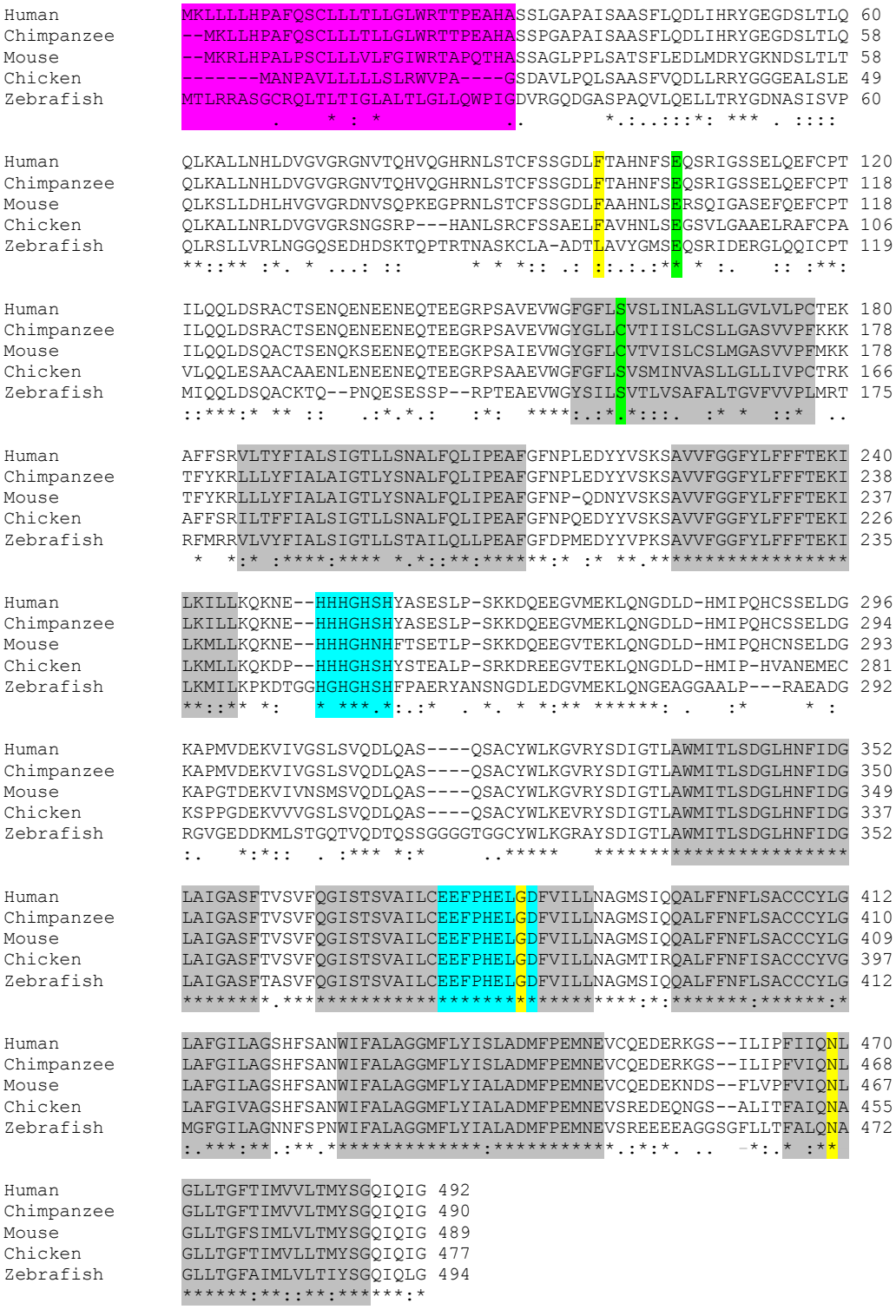

Figure 4.2 Evolutionary conservation data for SLC39A14.

ClustalW software (http://www.ebi.ac.uk/Tools/msa/clustalw2/) was used to generate the alignment. Residues identical to the human SLC39A14 sequence are marked with an asterisk (*). Conservation between amino acids of strongly and weakly similar properties is indicated by a colon (:) and a period (.), respectively. Putative protein

*domains are highlighted and include a signalling peptide (position 1-30; purple; numbering according to the human protein sequence), eight TMDs (position 156-177, 186-211, 225-245, 337-359, 365-389, 397-420, 427-450, 465-487; grey), a histidine-rich region (position 251-257, turquoise), and the LIV subfamily of ZIP transporters (LZT) consensus motif (375-384; turquoise). Amino acids affected by missense mutations are highlighted in yellow (F98V, G383R, N469K) and those pertaining to truncating mutations in green (E105X, S160Cfs*5). Protein sequences used to generate this alignment are NP_056174.2 (human, isoform 2), XP_531112.3 (chimpanzee), NP_659057.2 (mouse), XP_427108.3 (chicken), and XP_005171823.1 (zebrafish).*

The G383R mutation lies within the EEXPHEXGD motif required for metal binding[228,229]. Because this missense mutation (c.1147G>A) affects the last base of exon seven it was possible that this nucleotide substitution leads to abnormal splicing. RT-PCR was performed to assess whether an unspliced transcript is present (**Section 2.3.6**). RNA was extracted from a post mortem liver sample from patient D-II-1 to generate cDNA. Fetal liver, known to express *SLC39A14* was used as a control sample. RT-PCR confirmed that normal splicing is unaffected (**Figure 4.3**).

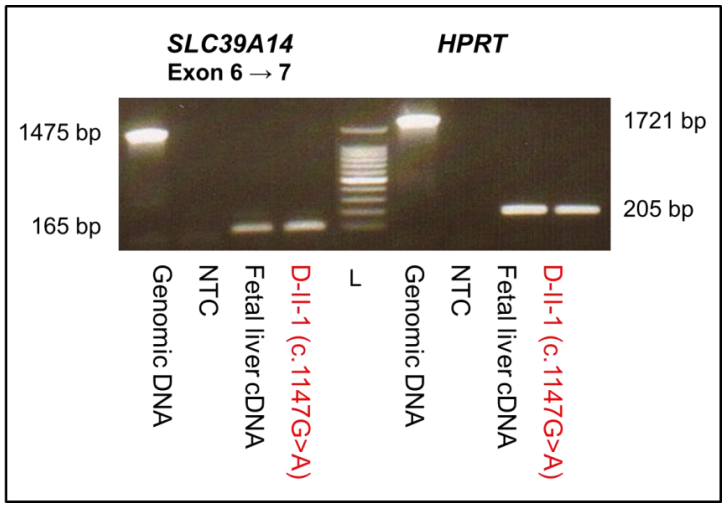

Figure 4.3 The c.1147G>A mutation does not affect normal splicing.
Gel electrophoresis image of RT-PCR amplicons from liver cDNA from individual D-II-1 and control fetal liver. Both show a single band of 165 bp confirming normal mRNA splicing. Primers used span SLC39A14 exon 6 and exon 7. Genomic and unspliced cDNA are predicted to generate a 1475 bp amplicon, whilst normally spliced cDNA produces a 165 bp amplicon. Hypoxanthine-guanine phosphoribosyltransferase (HPRT) was used as a housekeeping control gene. L, 100 bp ladder (Promega). NTC, non-template control.

4.3 Properties of *SLC39A14*

Prior to this work, mutations in *SLC39A14* had not been reported in humans. SLC39A14 is a divalent cation transporter that belongs to the LIV-1 subfamily whose members contain eight transmembrane domains (TMDs), a histidine-rich motif (HXHXHX), and a metalloprotease motif (H/EEXPHEXGD) required for metal transport[228,230] (**Figure 4.4**).

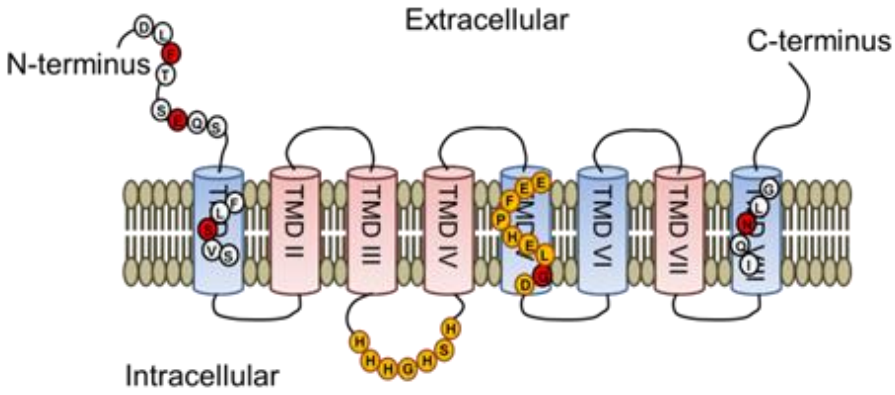

Figure 4.4 SLC39A14 protein structure.

Schematic of SLC39A14 showing its eight TMDs (pink and blue cylinders) interlinked by intracellular and extracellular loops[228,230]. TMD II, III, IV and VII (pink) are postulated by the transmembrane protein topology prediction tool MemSatSVM (http://bioinf.cs.ucl.ac.uk/psipred/?memsatsvm=1) to form a pore. The histidine-rich (HXHXHX) and metalloprotease motif (EEXPHEXGD) are highlighted in orange. Patient mutations are marked in red.

Human *SLC39A14* encodes three isoforms due to alternative splicing of exon four (4A and 4B) and nine (9A and 9B), respectively[70] (**Figure 4.5**). Isoform 1 (NP_001121903) is encoded by two different transcripts that have an alternative 5'UTR (NM_001128431.2 and NM_001135153.1). Isoform 2 (NP_056174) is encoded by one transcript only (NM_015359.4). Isoform 1 and 2 span 492 amino acids and differ by 20 amino acids encoded by an alternatively spliced exon four (4A and 4B). Transcript NM_001135154.1 which encodes isoform 3 (NP_001128626) has an alternative exon nine but shares the remaining protein sequence with isoform 1.

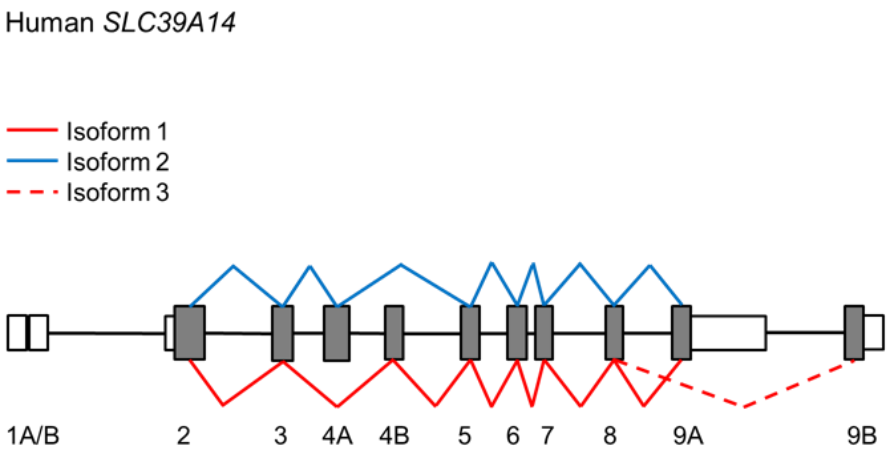

Figure 4.5 Schematic of the human *SLC39A14* gene.
SLC39A14 is composed of nine exons, two of which (exon 4 and 9) can be alternatively spliced to generate three isoforms. Coding exons in grey, untranslated regions unshaded (not drawn to scale).

While most SLC39 transporters are specific for Zn there is substantive evidence that SLC39A14 also transports other metal ions such as Mn, Fe and Cd. The altered metal specificity might be caused by an amino acid change from histidine (H) to glutamate (E) within the metalloprotease motif EEXPHEXGD[70,228-232]. Given its known role in Mn transport *SLC39A14* it seemed plausible that loss-of-function of this gene leads to the phenotype observed in the studied patient cohort.

4.4 Clinical presentation

This cohort of nine patients from five consanguineous families shared common clinical features. Following an uncomplicated birth and normal initial development, affected individuals presented with loss of developmental milestones, progressive dystonia and dysphagia between six months and three years. By the age of seven to ten years they had developed severe generalised dystonia, spasticity, pyramidal tract signs, limb contractures and scoliosis, and loss of ambulation. There appeared to be relative cognitive sparing with only a mild degree of learning disability.

Patient demographics and whole blood Mn levels are summarised in **Table 4.2**. Case descriptions for family Y and Z can be found in **Section 3.2**.

Subject	Gender	Consan-guinity	Origin	Age of onset	Current age	Whole blood Mn (73-325 nmol/L)
Y-II-1*	F	Y	Yemen	7m	† (13m)	N/A
Y-II-4	F			7m	3	8101
Z-II-1	M	Y	Spain	10m	† (4y)	965[#]
A-II-1	F	Y	Yemen	7m	13	2887
A-II-2	F			6m	† (7y)	N/A
B-II-2	F	Y	Lebanon	2y	17y	2280
B-II-3	F			2y	16y	3830
B-II-4	M			2y	9y	1260
C-II-2	F	Y	India	3y	5y	962

Table 4.2 Demographics of individuals affected with hypermanganesaemia associated infantile dystonia-parkinsonism.

*Individual families are numbered A-C and Y-Z with each affected sibling listed. F, female. M, male. Y, yes. m, months. y, years. †, deceased. N/A, not available. *DNA of this subject was not available for mutation testing although her clinical phenotype was similar to her sibling suggesting that they were both affected by the same disorder. Reference range for whole blood Mn is given in parantheses. [#]Mn estimation performed in different hospital laboratory, reference range <145.6 nmol/L.*

Family A

Family A are of Yemeni origin. Parents are distantly related with two affected daughters. The older sibling was reported to have onset of severe neurological deterioration from seven months of age. Her clinical features at the age of nine years included progressive spasticity, dystonia, mental retardation and microcephaly. She was wheelchair bound and had increased tone in all four limbs with prominent spasticity, especially at the ankles. Reflexes were brisk throughout with evidence of ankle clonus. She tracked with her eyes and had prominent dystonia particularly affecting her mouth and face. The second younger female sibling had disease onset at a similar age to her older sister. Examination at seven years old revealed that she was alert and responsive, seated in a supportive wheelchair, non-ambulatory, non-verbal, and unable to follow commands. She tracked with her eyes. She did not have the facial dystonia described in her older sister. Her facial movements were scant but symmetrical. She

had prominent spasticity in all 4 limbs and increased reflexes and clonus in both ankles. She died at the age of eight years from a respiratory infection.

Family B

Family B are of Lebanese origin with consanguineous first cousin parents. There are three affected children (17 year old girl, 16 year old girl and a 9 year old boy) and three unaffected children (all boys). All children were born following a normal pregnancy and birth and developmental milestones were normal until two to three years of age. All three affected children show a homogeneous clinical presentation predominated by a progressive and severe generalised dystonia. Initial presentation in all three children was with an abnormality in gait (unsteadiness and difficulty in independent walking) associated with lower limb dystonia, with features of symmetrical lower limb postural dystonia, toe walking, scissoring and plantar flexion. Over the next six to twelve months ambulation became increasingly difficult and the dystonia became more generalized in nature with involvement of the upper limbs (dystonic posturing, fisting). Oromandibular dystonia is also a prominent feature in all three children. Loss of ambulation occurred between seven and ten years of age and all children developed limb contractures and scoliosis. All three children developed acquired microcephaly. There are no cerebellar features clinically and neuropsychiatric features have not been evident. There appears to be relative cognitive sparing (psychometric testing has not been impossible) although still a mild degree of learning disability is present in all children. Ophthalmological assessment, visual evoked response and electroretinogram are unremarkable. None of the children have shown clinical response to medication including levodopa therapy, trihexyphenidyl and benzodiazepines.

Family C

Parents are second degree cousins from India and have one affected and one unaffected child. The affected girl was born in good condition following an uncomplicated pregnancy by routine caesarean section. Her early developmental milestones were normal. She had two episodes of seizures at one and a half years of age for which she was started on Valproate. After remaining seizure free for two years Valproate was tapered and stopped. At the age of three years she presented with clumsiness while writing and drawing. Shortly after, she developed toe walking and lost her ability to stand and walk unaided. At the age of four years she showed marked hypomimia, dystonic posturing of both lower limbs, bilateral ankle contractures, tremor

in her upper limbs and athetoid movements in both hands. She had increased tone in all four limbs and pyramidal tract signs including increased tendon reflexes and bilateral extensor plantar reflexes. There was no sign of cerebellar dysfunction. Nerve conduction studies and evoked potentials were normal. Treatment with anti-dystonic medications including baclofen, tetrabenazine and levodopa did not lead to significant improvement of symptoms. After a diagnosis of hypermanganesemia was made at the age of four years she was commenced on monthly $Na_2CaEDTA$ infusions. Chelation treatment lead to cessation of tremors and athetoid movements in her upper limbs and improvement of dystonic posturing of both lower limbs. Despite remaining dystonia in her lower limbs she is able to walk independently wearing ankle foot orthoses. Currently, she receives monthly five day courses of $Na_2CaEDTA$ (500 mg BD), Zn, vitamin E and C supplements, Carbi/Levodopa and Baclofen.

4.5 Diagnostic features of SLC39A14 deficiency

Alongside the distinctive clinical phenotype with early-onset parkinsonism-dystonia all affected individuals shared characteristic MRI brain appearances. These were consistent with Mn deposition within the basal ganglia similar to SLC30A10 deficiency (**Figure 4.6**). Within the deep grey matter, T1 hyperintensity affected the globus pallidus and, to a lesser extent, the striatum, with thalamic sparing. Generalised hyperintensity on T1-weighted imaging indicated extensive white matter involvement including the cerebellum, spinal cord and dorsal pons, with sparing of the ventral pons. Sagittal T1-weighted sequences showed a hyperintense signal of the pituitary gland. Axial T2-weighted imaging including T2, T2* and FLAIR sequences demonstrated hypointensity of the globus pallidus reminiscent of neurodegeneration with brain iron accumulation (NBIA), which was progressive in one patient on serial imaging (**Figure 4.7**). Because of the prominent T2 changes resembling Fe deposition affected individuals from family A and B were initially diagnosed as NBIA. In addition to the features of Mn deposition some patients had evidence of both cerebral and cerebellar atrophy. Computed tomography (CT) imaging of the brain on the other hand was normal as demonstrated in individual C-II-2 (**Figure 4.7**). The severity of the characteristic MRI brain features of SLC39A14 deficiency is compared between affected individuals in **Table 4.3**.

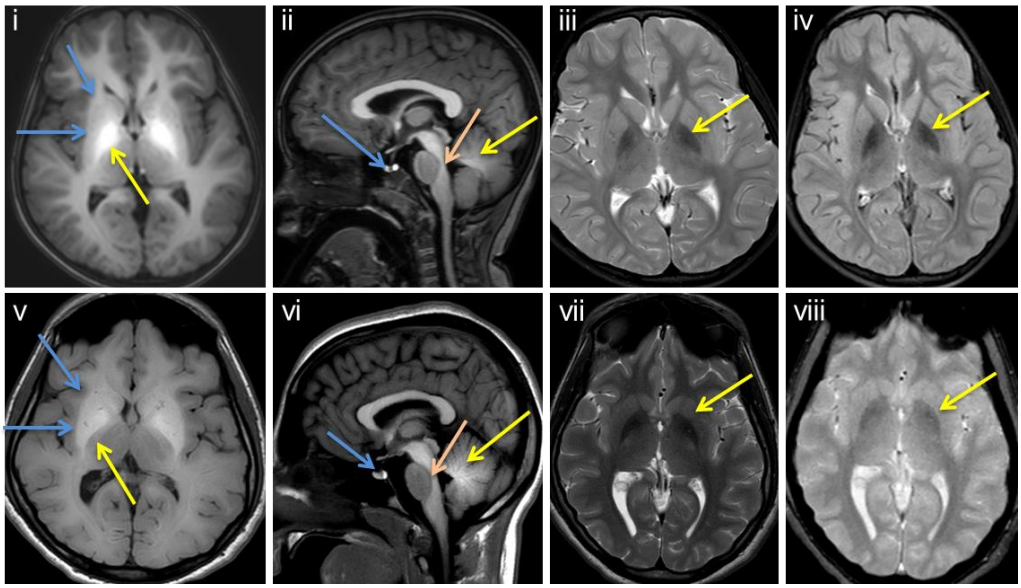

Figure 4.1 Mutations in human *SLC39A14* cause deposition of Mn in the globus pallidus associated with pathognomonic MRI brain appearances.

*Representative MR brain images are shown for affected individual C-II-2 aged 3 years (**i-iv**) and B-II-2 aged 17 years (**v-viii**); (i, v, axial T1; ii, vi, sagittal T1; iii, vii, axial T2; and iv, viii, axial T2* weighted imaging). Generalised hyperintensity is seen on T1-weighted imaging of the cerebral white matter, globus pallidus (i and v, yellow arrow) and striatum (i and v, blue arrows), pituitary gland (ii and vi, blue arrow), dorsal pons (ii and vi, pink arrow) and cerebellum (ii and vi, yellow arrow). Hypointensity of the globus pallidus was also evident on T2- (iii, vii) and T2*- (iv, viii) weighted imaging (yellow arrows).*

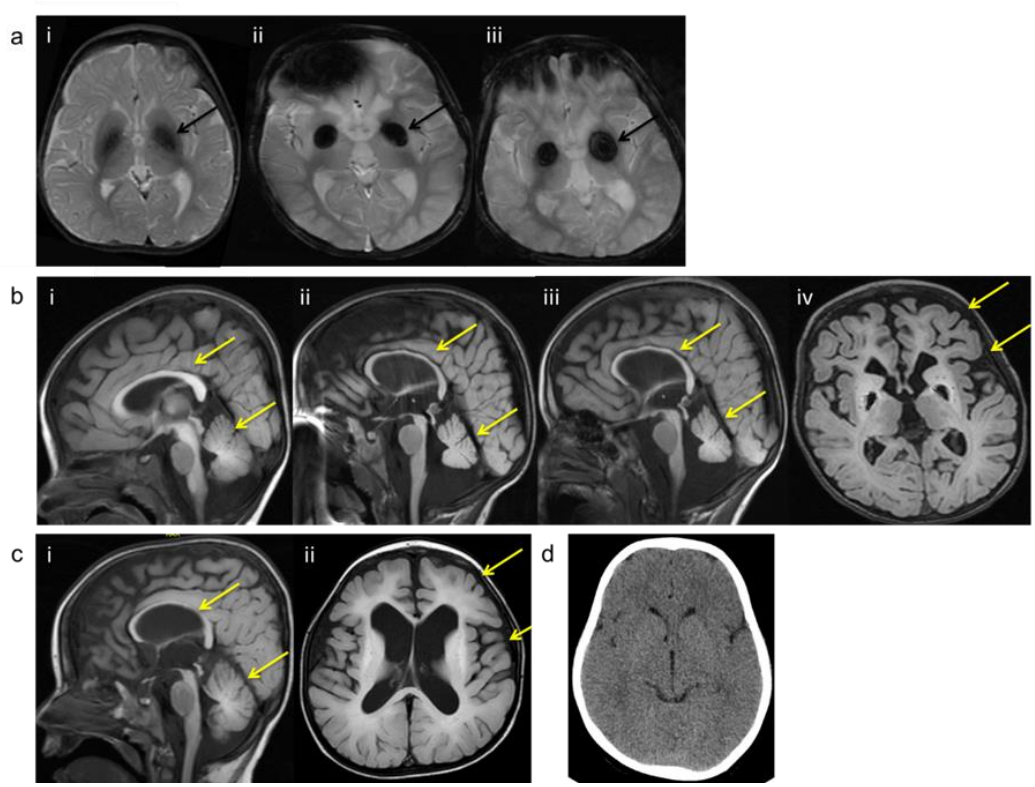

Figure 4.2 Additional neuroradiological MRI brain features of individuals with mutations in *SLC39A14*.

*(**a**) Serial T2-weighted imaging of individual A-II-1 shows progressive signal hypointensity within the globus pallidus. Images taken at age 3y3m (i, axial T2), 6y3m (ii, axial T2*) and 9y9m (iii, axial T2*). (**b**) and (**c**) Some patients develop pronounced cerebral and cerebellar atrophy demonstrated by a thinning of the corpus callosum and widening of the extracerebral space and ventricles (indicated by yellow arrows). (**b**) Sagittal T1-weighted imaging of individual A-II-1 at age (i) 3y3m (ii) 6y3m and (iii) 9y9m; axial T1-weighted imaging at age 6y3m (iv). Note hyperintense signal within the basal ganglia associated with central pallidal signal hypointensity due to extreme T2 effects dominating the central region of the pallidum on the T1-weighted image. (**c**) Sagittal and axial T1-weighted imaging (i, ii) of individual Z-II-1 at age 3y. (**d**) CT brain imaging of individual C-II-2 aged 3y is normal.*

		White matter involvement[1]	Deep grey matter involvement (T1)				Deep grey matter involvement (T2)			Pituitary gland involvement	Cerebral/ cerebellar atrophy
		Generalized hyperintensity on T1	*Hyperintensity on T1*				*Hypointensity on T2*			*Hyperintensity on T1*	
			Caudate	Putamen	Globus pallidus	Thalamus	Globus pallidus				
		Axial/Sagittal images	Axial images				Axial images			Sagittal images	Sagittal/Coronal images
	Age						T2	T2*	Flair		
Y-II-4	2	++	+	+	++	-	+[3]	N/A	++	+	-
Z-II-1	3	+++			+++	-				+	+++
A-II-1	3	++[2]	+	+	++	-	++	N/A	++	+/-	-
	6	++[2]	++	++	+++	-	+	++	+	+	+
	9	+++[2]	N/A	N/A	N/A	N/A	+	+++	+	+	++
B-II-2	2	++	+	+	++	-	++	+	N/A	++	-
	4	++	+	+	++	-	+	+/-	N/A	++	-
	17	++	++	++	++	-	++	+	N/A	++	-
B-II-3	2	++	+/-	+/-	++	-	+	N/A	N/A	+	-
C-II-2	3	++	+	+	++	-	++	N/A	++	++	-

Table 4.1 Neuroradiological features of individuals with mutations in *SLC39A14*.

Table comparing the grade of MRI brain characteristics between affected indiviuals. [1]Generalised white matter changes including involvement of the cerebellum, spinal cord, dorsal pons with sparing of the ventral pons. [2]Evidence of progressive cerebral atrophy especially involving frontal lobe and corpus callosum. [3]T2-weighted hypointensity associated with a central hyperintensity, similar to the eye-of-the-tiger sign, possibly due to "T1-shine through". N/A – not available. (-) radiological feature absent. (+/-) radiological feature borderline. (+) radiological feature present. (++) radiological feature strongly present. (+++) radiological feature very strongly present.

Consistent with MRI brain appearances of Mn deposition, whole blood Mn levels were raised in all affected children up to 25 times that of normal (482 to 8,101 nmol/L, reference range 73-325 nmol/L) (**Table 4.2**). Because SLC39A14 has been reported previously to transport other metal ions including Fe, Zn and Cd[69,70,72,222,230-237] metal blood levels were assessed in two affected individuals (A-II-1 and Z-II-4) using ICP-MS (**Section 2.5.1**). While Mn levels were significantly raised Fe, Cu, Zn and Cd levels were within the normal range (**Table 4.4**). Compared to published reference ranges a mild decrease in Zn levels was found for individual Z-II-4. However, as the level lies within the reference range of controls analysed using this method it is unlikely that this is of significance. Heterozygous carrier state in parents Z-I-I and Z-I-II did not affect Mn levels. These results suggest that *in vivo* the major role of SLC39A14 is that of Mn transport with a less dominant role for other divalent metals.

ng/mL	Controls	Patients		Parents		Published
		A-II-1	Z-II-4	Z-I-1	Z-I-2	Reference*
Mn	6.69-11.29	**159**	**445**	15.1	12.2	5-12.8
Fe	409-462	434	397	370	386	236-614
Cu	635-1,096	1,130	944	770	1,108	590-1470
Zn	4,364-5,284	5,076	4,580	5,804	5,424	4800-7800
Cd	0.35	1.42	0.18	0	0.89	0.15-2.04

Table 4.2 Mn is the sole metal deranged in SLC39A14 deficiency.

*Table showing whole blood metal levels determined using ICP-MS in two affected individuals A-II-1 (F98V) and Z-II-4 (E105X), three healthy control subjects and parents heterozygous for the E105X mutation (Z-I-1 and Z-I-2). *published reference ranges[238,239]. Both affected individuals show markedly raised whole blood Mn levels while other divalent metal levels (Fe, Cu, Zn and Cd) are normal. Abnormal metal levels in red.*

In contrast to SLC30A10 deficiency, children with *SLC39A14* mutations did not develop haematological abnormalities. Polycythaemia was absent and Fe indices including TIBC and ferritin were normal. Furthermore, they did not show signs of liver disease. Unfortunately, liver tissue samples were not available to determine hepatic Mn concentrations. However, liver MRI of individual E-II-4 demonstrated T1 normointensity

indicating that Mn does not accumulate in the liver in this disorder. Liver MRIs from individual B-II-4 was compared to that of a patient with SLC30A10 deficiency and a healthy control subject (**Figure 4.8**).

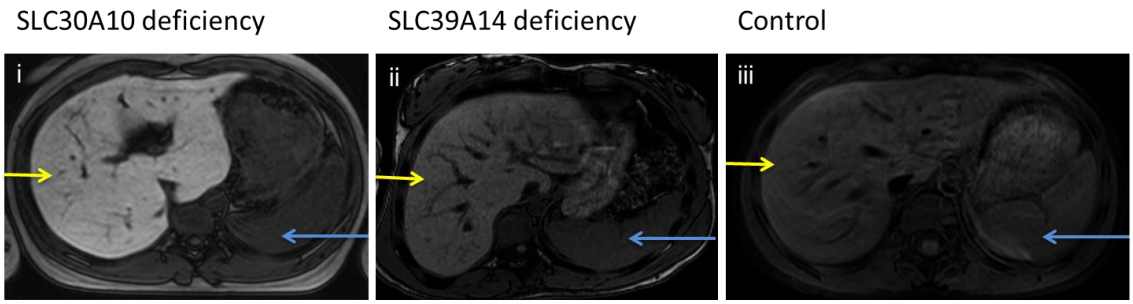

Figure 4.3 There is no evidence of hepatic Mn accumulation in patients with *SLC39A14* mutations.

*Transverse abdominal T1-weighted MR images of an individual with **(i)** SLC30A10 deficiency, **(ii)** subject B-II-4 with SLC39A14 deficiency and **(iii)** a healthy control individual. The extensive T1 signal hyperintensity caused by hepatic Mn deposition in SLC30A10 deficiency (i) is absent in individual B-II-2 (ii). However, there appears to be a mild degree of T1 hyperintensity when compared to a control subject (iii). Signal intensity of the liver (yellow arrow) is compared to that of the spleen (blue arrow).*

Histopathological analysis (performed at the Department of Histopathology, Great Ormond Street Hospital) of brain tissue samples from a post mortem examination of individual D-II-1 showed marked neuronal loss in the globus pallidus with relatively good preservation of neurons in the caudate nucleus, putamen, thalamus and cerebral cortex (**Figure 4.9**). There was similar severe neuronal loss and gliosis in the dentate nucleus of the cerebellum with relative preservation of the cortex. Patchy loss of myelin was found in the cerebral and cerebellar white matter associated with coarse vacuoles and patchy axonal loss. As some of the brain MRI features appeared to be similar to those seen in NBIA, neuropathological markers for NBIA were analysed. However, NBIA characteristics including Fe deposition, axonal spheroids, tau and α-synuclein[240] were not observed.

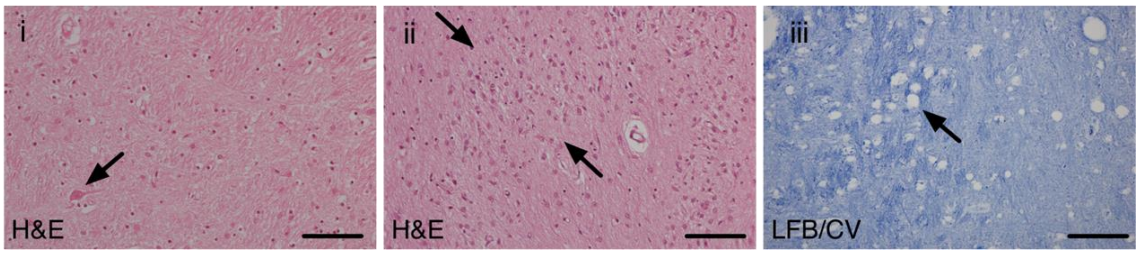

Figure 4.4 Histopathological features of SLC39A14 deficiency.

*(**i**) H&E staining of the globus pallidus shows marked neuronal loss which is not accompanied by significant stainable Fe on Perls' stain (not shown). (**ii**) H&E staining of the dentate nucleus of the cerebellum shows similar severe neuronal loss and gliosis with relative preservation of the cortex. (**iii**) There is patchy loss of myelin staining (LFB/CV, Luxol fast blue/Cresyl violet) from the cerebral and cerebellar (not shown) white matter associated with coarse vacuoles (some over 50 µm) and patchy axonal loss (on neurofilament staining – not shown). Scale bar, 100 µm.*

4.6 $Na_2CaEDTA$ effectively lowers whole blood Mn levels and can lead to improvement of clinical symptoms

In an attempt to reduce the systemic Mn load, individuals C-II-2 and E-II-2 were commenced on four weekly chelation therapy with intravenous $Na_2CaEDTA$ according to a protocol previously published for the treatment of SLC30A10 deficiency[50,57] (**Section 1.2.3**). Individual C-II-2, who was started early on in the disease course at the age of five years, tolerated chelation therapy well without notable side effects and showed a dramatic clinical improvement. After six months of monthly $Na_2CaEDTA$ courses (500 mg twice daily for five consecutive days) upper limb tremors and athetoid movements had ceased and lower limb dystonia improved so that she has now regained the ability to walk independently with foot orthoses. For subject E-II-2 $Na_2CaEDTA$ (20 mg/kg once daily) administration led to a marked increase in urinary Mn excretion accompanied by a reduction of whole blood Mn levels (**Figures 4.10 and 4.11**). Despite the apparent mobilisation of Mn stores she has not shown an immediate clinical response but has continued to deteriorate with worsening tremor and stiffness.

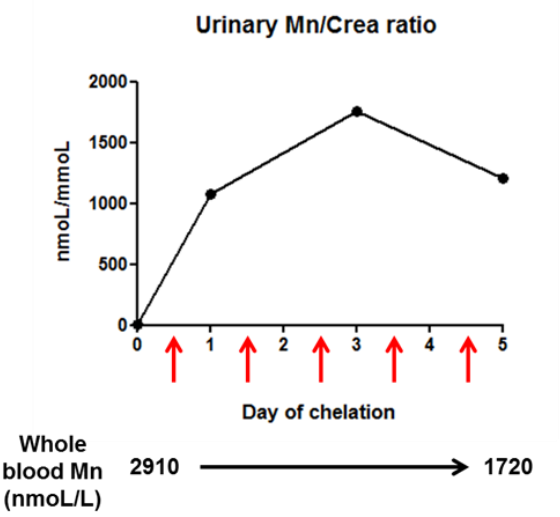

Figure 4.5 $Na_2CaEDTA$ increases urinary Mn excretion and reduces whole blood Mn in a patient with SLC39A14 deficiency (E-II-2).

Graph showing the urinary Mn/creatinine ratio and whole blood Mn levels over five days of chelation therapy. $Na_2CaEDTA$ (20 mg/kg) was given intravenously once daily (indicated by red arrow). Crea, creatinine. Whole blood Mn levels measured on day 1 and 5 of treatment are displayed below.

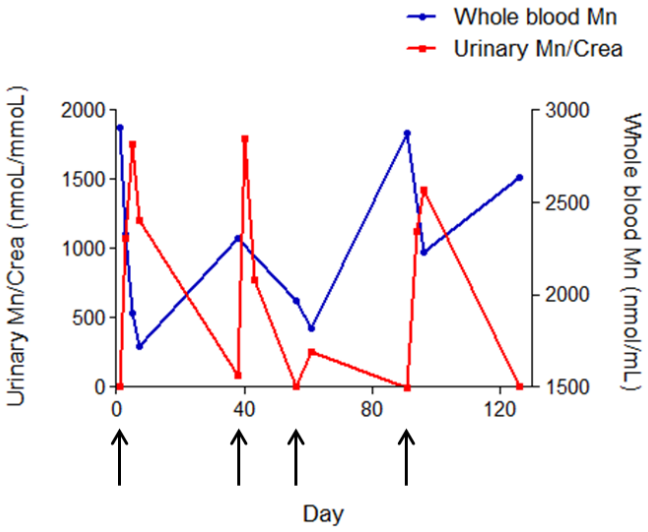

Figure 4.6 Whole blood Mn levels and urinary Mn excretion over four courses of $Na_2CaEDTA$ treatment in individual E-II-2.

Graph showing urinary Mn/Crea ratio (red) and whole blood Mn levels (blue) of subject E-II-2 during four cycles of chelation therapy. Arrows indicate timing of $Na_2CaEDTA$ infusions. Administration of $Na_2CaEDTA$ led to a significant increase in urinary Mn excretion accompanied by a drop in whole blood Mn levels. Crea, creatinine.

4.7 SLC39A14 is a Mn uptake transporter at the cell membrane; isoform 1 and 2 show differences in tissue expression, Mn transport ability and transcriptional regulation

4.7.1 Tissue expression

To analyse the cellular localisation of SLC39A14 immunostaining in post mortem liver sections from an individual unaffected by this disorder was performed using an antibody to region 250 to 344 of the amino acid sequence that is shared by all three isoforms (performed at the Department of Histopathology, Great Ormond Street Hospital). SLC39A14 localised to the cell membrane and cytoplasmic structures of hepatocytes in a punctate pattern (**Figure 4.12i**) consistent with previous studies in HepG2 cells that detected SLC39A14 at the plasma membrane and in endosomes[241]. Similarly, SLC39A14 localised to the cell membrane and cytoplasm in neurons of the globus pallidus (immunohistochemistry was performed at the Department of Pathology, Oregon Health & Science University) (**Figure 4.12ii**).

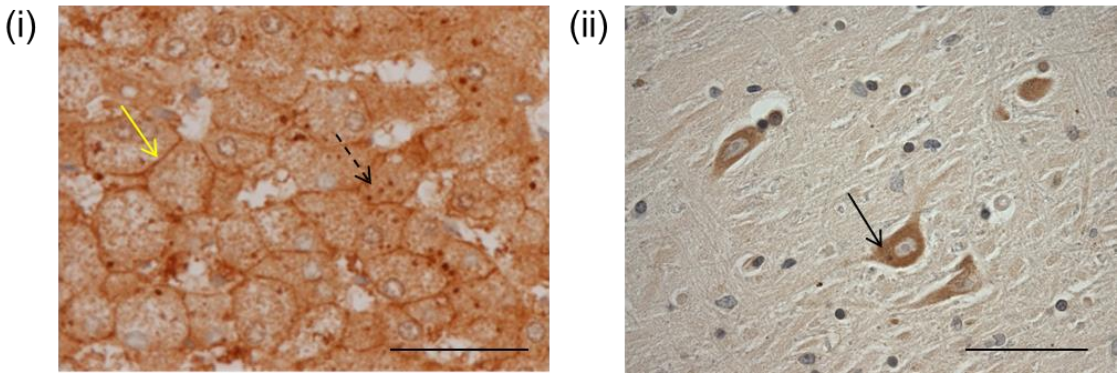

Figure 4.7 SLC39A14 localises to the cell membrane and the cytoplasm of hepatocytes and neuronal cells in the globus pallidus.

Immunostaining for SLC39A14 (all isoforms) in (i) healthy control liver shows cell membrane expression (yellow arrow) and punctate cytoplasmic staining (dashed arrow); scale bar 50µm; Abcam anti-SLC39A14 antibody (ab106568, 1:100); and in (ii) globus pallidus from a healthy control shows positively stained large neurons; scale bar 100µm; Novus anti-SLC39A14 antibody (NBP1-81551, 1:1,000).

Given that individual C-II-1 carries mutations that only affect isoform 2, tissue expression, subcellular localisation and function of both SLC39A14 isoform 1 and 2 were examined to ascertain whether they might play different roles in Mn transport. The isoforms differ only by 20 amino acids encoded by exon 4B and 4A, respectively (**Figures 4.2 and 4.13**).

```
Exon4A      TGTGGGGCTTTGGTTTTCTCAGTGTCTCACTGATTAACCTGGCCTCTCTCCTGGGAGTCC 60
Exon4B      TGTGGGGATACGGTCTCCTCTGTGTGACCGTCATCTCCTCTGCTCCCTCCTGGGGGCCA 60
            ******* *  *** * *** ****  *  * **   ***   *** ******** * *

Exon4A      TCGTCCTGCCCTGCACAGAGAAAGCGTTTTTCAGCCGTGTGCTCACTTACTTCATCGCCC 120
Exon4B      GCGTGGTGCCCTTCATGAAGAAGACCTTTTACAAGAGGCTGCTGCTCTACTTCATAGCTC 120
             ***  ****** **   ****  * **** **   *  ****    ******** ** *

Exon4A      TGTCCATTGGAACGCTGCTGTCTAACGCGCTATTCCAGCTCATCCCAGAG 170
Exon4B      TGGCGATTGGAACCCTCTACTCCAACGCCCTCTTCCAGCTCATCCCGGAG 170
            ** * ******** **    ** ***** ** ************** ***
```

Figure 4.8 Alignment of human *SLC39A14* exon 4A and 4B.

Nucleotide sequences used to generate this alignment are NM_015359.4 (exon 4A) encoding isoform 2 and NM_001128431.2 (exon 4B) encoding isoform 1. Nucleotides differing between the two exons are highlighted in yellow. Primers used for RT-PCR are underlined.

mRNA expression of the two transcripts encoding isoform 1 and 2 was assessed in fetal and adult human tissues using RT-PCR (**Section 2.3.6**). Differences in mRNA expression between isoform 1 and 2 were observed. While transcript 1 was ubiquitously expressed in the tissues examined transcript 2 expression was restricted to liver, intestine, kidney, lung and pancreas, and was not present within the brain (**Figure 4.14**).

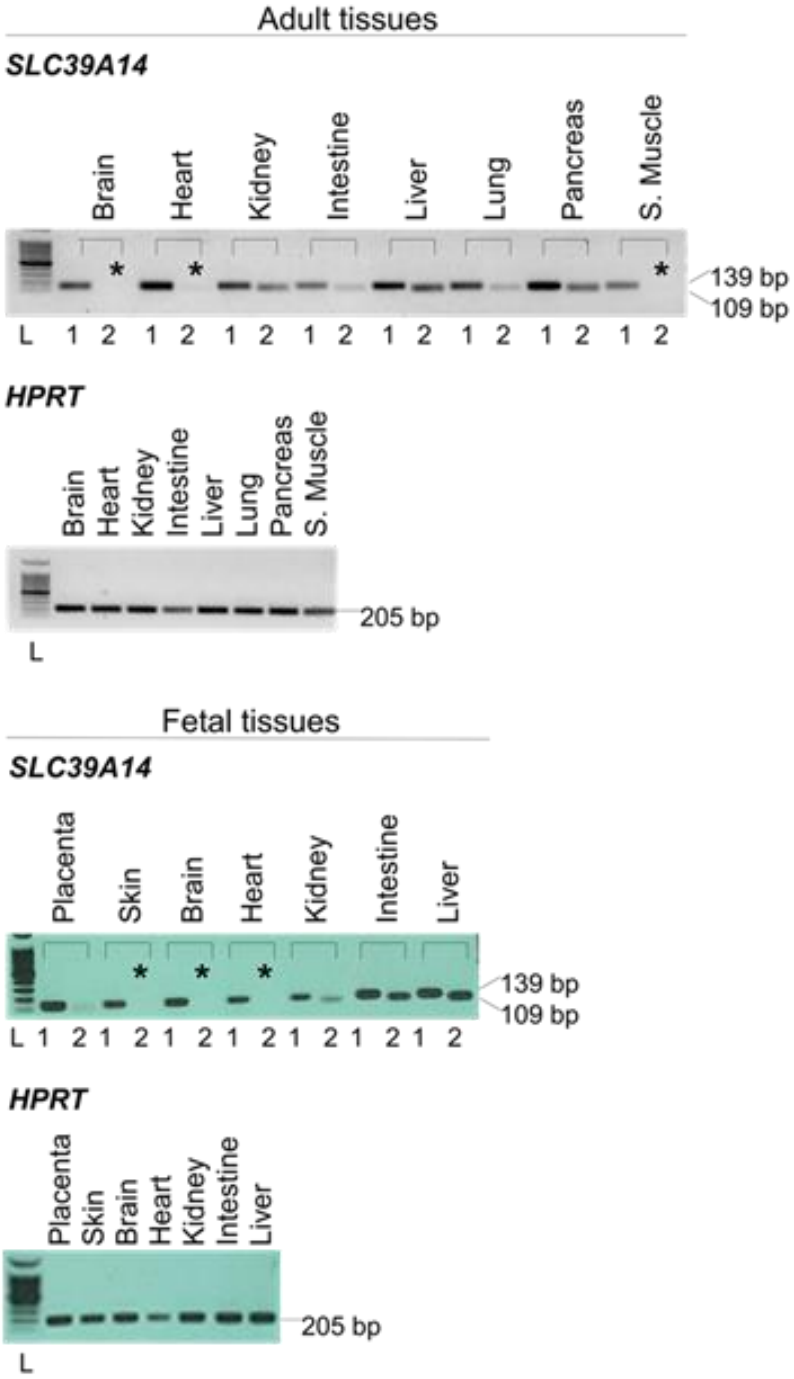

Figure 4.9 *SLC39A14* isoform 1 and 2 are differentially expressed in human tissues.

*Gel electrophoresis images of RT-PCR amplicons of SLC39A14 isoform 1 and 2 from adult (top) and fetal (bottom) human tissues. *absent expression in brain, heart, skeletal muscle and skin. Amplicons for isoform 1 and 2 span 139 and 109bp, respectively. Hypoxanthine-guanine phosphoribosyl-transferase (HPRT) was used as a housekeeping gene. L, 100bp ladder (Promega).*

To examine whether differences in the subcellular localisation of human SLC39A14 isoform 1 and 2 exist EGFP-tagged *SLC39A14* constructs were overexpressed in zebrafish embryos (**Sections 2.3.10 and 2.4.7**). *SLC39A14* mRNA of transcript 1 or 2 was co-injected with mRNA encoding membrane mCherry in one cell stage embryos and expression analysed at 6 hpf. Expression of either isoform did not reveal differences in subcellular localisation. Both isoforms localised to the cell membrane and the cytoplasm, however, isoform 2 appeared less pronounced within the cytoplasm (**Figure 4.15**).

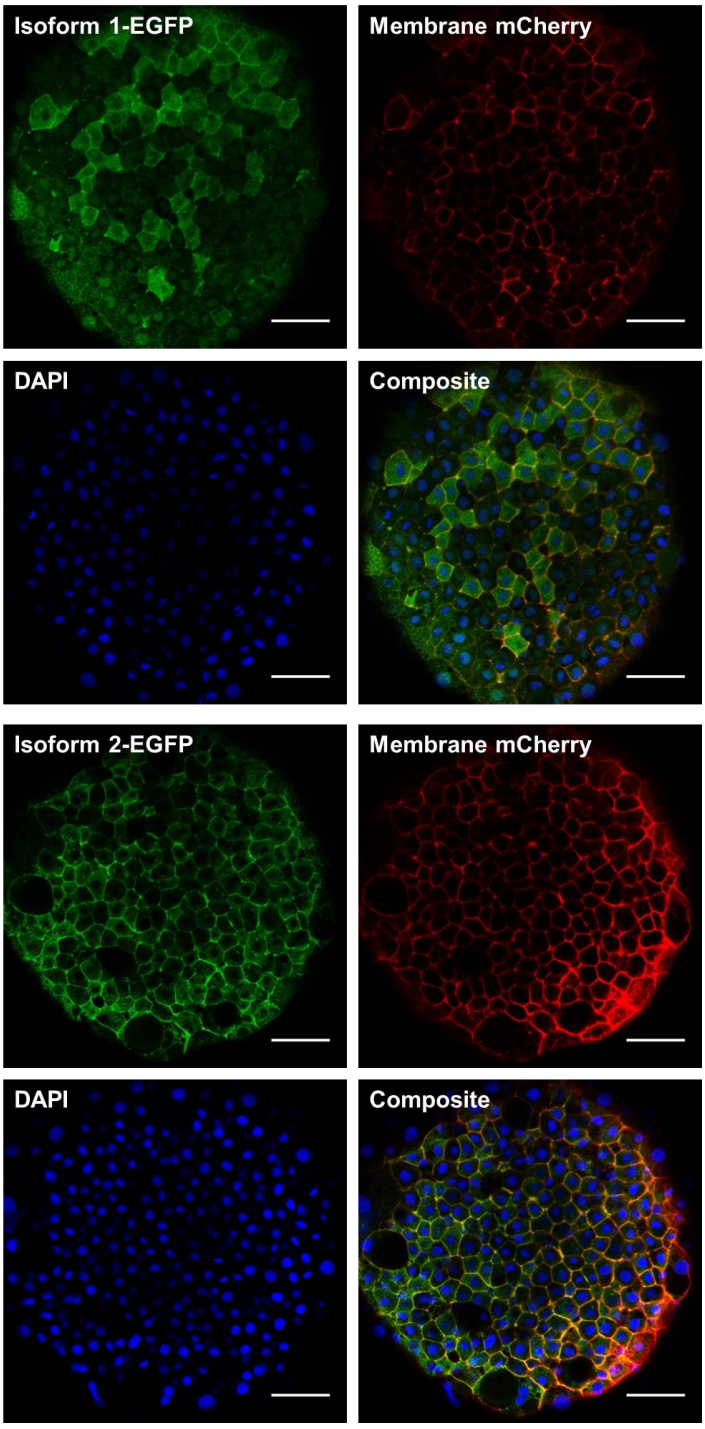

Figure 4.10 SLC39A14 isoform 1 and 2 are expressed on the cell membrane and within the cytoplasm of zebrafish embryos at 6 hpf.

Confocal images demonstrating the subcellular localisation of EGFP-tagged human SLC39A14 isoform 1 and 2 expressed in zebrafish embryos. Colocalisation of the immunostaining for EGFP and mCherry at 6hpf shows that both isoforms are expressed at the cell membrane (colocalisation with membrane mCherry) and in the cytoplasm. DAPI was used as a nuclear stain. Scale bar 50µm.

4.7.2 Mn transport efficacy

To investigate functional differences in Mn transport between isoform 1 and 2, Mn levels were measured by ICP-MS in HEK293 cells transfected with wild-type constructs of SLC39A14 isoform 1 and 2, and empty vector (**Sections 2.3.8 and 2.5.4**). This work was done in collaboration with Dr Manju Kurian at UCL Institute of Child Health who performed the cell culture and transient transfections. Exposure to 1 µM $MnCl_2$ in the medium for 15 and 30 minutes led to a marked increase in Mn levels for both isoforms when compared to the empty vector control. These results confirm that both isoforms facilitate Mn uptake. Cells transfected with isoform 2 have significantly higher Mn levels than those transfected with isoform 1 suggesting a greater ability of isoform 2 to transport Mn (**Figure 4.17**). The observed results were almost identical for the two time points examined (15 and 30 minutes). This seems unlikely to reflect cell saturation for isoform 1 as isoform 2 shows greater Mn accumulation.

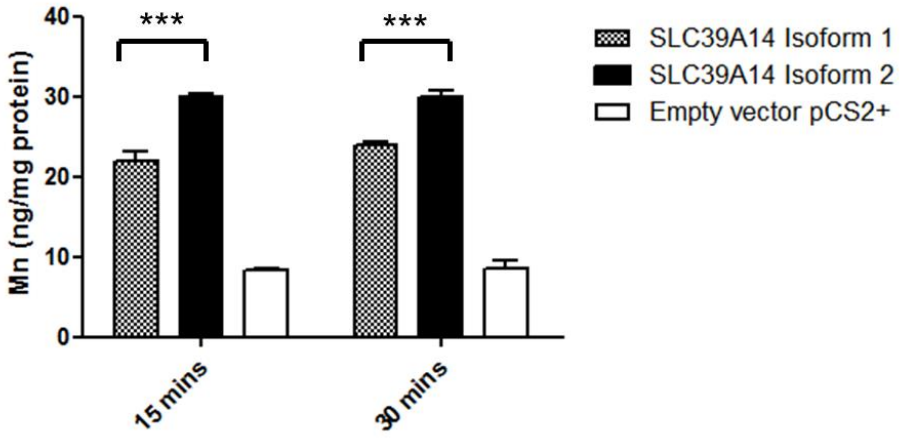

Figure 4.11 SLC39A14 isoform 2 has a greater ability of Mn uptake compared to isoform 1.

*Graph showing Mn uptake in HEK293 cells transiently transfected with wild-type SLC39A14 isoform 1 and 2, and empty pCS2+ vector following 15 and 30 minutes of $MnCl_2$ (1µM) exposure. Data are presented as means ± standard deviation (s.d.) from two independent experiments. Statistical analysis was performed using one way ANOVA ($p<0.0001$) and Tukey's multiple comparison test (***$p<0.001$).*

4.7.3 Transcriptional regulation

In other contexts, expression of metal transporters is controlled by the concentration of their substrate at transcriptional level to ensure tight regulation of metal levels and prevent toxic accumulation. For instance in yeast, expression of the *ZRT1* and *ZRT2* genes, both encoding Zn transporters required for Zn uptake, is induced upon Zn depletion[242]. A similar effect is observed for the Fe transporters Fet3, Ftr1, and Fet4 for which gene expression is increased in response to low Fe[243]. To investigate whether Mn has an effect on the transcriptional regulation of *slc39a14* expression, transcript levels were assessed by qRT-PCR in zebrafish larvae exposed to $MnCl_2$ (**Section 2.3.7**). Acute exposure to $MnCl_2$ (500 µM) for 24 hours at four dpf led to a significant increase in *slc39a14* expression in 5 dpf larvae (**Figure 4.18.i**). The increase in gene expression appeared to be caused by up-regulation of mRNA levels of transcript 2 with a 4.6 fold rise while levels of transcript 1 remained unchanged. Transcriptional regulation of *slc39a14* by its substrate is therefore likely to contribute to Mn homeostasis. Subacute $MnCl_2$ exposure of 50 µM for 72 hours on the other hand did not significantly affect *slc39a14* transcript levels (**Figure 4.18.ii**).

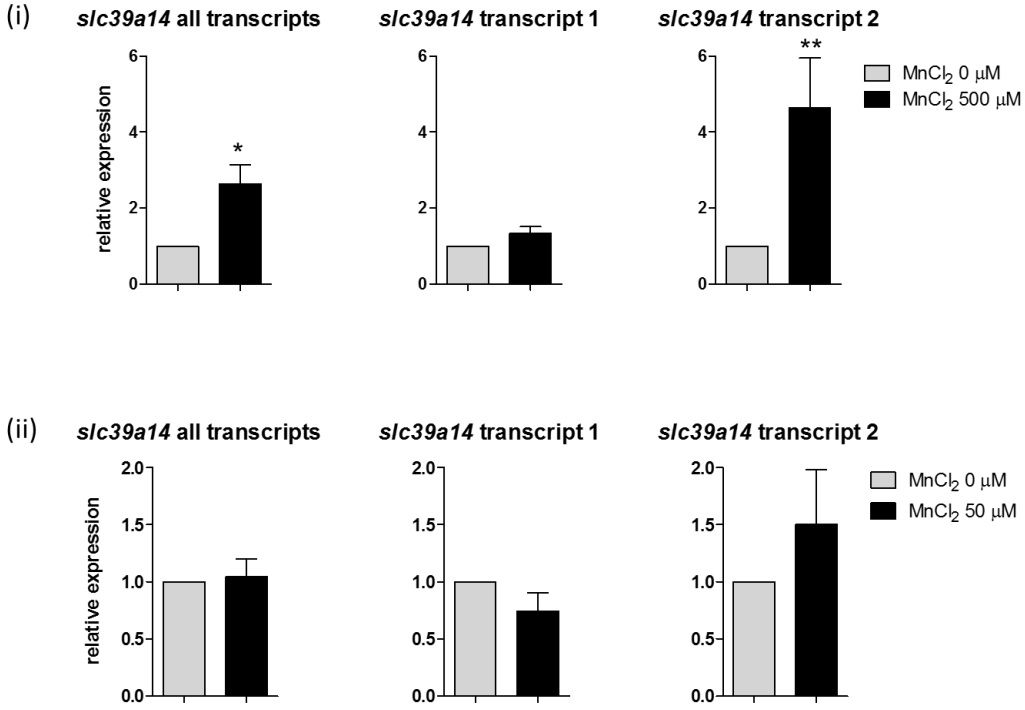

Figure 4.12 Mn exposure affects transcriptional regulation of *slc39a14*.

*Graph showing slc39a14 transcript levels assessed by qRT-PCR in 5 dpf zebrafish larvae after exposure to (**i**) 500 µM $MnCl_2$ for 24 hours (p=0.035 [all transcripts], p=0.41 [transcript 1], p=0.005 [transcript 2]) and (**ii**) 50 µM $MnCl_2$ for 72 hours. (p=0.9 [all transcripts], p=0.21 [transcript 1], p=0.15 [transcript 2]. Data are presented as means ± s.d. from three independent experiments. Statistical analysis was performed using Student's two tailed t test on individual ∆Ct values (*p<0.05, **p<0.01).*

4.8 Discussion

4.8.1 SLC39A14 deficiency – a novel Mn transportopathy

In this work, SLC39A14 was identified as a pivotal Mn transporter that, when mutated, causes a novel autosomal recessive neurodegenerative disorder associated with dysregulation of Mn homeostasis. The clinical phenotype is characterised by hypermanganesemia and prominent cerebral Mn toxicity. Neuronal loss within the basal ganglia, particularly the globus pallidus, leads to progressive generalised dystonia associated with severe physical disability and premature death in childhood. Identified mutations include three missense, one nonsense and one frameshift mutation, and are predicted to affect transporter function either through nonsense mediated mRNA decay, protein truncation or impairment of transporter activity. Interestingly, one individual carries mutations that solely affect SLC39A14 isoform 2 while the clinical phenotype does not differ from the rest of the patients.

The patient cohort consisted of nine individuals from five consanguineous families who shared a consistent clinical phenotype with early-onset dystonia-parkinsonism causing delayed developmental milestones, loss of ambulation, dysphagia and severe spasticity. The dystonic-hypokinetic movement disorder is similar to that seen in SLC30A10 deficiency suggesting a shared pathophysiology due to Mn deposition in the basal ganglia[46,48-50]. Disease onset appears to be slightly earlier in SLC39A14 deficiency with five children presenting within infancy. In SLC30A10 deficiency on the other hand disease onset has been reported to occur after the first year of life. Furthermore, disease progression seems more rapid in SLC39A14 deficiency with severe dystonia and dysphagia developing already during infancy. Three of the nine children reported here died following complications due to advanced neurological disease within the first few years of life.

Similar to SLC30A10 deficiency[46,48-51] the MRI brain appearances are pathognomonic of Mn deposition and include hyperintensity of the basal ganglia, the cerebral white matter and pons with sparing of the ventral pons on T1-weighted imaging. The T1 hyperintensity is accompanied by pronounced hypointensity on T2-weighted imaging so that for some patients a misdiagnosis of NBIA was made initially. Fe deposition

equally causes T2 hypointensity[240] and, hence, NBIA is an important differential diagnosis for SLC39A14 deficiency.

Histopathological findings of SLC39A14 deficiency are similar to SLC30A10 deficiency and include severe neuronal loss of the globus pallidus and dentate nucleus, and a vacuolated myelopathy[210]. On the other hand, neuropathological characteristics of NBIA including axonal spheroids, tau and α-synuclein are not observed[240].

Although SLC39A14 has been shown to transport a range of divalent metals *in vitro*[69,70,72,222,230-237,241] affected individuals presented with an increase in blood Mn levels while Fe, Zn and Cd, possible substrates of this transporter, were normal. Blood Mn was dramatically raised in all patients with levels up to ten times that of normal. This suggests that regulation of Mn homeostasis is the main function of SLC39A14 *in vivo*.

While hypermanganesaemia and neurological disease associated with characteristic MRI brain appearances are shared by both SLC39A14 and SLC30A10 deficiency important differences between the two Mn transportopathies exist that allow differential diagnosis. Patients with SLC39A14 deficiency do not develop polycythaemia, abnormal Fe indices or liver disease. The absence of haematological abnormalities in SLC39A14 deficiency may be attributed to the different role and tissue expression of the two Mn transporters. SLC30A10 functions as Mn exporter at the cell membrane with subsequent Mn accumulation in all parts of the cell[47]. The Mn importer SLC39A14 on the other hand may be required for Mn uptake into specific organelles and tissues leading to deficiency of Mn in parts of the cell or certain tissues. In SLC30A10 deficiency polycythaemia is thought to occur due to Mn associated induction of *EPO* gene expression[60]. Divalent metals other than Fe^{2+} lead to stabilisation of the heterodimeric transcription factor, hypoxia-inducible factor (HIF), with subsequent induction of *EPO* transcription (**Figure 1.1**). This is thought to occur due to a decrease in Fe^{2+} availability or increased oxidation of Fe^{2+} [61,206]. In SLC30A10 deficiency both the Mn overload directly or the secondary depletion of Fe stores can affect *EPO* gene expression. *EPO* gene expression occurs in the liver and kidney[62]. Patients with SLC39A14 deficiency lack the hepatic Mn accumulation that is likely to lead to increased *EPO* transcription in SLC30A10 deficiency.

In SLC30A10 deficiency hepatotoxicity is caused by impaired hepatic Mn efflux with subsequent Mn accumulation that causes prominent T1 hyperintensity on liver MR imaging. Although liver tissue for determination of hepatic Mn concentration was not available, liver MRI of one patient clearly demonstrated that hepatic Mn accumulation is absent in SLC39A14 deficiency. Given that SLC39A14 is highly expressed in the liver[70,230], the organ responsible for the maintenance of Mn homeostasis, it seems plausible that SLC39A14 is required for hepatic Mn uptake for subsequent biliary excretion through SLC30A10 (**Figure 4.19**). Malfunctioning of this transporter may therefore lead to dysregulation of Mn homeostasis with a secondary build-up of Mn in the blood and brain (**Figure 4.20**). In SLC30A10 deficiency on the other hand hepatic Mn excretion is impaired leading to subsequent liver and brain accumulation of Mn (**Figure 4.21**).

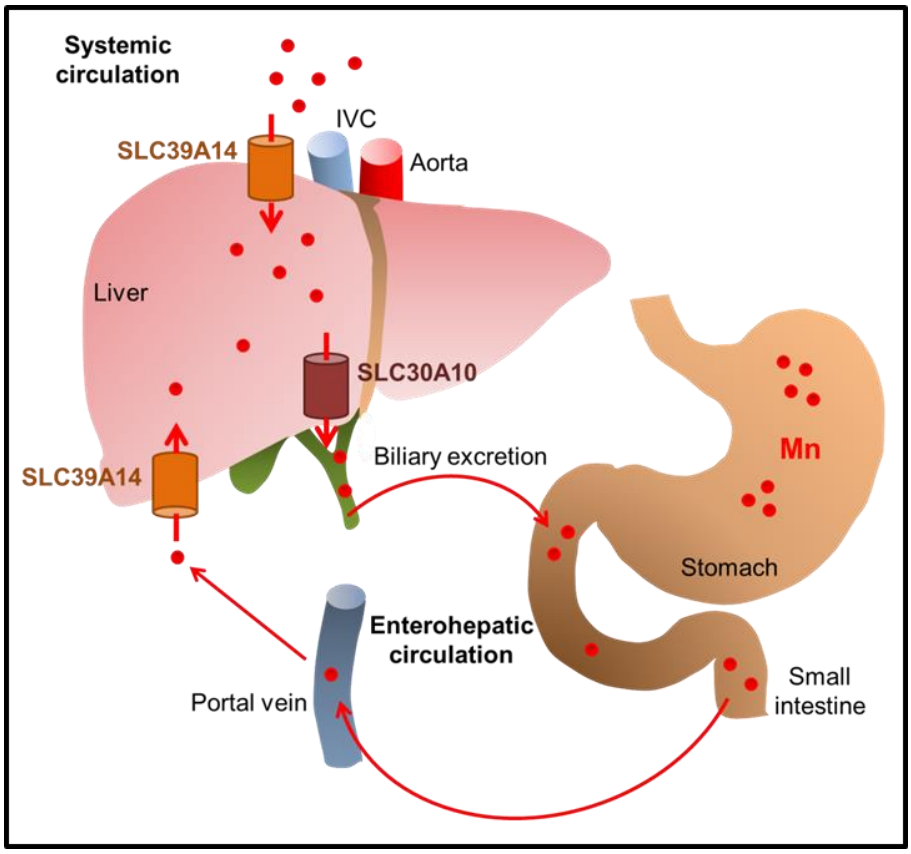

Figure 4.13 SLC30A10 and SLC39A14 are crucial regulators of Mn homeostasis. *Schematic demonstrating our current understanding of how Mn metabolism is regulated in humans. Mn is absorbed in the intestine and enters the portal circulation. SLC39A14 faciliates uptake of Mn from the portal and systemic circulation while SLC30A10 allows hepatic excretion of Mn into the bile. IVC, inferior vena cava.*

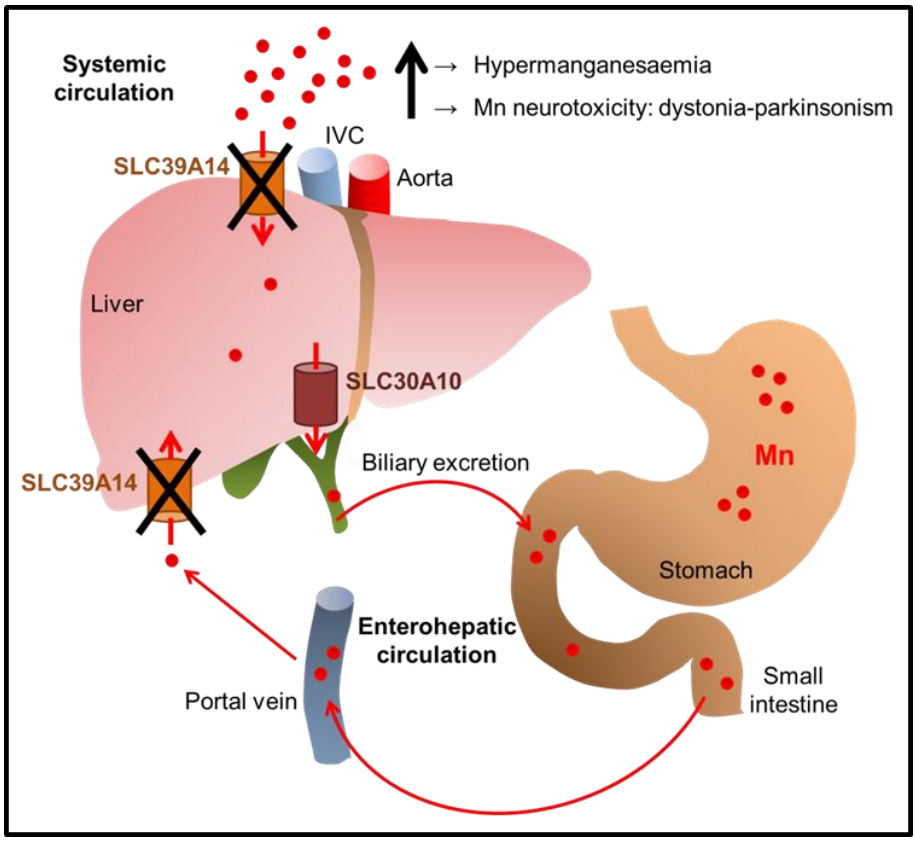

Figure 4.14 SLC39A14 deficiency leads to impaired hepatic Mn uptake with subsequent brain Mn deposition.

Schematic demonstrating the consequences of impaired SLC39A14 function. Failure to transport Mn into the liver for biliary excretion through SLC30A10 results in a build-up of Mn in the blood with secondary accumulation of Mn in the brain. IVC, inferior vena cava.

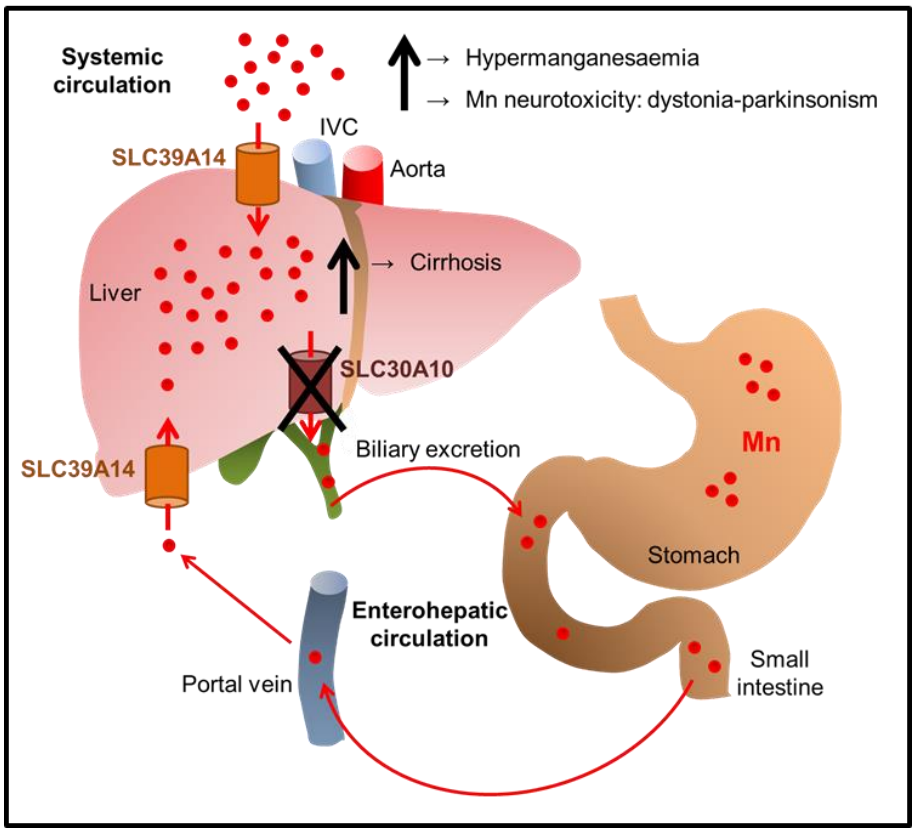

Figure 4.15 SLC30A10 deficiency leads to impaired biliary Mn excretion with Mn deposition in the liver and brain.

Schematic demonstrating the consequences of impaired SLC30A10 function. Failure to export Mn into the bile results in a build-up of Mn in the liver, blood and brain. IVC, inferior vena cava.

Although Mn associated neuronal damage is extensive in this disorder, early treatment with $Na_2CaEDTA$ appears to halt disease progression. Monthly courses of intravenous $Na_2CaEDTA$ significantly increased urinary Mn excretion and lowered blood Mn levels in two individuals. For subject C-II-2 chelation therapy was accompanied by marked improvement of extrapyramidal symptoms while treatment response was poor in the older subject B-II-2 who is affected by late stage disease. We know from SLC30A10 deficiency that Mn toxicity is, to a great extent, reversible[46,48,50]. However, it is expected that treatment must be initiated before neuronal degeneration occurs in order to take effect. This might explain the difference in treatment response between the two patients. Chelation therapy may also lead to a worsening of neurological symptoms due to mobilisation of Mn with a shift into the brain similar to observations in Wilson's

disease. Indeed, 10 to 50% of patients with neurologic Wilson's disease deteriorate during the initial phase of treatment with D-Penicillamine[216]. The type of mutation might also affect treatment outcome. In subject C-II-2 function of isoform 1 and 3 is maintained and might partly compensate for loss of function of isoform 2, whilst the mutation identified in patient B-II-2, the older subject who had a less favourable response to chelation treatment, affects all three isoforms.

4.8.2 SLC39A14 functions as a Mn uptake transporter and its isoforms play diverse roles in the regulation of Mn homeostasis

Overexpression studies in HEK293 cells confirmed that SLC39A14 facilitates Mn uptake (**Section 4.6**). This is corroborated by previous observations in human SH-SY5Y neuroblastoma cells where siRNA treatment of *SLC39A14* leads to a decrease in Mn uptake[244]. Consistent with its role of Mn uptake SLC39A14 was shown to localise to the cell membrane in zebrafish embryos and HEK293 cells[65]. These results confirmed the findings in brain where SLC39A14 localises to the cell membrane of neurons in the globus pallidus (**Section 4.6**). This is consistent with previous studies in HepG2 cells where SLC39A14 was detected at the plasma membrane and in endosomes[241]. Several studies have shown that Mn is a substrate for SLC39A14[69,70], however, there was substantial uncertainty to the *in vivo* specificity of this transporter as *in vitro* SLC39A14 can transport Zn, Fe and Cd[71]. Individuals with *SLC39A14* mutations show an isolated abnormality of Mn levels (**Section 4.4**) which indicates that *in vivo*, the major role for SLC39A14 is that of Mn transport.

The identified missense mutations in *SLC39A14* were demonstrated to impair Mn uptake in HEK293 cells[65]. Additional studies with regard to these mutations has shown that mutant protein, however, did not mislocalise suggesting that the observed loss of Mn transport is due to malfunction of the transporter itself rather than due to impaired traficking to the cell membrane. The G383R mutation in particular almost completely abolished Mn uptake[65]. The glycine residue is part of the highly conserved EEXPHEXGD motif required for metal binding[228]. A mutation within this motif is likely to impair binding of Mn responsible for the observed complete loss of Mn transport ability.

It was surprising that individual C-II-2 who carries a mutation affecting only SLC39A14 isoform 2 shows a similarly severe neurological phenotype as the rest of the patient

cohort. Analysis of the functional, spatial and regulative differences of isoform 1 and 2 (**Section 4.6**) has corroborated the hypothesis that the disease mechanism is that of impaired hepatic Mn uptake (**Figure 4.20**). Whilst isoform 1 is ubiquitously expressed with high levels of expression evident in the brain, isoform 2 shows a restricted expression pattern including liver, kidney and intestine – organs involved in the regulation of metal ion homeostasis. The absence of brain expression of isoform 2 suggests that the primary defect of Mn clearance does not occur in the brain and that cerebral Mn deposition arises secondarily due to the increased systemic Mn load.

The observed differences in the expression pattern of isoform 1 and 2 are in contrast to the findings of the UK Human Brain Expression Consortium (http://www.braineac.org) that have analysed the mRNA expression levels of 26 thousand genes in ten different brain regions from post-mortem studies of 134 control individuals. Their results suggest that both transcripts are expressed throughout all studied brain regions, however, with somewhat lower expression levels observed for isoform 2 compared to isoform 1. For either isoform, highest expression was observed in cortical regions with less expression in the white matter. Unfortunately, mRNA expression in the globus pallidus, the main region of manganese deposition, was not assessed. The discrepancy between this study and the results of this thesis may be due to an increased sensitivity of the array compared to traditional RT-PCR. Expression levels assessed in total RNA extracted from whole brain may also be different to that of individual brain regions. However, the probe sequences for exon 4A and 4B used in this array are to regions that are highly homologous – 75% homology between exon 4A and 4B captured by the probe to exon 4A (Affymetrix ID 3089375), and 70 % homology between exon 4A and 4B captured by the probe to exon 4B (Affymetrix ID 3089382). This may result in false positive detection of isoform 2 in the brain. While the primers used for RT-PCR in this thesis were tested for their specificity using plasmids encoding each isoform, there is no data regarding the specificity of the array probes.

As the main regulatory organ involved in Mn homeostasis in humans, the liver seems most likely to play the crucial role in the disease mechanism. Mn exposure in mice causes a marked increase in hepatic *SLC39A14* mRNA expression[245] which further highlights its role in hepatic Mn uptake under high Mn load. As reported previously for murine Slc39a14[70], the Mn uptake studies in HEK293 cells confirmed that human isoform 2 has a greater ability to transport Mn than isoform 1. Furthermore, Mn

dependent transcriptional regulation of *SLC39A14* expression appears to only affect isoform 2. In zebrafish mRNA expression of transcript 2 is upregulated upon Mn exposure while that of transcript 1 remains unchanged (**Section 4.6**). Similarly, transcription of *SLC30A10* is regulated by Mn in order to reduce the body Mn load through promotion of hepatic excretion[48]. These findings suggest that there may be specific roles for the individual SLC39A14 isoforms and that isoform 2 may be the crucial one for the regulation of Mn homeostasis.

Whether SLC39A14 is essential for Mn uptake in other tissues than the liver remains to be clarified. The ubiquitous expression pattern of isoform 1 suggests a role for SLC39A14 in a wide range of tissues. Although SLC39A14 is expressed in the intestine, the major site of Mn uptake, intestinal Mn uptake appears to be preserved in this disease as clinically we do not see deficiency of Mn. Similarly, Mn is deposited in the brain suggesting that transporters other than SLC39A14 facilitate cerebral Mn uptake. Several alternative Mn uptake transporters may compensate for loss of SLC39A14 function. These include DMT1, TfR1, SLC39A8, Mn citrate shuttle, glutamate receptors and various calcium channels/ATPases that have been implicated in Mn transport at the cell membrane either in the brain or the intestine (**Section 1.3**)[82,86,88,91,192,246,247].

Analyses of the subcellular localisation of human SLC39A14 in zebrafish embryos and HEK293 cells demonstrate that SLC39A14 is not only present on the cell membrane but also intracellularly. Hence, SLC39A14 might be required for intracellular trafficking of Mn and its transport into specific organelles. This concurs with a recent study showing that SLC39A14 facilitates endosomal trafficking of Zn in enterocytes[234]. Subcellular deficiency of Mn may therefore also contribute to the neuropathology in SLC39A14 deficiency.

While mutations in *SLC39A14* in humans primarily lead to Mn dyshomeostasis it is possible that loss of transporter function may also affect the homeostasis of other metals thereby contributing to the disease pathogenesis. Numerous studies have suggested a role for SLC39A14 in Zn handling in bone, adipose tissue and inflammation[234,248-251]. *SLC39A14* knock-out mice were shown to have abnormalities in both Zn and Fe homeostasis. Gastrointestinal absorption of Zn is decreased while that of Fe is increased. Furthermore, *SLC39A14* knock-out mice have greater hepatic Fe

accumulation[252]. The changes in metal homeostasis are accompanied by greater body fat, higher insulin levels and impaired gluconeogenesis leading to hypoglycaemia, and dwarfism with shortened long bones[252,253]. However, in humans hypoglycaemia or skeletal abnormalities have not been observed. Studies of *SLC39A14* knock-out mice have also demonstrated that SLC39A14 is involved in the regulation of intracellular signalling pathways such as G-protein coupled receptor mediated cAMP-CREB signalling required for systemic growth, and JAK2/STAT3 and NF-κB inflammatory pathways[250,253]. Unfortunately, effects of *SLC39A14* loss-of-function on Mn homeostasis in mice have not been studied to date.

There are some limitations to the interpretation of the HEK293 studies performed in this work. Mn transport activity of each isoform was assessed using overexpression of either protein by transient transfection. Protein expression levels may vary due to differences in transfection efficiency[254] and may not allow accurate assessment of the physiological protein activity. However, the consistent results with cells from different passage numbers for both isoforms and the similar results previously described in the literature[70] make the results more powerful. On the other hand, when assessing the manganese transport activity of the various mutant proteins a significant discrepancy between each experiment was observed. Therefore, a stable mutant cell line for each mutant protein was generated by our collaborators in order to more accurately assess the protein function rather than measure differences in transfection efficiency.

Chapter 5. *slc30a10* zebrafish do not recapitulate all phenotypes of human SLC30A10 deficiency

5.1 Introduction

Although the role of SLC30A10 has been thoroughly characterised *in vitro* little is known about the mechanisms of Mn toxicity due to loss of SLC30A10 function *in vivo*. To date, a vertebrate *slc30a10* gene knock-out model has not been studied. The aim of this work was to develop a *slc30a10* loss-of-function mutant in zebrafish with the view to provide a disease model to study disease mechanisms and identify novel drug treatment targets. The small size of zebrafish and large numbers of embryos available make them an ideal model organism for high-throughput drug screening[173]. The current treatment strategy for SLC30A10 deficiency in humans involves monthly intravenous chelation therapy with $Na_2CaEDTA$ which is both burdensome and costly[57]. Hence, identification of an oral chelating agent would immensely benefit patients with SLC30A10 deficiency. A zebrafish mutant with a simple read-out for drug screening would allow the screening of a chelator library in order to identify an oral drug with effective Mn binding capacity.

The following chapter describes the characteristics of the *slc30a10* gene in zebrafish, the generation of *slc30a10* mutants using TALEN and CRISPR/Cas9 genome editing and the effects of loss of gene function. Both TALEN and CRISPR/Cas9 genome editing methods were developed during this project. At the start of this work, only the TALEN method had been published at the time. Given the considerably simpler and less time consuming CRISPR/Cas9 protocol, this method was established subsequently.

5.2 Characterisation of the *slc30a10* orthologue in zebrafish

5.2.1 Temporal expression and sequence verification of zebrafish *slc30a10*

In order to identify the orthologues of human *SLC30A10*, the Basic Local Alignment Search Tool (**Section 2.3.2**) was used to align the human *SLC30A10* nucleotide sequence with the zebrafish genome. In zebrafish, many genes have a paralogue due to the evolutionary whole genome duplication that occurred in the common ancestor of

teleost fish[255,256]. The existence of only one *slc30a10* gene in zebrafish could be established. Alignment of the human (NP_061183.2) and zebrafish (NP_001121706) protein showed that they share 51% sequence homology. A higher degree of conservation is seen around the six TMDs that are required for metal transport (**Figure 5.1**, **Section 1.3.2**). Zebrafish *slc30a10* encodes a protein of 385 amino acids while human *SLC30A10* encodes a larger 485 amino acid protein. Given the considerable degree of sequence homology between human and zebrafish it seemed reasonable to assume that the function of the transporters are comparable between species.

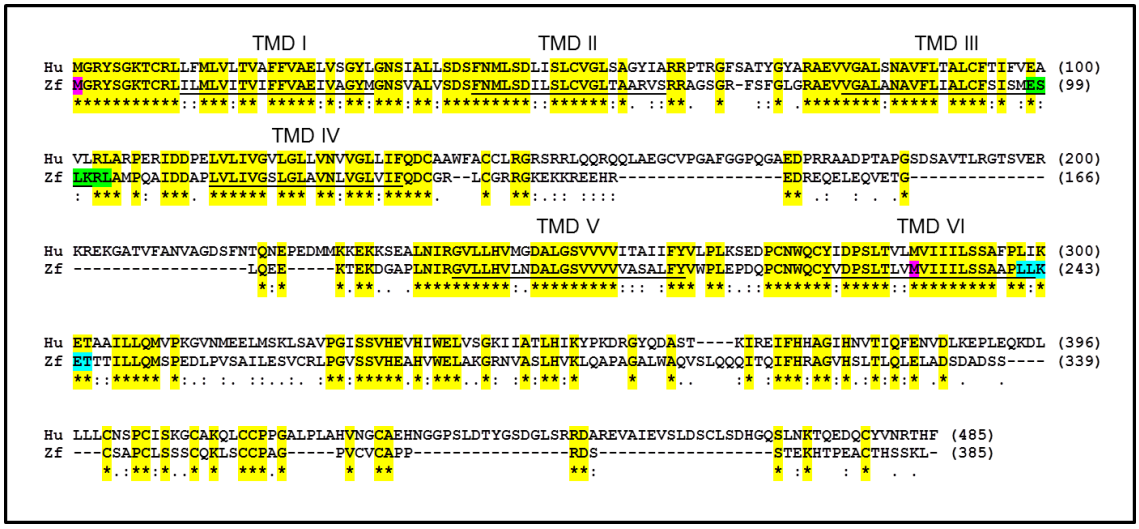

Figure 5.1 Protein sequence alignment of human and zebrafish Slc30a10.

*Alignment of human (top) and zebrafish Slc30a10 (bottom) using ClustalW2 software. Conserved amino acids highlighted in yellow, * indicates identical sequence, TMDs are underlined, TALEN target region is highlighted in green, CRISPR target region in turquoise, Start-methionine of isoform 1 and 2 in purple. TMDs were predicted using the MEMSAT3 & MEMSAT-SVM membrane helix prediction tool (http://bioinf.cs.ucl.ac.uk/psipred/).*

In order to characterise zebrafish *slc30a10*, expression of the gene during embryonic and larval development was examined by RT-PCR (**Section 2.3.6**). *slc30a10* expression was clearly demonstrated between 3 and 120 hpf (**Figure 5.2**) suggesting that this gene's protein product is utilised during early zebrafish development. Expression at 3 hpf suggests maternal genome contribution as zygotic gene expression is initiated at the midblastula transition (512 cell stage) at approximately 2.75 hpf after which maternal transcripts are gradually eliminated[257].

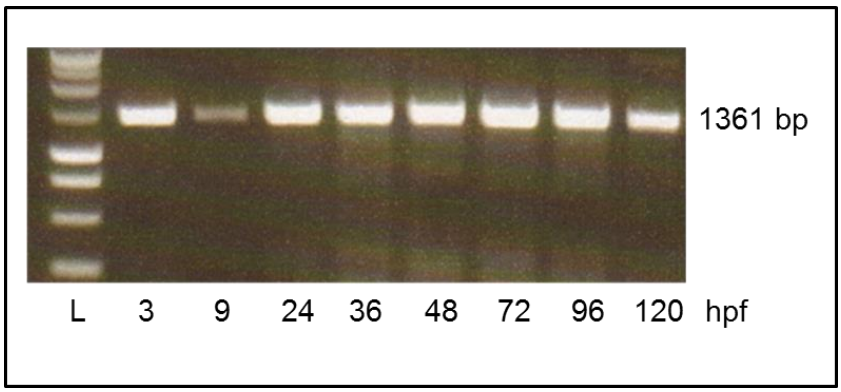

Figure 5.2 *slc30a10* is expressed during embryonic and early larval development of zebrafish between 3 and 120 hpf.

Gel electrophoresis image of slc30a10 amplicons from larval cDNA using primers spanning from the 5'UTR to the 3'UTR (amplicon size 1361 bp). L, 1 kb ladder (Promega). RNA was extracted from pools of 50 embryos/larvae at the given time points.

For sequence verification, the coding sequence of *slc30a10* spanning from the 5' UTR to 3' UTR was PCR amplified from zebrafish cDNA and cloned into the pBSK- vector (**Section 2.3.8**). Two differing transcripts were identified, transcript 1 and 2, respectively. Most clones contained the sequence of transcript 1 that is almost identical with the published reference sequence (NM_001128234.1), (**Figure 5.3**) and encodes a protein of 385 amino acids.

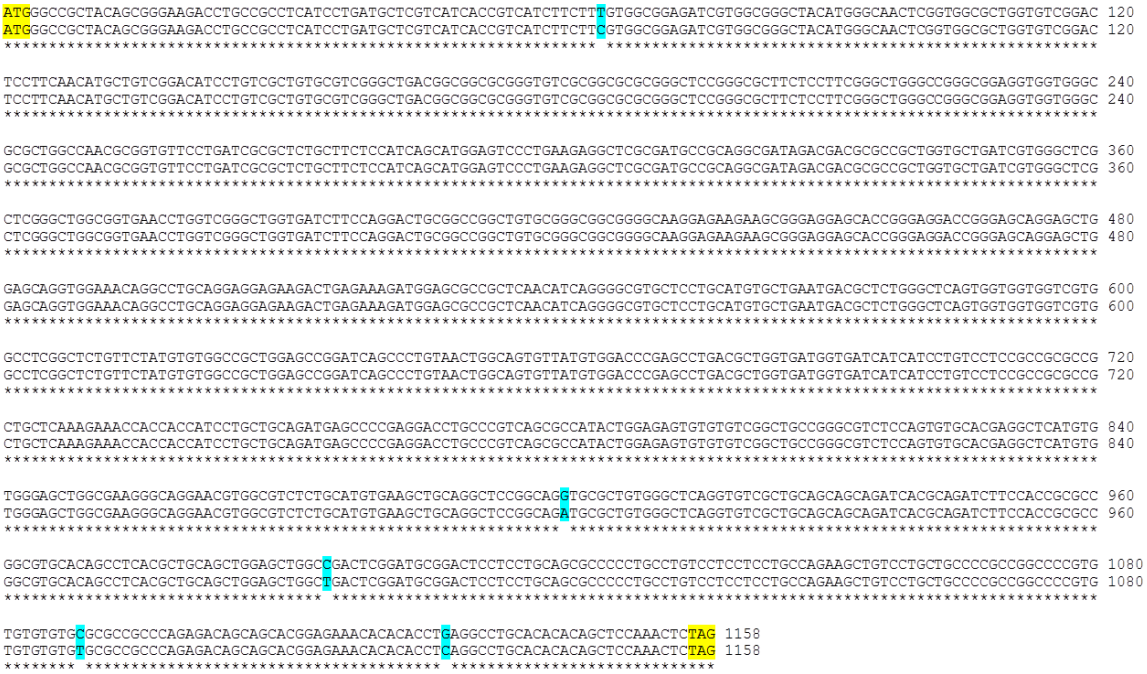

Figure 5.3 The cloned *slc30a10* transcript 1 aligns with the annotated transcript NM_001128234.1.

cDNA alignment of slc30a10. The annotated sequence NM_001128234.1 (top line) is aligned with the cloned sequence (bottom line) obtained from embryos at 72 hpf. Start and stop codons are marked in yellow. Identified variants are indicated in turquoise.

The second transcript identified by cloning contains an alternative first (1B) and larger second exon (2B), (**Figure 5.4**). The nucleotide sequences of both isoforms were aligned using ClustalW2 software (**Figure 5.5, Section 2.3.2**) and differ in a region spanning from part of the 5'UTR to part of the second exon while the third and fourth exons are identical. The start codon of this transcript, provided protein translation takes place, lies within exon 3. The ExPASy translation tool software predicts that this sequence may encode a significantly shortened protein of 134 amino acids (**Figure 5.4, Section 2.3.2**).

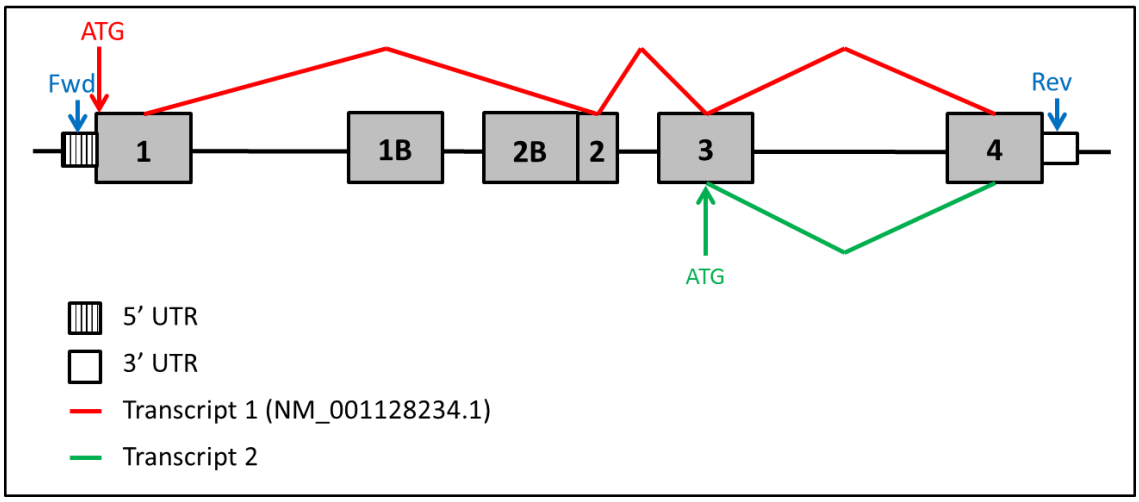

Figure 5.4 *slc30a10* transcripts identified by cloning.

Schematic overview of the potential isoforms encoded by slc30a10. Transcript 1 is identical with the published reference NM_001128234.1. Transcript 2 (green) has an alternative first (1B) and second exon (2B). Forward (Fwd) and reverse (Rev) primers used for PCR amplification of transcript 1 and 2 are indicated in blue. Exons in grey, introns indicated by black line (not drawn to scale).

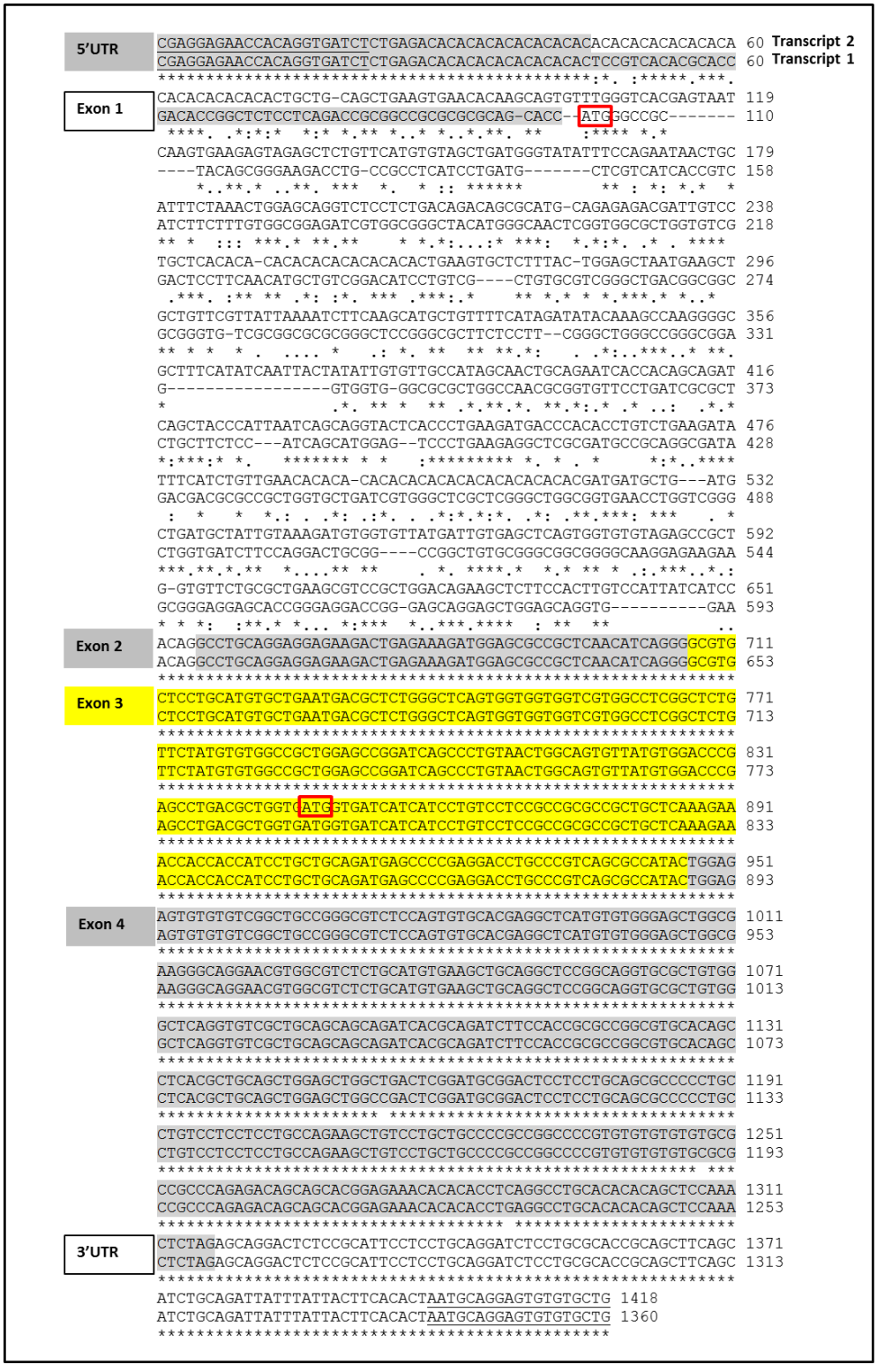

Figure 5.5 Nucleotide alignment of *slc30a10* transcript 1 and 2.

*Transcript 1 (bottom) and transcript 2 (top). * indicates identical sequence. ATG start codons marked by red box. Primer sequences used for PCR amplification of both transcripts underlined.*

In order to confirm the existence of a second transcript, cDNA was amplified using a forward primer to the first intron (alternative exon 2) and a reverse primer to exon 3 (**Section 2.3.6**). Genomic DNA was amplified alongside to confirm that no contamination of mRNA with genomic DNA had occurred. Consistent with the cloning result, PCR amplification of cDNA showed a single band of the expected size of 209 bp while the genomic amplicon was that of 396 bp (**Figure 5.6**).

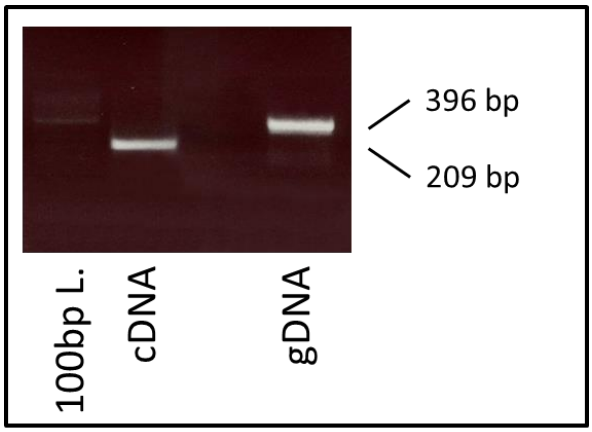

Figure 5.6 Zebrafish *slc30a10* encodes a second transcript.
Gel electrophoresis image of PCR amplicons from cDNA derived from zebrafish embryos at 72 hpf and zebrafish genomic DNA. Expected amplicon size of cDNA 209 bp, of genomic DNA 369 bp. L., 100 bp ladder (Promega).

5.2.2 Spatial expression of zebrafish *slc30a10*

Whole mount *in situ* hybridisation was used to determine the spatial domains in which *slc30a10* is expressed in the developing zebrafish. A digoxigenin labelled anti-sense RNA probe (Probe 1) was generated spanning 950 bp from the first exon to the 3'UTR (**Section 2.4.5**). Although this antisense probe is not complementary to isoform 2 in its entirety, it is expected that the 767 bases that are complementary will allow sufficient hybridisation of the probe with the transcript of isoform 2. Probe 1 is therefore likely to detect both *slc30a10* transcripts. Given that the sequence of transcript 1 overlaps with that of transcript 2 almost completely it was not attempted to generate a probe specific to transcript 1 only.

No specific spatial expression pattern was identified at early developmental stages between 3 and 48 hpf (**Figure 5.7a**). From 72 hpf strong expression of *slc30a10* was observed in liver, intestine and pharynx (**Figure 5.7a**) which was confirmed on sections following *in situ* hybridisation (**Figure 5.7b**). This was particularly evident at 96 hpf.

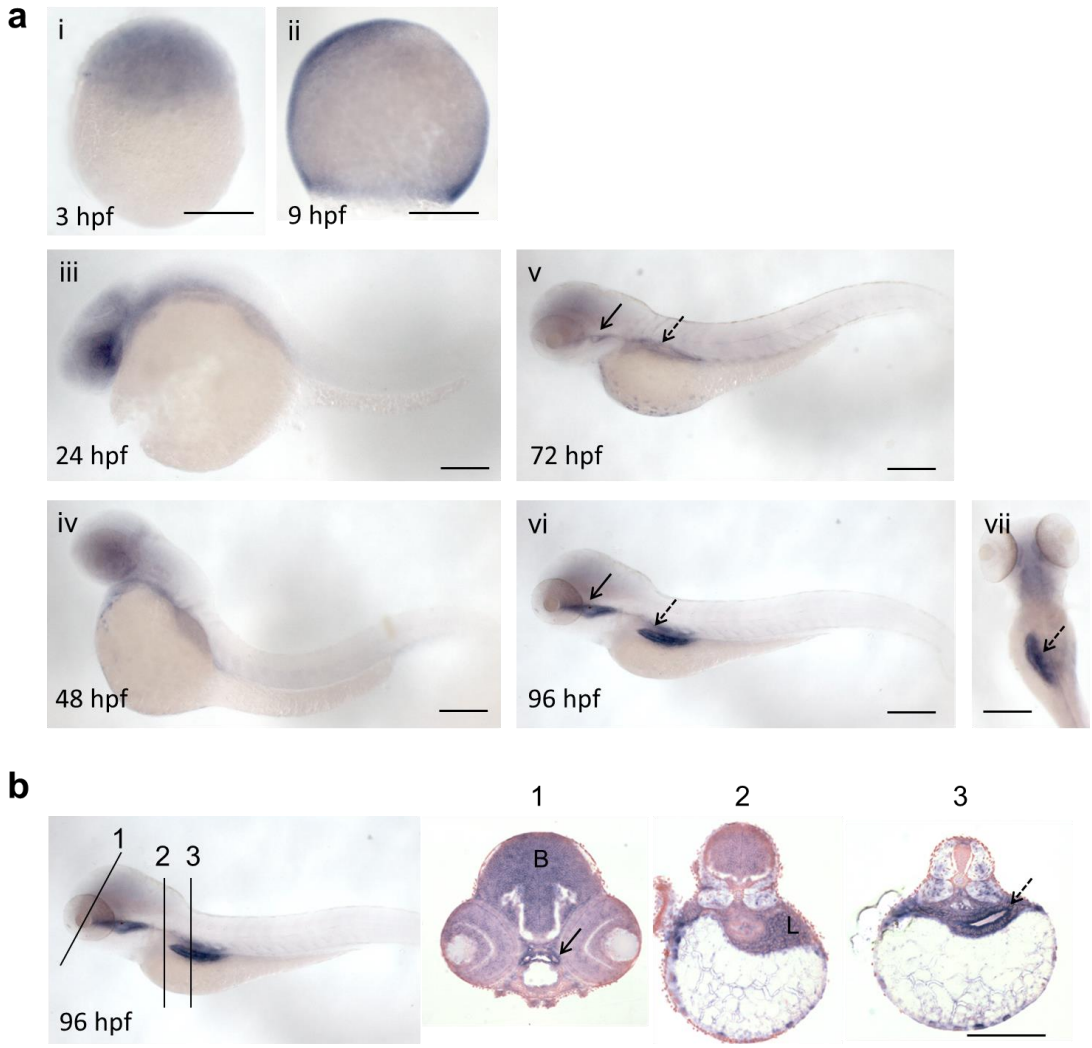

Figure 5.7 Expression pattern of *slc30a10* during early zebrafish development.
*(**a**) Whole mount in situ hybridisation was performed on embryos fixed at (i) 3 (ii) 9 (iii) 24 (iv) 48 (v) 72 and (vi) 96 hpf. (i-vi) Lateral views, (vii) dorsal view. slc30a10 is expressed in the intestine (dashed arrow) and pharynx (full arrow) from 72 hpf. Scale bar for (i) and (ii) 200 µm, for (iii)-(vii) 500 µm (**b**) Sections of 96 hpf embryos following in situ hybridisation confirmed a strong expression of slc30a10 in the intestine (dashed arrow) and the pharynx (full arrow). Staining is also evident in the liver (L) and in the brain (B), however, this expression is not confined to specific brain regions. Sections through 1 (brain and pharynx), 2 (liver), 3 (intestine). Scale bar 500 µm.*

In order to examine whether *slc30a10* transcript 2 has a distinct expression pattern, an antisense RNA probe specific to isoform 2 was generated (**Section 2.4.5.**). At 96 hpf the expression pattern was similar to that of probe 1, however, the liver staining was more evident (**Figure 4.7**).

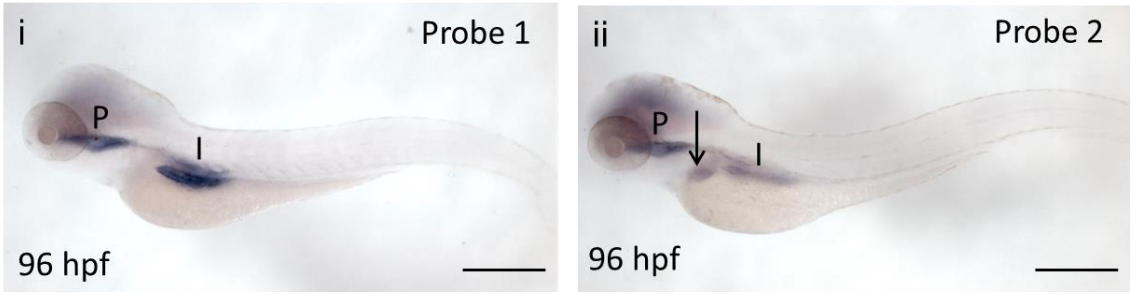

Figure 5.8 Differences in expression patterns of *slc30a10* detected by probe 1 and 2.

(i) Probe 1 (specific to transcript 1 and likely transcript 2) and (ii) probe 2 (specific to transcript 2) show a similar expression pattern in the pharynx (P) and intestine (I) at 96 hpf. For transcript 2 the liver staining is more evident (arrow). Scale bar 500 µm.

5.2.3 Yeast complementation studies to assess the function of zebrafish Slc30a10

Using a yeast complementation assay we have previously shown that human *SLC30A10* functions as a Mn transporter[1]. In order to examine whether the zebrafish protein shares similar properties zebrafish *slc30a10* was overexpressed in the Mn sensitive yeast strain ∆pmr1 as described previously (**Section 2.3.21**)[46,94]. Pmr1 encodes a Golgi membrane P-type ATPase involved in Ca and Mn transport into the Golgi. Deletion of pmr1 in yeast causes accumulation of Mn in the cytosol and increases the sensitivity of cells to high concentrations of Mn[13]. Transformation of ∆pmr1 with zebrafish *slc30a10* rescued growth of the ∆pmr1 strain. Whilst the cells did not grow as profusely as the wild-type BY4743 background strain, they were more confluent than evident for ∆pmr1 alone (**Figure 5.9**). A similar result was obtained for human SLC30A10. Transformation with ZRC1, the yeast homologue of SLC30A10, known to transport Zn only (**Section 1.3.2.1**), showed a similar growth pattern as ∆pmr1 alone. However, ZRC1 carrying the N44I mutation that was described previously to confer Mn resistance[94] protected cells from Mn toxicity (**Section 1.3.2.1**).

The ZRC1 transformations were run in parallel as positive and negative controls. This data shows that zebrafish Slc30a10, similarly to human SLC30A10 and ZRC1(N44I), rescues growth of Δpmr1 at high Mn concentrations confirming its ability to transport Mn.

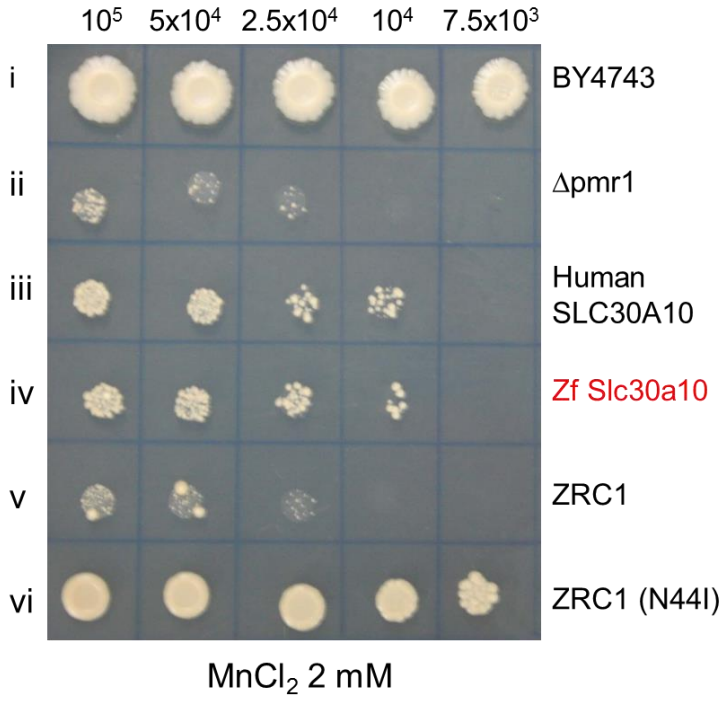

Figure 5.9 Zebrafish Slc30a10 protects Δpmr1 yeast from Mn toxicity.
Culture plate image of serial dilutions of yeast colonies: 10^5, $5x10^4$, $2.5x10^4$, 10^4 and $7.5x10^3$ cells of each strain were spotted onto SC-Ura plates supplemented with 2 mM $MnCl_2$ and incubated at 30°C for six days. Both (i) BY4743, wild-type and (ii) Δpmr1, Mn sensitive yeast strains were transformed with empty vector pYES-Dest52. Overexpression of human (iii) and zebrafish (iv) slc30a10 rescue growth of Δpmr1. (v) Transformation with ZRC1 does not confer Mn resistance (negative control). (vi) ZRC1 carrying the N44I mutation alters the transporter's metal specificity and restores Mn resistance (positive control). Zf, zebrafish.

5.3 TALEN and CRISPR genome editing to generate a zebrafish *slc30a10* null mutant

5.3.1 Generation of a *slc30a10* loss-of-function mutant using TALENs targeting exon 1

As *slc30a10* is expressed during early zebrafish development and the transporter has a similar function to the human one, it was reasonable to assume that loss of gene function in zebrafish would provide a disease model for the human disorder. Therefore, a pair of TALENs was designed to target a conserved region within the first exon of *slc30a10* encoding the third TMD of the protein, a region that is also affected in some patients with childhood-onset dystonia (p.Ala105_Pro107del[46]), (**Figure 5.1**, **Section 2.3.17**). The TALEN spacer region contained a restriction site for EarI (**Figure 5.10**) that allowed screening for somatic mutations and carriers by PCR and restriction enzyme digestion (**Section 2.3.5**). TALEN induced mutations are expected to alter the sequence within the spacer region preventing EarI digestion.

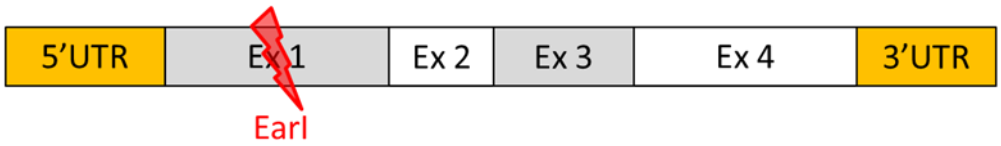

Figure 5.10 Target region of a TALEN pair to exon 1 of *SLC30A10*.

The rate of somatic mutagenesis was determined in healthy looking, TALEN injected embryos at 24 hpf. Complete EarI digestion of a wild-type sequence results in a single visible band of 359 bp and suggests no somatic mutagenesis; partial EarI digestion generates two visible bands of 459 and 359 bp indicating that somatic cells carry mutations in the EarI recognition site. Partial EarI digestion was observed in 19 out of 21 embryos confirming high mutagenic efficiency of the generated TALEN pair (**Figure 5.11a**). Undigested bands visualised on an agarose gel were gel purified and cloned into pCRII TOPO vector for sequencing (**Section 2.3.9**). The sequences of the identified Indel mutations in the F0 generation are given in **Figure 5.11b**.

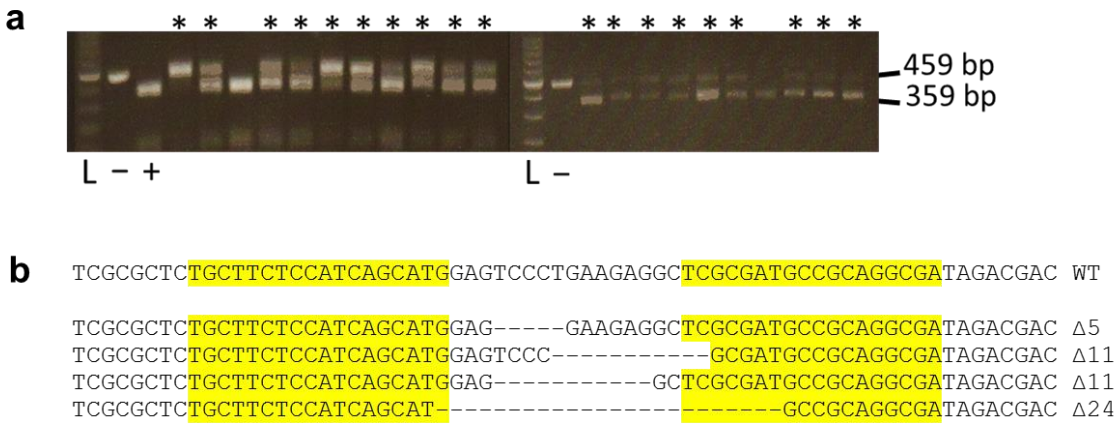

Figure 5.11 TALEN induced mutagenesis in exon 1 of *slc30a10* in the F0 generation.

*(**a**) Gel electrophoresis image of slc30a10 amplicons containing the TALEN target sequence and digested with EarI from un-injected and TALEN injected zebrafish F0 embryos. Partial digestion (*) was observed in 19/21 embryos. L, 100 bp DNA ladder. −, undigested control. +, digested wild-type control. (**b**) Schematic showing examples of Indel mutations identified in the F0 generation. Wild-type (WT) sequence in the top row. TALEN binding sites marked in yellow. (−) deleted nucleotide, insertions in grey, (Δ) number of deleted nucleotides.*

The remaining healthy looking, TALEN injected F0 embryos were raised to adulthood and seven F0 fish outcrossed to a wild-type AB strain. F1 embryos were screened by PCR and EarI digestion to assess whether mutations were passed on to the germ line. Out of the seven adult F0 fish, three were found to carry heritable mutations that were transmitted to the progeny in approximately 50% of analysed embryos (**Figure 5.12a**).

The remaining F1 embryos obtained from the three adult F0 fish that carried heritable mutations were raised to adulthood. Adult F1 fish were finclipped for DNA extraction (**2.3.1**) and again screened by PCR and EarI digestion. The digestion products were visualised on an agarose gel and the undigested bands cloned into the pCRII-TOPO vector for sequencing (**Section 2.3.9**). Sequencing identified a range of indel mutations causing frameshifts in the nucleotide sequence (**Figure 5.12b**). These are expected to be deleterious for protein function. An adult F1 carrier with a heterozygous frameshift mutation caused by a 10 bp deletion within exon 1 (c.298_307del, p.L100Sfs*7),

predicted to cause a significant truncation of the protein, was out-crossed to wild-type fish to generate a stable mutant line *slc30a10*^{U800} and was used for further studies.

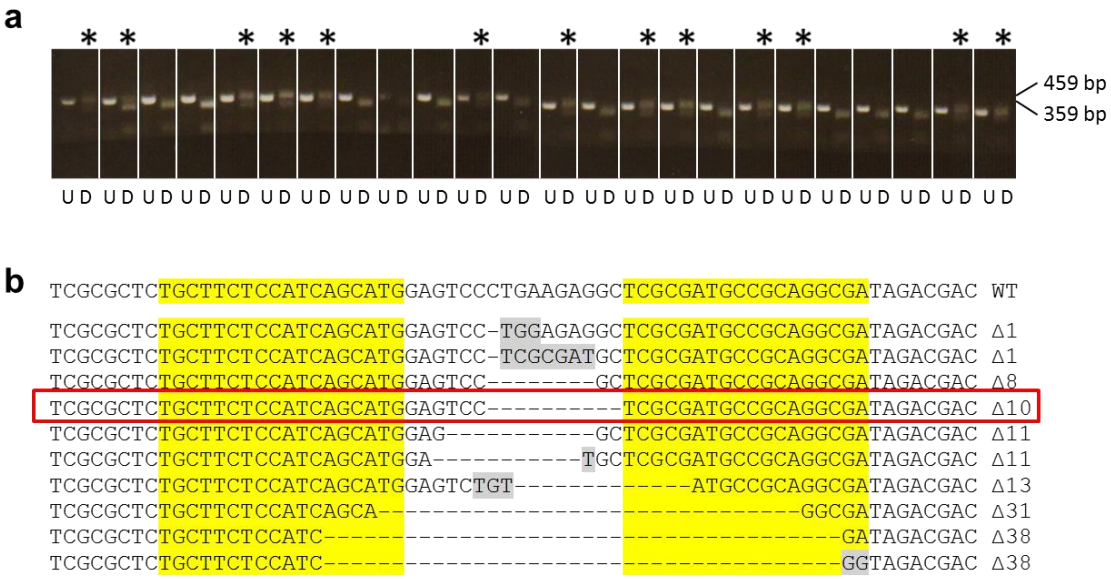

Figure 5.12 TALEN induced mutagenesis in exon 1 of *slc30a10* in the F1 generation.

*(**a**) Gel electrophoresis image of slc30a10 amplicons from F1 embryos containing the TALEN target sequence subsequent to digestion with EarI. EarI screening of F1 embryos from an outcross of a single F0 founder fish with an AB wild-type strain is shown. The undigested (U) PCR product was loaded on the left of each digest (D) reaction. Partial digestion (*) was observed in 13/24 embryos confirming carrier status for a TALEN induced mutation in approximately 50% of the progeny. (**b**) Schematic showing examples of Indel mutations identified in the F1 generation. Wild-type (WT) sequence in the top row. TALEN binding sites marked in yellow. (−) deleted nucleotide, insertions in grey, (Δ) number of deleted nucleotides. slc30a10*^{U800} *mutant highlighted in red.*

5.3.2 Generation of a *slc30a10* loss-of-function mutant using CRISPRs targeting exon 3

An additional mutant with a frameshift mutation in exon 3 was generated that affects both transcripts because there was a small chance that gene function in the TALEN mutant *slc30a10*^{U800} harbouring a 10 bp deletion within exon 1 of *slc30a10* would be rescued by the identified alternative transcript 2 (**Section 5.2.1**).

A CRISPR target region was chosen within exon 3 encoding TMD VI (**Figures 5.1 and 5.13a, Section 2.3.18**). The Cas9 construct used encodes a zebrafish codon-optimized version of *S. pyogenes* Cas9 with SV40 large T-antigen nuclear localisation signals (nls) at both its amino and carboxyl termini (nls-zCas9-nls)[191]. Co-injection of Cas9 mRNA and the gRNA to exon 3 induced efficient mutagenesis in the F0 generation. HRMA demonstrated a difference in the melt curve shape in 10 out of 11 injected embryos compared to un-injected wild-type embryos (**Figure 5.13b, Section 2.3.19**). Progeny from a F0 founder fish with a high rate of germ line transmission (80%) (**Figure 5.13c**) was raised to adulthood. Adult F1 fish were fin-clipped for DNA extraction (**Section 2.3.1**) and screened using HRMA. Sequence analysis was performed for five fish that showed an altered melt curve (**Figure 5.13c**). The only carrier fish with a frameshift mutation (5 bp deletion within exon 3) was chosen to generate a stable mutant line *slc30a10*^{U600} (c.717_721del, p.P240Afs*92), (**Figure 5.13d**).

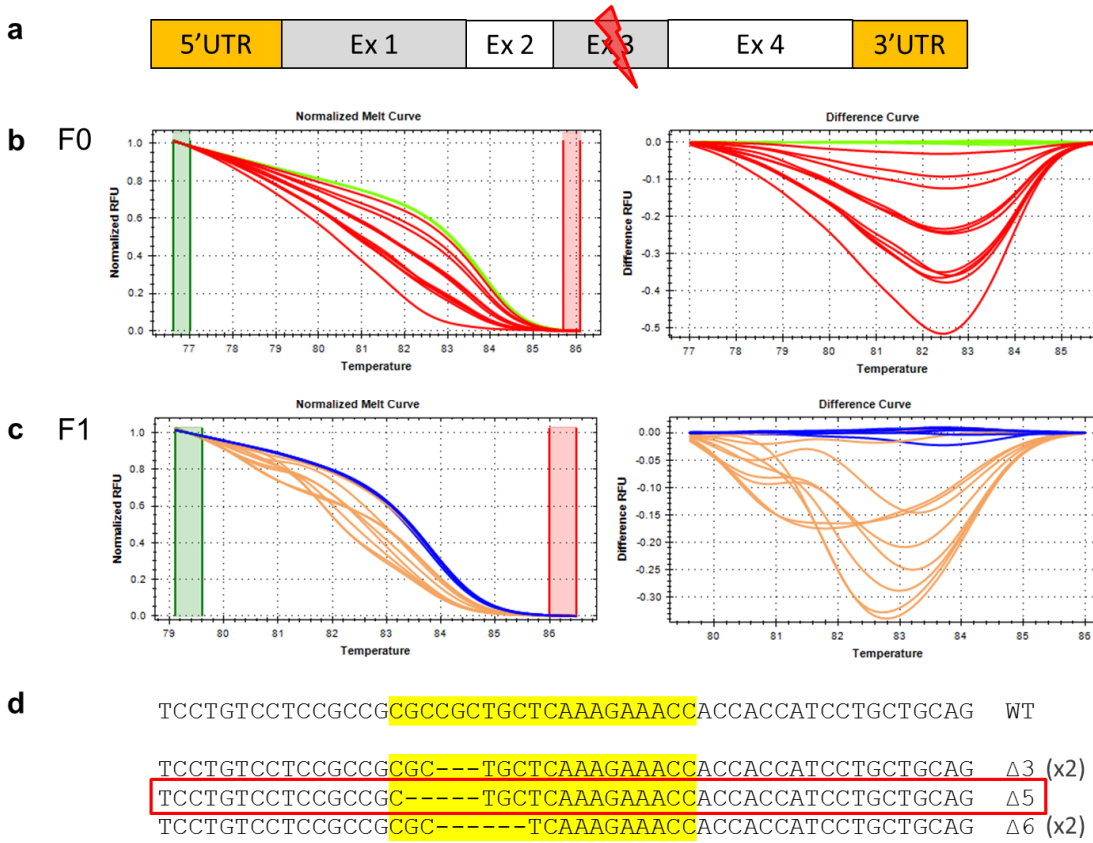

Figure 5.13 CRISPR induced mutagenesis in zebrafish *slc30a10* exon 3.

*(**a**) Schematic overview of the zebrafish slc30a10 gene and the region within exon 3 targeted by the gRNA/Cas9 complex. (**b**) HRMA shows that co-injection of the gRNA to exon 3 and Cas9 mRNA results somatic mutagenesis in 10 out of 11 injected embryos (F0 generation). Normalised melt curve (left) and difference curve (right) show changes in the melt curve shape between un-injected wild-type (green) and injected embryos (red). (**c**) A representative HRMA result of the progeny of a F0 founder fish is shown. Un-injected wild-type control in blue, F1 embryos in pink. 9/10 embryos show a change in the melt curve shape. (**d**) CRISPR induced indel mutations identified in five adult F1 fish. Wild-type (WT) sequence given in the top row. CRISPR target region marked in yellow, (−) deleted nucleotide, insertions in grey, (Δ) number of deleted nucleotides, (x2), these mutations were identified twice in different fish. The slc30a10^{U600} mutant is highlighted in red.*

5.4 Acute Mn toxicity in wild-type zebrafish

It was important to determine the concentrations of $MnCl_2$ that are toxic to wild-type larvae to estimate what concentrations of $MnCl_2$ to use to challenge Mn transporter mutants. In order to assess the effect of Mn on the development and survival of early larval stages of wild-type zebrafish, 72 hpf embryos were exposed to a range of $MnCl_2$ concentrations (50 µM to 100 mM), (**Section 2.4.4**). 72 hpf (protruding mouth stage) was chosen as a starting point because zebrafish begin to swallow water at this stage, supposedly aiding uptake of Mn[258]. Concentrations above 50 µM $MnCl_2$ were toxic and from 1.5 mM associated with high lethality for exposed larvae within two days of treatment (**Figure 5.14**). $MnCl_2$ at a concentration of 50 µM did not affect survival during the period of exposure and wild-type embryos appeared healthy.

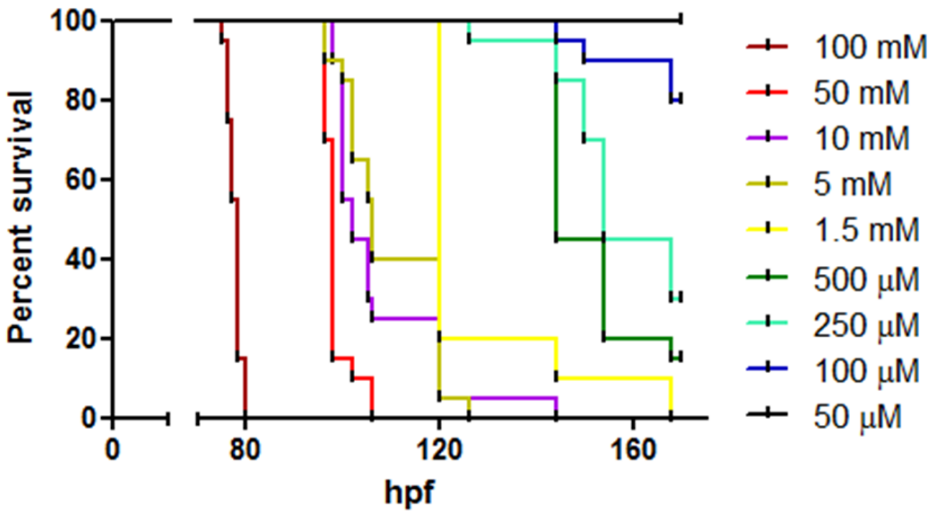

Figure 5.14 $MnCl_2$ exposure dose-dependently reduces larval survival.

Survival plot of wild-type zebrafish larvae exposed to $MnCl_2$. Exposure of wild-type larvae was commenced at 72 hpf and continued for four days. Treatments with $MnCl_2$ were performed in 6-well culture plates with 20 embryos per well. n=1 for concentrations ≥1.5 mM, n=2 for concentrations ≤500 µM.

At concentrations of $MnCl_2$ above 50 µM, toxicity effects were observed including superficial ulcerations, pericardial haemorrhage, curvature of the body axis and loss of balance (**Figure 5.15**). This is consistent with previous observations of environmental Mn toxicity in zebrafish[259].

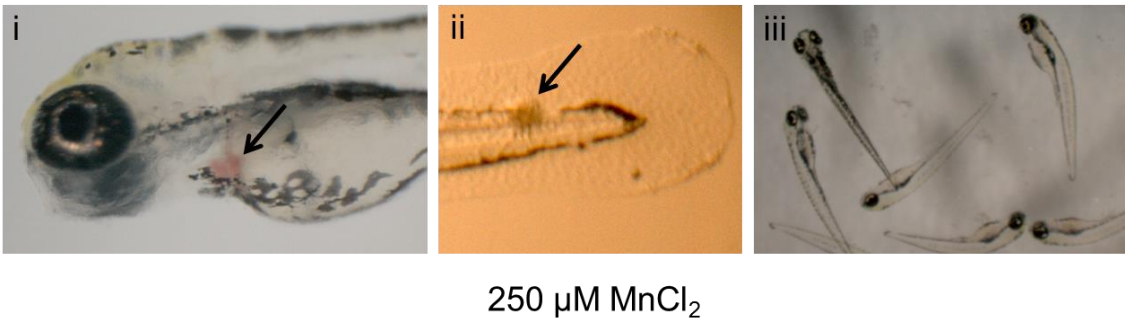

Figure 5.15 Toxic effects of $MnCl_2$ exposure in wild-type zebrafish larvae.
*Images of zebrafish larvae exposed to 250 µM $MnCl_2$ from 72 hpf showing **(i)** pericardial haemorrhage, **(ii)** superficial ulceration and **(iii)** body curvature, loss of balance and delayed swim bladder inflation.*

5.5 Phenotypic characterisation of *slc30a10^{U800}* mutants

slc30a10^{U800} mutants generated by TALEN genome editing carry a 10 bp deletion within exon 1 (c.298_307del) causing a frameshift predicted to significantly truncate the protein (p.L100Sfs*7) and likely to cause nonsense medicated decay. Raised under standard conditions they did not show an apparent phenotype. Homozygous *slc30a10^{U800}* mutants did not display morphological abnormalities or developmental defects, and had normal survival during embryonic and early larval development. They survived to adulthood and had normal fertility.

5.5.1 *slc30a10^{U800}* mutants show differences in Mn levels compared to wild-type larvae depending on their stage of development

To assess whether *slc30a10^{U800}* mutants accumulate Mn similar to humans Mn levels were determined by ICP-MS in pools of ten zebrafish larvae raised under standard conditions (**Section 2.5.2**). While there was no significant difference in Mn levels at 5 dpf, *slc30a10^{U800}* larvae accumulated three magnitudes higher levels of Mn compared to wild-type larvae at 14 dpf (**Figure 5.16i**). Other metal levels including Zn, Fe and Cu, potential substrates of the Slc30a10 transporter[92,93,260], were unchanged at 5 and 14 dpf (**Figure 5.17**). Surprisingly, $MnCl_2$ exposure to a range of concentrations between 10 and 50 µM that have been shown to be non-toxic to wild-type larvae (**Section 5.4**) led to a lesser degree of Mn accumulation in mutant than wild-type larvae at 5 dpf (**Figure 5.16ii**).

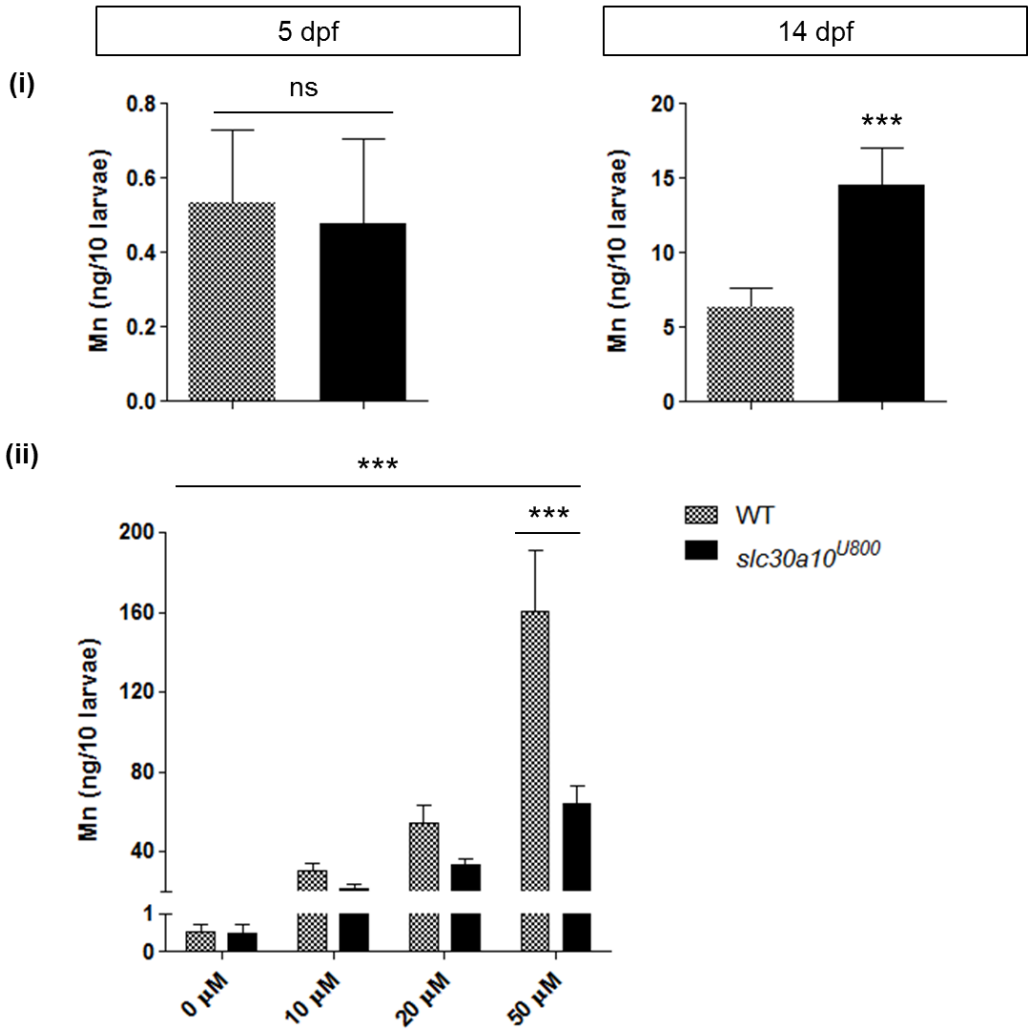

Figure 5.16 Mn levels of *slc30a10^{U800}* mutants are different from wild-type larvae.
*Graph showing Mn levels measured by ICP-MS from a pool of 10 larvae **(i)** without addition of $MnCl_2$ at 5 dpf (n≥12) and 14 dpf (n=5), **(ii)** at 5 dpf with the addition of 0 to 50 µM $MnCl_2$ to standard fishwater between 2 and 5 dpf (n≥3). Data are presented as means ± s.d. from a minimum of three independent experiments. Statistical analysis was performed using (i) Student's two tailed t test (ns, not significant, p>0.05. ***p<0.001), (p=0.5 [5 dpf], p=0.0005 [14 dpf]) (ii) 2 way ANOVA and Bonferroni posttests comparing wild-type versus slc30a10^{U800} larvae (***p<0.001).*

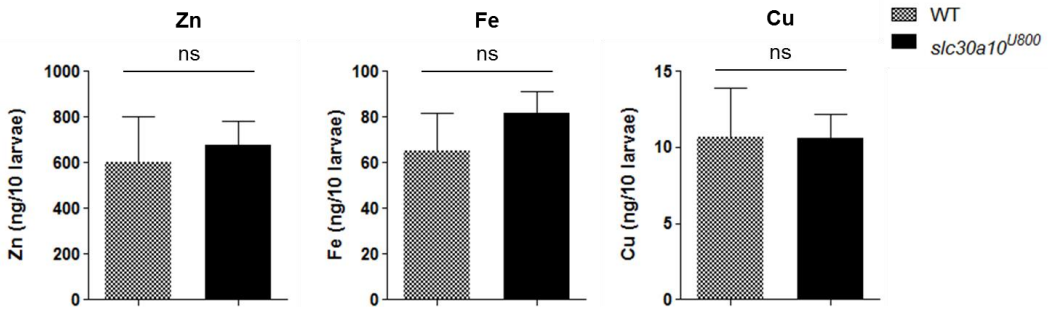

Figure 5.17 Zn, Fe and Cu levels are not altered in *slc30a10^{U800}* mutants at 14 dpf.
Graph displaying Zn, Fe and Cu levels analysed by ICP-MS in pools of 10 larvae at 14 dpf. Data are presented as means ± s.d. from a minimum of four independent experiments. Statistical analysis was performed using Student's two tailed t test (ns, not significant, p=0.49 [Zn], 0.1 [Fe], 0.96 [Cu]).

In order to verify that the observed changes in Mn levels were not due to differences in size, larval length from the most anterior part of the head to the tip of the tail was determined at 14 dpf under a light microscope. Although there appeared to be a small difference in length between mutant (mean of 6.566 mm) and wild-type (mean of 6.153 mm) larvae, Mn levels corrected for length did not change the result of raised Mn levels in *slc30a10^{U800}* mutants at 14 dpf (**Figure 5.18**).

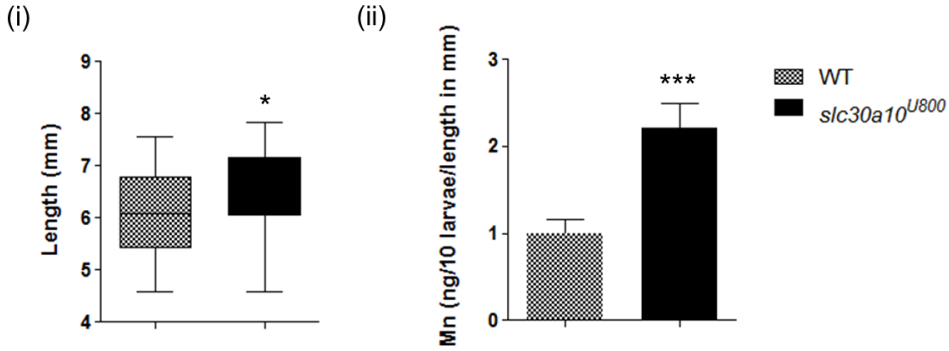

Figure 5.18 Homozygous *slc30a10^{U800}* mutants show a minimal increase in larval length that does not contribute in the observed differences in Mn levels.
*Graph showing (**i**) larval length measured at 14 dpf. The box and whisker plots indicate the 25th and 75th percentile, and the minimum and maximum length, respectively. Statistical analysis was performed using Student's t test (p=0.016). n≥46. (**ii**) Mn levels corrected for larval length at 14 dpf. Data are presented as means ± s.d. from a minimum of four independent experiments. Statistical analysis was performed using Student's two tailed t test (p=0.0001).*

5.5.2 *slc30a10*^{U800} mutants are more resistant to Mn toxicity during early larval development

The locomotor activity of wild-type and mutant larvae was tracked during 4 and 7 dpf using a behavioural profiling method described previously[202]. This setup allows automated detection of zebrafish locomotion by direct analysis of movements captured by video. 96 larvae in a 96 well plate are simultaneously observed in an analysis suite from Viewpoint LifeSciences using a frame-by-frame background subtraction method and automated analysis software (**Section 2.4.9**). The parameters analysed were “average total activity”, “average waking activity” and “average sleep”. Average total activity is measured as movement in seconds per minute. Average waking activity is the average activity during bouts of waking activity: total activity divided by the total active minutes (total time minus sleep time). Sleep is defined as inactivity for more than 1 minute. Average total sleep is measured as sleep bouts per 10 minutes. Larvae were raised on a 14:10 hour light:dark cycle. For wild-type larvae day and night can be clearly distinguished by the reduced activity and increased sleep duration under dark conditions (**Figure 5.19**).

The movement of larvae from a heterozygous incross of *slc30a10*^{U800} zebrafish in standard fishwater and compared to that of wild-type larvae of the same age was continuously tracked during 4 and 7 dpf (**Figure 5.19**). Analysis of the average total activity during day and night showed that there was no significant difference between wild-type and mutant larvae (**Figure 5.20**).

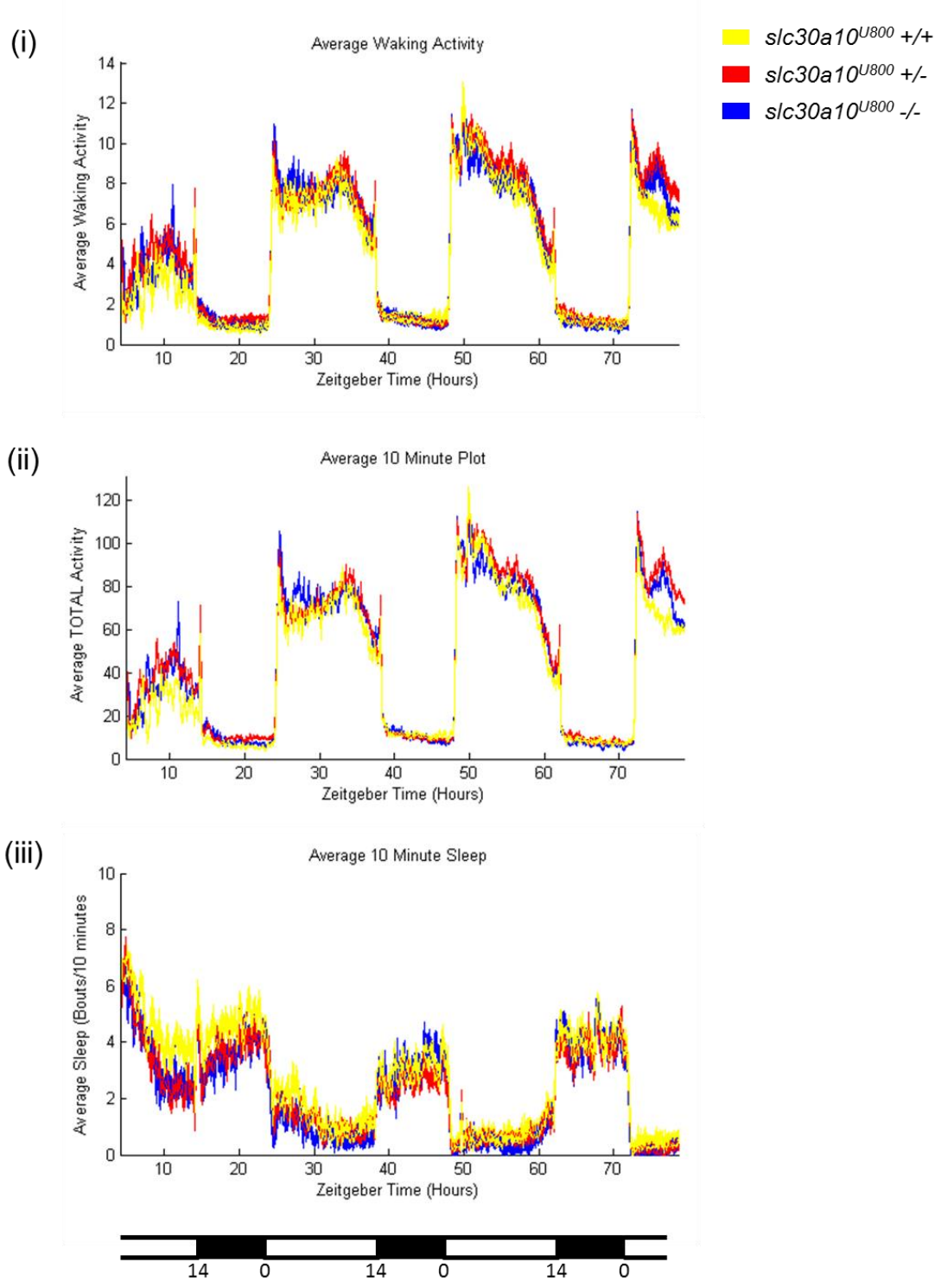

Figure 5.19 *slc30a10^{U800}* mutant and wild-type zebrafish larvae raised in standard fishwater show a similar locomotion pattern.

Plots of average (i) waking activity, (ii) total activity and (iii) total sleep comparing wild-type (yellow), heterozygous (red) and homozygous (blue) mutant zebrafish larvae. The 14:10 hour light:dark cycle is indicated on the bottom. n≥27 larvae.

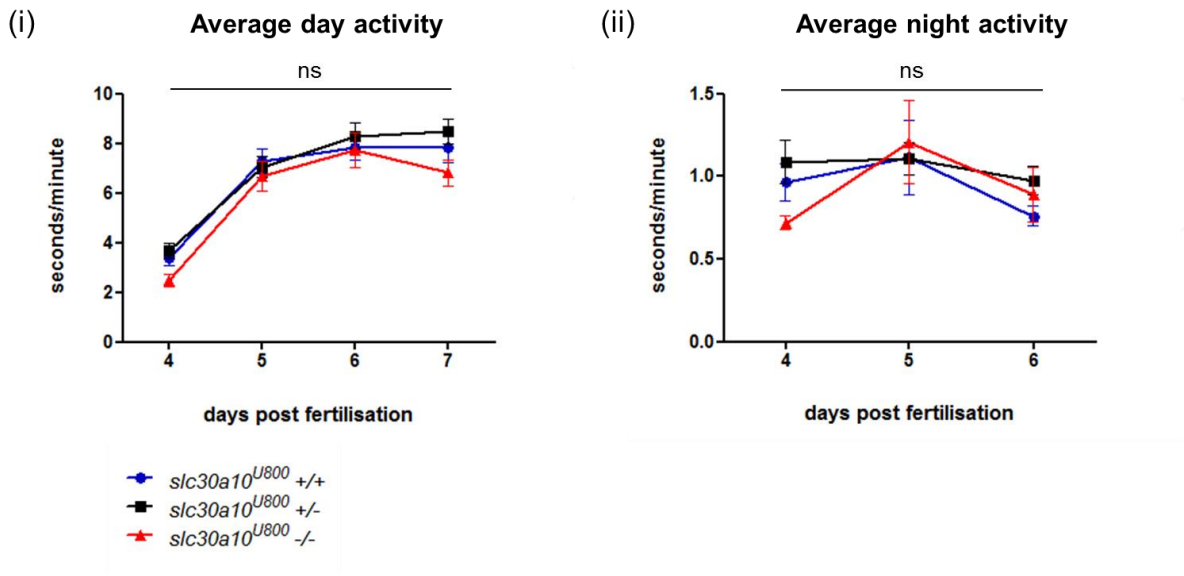

Figure 5.20 There is no difference in average total activity during the day and night between wild-type (+/+), heterozygous (+/-) and homozygous (-/-) *slc30a10^{U800}* larvae raised in standard fishwater without additional $MnCl_2$ exposure.

Graphs showing average (i) day (p=0.84) and (ii) night activity (p=0.45) analysed between 4 and 7dpf. Data are presented as mean ± standard error of the mean (s.e.m). Statistical analysis was performed using 2 way ANOVA (ns, not significant, p>0.05). n≥27 larvae.

The effect of $MnCl_2$ exposure on locomotor activity was analysed in *slc30a10^{U800}* mutant larvae and compared to wild-types. Homozygous *slc30a10^{U800}* mutants and wild-type cousins were exposed to increasing concentrations of $MnCl_2$ from 2 dpf onwards and their locomotor activity tracked between 4 and 8 dpf (**Figure 5.21**). Homozygous *slc30a10^{U800}* larvae had a significantly higher average day activity with a less pronounced dose dependent drop in average activity compared to wild-types at 8 dpf (**Figure 5.22**). Differences in average night activity were also observed at 6 and 7 dpf. Wild-type larvae demonstrated increased locomotor activity at night upon $MnCl_2$ exposure compared to mutant larvae (**Figure 5.23**). Hence, behavioural analysis suggested that *slc30a10^{U800}* larvae were more resistant to Mn toxicity than wild-types. This is consistent with the observation that *slc30a10^{U800}* larvae accumulate lower levels of Mn upon $MnCl_2$ exposure at 5 dpf.

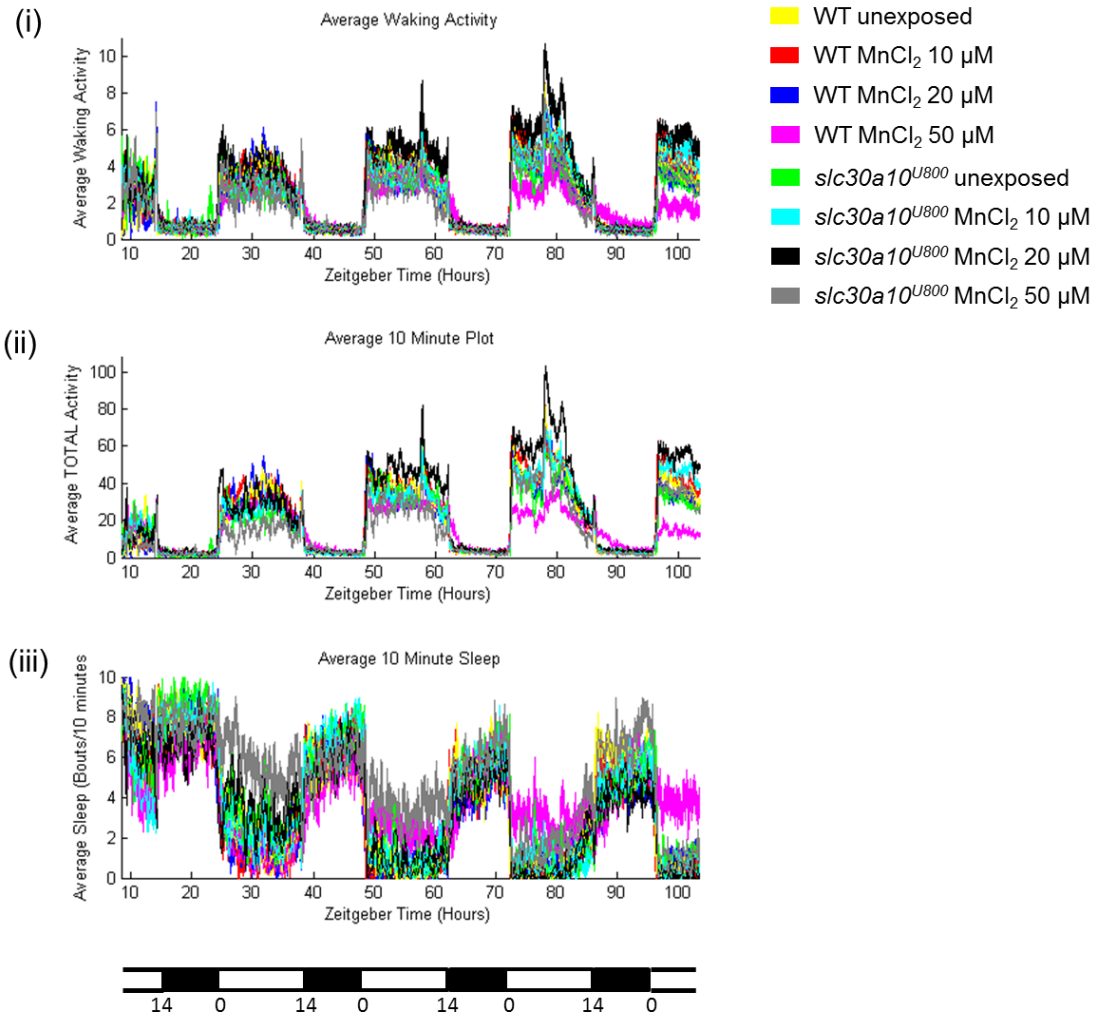

Figure 5.21 *slc30a10^{U800}* larvae are more resistant to $MnCl_2$ expsoure.

Plots of (i) average waking activity, (ii) total activity and (iii) total sleep of wild-type and homozygous slc30a10^{U800} larvae between 4 and 8 dpf in response to MnCl2. Larvae were exposed to increasing doses of $MnCl_2$ (0 to 50 µM) from 2 dpf. The 14:10 hour light:dark cycle is indicated on the bottom. n=12 larvae per condition.

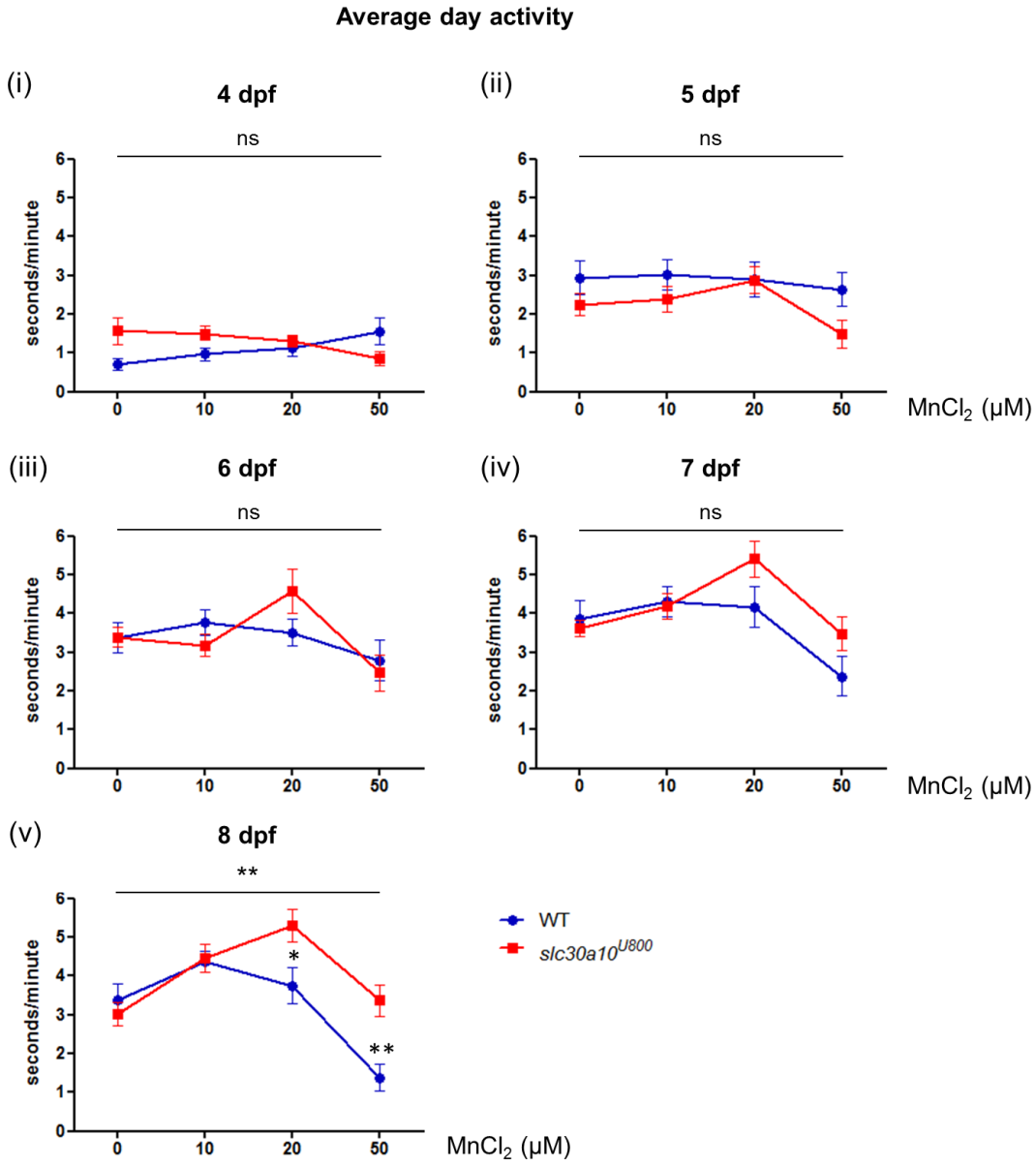

Figure 5.22 Exposure of *slc30a10^{U800}* mutants to $MnCl_2$ leads to a less pronounced decrease in average day activity compared to wild-type fish.

Graphs showing average day activity of larvae exposed to 0 to 50 μM $MnCl_2$ from 2 dpf. Homozygous slc30a10^{U800} larvae in *red and wild-type (WT) larvae in blue. Data are presented as mean ± s.e.m. Statistical analysis was performed using 2 way ANOVA and Bonferroni posttests comparing WT and slc30a10^{U800} larvae (*p<0.05; **p<0.001. n=12 larvae per condition.*

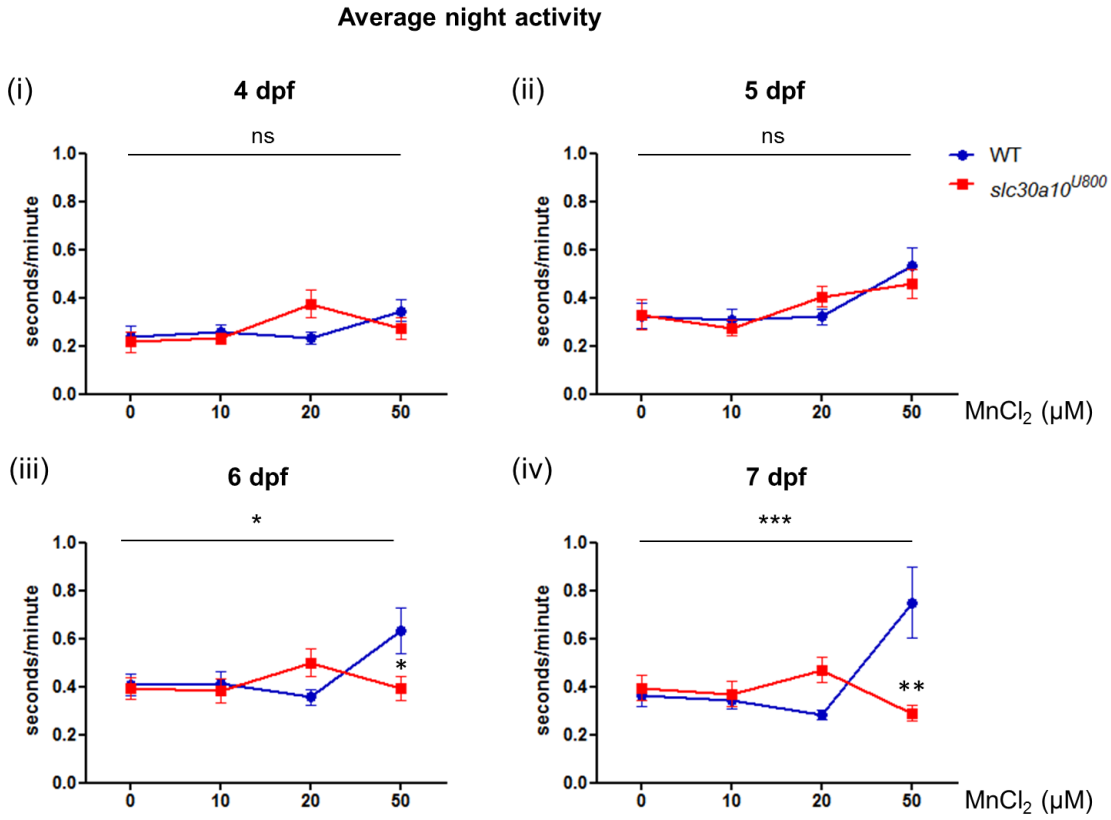

Figure 5.23 Exposure of *slc30a10^{U800}* mutants to $MnCl_2$ leads to a less pronounced increase in average night activity compared to wild-types.

*Graphs showing average night activity of larvae exposed to 0 to 50 μM $MnCl_2$ from 2 dpf. Homozygous slc30a10^{U800} larvae in red and wild-type (WT) larvae in blue. Data are presented as mean ± s.e.m. Statistical analysis was performed using 2 way ANOVA and Bonferroni posttests comparing WT and slc30a10^{U800} larvae. (*p<0.05; **p<0.01, ***p<0.001). n=12 larvae per condition.*

5.5.3 *slc30a10^{U600}* mutants harbouring the p.P240Afs*92 mutation do not show phenotypic differences to *slc30a10^{U800}* mutants

slc30a10^{U600} mutants generated by CRISPR/Cas9 genome editing carry a 5 bp deletion within exon 3 (c.717_721del) causing a frameshift predicted to significantly truncate the protein (p.P240Afs*92) and likely to cause nonsense medicated decay. Observations of an in-cross of heterozygous *slc30a10^{U600}* mutants suggested no phenotypic abnormalities during embryonic and early larval development until 5 dpf when raised under standard conditions. Also, exposure of *slc30a10^{U600}* larvae to 50 µM $MnCl_2$ did not show any gross alterations in their swimming behaviour when observed under a light microscope between 2 and 5 dpf. Given that no obvious phenotypic differences exist between the *slc30a10^{U600}* and *slc30a10^{U800}* mutant no further analysis of the *slc30a10^{U600}* mutant was pursued.

5.6 Discussion

5.6.1 Zebrafish *slc30a10* facilitates Mn export and encodes two transcripts

Overexpression of zebrafish *slc30a10* in pmr1 deficient *S. cerevisiae* clearly demonstrated its ability to protect yeast from Mn toxicity similar to the results seen with human *SLC30A10*[46]. Human SLC30A10 localises to the cell membrane while certain mutant proteins (L89P, 98-134del, 105-107del, T196P, and Q308X) are not trafficked correctly within the cell and become trapped in the ER[47]. SLC30A10 is therefore thought to facilitate the excretion of Mn from the cell. Expressed in liver, intestine and the nervous system it is a crucial regulator of Mn homeostasis facilitating hepatic excretion of Mn into the bile[46,50,92]. In zebrafish *slc30a10* is expressed during embryonic and early larval stages suggesting a crucial role of this transporter during zebrafish development. *In situ* hybridisation showed that *slc30a10* is expressed in the liver, gut and brain of zebrafish larvae. The zebrafish and human protein share 51% sequence homology which is particularly conserved around the six TMDs. It therefore seemed reasonable to conclude that the function of zebrafish *slc30a10* is similar to that in humans and that loss of *slc30a10* function in zebrafish may be a suitable model of Mn toxicity.

Zebrafish *slc30a10* was found to encode two transcripts; one spanning four exons similar to the human gene and at the time the only known transcript, the second one possibly encoding a considerably shortened protein lacking the conserved TMDs. The spatial expression pattern of both transcripts was similar with expression in liver, gut and brain. Given the predicted protein structure it seems unlikely that a protein lacking the conserved TMDs has a similar function to the original transporter protein. It is also possible that this transcript is not translated but has other regulative functions. The TALEN pair used to generate the *slc30a10*^{U800} mutant solely affects transcript 1. In order to leave no doubt a second mutant, *slc30a10*^{U800}*,* was generated targeting exon 3 of *slc30a10* that is shared by both transcripts. However, as this mutant did not show a different phenotype to the *slc30a10*^{U800} mutant it was not further analysed.

5.6.2 *Slc30a10* loss-of-function in zebrafish causes an unexpected phenotype

Given that zebrafish Slc30a10 facilitates Mn detoxification in yeast similar to the human protein, the *slc30a10*^{U800} zebrafish mutant was expected to display Mn accumulation. Indeed, at 14 dpf mutant larvae had significantly higher Mn levels compared to wild-types while at 5 dpf no significant difference was observed. This would suggest that chronic Mn exposure throughout early larval development is required in order to cause any Mn toxicity phenotype in mutant larvae. Under normal husbandry conditions zebrafish larvae are exposed to a small but essential concentration of Mn. Mn is present in the salt mix added to standard fishwater and in the food chain. However, under normal culture conditions *slc30a10*^{U800} mutant zebrafish did not develop any apparent phenotype. They remained healthy and fertile throughout adulthood and showed no locomotor behaviour abnormality.

Surprisingly, additional exposure to $MnCl_2$ (50 µM) between 2 and 5 dpf led to attenuated accumulation of Mn in mutant larvae compared to wild-type fish. Hence, *slc30a10*^{U800} mutants appeared to be more resistant to Mn deposition upon $MnCl_2$ exposure than wild-type larvae. This finding was consistent with the changes in the locomotor behaviour observed upon $MnCl_2$ expsoure. While there was no difference in swimming activity between unexposed mutant and wild-type larvae, $MnCl_2$ exposed *slc30a10*^{U800} mutants were less affected by Mn toxicity; wild-type larvae showed a greater reduction of their locomotor activity than mutants. This finding is indeed puzzling and further work is required to study the function of the zebrafish transporter in more detail. It may be that during early larval development compensatory mechanisms in the mutant larvae allow for the observed unexpected attenuation of Mn toxicity. It will be important to analyse the locomotor behaviour at 14 dpf when Mn accumulation occurs in mutant larvae. It is also plausible that although the human and zebrafish protein appear to have a similar Mn detoxification function *in vitro* additional functions and interactions lead to the observed phenomenon *in vivo*. Although land mammals and fish are both osmoregulatory vertebrates, fish are exposed to much more dramatic osmotic and ionic environmental fluctuations[261]. While many of the transepithelial transport mechanisms are conserved from fish to human it is likely that differences exist in order to maintain the osmotic and ionic balance of aquatic organisms. In fish, the majority of iono- and osmoregulation is carried out by ionocytes in the gills and, during early embryonic development, in the skin, while in mammals the

kidney performs the task of osmoregulation. Although *in situ* hybridisation did not detect signficant mRNA expression of *slc30a10* in skin or gill ionocytes, it is possible that a different subcellular localisation of *slc30a10* or orientation of the transporter in such cells facilitate Mn uptake from the aqueous medium rather than excretion.

Observations of *slc30a10*^{U600} mutants that supposedly lead to loss-of-function of both Slc30a10 isoforms suggest that similar to *slc30a10*^{U800} mutants this mutant line does not develop a Mn toxicity phenotype excluding the possibility that loss of gene function in *slc30a10*^{U800} mutant is rescued by an alternative transcript.

In conclusion, loss of *slc30a10* function in zebrafish does not recapitulate all aspects of the mature human phenotype and further work is required to unravel the mechanisms of early Mn resistance observed in the *slc30a10*^{U800} mutant. Unfortunately, five day *slc30a10*^{U800} mutants do not provide a disease model of SLC30A10 deficiency that would allow drug screening.

Chapter 6. CRISPR genome editing to generate a *slc39a14* loss-of-function mutant

6.1 Introduction

In **Chapter 4** it is described how SLC39A14 was identified as a crucial Mn transporter required for the maintenance of Mn homeostasis in humans. Homozygous mutations in this gene in a cohort of nine patients led to extensive Mn neurotoxicity associated with parkinsonism-dystonia. Until this study, there had been considerable uncertainty to the metal specificity of this transporter; SLC39A14 was shown to transport a range of metals *in vitro* including Zn, Fe, Mn and Cd[72,233,241]. In order to confirm that loss of *slc39a14* function causes Mn dyshomeostasis, a zebrafish loss-of-function mutant was generated using CRISPR/Cas9 genome editing with the view to study disease mechanisms, identify novel therapeutic targets and provide a vertebrate model for drug screening.

6.2 Characterisation of the *slc39a14* orthologue in zebrafish

6.2.1 Temporal expression and sequence verification of zebrafish *slc39a14*

Prior to generating a loss-of-function mutant it was essential to characterise the *slc39a14* gene in zebrafish to confirm correct gene annotation and ensure that gene expression occurs during the first five days of development when analysis of the mutant would take place. Similar to studies characterising *slc30a10* (**Section 5.2**) *slc39a14* expression was analysed between 3 and 120 hpf by RT-PCR. The primers used amplified a 240 bp region spanning exon 3 to 5 and detecting all *slc39a14* transcripts (**Section 2.3.6**). *slc39a14* expression was evident at all stages of embryonic and early larval development suggesting that this transporter is utilised during early zebrafish development (**Figure 6.1**).

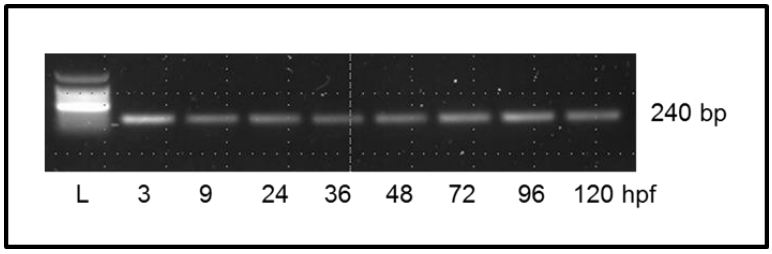

Figure 6.1 *slc39a14* is expressed during embryonic and early larval development of zebrafish between 3 and 120 hpf.

Gel electrophoresis image of RT-PCR amplicons of the expected size of 240 bp. L, 100 bp ladder (Promega).

Because the zebrafish *slc39a14* gene was poorly annotated in the literature, five and three prime rapid amplification of cDNA ends (5' and 3' RACE) was performed to identify all *slc39a14* transcripts expressed in zebrafish (**Section 2.3.16**). Similar to human *SLC39A14* an alternative fourth and ninth exon and, additionally, an alternative eighth exon encode four splice isoforms in zebrafish (**Figure 6.2**).

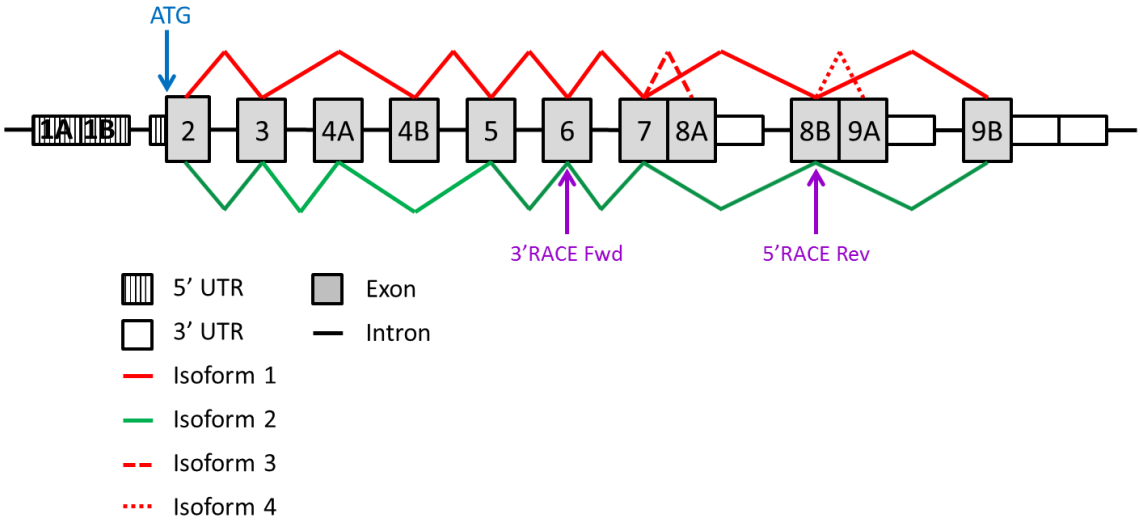

Figure 6.2 Zebrafish *slc39a14* encodes four isoforms.

Schematic showing the transcripts identified by 5' and 3' RACE using RNA extracted from zebrafish larvae at 3 dpf. Isoform 1 (red) and 2 (blue) are encoded by an alternatively spliced exon four. Isoform 3 (dotted red) is encoded by an alternative ninth exon and 3' UTR. Isoform 4 (dashed red) is encoded by a shorter transcript with only eight exons (not drawn to scale). Positions of primers used for 5' and 3' RACE are indicated in purple. Not drawn to scale.

The sequence homology between the human and zebrafish Slc39a14 protein was analysed using UniProt software (**Section 2.3.2**) and both proteins were shown to share high sequence homology; 62 percent of amino acid residues are identical. The eight transmembrane domains, the histidine-rich region and the metal binding motif (**Section 4.3.1**) are almost completely identical between human and zebrafish suggesting shared function (**Figure 6.3**).

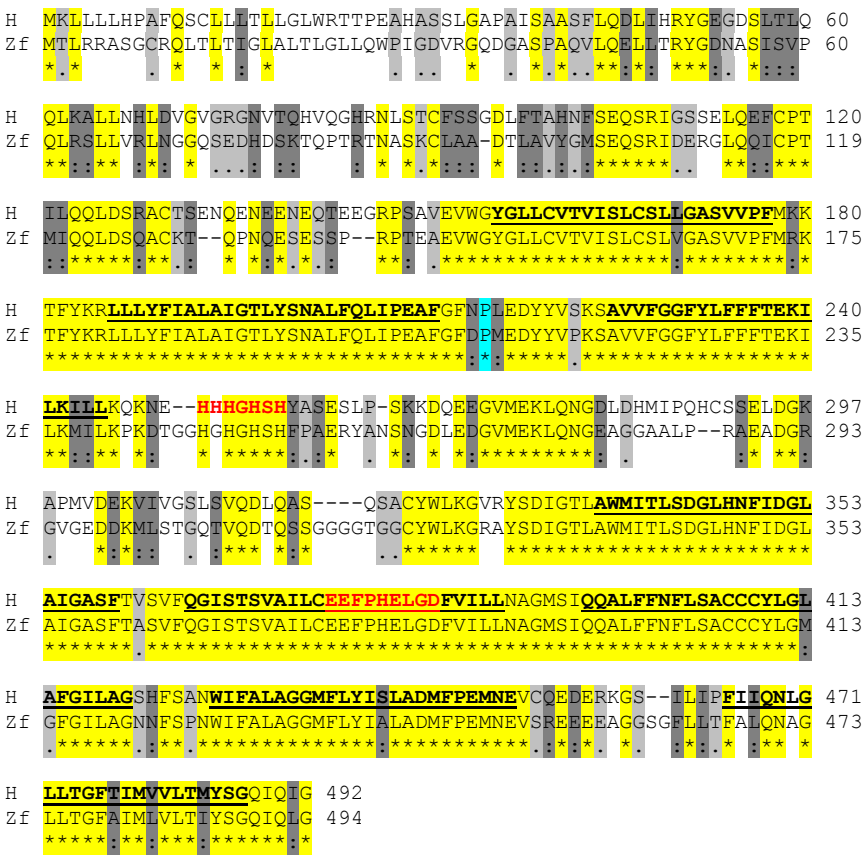

Figure 6.3 Zebrafish Slc39a14 shares 62 percent sequence identity with human SLC39A14.

*Sequence alignment of the human (XP_001340102.4) and zebrafish (NP_001121903.1) SLC39A14 protein sequence (isoform 1). Residues identical to the human SLC39A14 sequence are marked in yellow with an asterisk (*). Conservation between amino acids of strongly and weakly similar properties is indicated by a colon (: dark grey) and a period (. light grey), respectively. The putative TMDs are underlined. The histidine-rich region and the LZT consensus motif are highlighted in red. The position of the CRISPR induced deletion is indicated in turquoise (**Section 6.3.1**). H, human. Zf, zebrafish.*

6.2.2 Spatial expression of zebrafish *slc39a14*

To analyse whether *slc39a14* expression is similar to that of the human orthologue, whole mount *in situ* hybridisation was performed using a DIG labelled antisense RNA probe of 979 bp to *slc39a14* spanning a region from the fourth to ninth exon in order to assess the spatial expression pattern (**Section 2.4.5**). *slc39a14* expression was observed in the convoluted and straight part of the proximal pronephric ducts from as early as 2 dpf (**Figure 6.4**). In contrast to mature human tissues, no significant expression was detected in the brain, liver or intestine.

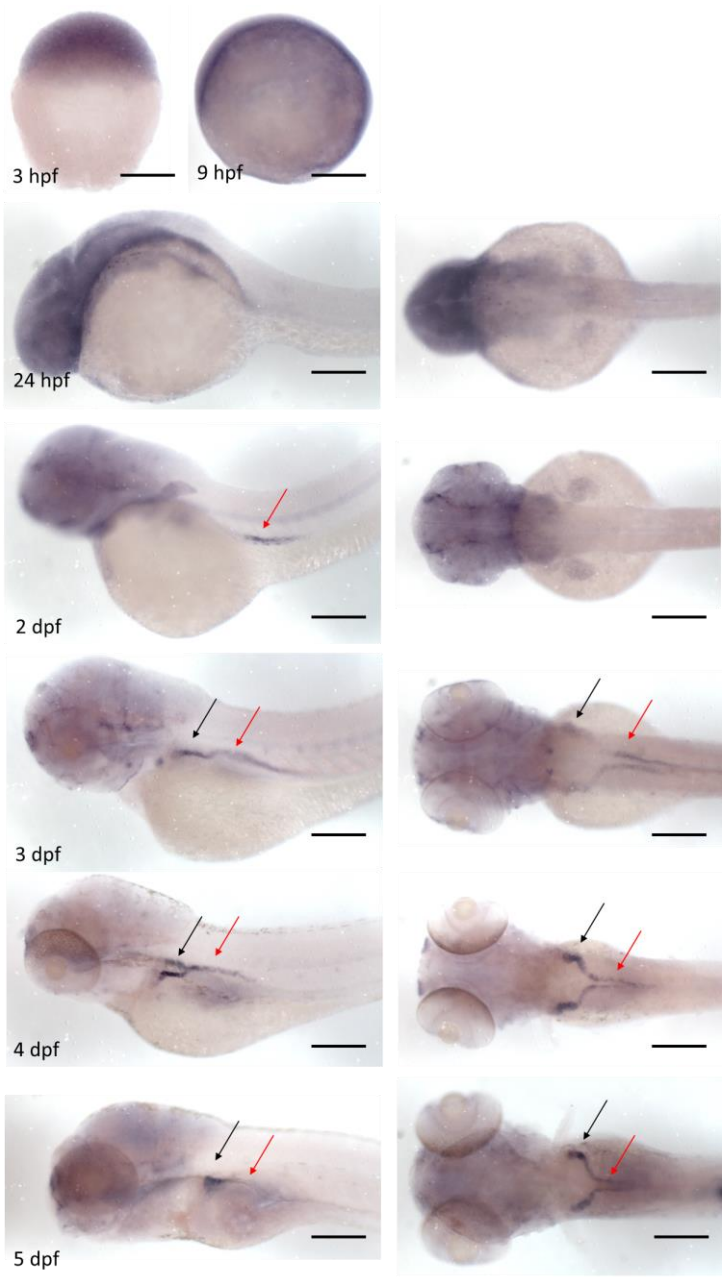

Figure 6.4 Spatial expression of *slc39a14* in zebrafish during 3 hpf and 5 dpf.
Light microscope images of whole mount in situ hybridisation of slc39a14. Convoluted and straight proximal pronephric ducts are indicated by black and red arrows, respectively. Scale bar 200 µm.

The spatial distribution of *slc39a14* was further confirmed in sections of larvae at 5 dpf following *in situ* hybridisation (**Figure 6.5, Section 2.4.6**).

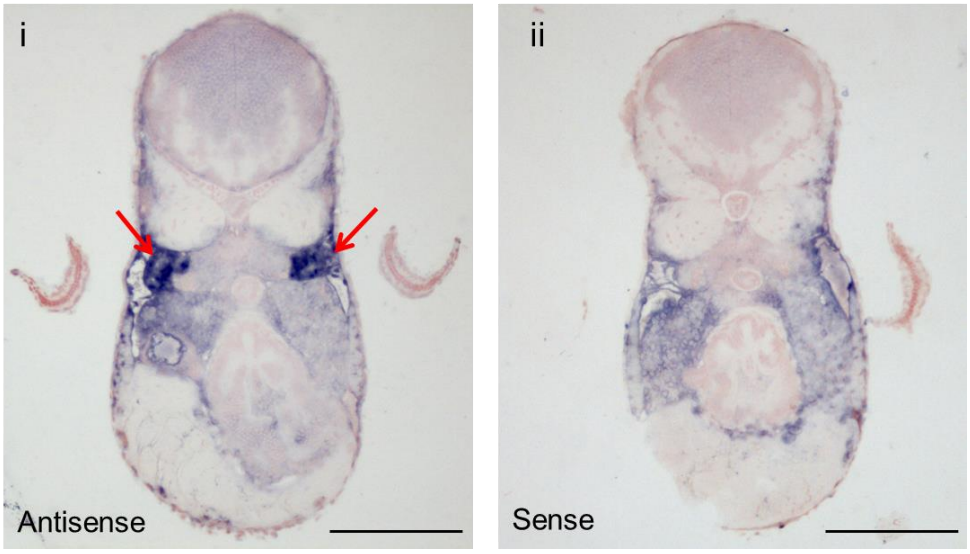

Figure 6.5 *slc39a14* is prominently expressed in the pronephric ducts of zebrafish larvae at 5 dpf.
*Light microscope images of whole mount in situ hybridisation sections of 10 µm thickness using a (**i**) antisense and (**ii**) sense probe (negative control) to slc39a14. Positive staining indicated by red arrows.*

6.3 CRISPR genome editing to generate a zebrafish *slc39a14* null mutant

6.3.1 Generation of a *slc39a14* loss-of-function mutant using CRISPR/Cas9 targeting exon 5

To assess if loss of *slc39a14* gene function leads to Mn dyshomeostasis *in vivo*, a zebrafish mutant carrying *slc39a14* null mutations was generated using CRISPR/Cas9 genome editing (**Section 2.3.18**). Given that *slc39a14* is expressed in zebrafish throughout embryonic and early larval development and that the protein is highly conserved with the human sequence (**Section 6.2**), it was reasonable to assume that loss of gene function may lead to a similar phenotype in zebrafish mutants as observed in humans with *SLC39A14* mutations. A gRNA was designed to target a conserved

region within exon 5 that is shared by all four transcripts identified using 5' and 3' RACE (**Section 6.2.1** and **Figure 6.2**). Following co-injection of the gRNA and Cas9 mRNA into one cell stage embryos the rate of somatic mutagenesis was determined in healthy looking, injected embryos at 24 hpf using HRMA (**Section 2.3.19**). All injected embryos showed a change in the melt curve shape confirming a high mutagenic efficiency of the generated gRNA/Cas9 complex. Eight amplicons with shifted melt peaks were cloned into the pCRII-TOPO vector for sequencing (**Section 2.3.9**). Sequencing identified a range of frameshifts causing indel mutations that were predicted to be deleterious for protein function (**Figure 6.6**).

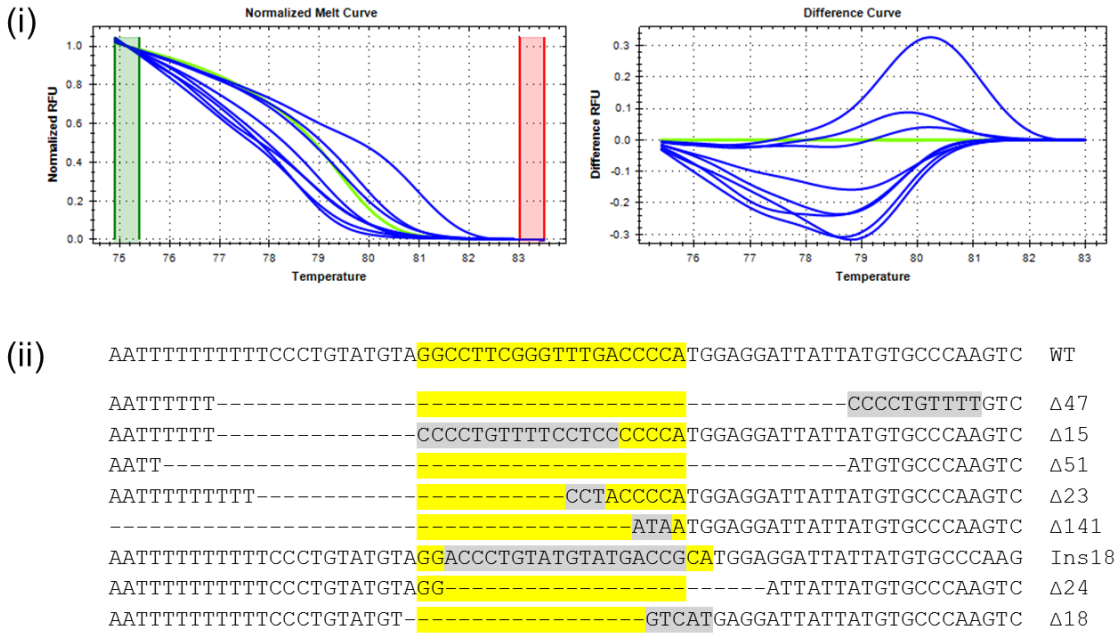

Figure 6.6 Mutagenesis induced by a gRNA/Cas9 to exon 5 of *slc39a14*.

*(**i**) HRMA result of injected (blue), and un-injected wild-type F0 embryos (green). Each melt curve represents a single embryo. Normalised melt curve (left) and difference plot (right) were generated using Biorad Precision Melt Analysis Software. (**ii**) Schematic of the CRISPR target region (yellow) and Indel mutations identified in injected F0 embryos. Wild-type (WT) sequence in the top row, mutations below. (−) deleted nucleotide, insertions in grey, (Δ) number of deleted nucleotides.*

The remaining healthy looking injected F0 embryos were raised to adulthood and outcrossed to a wild-type AB strain. The resulting F1 progeny of eight F0 fish were screened by HRMA at 1 dpf to identify founder fish with heritable mutations. All eight

F0 fish transmitted mutations to the progeny in a high fraction of embryos. In total, 110 out of 151 (73%) analysed embryos screened postive for a mutation (**Figure 6.7**).

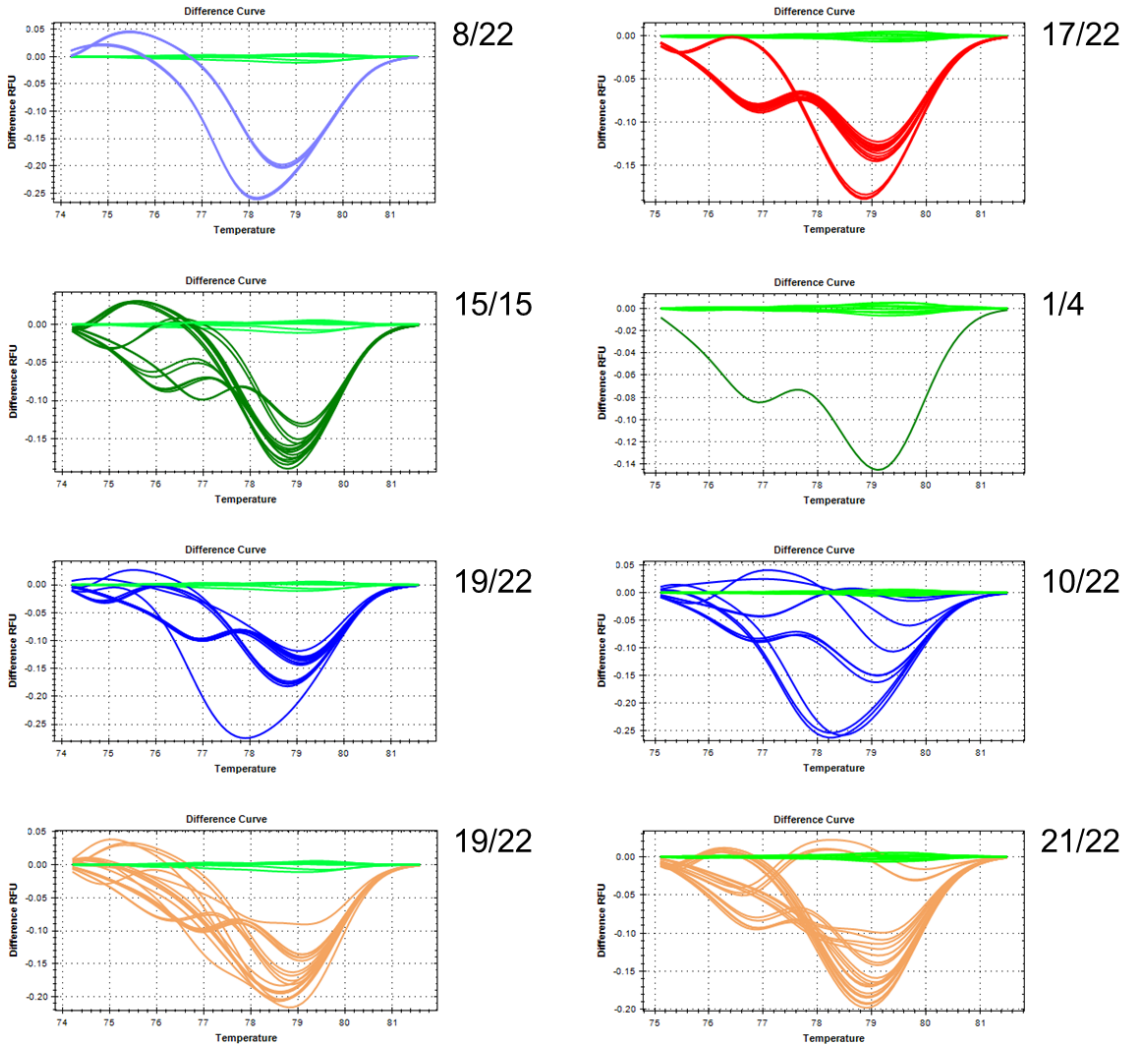

Figure 6.7 Difference curves from HRMA showing that F0 fish have a high germline transmission rate of CRISPR/Cas9 induced mutations.

HRMA results of the progeny (F1) of an outcross of eight injected F0 fish. Each difference curve represents the progeny from one founder fish. Un-injected wild-type control embryos in light green. The number of positive embryos (shifted melt curve) is given next to each difference plot.

F1 embryos from the identified founder fish were raised to adulthood and adult F1 fish again screened by HRMA. Six amplicons with shifted melt peaks were cloned into the pCRII-TOPO vector and sequenced (**Section 2.3.9.**). Several indel mutations were

identified (**Figure 6.8**). An adult F1 carrier fish with a frameshift mutation predicted to cause significant truncation of the protein caused by a 2 bp deletion within exon 5 (c.629_630del, p.P210Hfs*48) was out-crossed to wild-type fish to generate a stable mutant line (*slc39a14*^{U801}).

```
cctgtatgtagGCCTTCGGGTTTGACCCCATGGAGGATTATTATGTGCCCAA WT
cctgtatgtagGCCTTCGGGTTTGACCC-ATGGAGGATTATTATGTGCCCAA Δ1
cctgtatgtagGCCTTCGGGTTTGACC--ATGGAGGATTATTATGTGCCCAA Δ2
cctgtatgtagGCCTTCGGGTTT----CCATGGAGGATTATTATGTGCCCAA Δ4
cctgtatgtagGCCTTCGGGTTT--------GAGGATTATTATGTGCCCAA Δ9
cctgtatgtagGCCTTCGGGTTTGA-----------TTATGTGCCCAA Δ15
cctgtatgtagGCCTTCGGGTTTGAGAGGATTAATAATCCATGGAGGATTAT Δ2, Ins13
```

Figure 6.8 Frameshift Indel mutations identified in the F1 generation.
Schematic showing the wild-type (WT) sequence in the top row and the introduced mutations below. CRISPR target region in yellow, (−) deleted nucleotide, insertions in grey, (Δ) number of deleted nucleotides. slc39a14^{U801} *mutant highlighted in red.*

Because an antibody to zebrafish Slc39a14 is not available to assess protein expression in the generated mutant, qRT-PCR was used to confirm that the introduced mutation had an effect on transcript processing (**Section 2.3.7**). *slc39a14* mRNA expression in homozygous *slc39a14*^{U801} mutants was reduced 2.2 fold suggesting nonsense mediated decay of the mutant transcripts and likely loss of protein function (**Figure 6.9**).

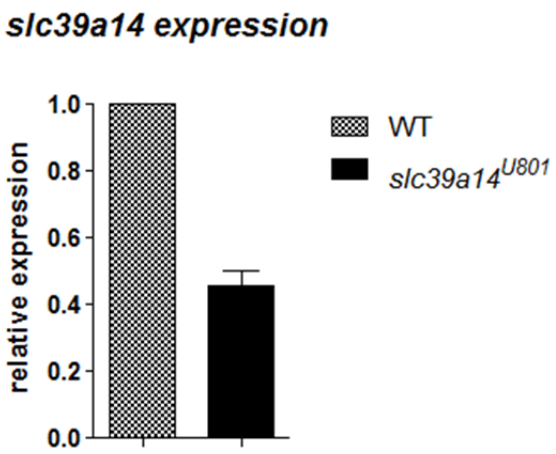

Figure 6.9 *slc39a14* transcript levels are reduced in homozygous *slc39a14*^{U801} mutants.
Graph showing slc39a14 transcript levels of wild-type (WT) and mutant larvae. Data are presented as means ± s.d. from three independent experiments. Statistical analysis was performed using Student's two tailed t test on individual ΔCt values (p=0.012).

6.4 Phenotypic characterisation of *slc39a14^{U801}* mutants

Homozygous *slc39a14^{U801}* mutants harbouring the *c.629_630del* (p.P210Hfs*48) mutation (**Section 6.3.1**) did not display an apparent phenotype when raised under standard conditions. They did not show obvious morphological abnormalities or developmental defects and had normal survival during embryonic and early larval development. They survived into adulthood with normal fertility. However, exposure to raised environmental Mn levels above the physiological amounts present in the food chain and fishwater triggered a distinct phenotype of motor and vision impairment.

6.4.1 *slc39a14^{U801}* mutants accumulate high levels of Mn and are sensitive to Mn toxicity

ICP-MS analysis was used to determine metal levels in homozygous *slc39a14^{U801}* and wild-type larvae (**Materials and Methods 2.5.2**). Homozygous *slc39a14^{U801}* mutants raised in fish water without additional Mn exposure showed a 35% increase in Mn levels at 5 dpf and a 72% increase at 14 dpf confirming a crucial role for Slc39a14 in Mn clearance (**Figure 6.10**).

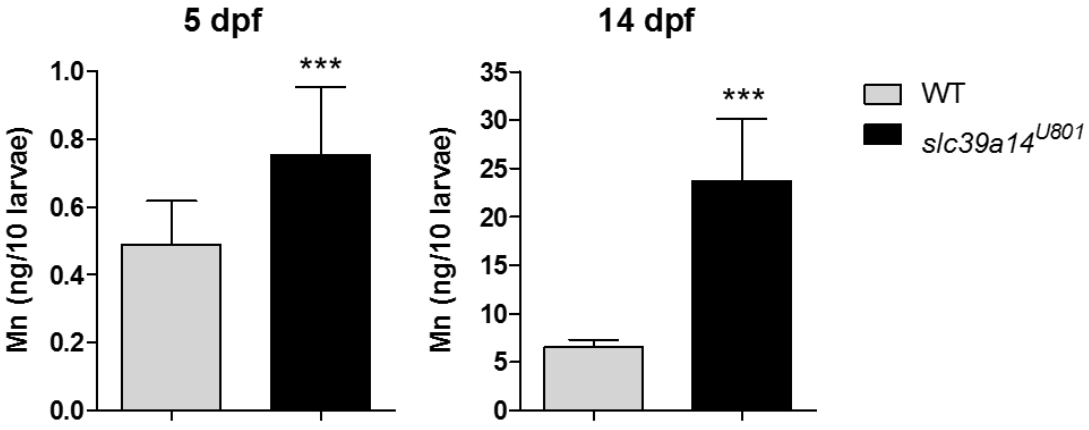

Figure 6.10 Homozygous *slc39a14^{U801}* larvae show increased Mn levels at 5 and 14 dpf.

*Graph showing Mn levels measured by ICP-MS from pools of 10 larvae at 5 dpf (p=0.001) and 14 dpf (p=0.0002). Data are presented as means ± s.d. from a minimum of five independent experiments. Statistical analysis was performed using Student's two tailed t test (***p<0.001).*

On the other hand, other previously reported substrates of the transporter[69,70,72,230-237,241] including Fe, Zn and Cd, remained unchanged at 5 and 14 dpf (**Figure 6.11**).

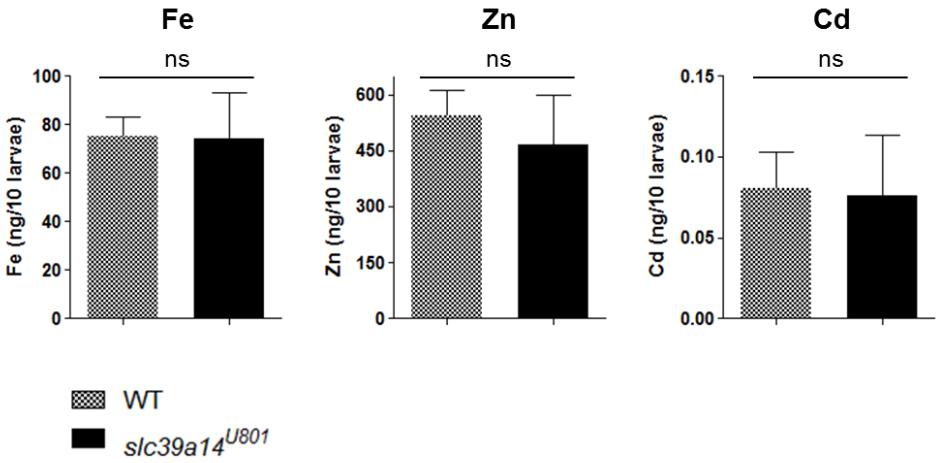

Figure 6.11 Fe, Zn and Cd levels in 14 dpf mutant larvae are similar to those of wild-types.

Graph showing Fe, Zn and Cd levels measured by ICP-MS from pools of 10 larvae of 10 homozygous slc39a14^{U801} or wild-type (WT) larvae at 14 dpf. Data are presented as means ± s.d. from five independent experiments. Statistical analysis was performed using Student's two tailed t test (ns, not significant. p=0.9 [Fe], 0.26 [Zn], 0.83 [Cd]).

To exclude that differences in size accounted for the observed difference in Mn levels, larval length was determined at 14 dpf in mutant and wild-type larvae. No difference in size was detected between mutant and wild-type larvae (**Figure 6.12**).

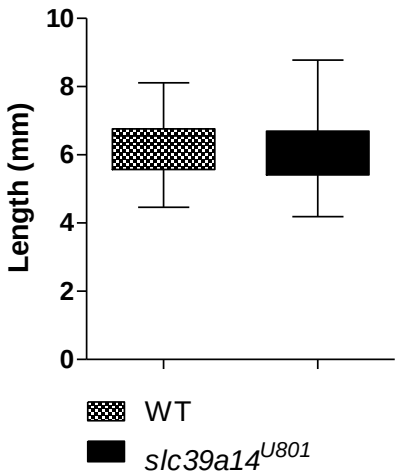

Figure 6.12 Homozygous *slc39a14^{U801}* mutants do not show differences in size compared to wild-type siblings.

Graph showing the average length of wild-type (WT) and slc39a14^{U801} larvae at 14 dpf. The box and whisker plots indicate the 25th and 75th percentile, and the minimum and maximum length, respectively. Statistical analysis was performed using Student's t test (p=0.061). n=56.

Despite the observed abnormality of Mn levels under standard husbandry conditions, *slc39a14*^{U801} mutants survived into adulthood without any obvious morphological or developmental defects. However, exposure to sublethal $MnCl_2$ concentration (20 to 50 µM) from 2 to 5 dpf led to a much greater accumulation of Mn in homozygous *slc39a14*^{U801} mutants compared to wild-types at 5 dpf (**Figure 6.13**). Observations under a light microscope showed that this was accompanied by reduced spontaneous swimming with some larvae floating on their side and delayed swim bladder development. Wild-type larvae on the other hand appeared unaffected.

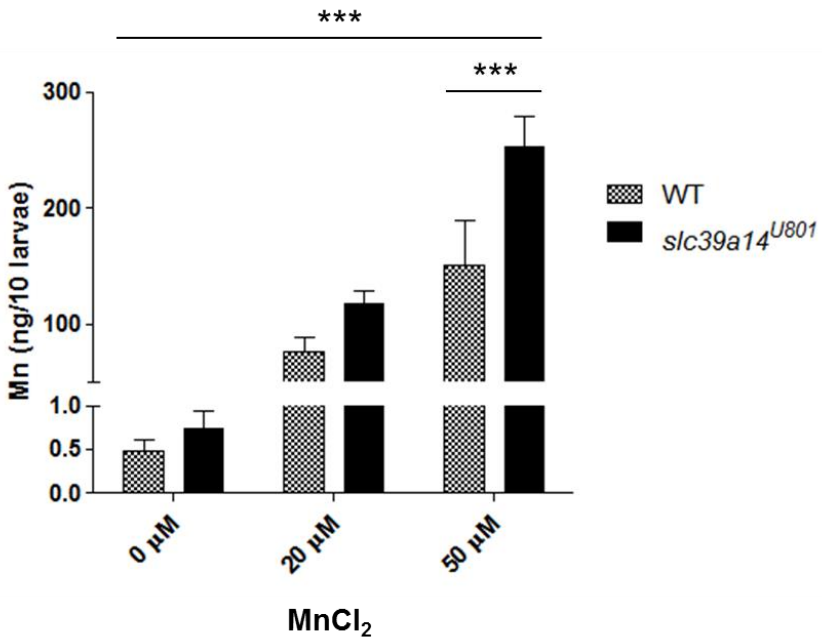

Figure 6.13 Mn exposure leads to greater Mn accumulation in *slc39a14*^{U801} mutants compared to wild-type larvae.

Graph showing Mn levels in homozygous slc39a14^{U801} *and wild-type (WT) larvae exposed to increasing concentrations of* $MnCl_2$ *(0 – 50 µM) from 2 dpf. Mn levels were determined in pools of 10 larvae at 5 dpf. Data are presented as means ± s.d. from three independent experiments. Statistical analysis was performed using 2 way ANOVA (p<0.0001) and Bonferroni posttests comparing slc39a14*^{U801} *versus wild-type larvae (**p<0.01, ***p<0.001).*

To assess whether the observed increased accumulation of Mn upon $MnCl_2$ exposure in mutants was accompanied by increased sensitivity to Mn-induced toxicity, homozygous *slc39a14*^{U801} mutants and wild-type larvae were exposed to a range of $MnCl_2$ concentrations (0-1.5 mM) during 2 and 5 dpf. The number of dead larvae was counted at 5 dpf (**Section 2.4.4**). Indeed, the median lethal concentration (LC_{50}) of $MnCl_2$ determined by Probit analysis (**Section 2.7**) was significantly lower for mutant (376.3 µM) compared to wild-type larvae (680.5 µM) (**Figure 6.14**). Analysis of the relative median potency of $MnCl_2$ (1.75, 95% confidence interval 1.2 to 2.9) suggested $MnCl_2$ to be 1.75 times more lethal for mutant than for wild-type larvae (**Figure 6.15**).

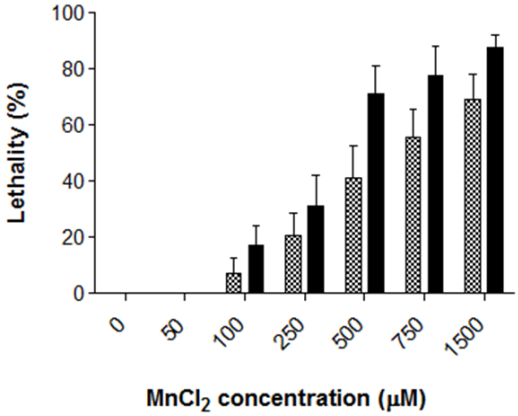

	LC_{50} (µM)	95% CI
WT	680.5	540.0-906.2
slc39a14^{U801}	376.3	299.7-473.3

Figure 6.14 $MnCl_2$ associated lethality is higher in *slc39a14*^{U801} mutants compared to wild-type larvae.

Graph showing the lethality (%) upon $MnCl_2$ exposure and the LC_{50} of $MnCl_2$ of wild-type (WT) and mutant larvae. CI, confidence interval. Data are presented as means ± s.e.m. from nine independent experiments.

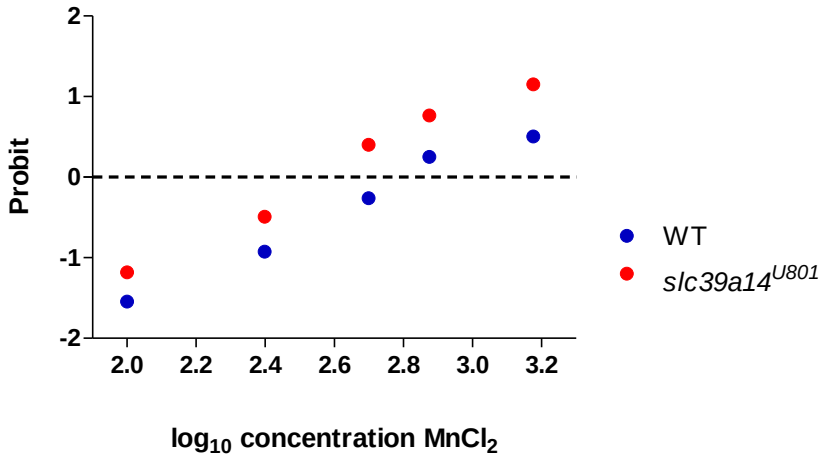

Figure 6.15 Homozygous *slc39a14*^{U801} mutants are more sensitive to $MnCl_2$ toxicity compared to wild-type larvae.

Graph showing the dose-response curves for wild-type (red) and mutant (blue) larvae determined by Probit analysis using IBM SPSS Statistics package version 21. The logarithmic concentration of $MnCl_2$ (x-axis) is plotted against the determined Probit (probability unit, y-axis). The Probit of 0 is used to determine the LC_{50} concentration.

6.4.2 Mn accumulates in the brain of *slc39a14*^{U801} mutants and causes transcriptional changes.

Several methods were used to try and determine the distribution of Mn deposition but failed to reliably visualise Mn in *slc39a14*^{U801} mutants (data not shown). Rhodanine, a Cu stain, has previously been suggested to stain Mn in liver sections from patients with SLC30A10 deficiency[50]. However, brain sections from *slc39a14*^{U801} mutants at 14 dpf exposed to high doses of $MnCl_2$ (250 µM for 24 hours) did not show positive Rhodanine staining while a liver control sample from a patient with Wilson's disease demonstrated the typical pattern of Rhodanine positive Cu deposition. There may be various explanations for this observation. It is possible that the fixation process leads to leakage of Mn from larval zebrafish sections. Alternatively, the positive staining in patients with SLC30A10 deficiency may not be due to Mn accumulation but that of Cu instead. Several patients with SLC30A10 deficiency have been reported to have raised hepatic Cu levels[50,210].

While laser absorption ICP-MS has been successfully used to study the uptake of Mn in *C. elegans*[262], this technique did not detect Mn in larval cryosections of *slc39a14*^{U801} zebrafish mutants at 14 dpf. This work was performed by Dr Alaa Abdul-Sada at Sussex University.

MR microhistology reliably visualises brain tissue substructures of mouse embryos using a Mn contrast agent[263]. Therefore, it was plausible that this technique may also visualise Mn accumulation in adult *slc39a14*^{U801} zebrafish mutants. Prof Mark Lythgoe at the UCL Centre for Advanced Biomedical Imaging kindly analysed *slc39a14*^{U801} zebrafish mutants, however, no differences between wild-type and mutant zebrafish could be detected.

Fura-2 has been used to indirectly measure total cellular Mn content via its quenching of fura-2 fluorescence by Mn[264]. However, live imaging of brain ventricle injected larvae at 5 dpf again did not show differences in fluorescence between wild-type and mutant zebrafish.

To determine whether the brain was the primary site of Mn deposition similar to that in humans Mn levels were measured by ICP-MS in tissues dissected from adult *slc39a14*^{U801} mutants (**Section 2.5.3**). Initial attempts on single organs dissected from adult zebrafish at 4 months of age that were freeze-dried proved unreliable with results at the lower threshold of detection for Mn. Next, fresh tissues (brains or abdominal organs) from four adult wild-type or mutant zebrafish at one year of age were pooled as one sample and analysed by ICP-MS. Because of the small size of the abdominal organs, intestine, liver, pancreas and spleen were pooled and analysed together. This allowed reliable measurement of Mn concentrations. Mn levels were 8 times higher in brains from homozygous *slc39a14*^{U801} mutants compared to wild-types whilst no difference in the Mn content of abdominal viscera was detected (**Figure 6.16**). While Mn estimation in brain tissues proved reproducible with high statistical significance, the Mn assay of pooled abdominal tissues has its limitations. Due to the high standard deviation and nature of the assay analysing pooled tissues, differences in metal concentrations of individual organs may be missed. In order to make an accurate conclusion, single organs will need to be analysed and Mn levels corrected for weight and size of the tissues.

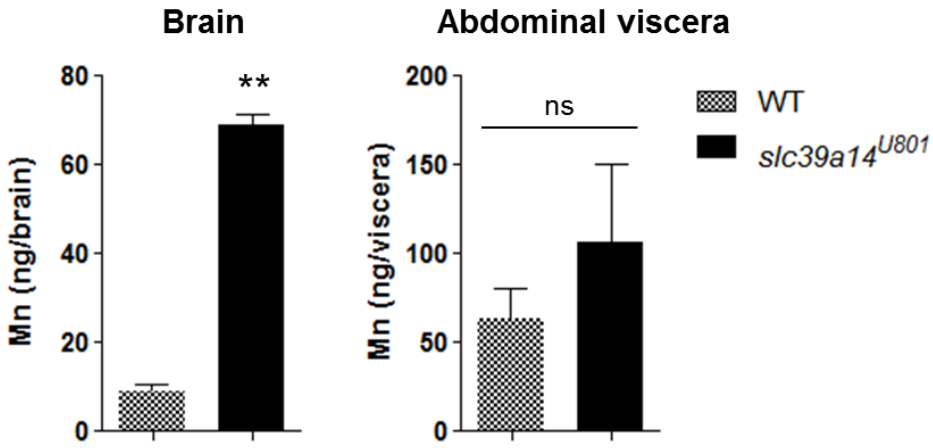

Figure 6.16 Mn deposition occurs in the brain of *slc39a14*^{U801} mutants.

Graph showing Mn levels in brain and abdominal viscera of wild-type (WT) and homozygous slc39a14^{U801} *zebrafish at one year of age. Data are presented as means ± s.d. from two independent experiments in which four brains/abdominal viscera were pooled as one sample. Statistical analysis was performed using Student's two tailed t test (**p<0.01; ns, not significant; p=0.001 [brain]; p=0.116 [abdominal viscera]).*

Other metal levels including Fe, Zn and Cd were unchanged in mutant brain tissue. However, there was a small increase in Fe levels in abdominal viscera of *slc39a14*^{U801} mutants (**Figure 6.17**). Thus, the brain represents the main organ of Mn deposition in mutant zebrafish similar to observations in humans.

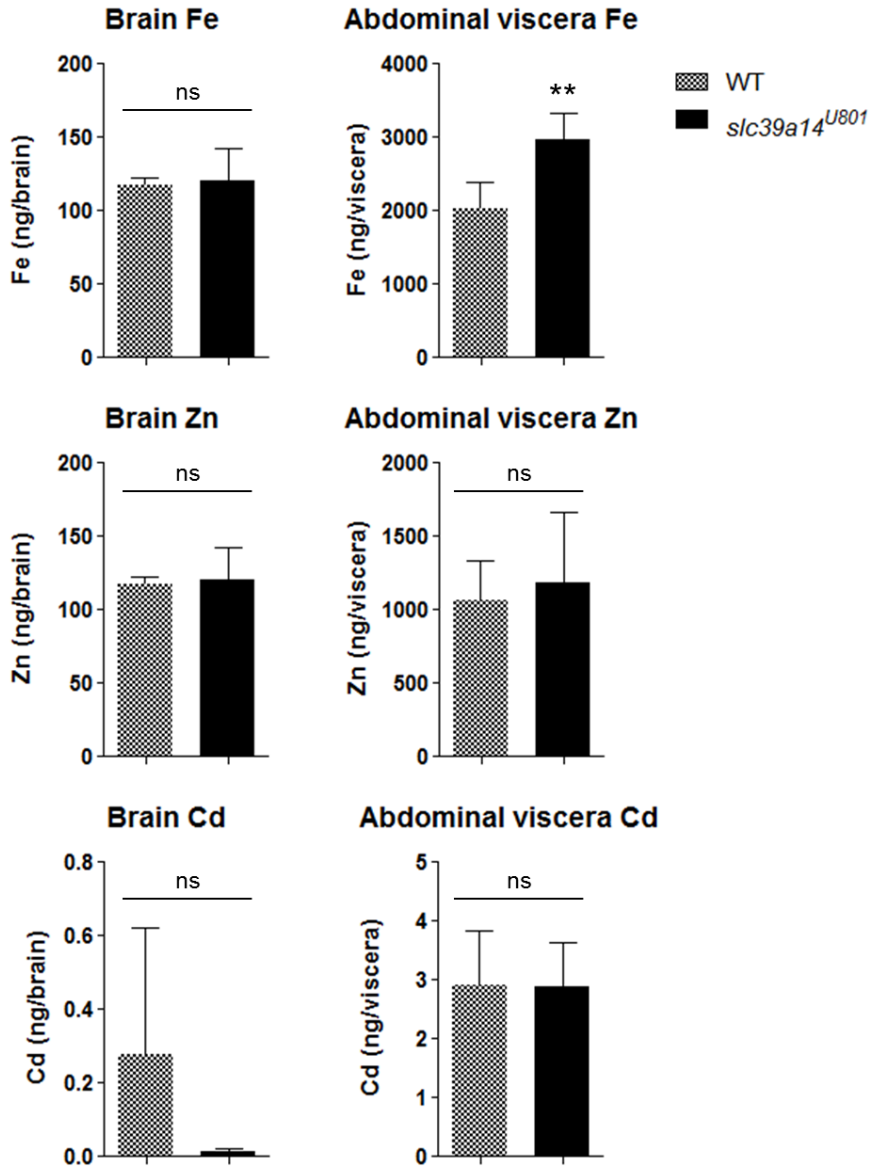

Figure 6.17 Analysis of Fe, Zn and Cd levels in brain tissues and abdominal viscera of wild-type and *slc39a14*^{U801} mutant zebrafish.

Graphs showing Fe, Zn and Cd levels of wild-type (WT) and slc39a14^{U801} *mutant zebrafish at 1 year of age in the brain (p=0.88 [Fe], p=0.74 [Zn], p=0.4 [Cd]) and abdominal viscera (p=0.0037 [Fe], p=0.66 [Zn], p=0.96 [Cd]). Data are presented as means ± s.d. from two independent experiments in which four brains/abdominal viscera were pooled as one sample. Statistical analysis was performed using Student's two tailed t test (**p<0.01; ns, not significant).*

To assess whether loss of Slc39a14 function and cerebral Mn deposition leads to differential expression of other Mn uptake transporter genes, transcript levels of transferrin receptor 1 (*tfr1a*, *tfr1b*), *DMT1* and *slc39a8* were compared between one year old mutant and wild-type adult brains and whole larvae at 5 dpf using qPCR (**Figure 6.18, Section 2.3.7**). Experiments were performed together with Dr Leonardo Valdivia who completed the qPCR analysis. *tfr1b* expression under physiological husbandry conditions was reduced in *slc39a14*^{U801} mutant adult brain (p=0.005) while there was no change for *tfr1a*, *DMT1* and *slc39a8* expression (**Figure 6.18a**). No changes were seen in $MnCl_2$ unexposed mutant larvae at 5 dpf (**Figure 6.18b**). Mn exposure (50µM $MnCl_2$ from 2 to 5 dpf) of zebrafish larvae lead to upregulation of *tfr1b* expression in both wild-type (p=0.042) (**Figure 6.18c**) and mutant zebrafish (p=0.038) at 5 dpf while *slc39a8* transcript levels were reduced in mutant larvae only (p=0.049) (**Figure 6.18d**). These results suggest that *tfr1b* and *slc39a8* are indeed involved in the regulation of Mn homeostasis, probably with different roles within different tissues.

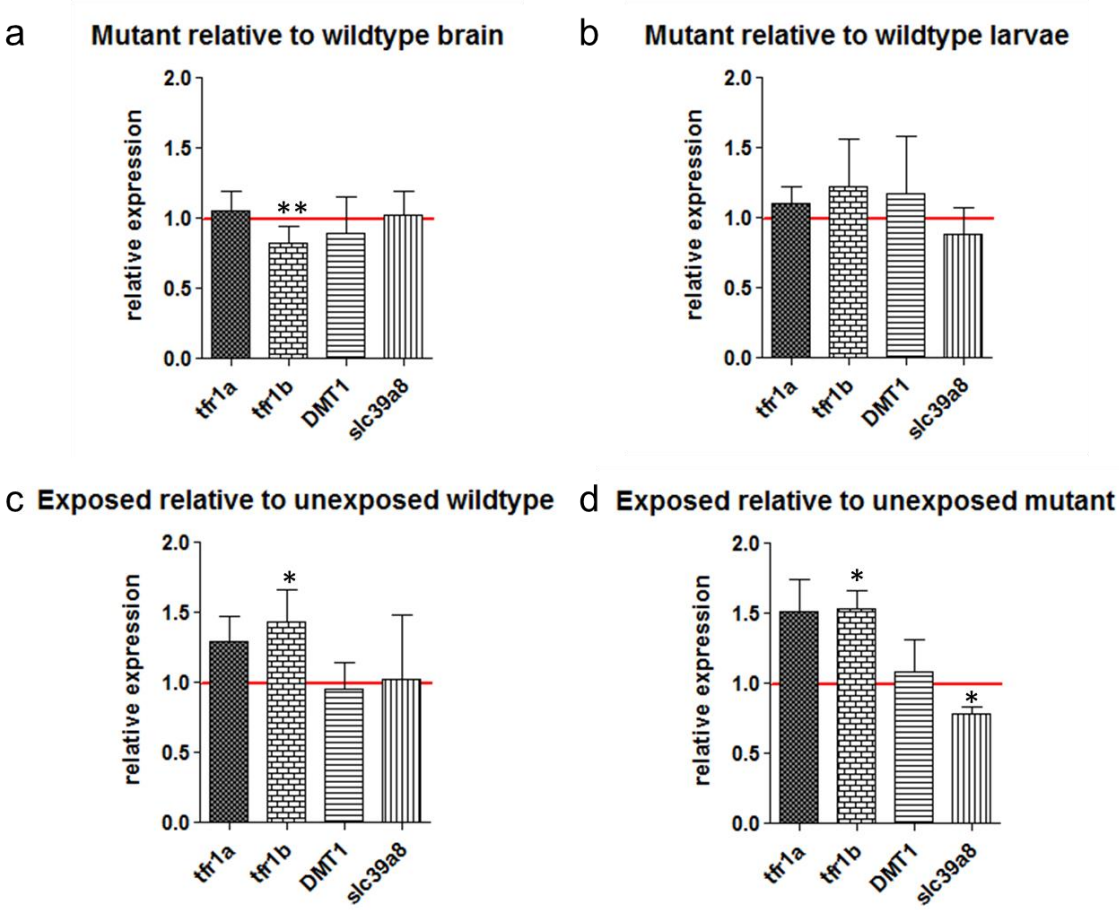

Figure 6.18 Mn uptake transporter gene expression (*tfr1a*, *tfr1b*, *DMT1*, *slc39a8*) in homozygous *slc39a14*^{U801} mutants and wild-type zebrafish.

*Graph showing the changes in tfr1a, tfr1b, DMT1 and slc39a8 gene expression in (**a**) slc39a14*^{U801} *mutant relative to wild-type brains dissected from zebrafish at one year of age, (**b**) mutant relative to wild-type larvae at 5 dpf (**c**) Mn exposed (50µM* $MnCl_2$ *from 2 to 5 dpf) relative to unexposed wild-type larvae at 5 dpf and (**d**) Mn exposed (50µM* $MnCl_2$ *from 2 to 5 dpf) relative to unexposed slc39a14*^{U801} *larvae at 5 dpf. Data are presented as means ± s.d. from three independent experiments. Statistical analysis was performed using Student's two tailed t test on individual ΔCt values (*p<0.05, **p<0.01).*

6.4.3 *slc39a14*^{U801} mutants show altered locomotor activity

The locomotor activity of wild-type and mutant *slc39a14*^{U801} larvae was analysed as described for *slc30a10*^{U800} mutants in **Section 5.5.2**. Analysis of larvae from a heterozygous in-cross of *slc39a14*^{U801} zebrafish raised in standard fishwater confirmed that there are no differences in locomotor activity between mutant and wild-type larvae under normal husbandry conditions (**Figure 6.19**).

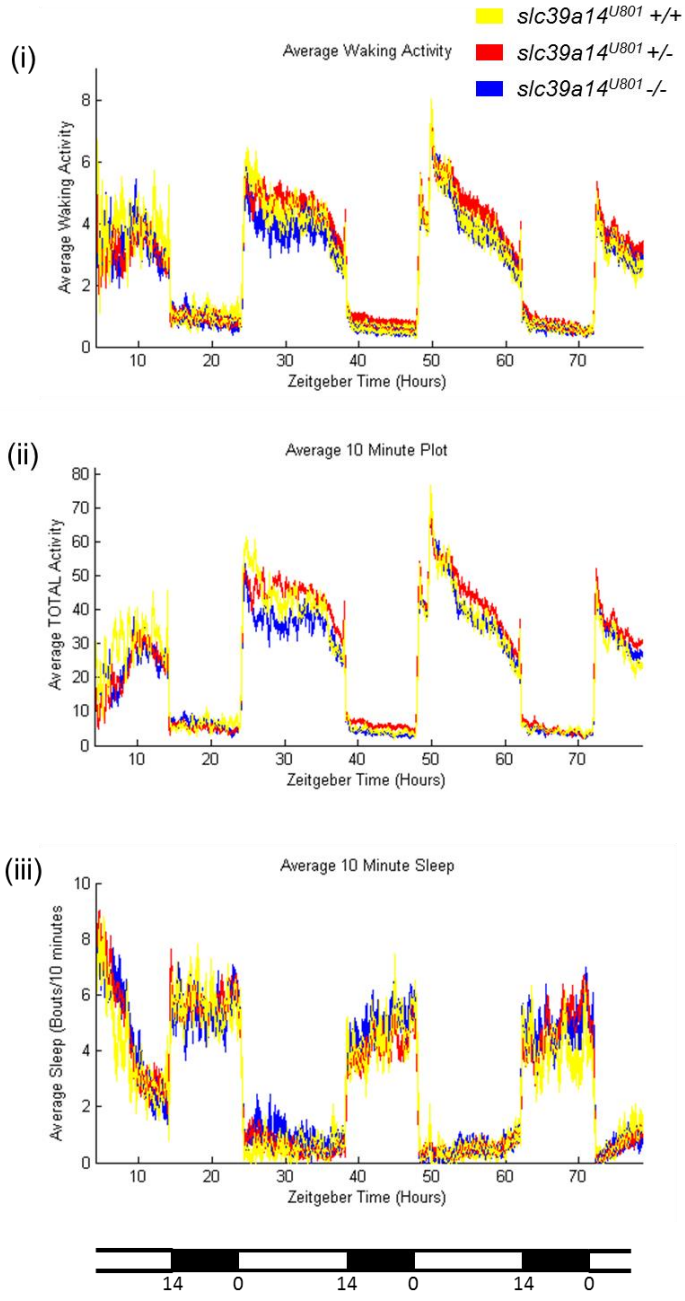

Figure 6.19 *slc39a14*^{U801} and wild-type zebrafish larvae share similar locomotor activity patterns. *Plots of (i) average waking activity, (ii) total activity and (iii) total sleep comparing wild-type (yellow), heterozygous (red) and homozygous (blue) mutant larvae. The 14:10 hour light:dark cycle is indicated on the bottom. n≥14 larvae.*

Average total activity during day and night was not significantly different between wild-type and mutant larvae (**Figure 6.20**).

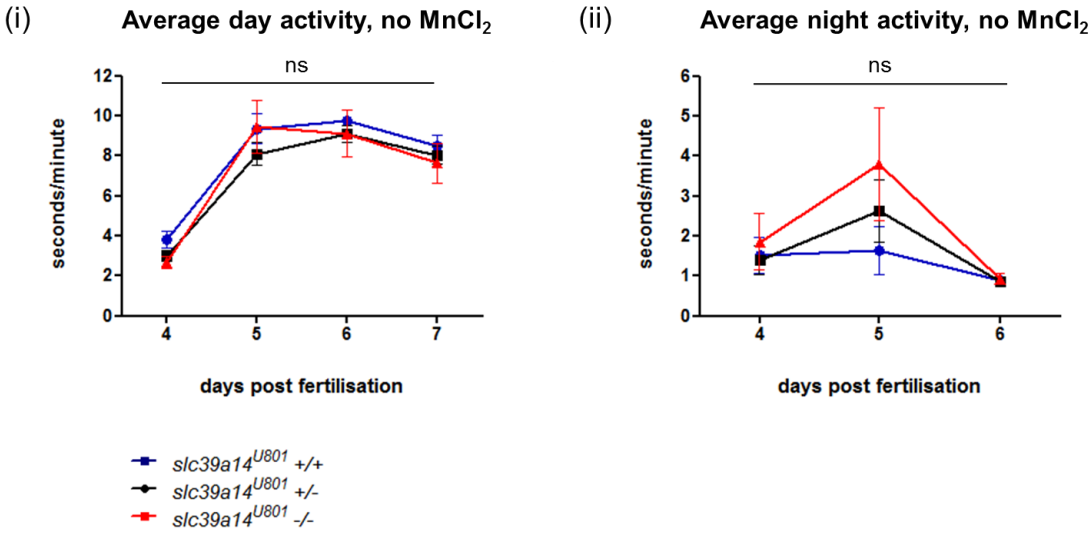

Figure 6.20 There is no difference in average total activity during day and night between wild-type and mutant *slc39a14^{U801}* larvae.

Graphs showing the average (i) day and (ii) night activity of wild-type (+/+), heterozygous (+/-) and homozygous (-/-) slc39a14^{U801} mutants between 4 and 7 dpf. Data are presented as mean ± s.e.m. Statistical analysis was performed using two way ANOVA (ns, not significant; p=0.29 [i], p=0.18 [ii]), n≥14 larvae.

While locomotor behaviour of *slc39a14^{U801}* mutants was not altered under physiological Mn concentrations, $MnCl_2$ exposure led to impaired locomotor activity. Homozygous s*lc39a14^{U801}* mutant and wild-type larvae were exposed to increasing concentrations of $MnCl_2$ from 2 dpf onwards and their locomotor activity tracked between 4 and 7 dpf (**Figure 6.21**).

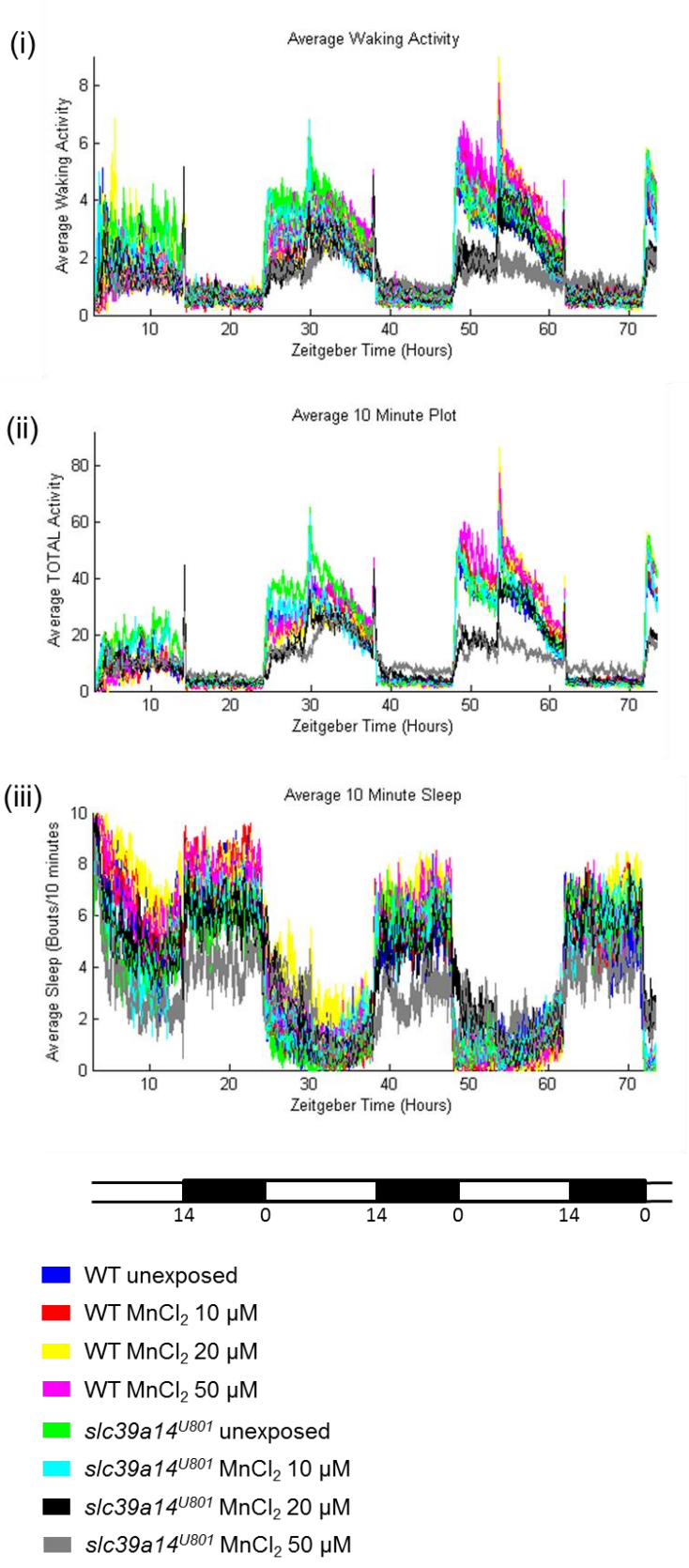

Figure 6.21 Mn exposure impairs the locomotor behaviour of *slc39a14*^{U801} larvae. *Plots of average waking activity, total activity and total sleep of wild-type and homozygous slc39a14*^{U801} *larvae between 4 and 7 dpf. Larvae were exposed to increasing doses of* $MnCl_2$ *(0-50 µM) from 2 dpf. The 14:10 hour light:dark cycle is indicated on the bottom. n=12 larvae per condition.*

Exposure of homozygous *slc39a14*^{U801} larvae to $MnCl_2$ led to a dose dependent reduction in average day activity between 5 and 7 dpf (**Figure 6.22**) whilst average night activity increased at 5 and 6 dpf (**Figure 6.23**). These results are consistent with the observation that homozygous s*lc39a14*^{U801} larvae are more sensitive to Mn toxicity and accumulate higher Mn levels upon $MnCl_2$ exposure than wild-types at 5 dpf (**Section 6.4.2**).

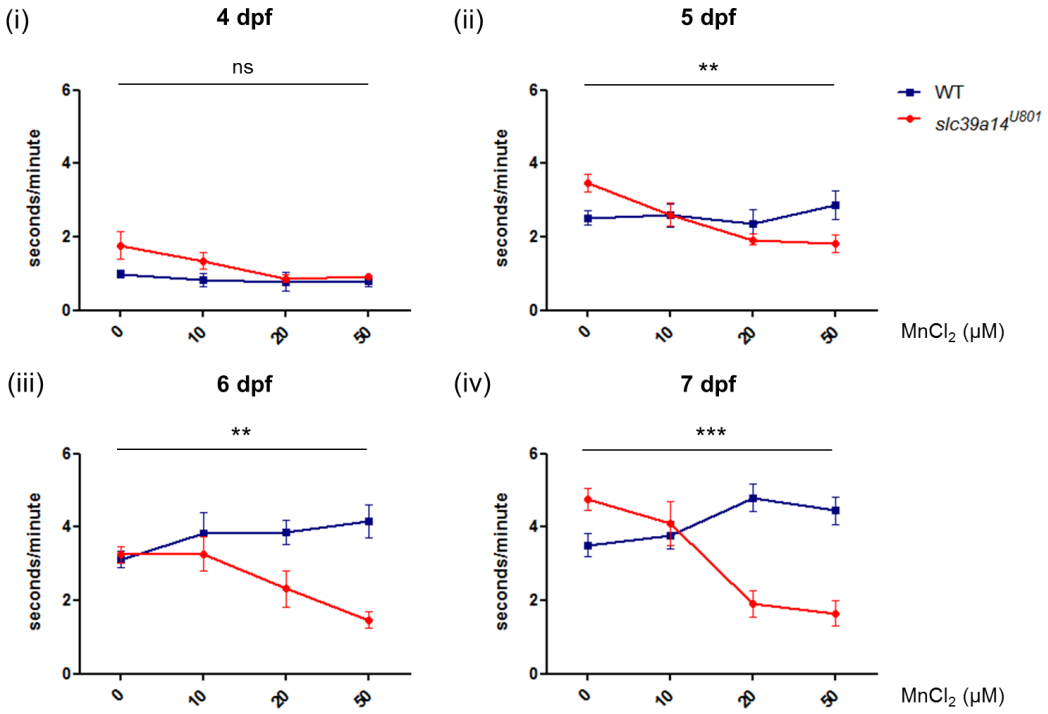

Figure 6.22 Mn exposure leads to a dose dependent reduction of average day activity in *slc39a14*^{U801} larvae.

Graphs showing the locomotor behaviour of wild-type (WT) and homozygous slc39a14^{U801} *larvae during 4 and 7 dpf (i-iv). Data are presented as mean ± s.e.m. 12 larvae were analysed per condition. Statistical analysis was performed using two way ANOVA (p=0.27 [4 dpf], p=0.009 [5 dpf], p=0.004 [6 dpf], p=0.001 [7 dpf]), (***p<0.001; **p<0.01; ns, not significant).*

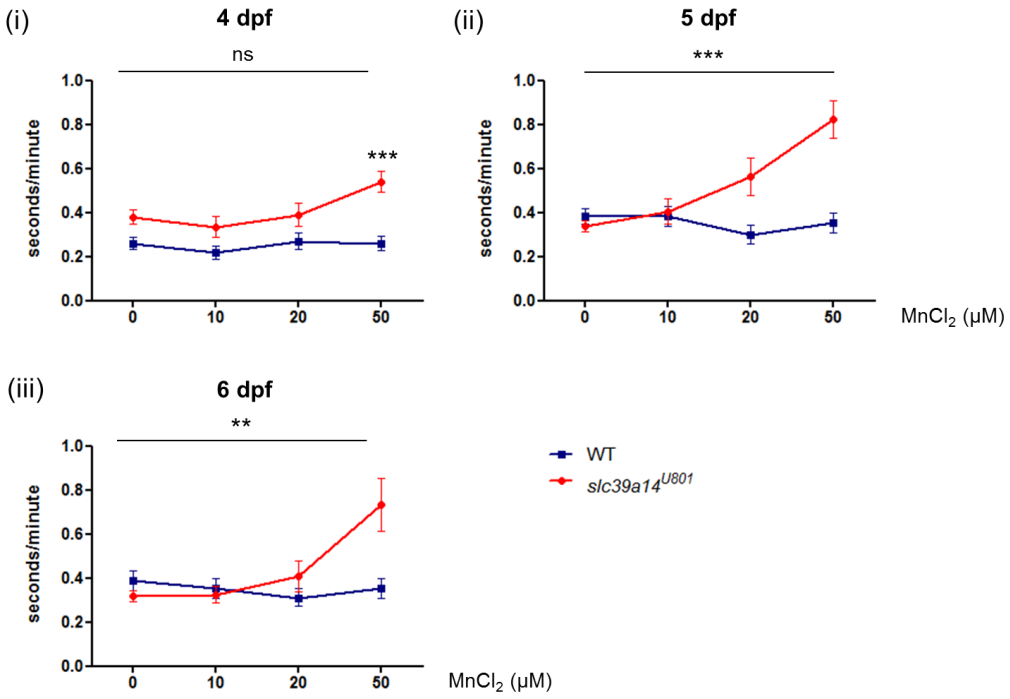

Figure 6.23 Mn exposure leads to a dose dependent increase in average night activity in *slc39a14^{U801}* larvae.

*Graphs showing the locomotor behaviour at night of wild-type (WT) and homozygous slc39a14^{U801} larvae during 4 and 6 dpf (i-iii). Data are presented as mean ± s.e.m. 12 larvae were analysed per condition. Statistical analysis was performed using two way ANOVA (p=0.1 [4 dpf], p=0.001 [5 dpf], p=0.0013 [6 dpf]) (***p<0.001; **p<0.01; ns, not significant).*

The observed changes in the locomotor activity pattern of *slc39a14^{U801}* mutants are a reliable phenotypic read-out for Mn toxicity which may be utilised as a read-out for drug screening. In order to test the effect of a chelating agent by adding it to the fishwater during behavioural analysis the phenotypic read-out would need to be present prior to the addition of the drug and throughout the period of drug testing. The administration of $MnCl_2$ would need to occur separately to the addition of the chelating agent. Otherwise, there is the possibility that the effect of chelation of Mn within the fishwater rather than the *in vivo* chelation efficiency is assessed. In order to determine the exposure time required to induce a phenotype *slc39a14^{U801}* mutants were exposed to $MnCl_2$ for variable durations (**Figure 6.24**). A minimum of 72 hours of exposure to $MnCl_2$ from 2 to 5 dpf was required to induce a locomotor phenotype. Larvae exposed for 72 hours

appeared to recover with no significant difference to unexposed larvae in average day activity at 8 dpf. However, there was a significant drop in activity in unexposed larvae at 8 dpf likely due to the lack of supplied nutrients during the experiment. Therefore, no conclusion can be drawn regarding the recovery of mutant larvae.

(i)

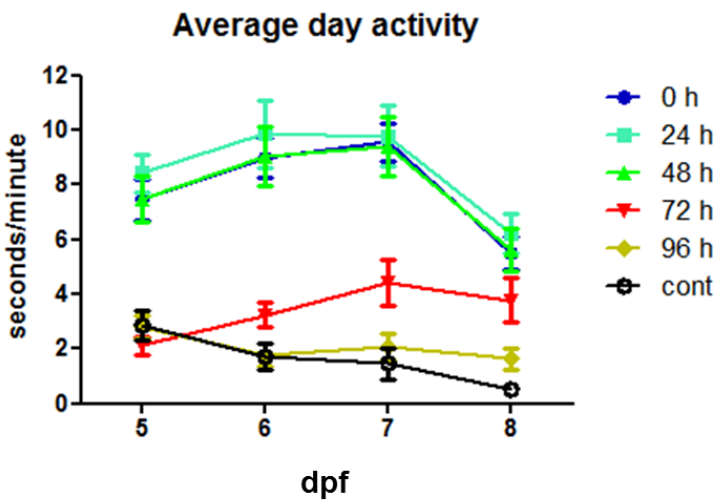

(ii)

dpf	5	6	7	8
0 vs 24 h	ns	ns	ns	ns
0 vs 48 h	ns	ns	ns	ns
0 vs 72 h	***	***	***	ns
0 vs 96 h	***	***	***	***
0 vs cont.	***	***	***	***

Figure 6.24 Influence of the duration of $MnCl_2$ exposure on the locomotor phenotype of *slc39a14^{U801}* mutants.

*Graph showing (**i**) the average day activity of homozygous slc39a14^{U801} mutant larvae between 5 and 8 dpf exposed to 50 µM $MnCl_2$. $MnCl_2$ exposure was commenced at 2 dpf for the duration stated. Data are presented as mean ± s.e.m. 8 larvae were analysed per condition (**ii**) Bonferroni post-tests comparing the effect of the duration of $MnCl_2$ exposure at each day of the experiment. Results of 72 h $MnCl_2$ in red. Statistical analysis was performed using two way ANOVA and Bonferroni post-tests (***p<0.001; ns, not significant).*

6.4.4 $MnCl_2$ exposure may lead to reduction of dopaminergic neurons in the ventral diencephalon in *slc39a14*^{U801} mutants.

Previous studies have suggested that Mn toxicity leads to impaired dopaminergic signalling in zebrafish larvae exposed to $MnCl_2$ concentrations as high as 1 mM[259]. To visualise dopaminergic cells in brains from wild-type and mutant larvae at 5 dpf immunostaining for tyrosine hydroxylase (TH) was performed (**Section 2.4.7**). TH is a marker for catecholaminergic neurons and therefore expected to label dopaminergic neurons in the fore- and midbrain and noradrenergic neurons in the hindbrain, respectively[265,266]. In zebrafish, two tyrosine hydroxylase genes, *th1* and *th2*, exist[267]. The antibody used (Millipore, MAB318) is specific for TH1 that is expressed in dopaminergic neurons of the ventral diencephalon, pretectum and olfactory bulb, and in noradrenergic neurons of the locus coeruleus, and the medulla oblongata. TH2 on the other hand is confined to the hypothalamus[268]. The antibody was used according to a published protocol (**Section 2.4.7**)[259]. Unfortunately, only cells in the ventral diencephalon could be reliably visualised for cell counting leaving some doubt as to the reliability of the antibody staining (**Figure 6.25**). The antibody failed to clearly visualise dopaminergic neurons in the olfactory bulb and pretectum. However, preliminary analysis showed a six percent reduction in the number of TH positive cells in the ventral diencephalon in unexposed homozygous *slc39a14*^{U801} mutants compared to wild-type larvae which was exacerbated by exposure to 50 µM $MnCl_2$ between 2 and 5 dpf leading to a 19 percent reduction (**Figure 6.26**). A small decrease in TH cell count was also observed in wild-type larvae exposed to $MnCl_2$. These results suggest that Mn toxicity may indeed affect the integrity of dopaminergic neurons within the ventral diencephalon.

With the aim of validating this result, immunostaining for TH and EGFP was performed in mutant and wild-type larvae in the *tg(slc6a3:EGFP)* background (**Figure 6.25**, **Section 2.4.7**). *slc6a3* encodes the dopamine transporter (DAT); its expression is specific to dopaminergic but not noradrenergic neurons. The transgenic line expresses EGFP under the control of cis-regulatory elements of the DAT gene[269]. The *tg(SLC6A3:EGFP)* line shows GFP labelled neurons in the olfactory bulb, the pretectum and ventral diencephalon. Additionally, cells in the caudal hypothalamus are labelled that are thought to correspond to TH2 positive neurons that are not stained with the TH antibody. The number of EGFP positive cells in the ventral diencephalon

significantly exceeded that of TH positive cells. The cell count of EGFP positive neurons within the ventral diencephalon did not show differences between wild-type and homozygous *slc39a14*^{U801} mutants (**Figure 6.26**). However, any small difference in the number of dopaminergic cells might have been masked by the high number of EGFP positive neurons in the caudal hypothalamus.

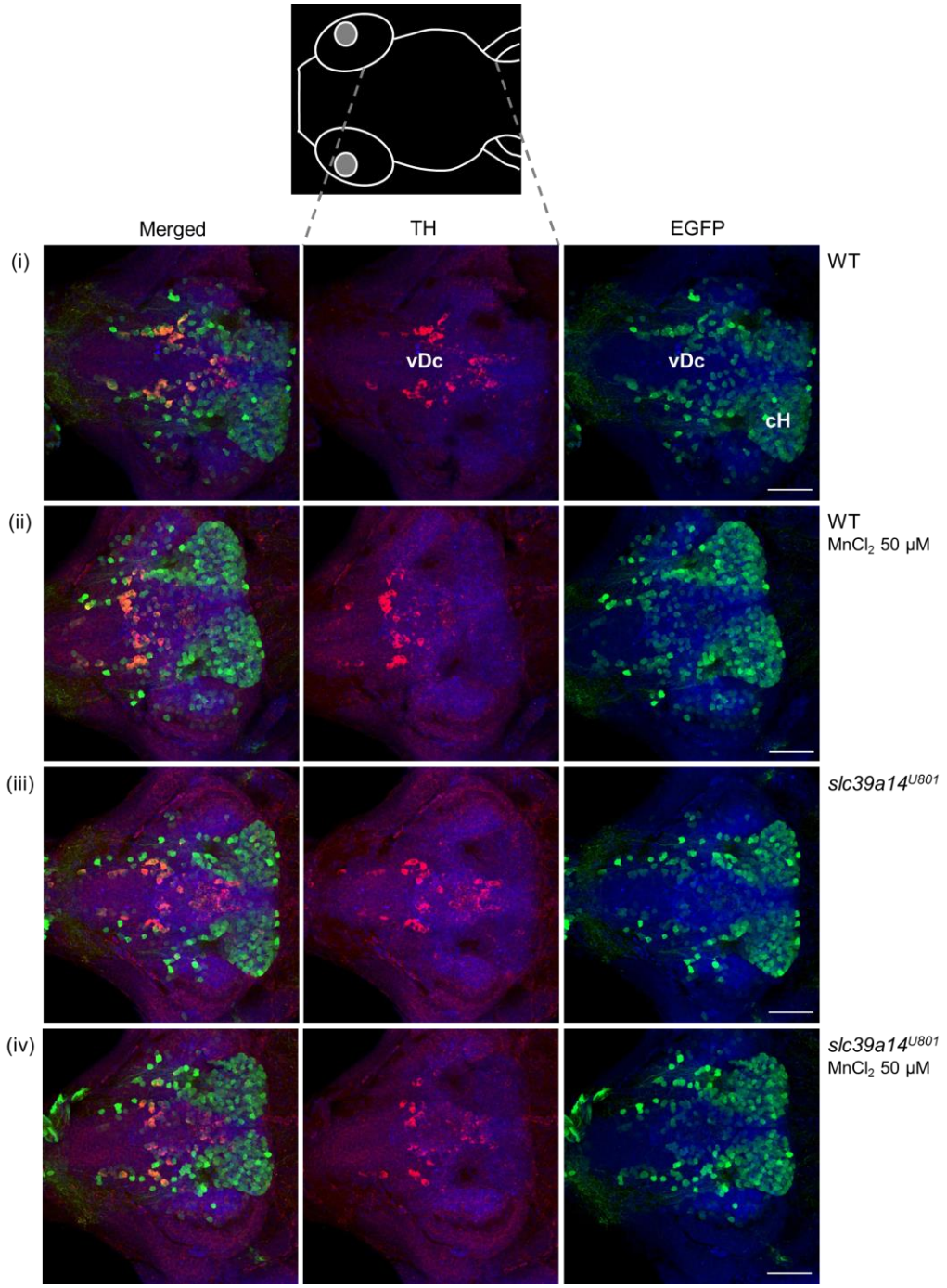

Figure 6.25 Representative images of TH and EGFP immunostaining of brains from wild-type and *slc39a14*^{U801} mutant larvae in the tg(*slc6a3:EGFP*) background. *The zebrafish schematic indicates the imaged brain region viewed from ventral. Brains were dissected from wild-type and homozygous mutant larvae at 5 dpf with and without $MnCl_2$ exposure. Nuclei were stained with TOTO-3 Iodide.TH staining in magenta is shown in the middle column, EGFP staining in green on the right and merged images on the left. Size bar 50 µm. vDc, ventral diencephalon. cH, caudal hypothalamus.*

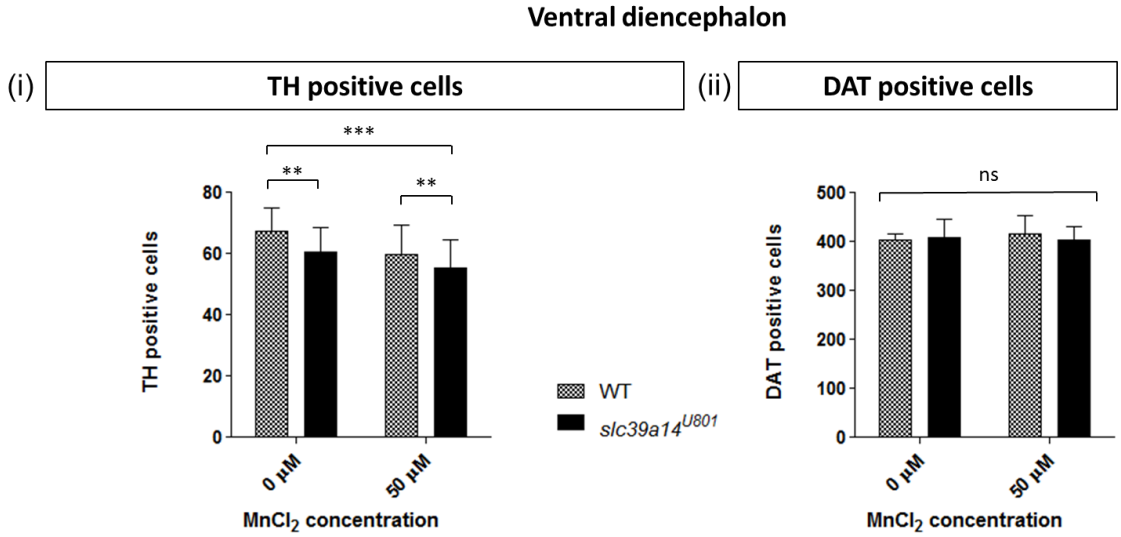

	Unexposed		$MnCl_2$ 50 µM	
	WT	*slc39a14*^{U801}	WT	*slc39a14*^{U801}
Mean number of TH positive cells	67	63	58	54
% reduction from unexposed WT	-	6.2	14.2	19.0

Figure 6.26 TH positive cells in the ventral diencephalon appear reduced in *slc39a14*^{U801} mutants and upon $MnCl_2$ exposure.

*Graphs show the number of neurons positively stained for **(i)** TH and **(ii)** DAT in the ventral diencephalon of wild-type (WT) and homozygous slc39a14*^{U801}*mutant larvae in the tg(slc6a3:EGFP) background at 5 dpf unexposed and exposed to 50 µM* $MnCl_2$*. Data are presented as means ± s.d. from two independent experiments (≥18 brains per condition). Statistical analysis was performed using one way ANOVA (p=0.001 [TH], p=0.78 [DAT]) and Tukey's multiple comparison tests (**p<0.01; ***p<0.001; ns, not significant).*

The dorsal groups of dopaminergic neurons in the olfactory bulb and pretectum showed very poor staining with the TH antibody and thus did not allow quantification of cell numbers (data not shown). However, the *tg(slc6a3:EGFP)* line demonstrated a strong expression pattern in the olfactory bulb and pretectum (**Figure 6.27**). DAT positive cells were counted in the pretectum but no difference in cell count between wild-type and mutant larvae was encountered (**Figure 6.28**).

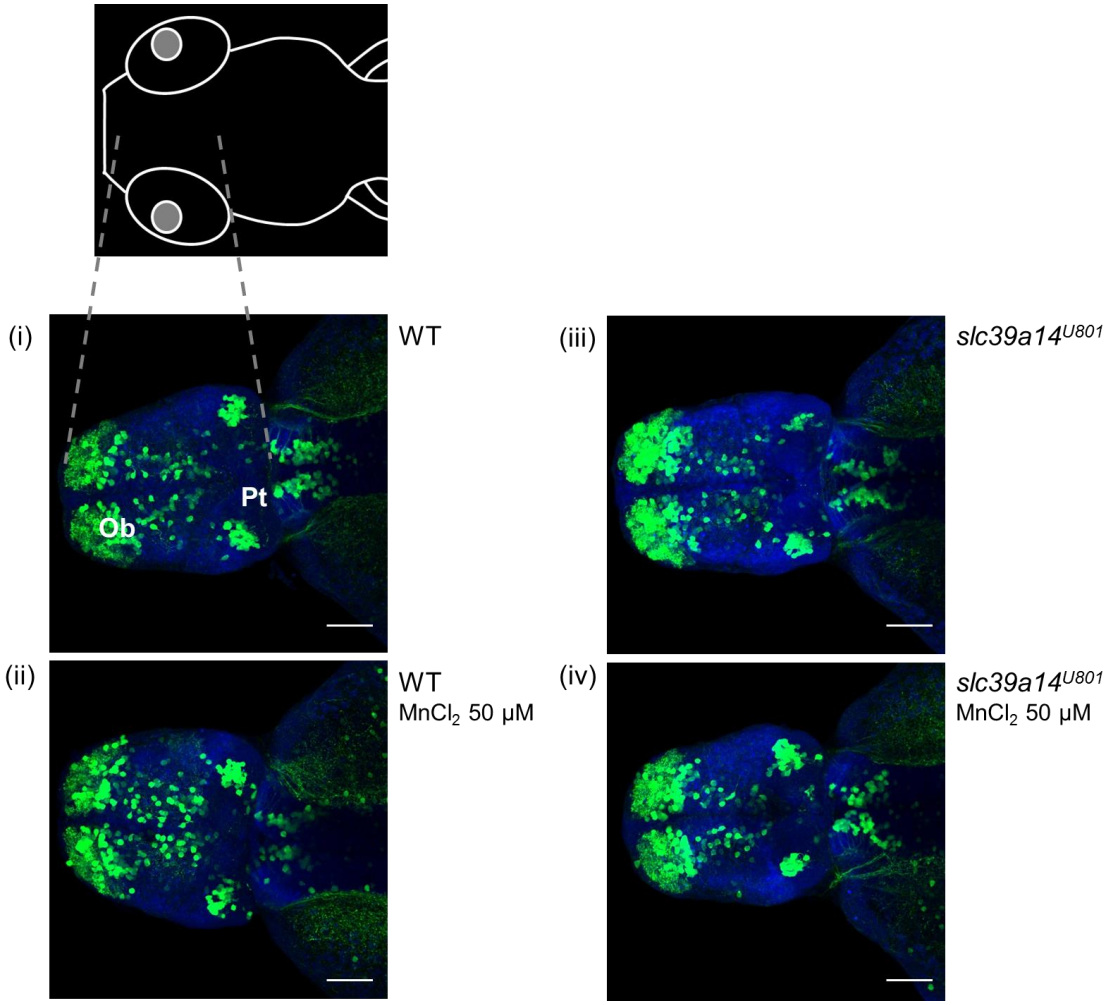

Figure 6.27 Representative images of EGFP immunostaining of brains from wild-type and *slc39a14*^{U801} mutant larvae in the tg(*slc6a3:EGFP*) background.

*The zebrafish cartoon on the top indicates the position within the brain viewed from dorsal. Brains from (**i, iii**) unexposed and (**ii, iv**) $MnCl_2$ exposed wild-type and homozygous mutant larvae immunostained for EGFP at 5 dpf. Nuclei were stained with TOTO-3 Iodide. Size bar 50 µm. Ob, olfactory bulb. Pt, pretectum.*

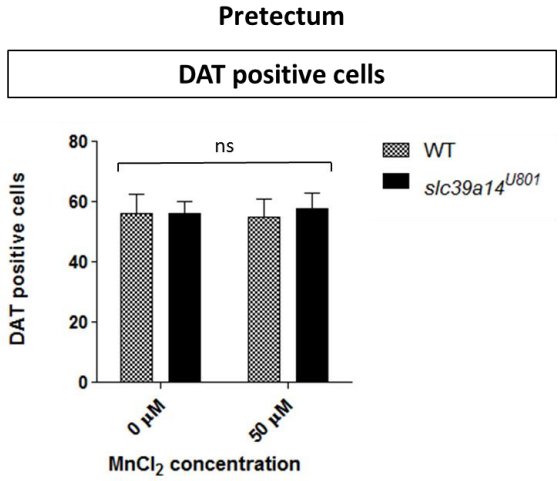

Figure 6.28 There is no difference in DAT positive neurons in the pretectum between *slc39a14^{U801}* mutant and wild-type larvae.

Graph showing the number of neurons positively stained for EGFP in the pretectum of wild-type (WT) and homozygous slc39a14^{U801} mutant larvae in the tg(slc6a3:EGFP) background at 5 dpf. Data are presented as means ± s.d. from two independent experiments (≥18 brains per condition). Statistical analysis was performed using one way ANOVA (p=0.91; ns, not significant).

In order to assess whether the reduced number of TH positive cells in the ventral diencephalon was caused by increased apoptosis of neurons in response to Mn toxicity TUNEL staining was performed on brains from 5 dpf larvae (**Section 2.4.8**). Previous studies in rats and mice have suggested that Mn overexposure leads to increased neuronal apoptosis[270,271]. However, there was no evidence of increased apoptotic cell death in unexposed and $MnCl_2$ exposed *slc39a14^{U801}* mutants at this stage (**Figure 6.29**).

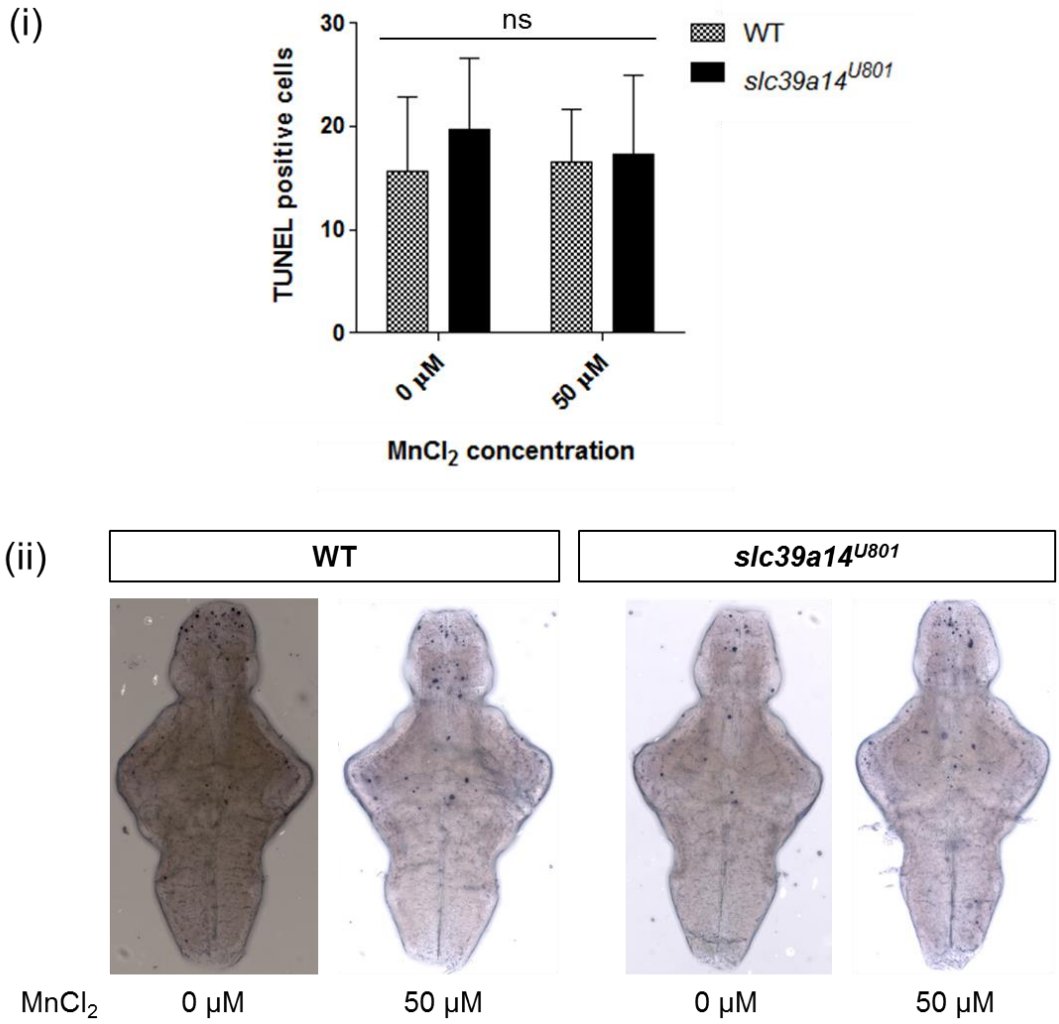

Figure 6.29 Mn toxicity does not induce apoptosis in wild-type or *slc39a14^{U801}* mutant larvae.

*(**i**) Graph showing apoptotic (TUNEL positive) cells in the ventral diencephalon of wild-type (WT) and homozygous slc39a14^{U801} larvae at 5 dpf. Data are presented as means ± s.d. Statistical analysis was performed using one way ANOVA (ns, not significant). n≥7 (**ii**) Representative images of wild-type and mutant larvae stained for apoptotic cells (dark purple).*

6.4.5 Mn toxicity leads to impaired visual background adaptation and optokinetic response

When *slc39a14*^{U801} larvae were raised under a 14:10 hour light:dark cycle for locomotor behaviour studies it became apparent that homozygous larvae did not change their pigmentation pattern in response to light when exposed to 50 µM $MnCl_2$. Wild-type larvae on the other hand did not show this abnormality. However, at higher concentrations of $MnCl_2$ (100 µM) both mutant and wild-type larvae exhibited an abnormal pigmentation pattern (**Figure 6.30**). The physiological phenomenon of pigmentation change upon light exposure is known as visual background adaptation (VBA)[272,273]. It occurs through subcellular redistribution of melanophores in zebrafish larvae in order to adapt the body colour to the background. Visual background adaptation requires normal vision and is therefore impaired in blind larvae[273]. In order to determine whether *slc39a14*^{U801} larvae develop visual impairment upon Mn exposure, the optokinetic response (OKR) was analysed in homozygous *slc39a14*^{U801} larvae at 5 dpf after exposure to 50 µM $MnCl_2$ from 2 to 5 dpf whilst the controls were not exposed (**Section 2.4.10**). The OKR is elicited by moving objects through the visual field which triggers a two component eye movement: a smooth pursuit movement to follow the object and a fast saccadic movement once the stimulus leaves the field of vision[273]. In our setup, black and white stripes with variable spatial frequency were presented as visual stimuli as previously described[274]. While unexposed *slc39a14*^{U801} larvae showed an appropriate OKR to the spatial frequencies examined compared to previously published wild-type data, $MnCl_2$ exposed larvae demonstrated a significant reduction in eye velocity at high spatial frequencies (**Figure 6.31**). These results suggest that Mn exposure does indeed lead to visual impairment and subsequent diminished visual background adaptation.

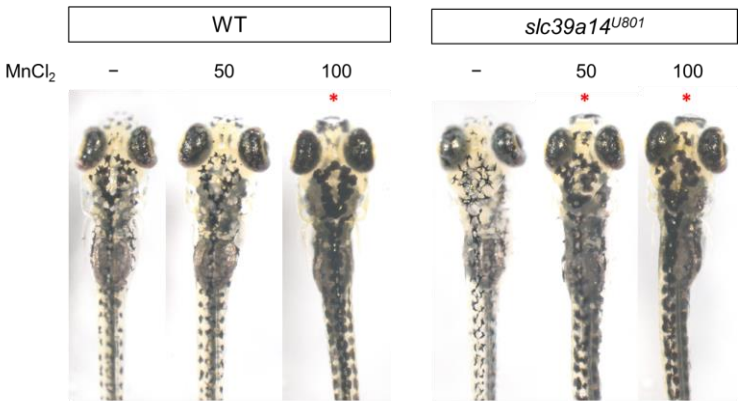

Figure 6.30 $MnCl_2$ exposure impairs visual background adaptation. *Images showing wild-type (WT) and slc39a14*^{U801} *larvae at 5 dpf exposed to $MnCl_2$ (0-100 µM). Scale bar 500 µm.*

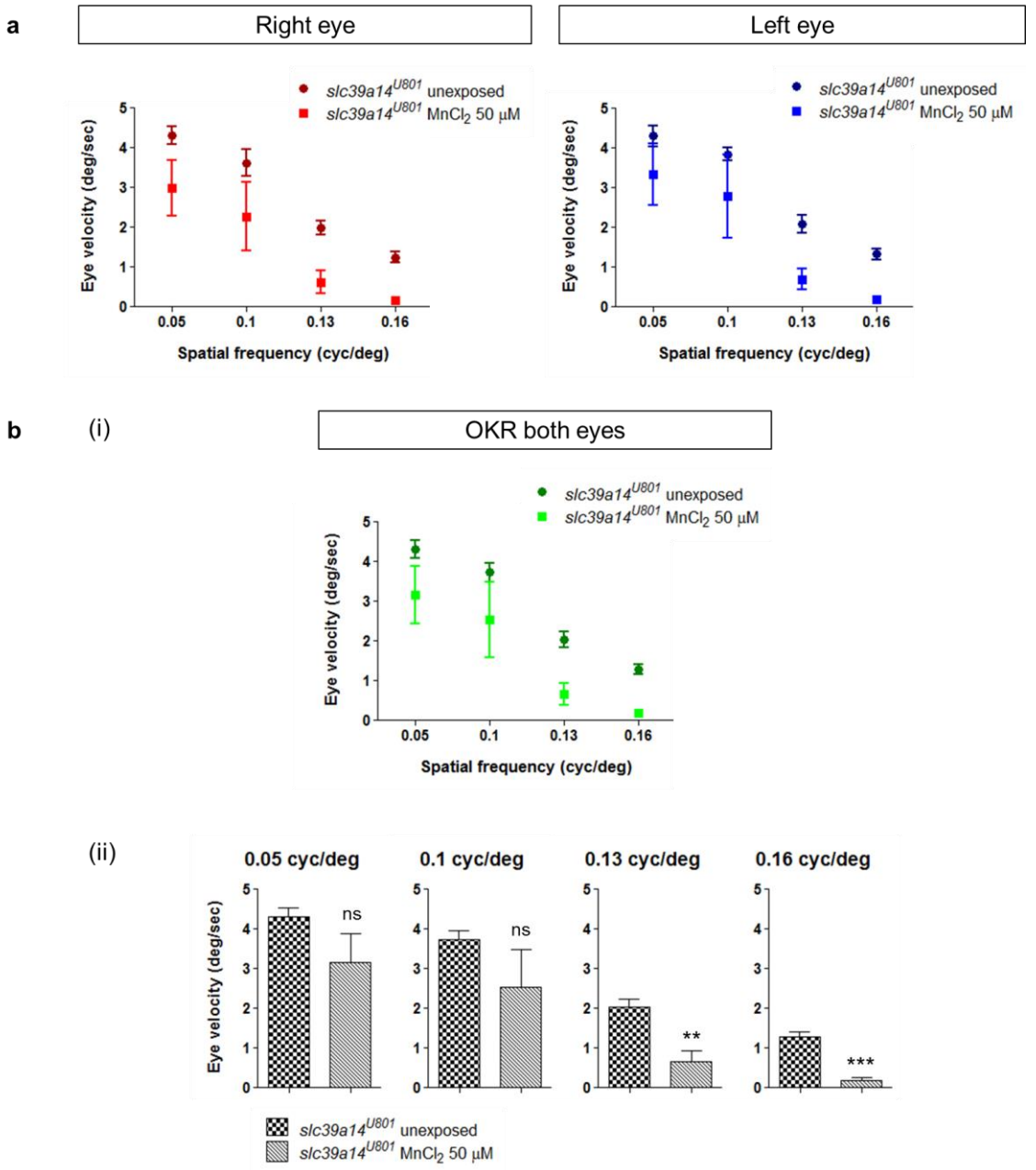

Figure 6.31 The optokinetic response is impaired upon $MnCl_2$ exposure in *slc39a14^{U801}* larvae.

*(**a**) Graph showing the OKR of the right (red) and left (blue) eye of homozygous slc39a14^{U801} larvae unexposed and exposed to 50 µM $MnCl_2$. (**b**) (i) Graph showing the OKR of both eyes combined unexposed and exposed to 50 µM $MnCl_2$. (ii) Eye velocity of unexposed and exposed larvae are compared for each spatial frequency. Data are presented as mean ± s.e.m. from five independent experiments. Statistical analysis was performed using Student's two tailed t test (**p<0.01; *** p<0.001; ns, not significant).*

6.4.6 $Na_2CaEDTA$ effectively lowers Mn levels in *slc39a14^{U801} larvae*

The chelator $Na_2CaEDTA$ has been successfully used in patients with SLC30A10 and SLC39A14 deficiency to lower Mn blood levels with subsequent improvement of neurological symptoms[46,48,50]. In order to assess whether $Na_2CaEDTA$ can effectively chelate Mn in *slc39a14^{U801}* mutants, $MnCl_2$ exposed larvae were treated with $Na_2CaEDTA$. We know from drug treatment in humans that $Na_2CaEDTA$ requires intravenous application because it is not absorbed from the gastrointestinal tract, and remains in the extracellular fluid[57]. Therefore, it was unlikely that immersion of larvae in $Na_2CaEDTA$ supplemented fishwater would have any effect. To circumvent the absorption issue $Na_2CaEDTA$ was directly injected into the heart of mutant larvae.
$MnCl_2$ exposure of wild-type and mutant larvae was performed between 2 and 5 dpf. Mutant larvae were additionally injected into the heart with 5 or 50 ng $Na_2CaEDTA$ daily between 2 and 5 dpf (**Section 2.4.2**). Subsequently, Mn levels were determined by ICP-MS in pooled samples of 10 larvae at 5 dpf. Cardiac injections of $Na_2CaEDTA$ prevented excessive accumulation of Mn in mutant larvae and lowered Mn levels to that of exposed wild-types (**Figure 6.32i**). This proof of principle experiment demonstrates the suitability of the *slc39a14^{U801}* mutant as a disease model for drug screening. Furthermore, it confirms that $Na_2CaEDTA$ is a potent Mn chelator in *slc39a14^{U801}* mutants similar to observations in treated patients.

As expected, immersion of *slc39a14^{U801}* larvae in $Na_2CaEDTA$ supplemented fishwater did not affect the Mn load (**Figure 6.32ii**). Following $MnCl_2$ exposure (50µM) between 2 and 5 dpf the larvae were transferred to fishwater without $MnCl_2$ supplementation but addition of 1mM $Na_2CaEDTA$ at 5 dpf. The $Na_2CaEDTA$ supplemented fishwater was renewed daily. Mn levels were determined by ICP-MS at 7 dpf in samples of 10 pooled larvae. No difference in Mn levels was observed between $Na_2CaEDTA$ treated and untreated mutant larvae.

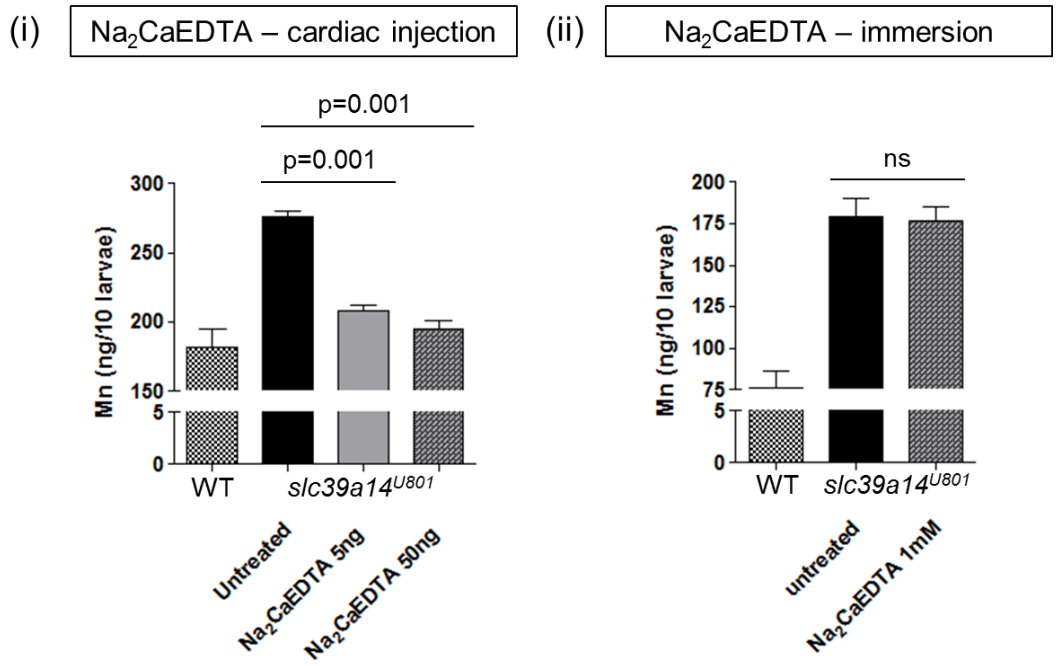

Figure 6.32 Systemic administration of $Na_2CaEDTA$ effectively chelates Mn in *slc39a14^{U801}* mutant larvae.

*Graphs showing Mn levels of (**i**) $MnCl_2$ (50 µM) exposed un-injected wild-type and homozygous slc39a14^{U801} larvae un-injected and injected into the heart with 5 or 50 ng $Na_2CaEDTA$. Data are presented as mean ± s.d. from a minimum of three independent experiments. Statistical analysis was performed using one way ANOVA (p=0.001) and Tukey's Multiple Comparison Test. (**ii**) untreated wild-type and homozygous slc39a14^{U801} larvae untreated and immersed in $Na_2CaEDTA$ (1mM). Data are presented as mean ± s.d. from a minimum of three independent experiments. Statistical analysis was performed using one way ANOVA and Tukey's Multiple Comparison Test (ns; not significant).*

6.4.7 Loss-of-function of both *slc30a10 and slc39a14* in zebrafish does not aggravate the Mn accumulation phenotype.

Analysis of Mn levels in single *slc30a10*^{U800} and *slc39a14*^{U801} mutants suggested that both accumulate Mn at 14 dpf. In humans, SLC39A14 appears to be ultimately required for Mn uptake into the liver for subsequent biliary excretion via SLC30A10 (**Figure 4.18**). Hence, it seems that both Mn transporters are required for effective Mn clearance. To test whether both transporters contribute concordantly to Mn clearance in zebrafish, a double mutant line *slc30a10*^{U800}*, slc39a14*^{U801} was generated by out-crossing. Homozygous double mutants appeared healthy without any apparent developmental or morphological abnormalities and survived into adulthood.

Mn levels at 14 dpf determined under standard husbandry conditions without the addition of $MnCl_2$ to the fishwater were significantly higher in double mutants compared to wild-type and *slc30a10*^{U800} larvae (**Figure 6.33i**). Mn levels appeared to be minimally higher in the double mutant compared to *slc39a14*^{U801} larvae, however, without reaching statistical significance. In order to enhance any occurring differences between the *slc39a14*^{U801} single and the *slc30a10*^{U800}*, slc39a14*^{U801} double mutant, Mn levels were assessed 24 hours after exposure to 50 µM $MnCl_2$ at 14 dpf. Surprisingly, Mn exposure led to a much lesser degree of Mn accumulation in double compared to *slc39a14*^{U801} single mutants suggesting that *slc30a10* and *slc39a14* do not share a concordant function in zebrafish and that the role of zebrafish *slc30a10* may be different to that in humans (**Figure 6.33ii**).

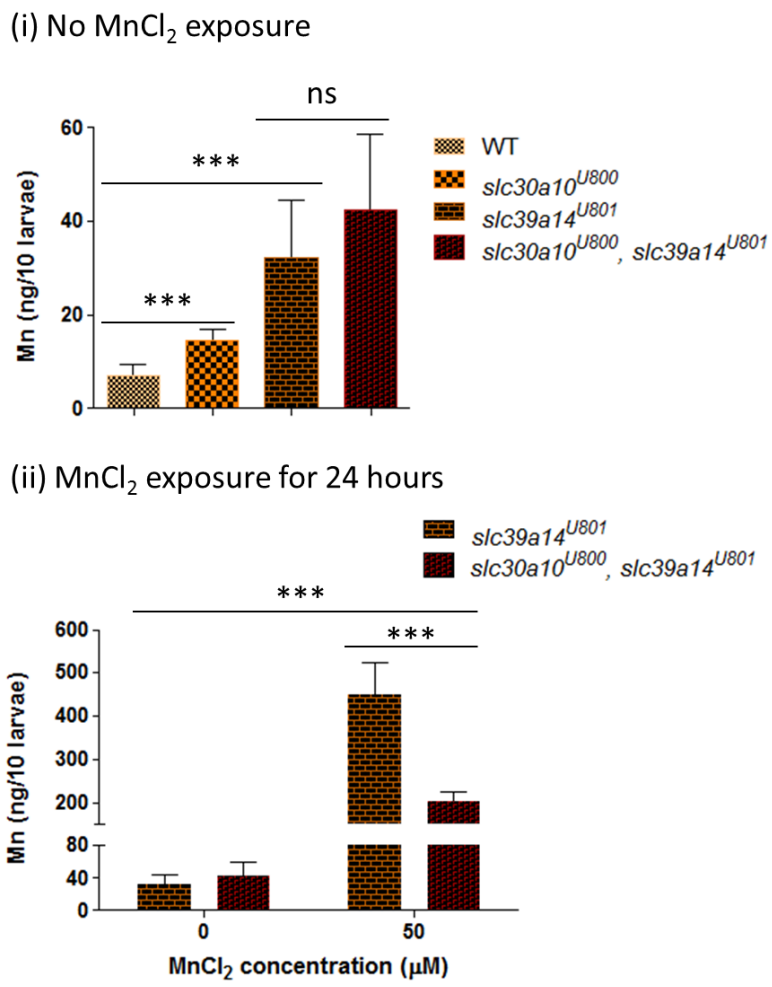

Figure 6.33 Double *slc30a10^{U800}*, *slc39a14^{U801}* mutants accumulate less Mn upon $MnCl_2$ exposure than *slc39a14^{U801}* larvae.

*Graphs showing Mn levels of Mn transporter mutants at 14 dpf (**i**) without $MnCl_2$ exposure. slc30a10^{U800} (p=0.001), slc39a14^{U801} (p=0.001), and double mutants (p=0.001) display higher Mn levels compared to wild-types. However, no differences in Mn levels are seen between slc39a14^{U801} larvae and double mutants (p=0.128). Data are presented as means ± s.d., n≥5. Statistical analysis was performed using two tailed Student's t-test (***p<0.001; ns, not significant) (**ii**) following exposure to 50 µM $MnCl_2$ for 24 hours. Data are presented as means ± s.d., n≥5. Statistical analysis was performed using two way ANOVA (p=0.001) and Bonferroni posttests (***p<0.001).*

6.4.8 Transcriptome analysis of *slc39a14*^{U801} mutants

Despite its recognised role in neurodegenerative disease processes, we lack a deeper understanding of the mechanisms of Mn related neurotoxicity[275] (**Section 1.4**). In order to identify novel potential targets of Mn toxicity RNA sequencing was performed on an in-cross of heterozygous *slc39a14*^{U801} zebrafish, unexposed and exposed to $MnCl_2$. It was likely that Mn induced changes in gene expression unravel new pathways and regulatory networks affected by Mn toxicity.

This work was done in collaboration with Dr Elisabeth Busch, Wellcome Trust Sanger Institute, who has developed a high-throughput mRNA 3' end sequencing method (DeTCT) that allows quantification of expression levels of large numbers of individually genotyped zebrafish embryos. This polyA enriched RNA sequencing method maps each identified transcript to the closest annotated gene. Data analysis was performed to compare mutant (data obtained from 12 x *slc39a14*^{U801} -/- larvae at 5dpf) and control (6 x *slc39a14*^{U801} +/- and 6 x *slc39a14*^{U801} +/+ siblings at 5dpf) larvae as well as Mn exposed and unexposed groups of either genotype. This approach allowed the analysis of the following differentially expressed (DE) gene groups (**Figure 6.34**):

1. $MnCl_2$ untreated mutants versus untreated siblings to demonstrate the effect of the mutation – 375 differentially expressed genes were identified.
2. Untreated siblings versus $MnCl_2$ treated siblings to analyse the effect of Mn toxicity in wild-type larvae – 197 differentially expressed genes were identified.
3. Untreated mutants versus $MnCl_2$ treated mutants to identify DE genes that normalised upon $MnCl_2$ treatment – 314 differentially expressed genes were identified.
4. Untreated mutants versus treated mutants to demonstrate the effect of Mn toxicity in mutant larvae – 408 differentially expressed genes were identified.

Preliminary analysis of the resulting gene lists was performed using ZFIN, OMIM and PubMed databases (**Table 6.1, 6.3 and 6.5, Section 2.6**). Particular attention was paid to transcripts with a low p-value and a short distance to the closest annotated 3' end to avoid false positive reads. Initial conclusions can be drawn from analysing groups of genes with similar function and expression pattern and are discussed below. Results will require validation by qRT-PCR and *in situ* hybridisation in the future.

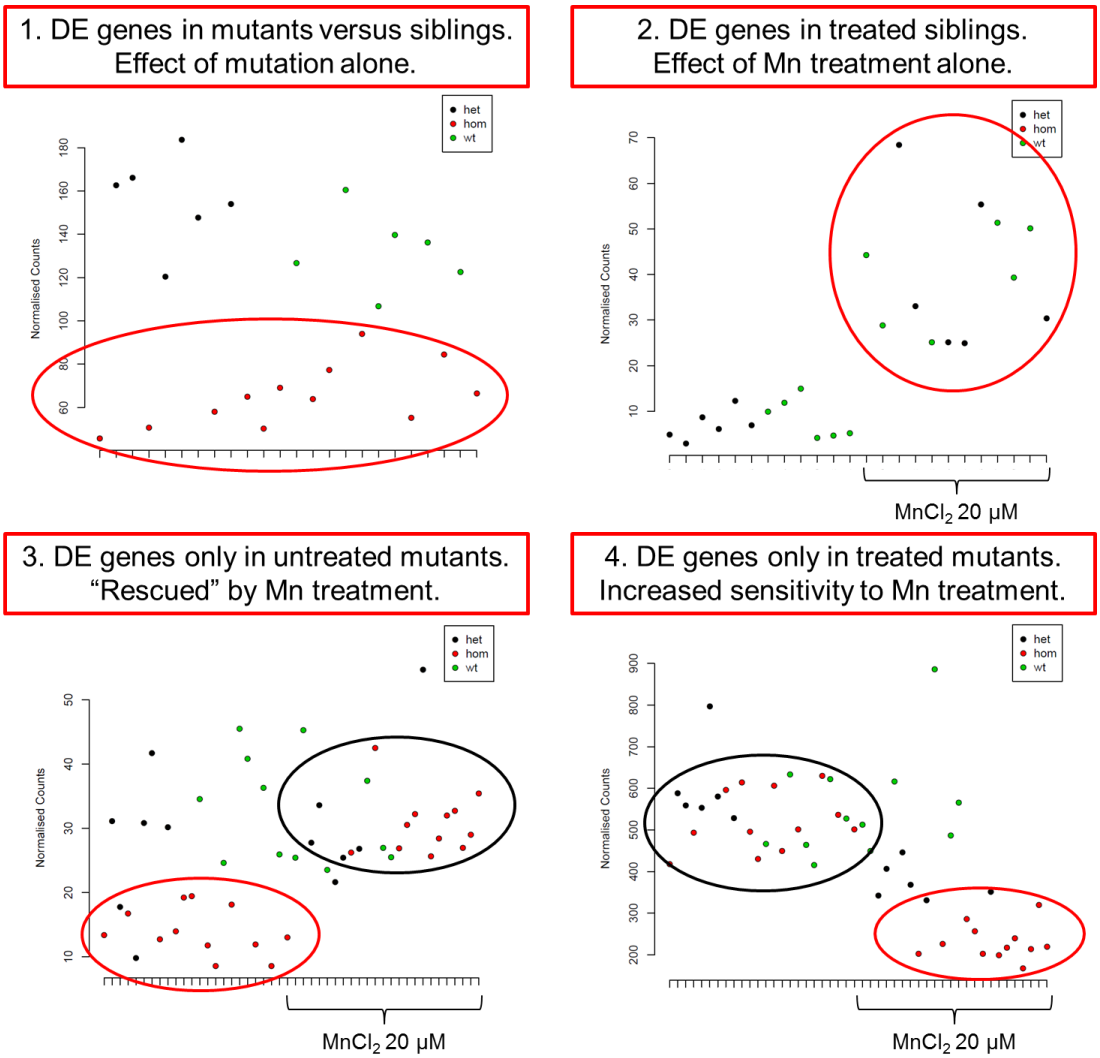

Figure 6.34 Differentially expressed gene groups analysed by RNA sequencing.

*A representative plot of the transcript count is given for each condition. Each point represents the transcript count of a single larva. The genotype is colour coded: (red) homozygous, (blue) heterozygous, (green) wild-type slc39a14^{U801} larvae. $MnCl_2$ treatment (20 µM) is indicated by a parenthesis. (**1.**) Differentially expressed (DE) genes between unexposed mutants and siblings. The plot shows the typical result of a downregulated gene in mutant larvae (marked with a red circle). (**2.**) DE genes between unexposed and $MnCl_2$ exposed wild-type and heterozygous siblings. The plot shows the typical result of a gene up-regulated upon $MnCl_2$ treatment (marked with a red circle). (**3.**) DE genes (marked with a red circle) that normalised upon $MnCl_2$ (marked with a black circle) in homozygous slc39a14^{U801} mutants. (**4.**) DE genes upon $MnCl_2$ treatment (marked with a red circle) that only changed in homozygous mutants compared to siblings. The black circle indicates these genes are not differentially expressed in untreated conditions.*

6.4.8.1 Differentially expressed genes in mutants versus siblings – effect of the mutation alone

Untreated homozygous *slc39a14*^{U801} mutants demonstrated a downregulation of specific groups of brain expressed genes relative to control zebrafish that are involved in neurotransmitter release, glutamatergic and GABAergic signalling (**Table 6.1**). Particularly striking was the differential expression of several synapototagmin genes that facilitate synaptic vesicle exocytosis[276]. The function and possible link to Mn associated pathophysiology is discussed in **Section 6.5.2**. Anatomical gene enrichment analysis found that the differentially expressed genes map exclusively to the central nervous system and eye (**Table 6.2**).

Table 6.1 Differentially expressed genes in unexposed homozygous *slc39a14*^{U801} mutants that can be linked to Mn homeostasis.

Gene name	Fold change	Function	e76 Ensembl gene ID (ENSDARG)	Distance to 3' end (bp)	p-value
Neurotransmitter release					
syt6a	-2.5	Synaptotagmin VIa (SNARE complex)	00000076730	1860	0.0444
syt2a	-1.8	Synaptotagmin IIa (SNARE complex)	00000025206	-3	0.0203
syt9a	-1.6	Synaptotagmin IXa (SNARE complex)	00000003994	268	0.0165
syt1a	-1.4	Synaptotagmin Ia (SNARE complex)	00000030614	5	1.51E-05
sv2a	-2.5	Synaptic vesicle glycoprotein 2A, interaction with synaptotagmin I	00000059945	2352	0.0000
rab3ab	-1.4	Interaction with synaptotagmin I	00000043835	3817	0.0148
snap25a	-1.1	Synaptosome-associated protein 25a (SNARE complex)	00000020609	-2	0.0177
Glutamatergic signalling					
slc17a6a	-4.9	Vesicular glutamate transporter 2 (vglut2)	00000001127	2444	0.0016
grin2db	-3.5	Ionotropic NMDA glutamate receptor	00000070620	4953	0.0001
camk2b1	-3.3	Calcium/calmodulin-dependent protein kinase, glutamate release	00000011065	1694	0.0442
grip1	-2.2	Glutamate receptor interacting protein	00000015053	1495	6.52E-10
GABAergic signalling					
gabrb2	-2.1	GABA A receptor, beta 2	00000079586	25	4.09E-05
gabrg2	-1.5	GABA A receptor, gamma 2	00000053665	25	0.0011
abat	-1.3	4-aminobutyrate aminotransferase -	00000006031	2115	0.0123

		GABA synthesis			
Calcium binding / transport					
camk2b1	-3.3	Calcium/calmodulin-dependent protein kinase, glutamate release	00000011065	1694	0.0442
atp2b3a	-1.8	Plasma membrane Calcium ATPase (PMCA3) – brain	00000043474	-72	0.0087
calm2a	-1.4	Calmodulin 2a – myocardium	00000034187	0	0.0112
calm1a	1.3	Calmodulin 1a – brain	00000074057	0	0.0430
Established link with Mn					
ntrk3b	-2.3	Neurotrophic tyrosine kinase, receptor – ligands include neurotrophins	00000063035	-1	0.0017
bdnf	-1.4	Brain-derived neurotrophic factor	00000018817	259	0.0104

Table 6.2 Anatomical gene enrichment of differentially expressed genes in unexposed homozygous *slc39a14*^{U801} mutants.

Anatomical region		
retinal ganglion cell layer	neuron	midbrain
forebrain	presumptive diencephalon	brain
retinal neural layer	posterior neural tube	neuroblast
telencephalon	electrically responsive cell	sensory system
forebrain neural rod	electrically active cell	presumptive telencephalon
forebrain neural tube	posterior neural rod	eye
presumptive forebrain	posterior presumptive neural plate	hindbrain
forebrain neural keel	midbrain neural tube	CNS neuron
forebrain neural plate	posterior neural plate	retina
nervous system	lateral line ganglion	posterior segment eye
spinal cord	midbrain neural rod	ganglion
central nervous system	head	cranial ganglion
presumptive neural retina	presumptive brain	spinal cord neural tube
visual system	presumptive midbrain	cavitated compound organ
diencephalon	retinal ganglion cell	neurectodermal cell
anterior neural tube	posterior neural keel	neuroblast
anterior neural rod	retinal inner nuclear layer	anterior presumptive neural plate
ectodermal cell	multi-tissue structure	immature eye
neuronal stem cell	hindbrain neural tube	anatomical group
peripheral nervous system	granular layer corpus cerebelli	presumptive hindbrain
anterior neural keel	lateral line system	neurogenic placode
anterior neural plate	tegmentum	hindbrain neural plate
electrically signaling cell	brainstem	ventro-rostral cluster
midbrain neural keel	hindbrain neural rod	organism subdivision
midbrain neural plate	embryonic structure	blastodisc

6.4.8.2 Differentially expressed genes in treated siblings - effect of Mn treatment alone

The effect of $MnCl_2$ exposure on the transcriptome of wild-type zebrafish was analysed in heterozygous and wild-type *slc39a14*^{U801} larvae at 5 dpf (**Table 6.3**). A large group of differentially expressed transcripts included genes involved in the regulation of the circadian clock[277]. This finding links the observed diurnal alteration of the locomotor behaviour upon Mn exposure in *slc39a14*^{U801} mutants with transcriptional changes of circadian clock genes. Re-analysis of the transcriptome data to examine the effect of Mn exposure independent of the genotype provided the same result suggesting that these circadian clock genes are differentially expressed in both wild-type and mutant larvae.

Other differentially expressed genes included *hamp2, egln3* and three genes encoding isoenzymes of the glutathione S transferase family – genes previously known to be affected by Mn[11,278,279]. The function of these genes is discussed in **Section 6.5.2**. Anatomical gene enrichment analysis showed that differentially expressed genes map to fore- and midbrain, optic tectum and retina (**Table 6.4**).

Table 6.3 Differentially expressed genes in $MnCl_2$ exposed heterozygous and wild-type *slc39a14*^{U801} larvae that can be linked to Mn homeostasis.

Gene name	Fold change	Function	e76 Ensembl Gene ID (ENSDARG)	Distance to 3' end (bp)	p-value
Circadian clock					
cry5	-9.6	Cryptochrome 5	00000019498	-73	1.53E-07
cry2b	-2.8	Cryptochrome 2b	00000091131	-2	1.26E-08
cry-dash	-2.3	Cryptochrome DASH	00000002396	0	0.0006
cry1a	-2.0	Cryptochrome 1a	00000045768	0	0.0001
per2	-4.7	Period homolog 2	00000034503	0	4.78E-08
nr1d4b	2.1	Nuclear receptor subfamily 1, group D, member 4b	00000059370	0	6.07E-10
nr1d4a	1.8	Nuclear receptor subfamily 1, group D, member 4a	00000031161	326	0.0111
nr1d2a	1.6	Nuclear receptor subfamily 1, group D, member 2a	00000003820	662	0.0012
Fe metabolism					
hamp2	-2.1	Hepcidin antimicrobial peptide 2	00000053227	0	0.0014
Hif pathway					

egln3	-3.4	Hif prolyl 4-hydroxylase 3 (Phd3)	00000032553	54	0.0199
Glutathione S transferases					
gstm3	-1.9	Glutathione S-transferase M3	00000088116	-1	0.0118
gsto2	-1.8	Glutathione S-transferase omega 2	00000033285	-5	0.0016
gstal	-1.5	Glutathione S-transferase, alpha-like	00000090228	-1	0.0066

Table 6.4 Anatomical gene enrichment of differentially expressed genes in $MnCl_2$ exposed wild-type *slc39a14^{U801}* larvae.

Anatomical region
optic tectum
midbrain
forebrain
retinal ganglion cell layer
alar plate midbrain region

6.4.8.3 Differentially expressed genes only evident in untreated mutants that are rescued by Mn treatment

The differentially expressed genes overlapped largely with those of homozygous *slc39a14^{U801}* mutants under physiological conditions without exposure to $MnCl_2$ (**Table 6.1**) with the exception of *syt6a*, *slc17a6a*, *abat* that were absent in this group. The result for the anatomical gene enrichment analysis was also similar to the findings of unexposed *slc39a14^{U801}* mutants (**Table 6.2**). This suggests that under physiological conditions without additional $MnCl_2$ exposure, homozygous *slc39a14^{U801}* mutants may display features of Mn deficiency possibly due to a tissue specific subcellular role of *slc39a14*.

6.4.8.4 Genes that are differentially expressed upon Mn treatment in treated mutants only

$MnCl_2$ exposure of homozygous *slc39a14^{U801}* mutants led to transcriptomic changes consistent with their impaired vision phenotype (**Table 6.5**). The biggest group of differentially expressed transcripts included retinal genes involved in photoreceptor

signalling and agrees with the observed impaired optokinetic response and abnormal visual background adaptation described in **Section 6.4.5**. Other gene groups included those involved in endoplasmic reticulum (ER) stress and apoptosis, GABA and glutamatergic signalling, circadian rhythm and a range of other brain expressed genes. The function of these genes is discussed in **Section 6.5.2**. Anatomical gene enrichment analysis again mapped the differentially expressed genes to the central nervous system including the retina (**Table 6.6**).

Table 6.5 Differentially expressed genes in $MnCl_2$ exposed homozygous *slc39a14*^{U801} larvae that can be linked to Mn homeostasis.

Gene name	Fold change	Function	e76 Ensembl Gene ID (ENSDARG)	Distance to 3' end (bp)	p-value
Retinal genes					
opn1mw2	5.2	Opsin 1, medium-wave-sensitive, 2	00000044280	0	2.45E-23
opn1mw1	-2.1	Opsin 1, medium-wave-sensitive, 1	00000097008	-1	7.25E-19
opn1lw2	-1.6	Opsin 1, long-wave-sensitive, 2	00000044861	-16	2.71E-06
gnat2	-2.2	G-protein, alpha transducing activity polypeptide 2	00000042529	-1	1.85E-18
gnat1	-1.5	G-protein, alpha transducing activity polypeptide 1	00000044199	1	0.0475
gnb3b	-2.1	G-protein beta polypeptide 3b	00000002696	-1	8.02E-15
gnb3a	-1.5	G-protein beta polypeptide 3a	00000004358	-6	0.0377
gngt2b	-1.7	G-protein, gamma transducing activity polypeptide 2b	00000089997	0	1.46E-09
gngt1	-1.6	G-protein, gamma transducing activity polypeptide 1	00000035798	-7	0.0080
grk7a	-2.8	G-protein-coupled receptor kinase 7a	00000020602	1640	0.0001
grk1b	-2.4	G protein-coupled receptor kinase 1b	00000011184	-7	1.25E-06
guca1d	-3.7	Guanylate cyclase activator 1d	00000044629	3140	1.90E-05
guca1c	-3.5	Guanylate cyclase activator 1c	00000030758	0	0.0004
guca1g	-3.3	Guanylate cyclase activator 1g	00000045737	657	1.50E-05
rgs9a	-2.9	Regulator of G-protein signaling 9a	00000037925	-4	2.95E-16
rgs9bp	-2.8	Regulator of G protein signaling 9 binding protein	00000009466	0	0.0138
pde6h	-6.2	Phosphodiesterase 6h	00000070439	-2	6.06E-49
rcv1	-1.6	Recoverin 1	00000019902	-5	1.26E-07
rcvrna	-2.3	Recoverin a	00000052223	1068	5.56E-09

arr3a	-1.9	Arrestin 3a	00000056511	-1	2.04E-09
cngb3	-2.6	Cyclic nucleotide gated channel beta 3	00000087082	225	2.52E-06
cnga3a	-2.4	Cyclic nucleotide gated channel alpha 3a	00000070726	2402	2.57E-05
cnga1	-1.9	Cyclic nucleotide gated channel alpha 1	00000029898	-75	0.0031
prph2b	-1.8	Peripherin 2b	00000014840	0	2.82E-08
prph2a	-1.5	Peripherin 2a	00000038018	2	0.0004
clul1	-3.2	Clusterin-like 1	00000055595	-10	8.60E-08
crb2b	-1.4	Crumbs homolog 2b	00000060081	523	0.0007
nxnl1	-3.1	Nucleoredoxin-like 1	00000052035	-73	0.0007
Circadian clock					
nr1d4a	-4.0	Nuclear receptor subfamily 1, group D, 4a	00000031161	1153	9.52E-13
nr1d4b	-1.6	Nuclear receptor subfamily 1, group D, 4b	00000059370	0	0.0008
nr1d1	-1.5	Nuclear receptor subfamily 1, group d, member 1	00000033160	3	0.0007
nr2f6b	-1.5	Nuclear receptor subfamily 2, group F, 6b	00000003165	82	0.0024
Unfolded protein response / apoptosis					
hspa5	2.9	Heat shock protein 5, GRP78	00000004665	0	3.94E-22
hsp90b1	1.7	Heat shock protein 90, beta member 1	00000003570	-1	0.0005
eif2ak3	1.9	Eukaryotic translation initiation factor 2-alpha kinase 3 (PERK)	00000062139	-1	0.0002
ddit4	-1.6	DNA-damage-inducible transcript 4, hif1-responsive protein	00000037618	-3	0.0117
sesn2	2.4	Sestrin 2, hypoxia or oxidative stress induced gene	00000070012	-1	0.0280
bri3bp	-5.6	Bri3 binding protein, apoptosis mediated by TNF	00000010108	1814	9.49E-12
nrm	-2.2	Nuclear envelope membrane protein, apoptosis	00000063690	4818	8.84E-10
faim2	2.8	Fas apoptotic inhibitory molecule 2	00000039444	0	3.57E-09
clu	1.6	Clusterin, brain, cell death	00000010434	0	3.75E-07
atf3	2.6	Activating transcription factor 3, apoptosis	00000007823	-1	0.0017
atf6	1.4	Activating transcription factor 6, apoptosis	00000012656	0	0.0363
atf5b	1.8	Activating transcription factor 5b,	00000077785	1143	0.0410

		apoptosis			
atf4b2	1.3	Activating transcription factor 4b2, apoptosis	00000038141	-2	0.0459
Mn transport					
tfr1a	2.3	Transferrin receptor 1a	00000058784	1869	0.0091
atp2b1b	-1.5	PMCA1	00000007788	6	0.0483
Other brain expressed genes					
slc1a2a	-4.4	Glial high affinity glutamate transporter member 2a	00000052138	1767	2.81E-18
slc1a2b	1.4	Glial high affinity glutamate transporter member 2b	00000009563	-2	5.92E-06
slc32a1	-1.4	GABA vesicular transporter, member 1 (VGAT1)	00000059775	5	0.0048
gabarap	-1.3	GABA(A) receptor-associated protein	00000052082	662	0.0363
syt5a	-1.8	Synaptotagmin Va	00000037941	5	0.0117
cplx4a	-1.8	Complexin 4a (SNARE complex)	00000059978	1040	2.70E-06
ntrk2b	3.1	Neurotrophic tyrosine kinase, type 2b	00000059645	2141	1.20E-08
inaa	-2.5	Internexin neuronal intermediate filament protein, alpha a	00000011862	0	1.99E-06

Table 6.6 Anatomical gene enrichment of DE genes in $MnCl_2$ exposed homozygous *slc39a14*^{U801} larvae.

Anatomical region		
epiphysis	diencephalon	forebrain neural rod
pineal complex	sensory system	presumptive forebrain
epithalamus	presumptive neural retina	eye photoreceptor cell
retina	optic vesicle	neuroblast
posterior segment eye	optic primordium	neuronal stem cell
visual system	portion of tissue	photoreceptor cell
retinal neural layer	anatomical cluster	organism subdivision
retinal photoreceptor layer	head	electrically signaling cell
forebrain	anterior neural plate	neuron
eye	anterior neural keel	electrically responsive cell
multi-tissue structure	anterior presumptive neural plate	electrically active cell
anatomical group	central nervous system	presumptive diencephalon
anatomical system	retinal outer nuclear layer	anatomical structure
endocrine system	brain	whole organism
cavitated compound organ	forebrain neural tube	neurectodermal cell

optic cup	retinal cone cell	ectodermal cell
nervous system	forebrain neural plate	multi fate stem cell
embryonic structure	forebrain neural keel	receptor cell

6.5 Discussion

6.5.1 Loss of *slc39a14* function in zebrafish mirrors the human phenotype

The *slc39a14*^{U801} zebrafish mutant demonstrates prominent Mn accumulation with Mn deposition in the brain similar to the human phenotype (**Section 6.4.2**). Homeostatic dysregulation is only observed for Mn while other divalent metal levels including Zn, Fe and Cd remain unchanged during larval development (**Section 6.4.1**). In *slc39a14*^{U801} mutants, Mn dyshomeostasis results in increased sensitivity to $MnCl_2$ toxicity and impaired locomotor behaviour upon $MnCl_2$ exposure (**Section 6.4.3**). This indicates a conserved function of SLC39A14 across vertebrates and confirms that SLC39A14 is a pivotal Mn transporter. It further corroborates the findings in humans that mutations in *SLC39A14* cause Mn neurotoxicity leading to parkinsonism-dystonia.

Increased sensitivity to Mn toxicity was indicated by a lower LC_{50} of $MnCl_2$ for *slc39a14*^{U801} mutants compared to wild-type larvae (**Section 6.4.1**). The observed LC_{50} for wild-types is significantly lower than reported in a similar study of environmental Mn exposure where it was more than ten times higher for wild-type larvae[280]. This variation may be caused by differences in zebrafish strains and culture media used. The number of embryos per well exposed to $MnCl_2$ may also influence the LC_{50}. In this work 20 larvae were placed in a well of a 6 well plate containing 10 mL of fishwater, however, only one larva per well of a 24 well plate in 2 mL of medium was analysed in the other study. Where several larvae are cultured together the dying larvae will adversely affect the water quality. Analysis of a single larva per well is therefore more likely to accurately assess a LC_{50}. However, as this work assessed differences between two genotypes rather than an absolute LC_{50}, the current approach should still be reliable.

Locomotor behaviour analysis showed a decrease in swimming activity in *slc39a14*^{U801} zebrafish mutants upon $MnCl_2$ exposure compared to wild-type larvae during the day while night activity appeared to be increased (**Section 6.4.3**). This was accompanied

by a subtle reduction of tyrosine hydroxylase positive cells in the ventral diencephalon (**Section 6.4.4**) suggesting an involvement of dopaminergic circuits. Environmental $MnCl_2$ exposure has been linked to locomotor deficits in wild-type zebrafish previously[259]. In that study, Mn exposure led to fewer startle movements and circling locomotion. The locomotor phenotype was attributed to a reversible impairment of dopamine neuromodulation. Similarly, $MnCl_2$ exposure in rats led to reduced locomotor activity and motor coordination which was associated with a decrease in the firing rate of neurons in the globus pallidus and substantia nigra. This was accompanied by decreased tissue levels of norepinephrine and serotonin while dopamine levels were increased[281]. Impairment of locomotor behaviour upon Mn exposure has also been shown for mice, however, this was accompanied by dopamine depletion and downregulation of DA transporter and receptors[118]. In flies the locomotor deficits upon Mn exposure were associated with increased acetylcholinesterase activity[282]. While Mn toxicity clearly affects locomotor behaviour characterised by hypokinesia the exact mechanisms of neurotransmitter impairment remain uncertain[22].
In rats, the locomotor behaviour impairment upon Mn exposure undergoes diurnal changes suggesting that Mn toxicity may disrupt the circadian clock[283]. Changes in levels of glutamine, GABA and dopamine have been linked to alterations in the circadian rhythm and may explain how Mn exposure affects the circadian clock[284]. Therefore, the observed diurnal alteration of locomotion in $MnCl_2$ exposed *slc39a14*^{U801} zebrafish mutants may be a consequence of disrupted circadian regulation which is further corroborated by the observation that the expression of circadian clock genes is altered upon $MnCl_2$ exposure (**Section 6.4.8.2**).

While *slc39a14*^{U801} zebrafish larvae show increased sensitivity to Mn toxicity when exposed to additional $MnCl_2$, under normal husbandry conditions they do not develop an apparent locomotor phenotype and have normal survival into adulthood. It is possible that zebrafish are better equipped with homeostatic mechanisms than humans given their harsh exposure to aquatic environmental toxins[285]. The gills are the major organ in teleost fish to conduct (metal) ion regulation and are specially adapted to respond to environmental challenges[286]. This might explain the more severe phenotype observed in humans than zebrafish.

In addition to the altered locomotor behaviour upon Mn exposure, *slc39a14*^{U801} mutants present with impaired visual background adaptation and optokinetic response (**Section**

6.4.5). Zebrafish larvae adjust the distribution of melanosomes within melanophores in their skin in order to adapt their body colour to the background. Light exposure leads to aggregation of melanophores while darkness causes dispersion allowing the body colour to turn paler or darker, respectively. Many zebrafish mutants with impaired visual behaviour and blindness lack this visual background adaptation[272,273]. Indeed, *slc39a14*^{U801} mutants develop impaired vision upon Mn exposure as shown by the diminished optokinetic response. Similar observations have been made in *slc30a8* loss-of-function zebrafish mutants that develop Zn overload and blindness (data from personal communication with Dr Eirinn Mackay, Department of Cell and Developmental Biology, University College London). Furthermore, Cd treatment in zebrafish causes microphthalmia, blindness and absent visual background adaptation. Cd affects neuronal differentiation of the retina with impaired retinal ganglion cell axon formation and absence of cone photoreceptors[287]. However, in patients with SLC39A14 and SLC30A10 deficiency, and environmental manganism vision is unaffected. Therefore, it seems that metal toxicity to the visual system is specific to zebrafish. Whether this is caused by neuronal death or functional defects in retinal circuitry needs to be determined.

Loss of *Slc39a14* function in mice causes growth retardation associated with reduced length of the long bones and fasting hypoglycemia with elevated insulin levels[233,253]. Neither of these features have been observed in human and there is no evidence of skeletal abnormalities in the zebrafish mutant. Whilst Mn levels have not been assessed in *Slc39a14-/-* mice, alterations in Zn and Fe absorption and trafficking have been reported[233,234]. *Slc39A14-/-* mice demonstrate enhanced hepatic Fe uptake via transcriptional upregulation of *DMT1* and *TfR-1*[233]. This is consistent with probable increased Fe content in abdominal viscera of adult *slc39a14*^{U801} zebrafish. It is possible that increased *DMT1* and *TfR-1* expression occurs in response to the high Mn load and indeed *tfr1b* expression increases upon Mn exposure in both wild-type and mutant zebrafish larvae[65]. Both of these transporters transport Mn and Fe interdependently[11,86]. A recent study of *Slc39a14-/-* mice suggests that Slc39a14 is also instrumental in the uptake of Cd into the liver with hepatic Cd levels being diminished while other organs including kidney, gut and lung showing Cd accumulation[288]. The *slc39a14*^{U801} mutants on the other hand do not demonstrate abnormalities in Cd levels.

The *slc39a14*^{U801} zebrafish mutant presents a model of Mn toxicity reflecting the human phenotype. It therefore has the potential to illuminate the mechanisms of Mn toxicity and provide new avenues for drug discovery for both rare and common neurodegenerative disorders associated with Mn toxicity. The mutant demonstrates several read outs for drug screening including the locomotor behaviour, the visual background adaptation and Mn levels. Indeed, Na_2CaEDTA when injected into the heart effectively lowers Mn levels in *slc39a14*^{U801} mutants. A drug screen to identify chelators that lower Mn levels effectively by immersion of zebrafish larvae may discover novel Mn chelators capable of gastrointestinal absorption.

Given that both SLC39A14 and SLC30A10 deficiency lead to Mn overload in humans, Slc39a14 and Slc30a10 were also assumed to function in the same pathway to facilitate Mn clearance in zebrafish. However, Mn accumulation in *slc30a10;slc39a14* double mutants was attenuated compared to *slc39a14*^{U801} mutants. This corroborates the findings in single *slc30a10*^{U800} mutants that suggest that *slc30a10* may play a different role in zebrafish (discussed in **Section 5.6.2**).

6.5.2 Mechanisms of Mn toxicity and consequences of SLC39A14 deficiency

Recently, environmental Mn exposure has been linked to impaired dopamine neuromodulation in zebrafish[259]. Indeed, TH immunohistochemistry indicated that *slc39a14*^{U801} mutants have reduced TH positive neurons in the ventral diencephalon that is augmented by Mn exposure (**Section 6.4.4**). Normal TUNEL staining further suggests that the reduction of TH positive cells is specific to dopaminergic cells rather than a generalised increase of apoptosis in the brain. While Mn neurotoxicity has been linked to dopaminergic dysfunction there is significant uncertainty to the exact mechanisms of altered dopaminergic signalling. Overall, the majority of published evidence suggests that Mn functionally affects dopaminergic neurotransmission with preserved dopaminergic cell morphology[22,114]. This is in contrast to the observation described in **Section 6.4.4** that TH positive cells are diminished in *slc39a14*^{U801} mutants. Whether this finding is real will need further confirmation and indeed there is some concern regarding the efficiency of the antibody used. Penetration of areas other than the ventral diencephalon and the signal return in general was poor indicating that the experimental protocol requires adaptation. The alternative approach using the *tg(SLC6A3:EGFP)* line was unsuccessful because the vast number of EGFP positive

neurons in the ventral diencephalon made an accurate assessment of the cell count using this methodology unachievable. Immunohistochemistry using an alternative anti-TH antibody and TH *in situ* hybridisation are likely to be more informative and answer this crucial question.

In order to globally assess the mechanisms of Mn neurotoxicity, RNA sequencing of *slc39a14*^{U801} mutants and wild-type larvae with and without Mn exposure was performed. Differing from expectation, RNA sequencing did not identify differentially expressed genes involved in dopaminergic signalling. However, it is possible that changes occur at a protein level and may therefore be missed by transcriptomic analysis.

RNA sequencing on the other hand did provide substantial evidence that neurotransmitter signalling is affected in SLC39A14 deficiency with differentially expressed genes mapping to the brain and eye which is consistent with the locomotor and optokinetic phenotype observed in *slc39a14*^{U801} mutants. Given that gaps remain in the annotation of the zebrafish genome, any results obtained by this method require confirmation by qPCR and/or *in situ* hybridisation. However, preliminary conclusions can be drawn from analysing groups of genes with similar gene ontology.

One intriguing observation was the finding that differentially expressed genes in unexposed *slc39a14*^{U801} mutants overlapped with those that normalised upon Mn treatment (**Section 6.4.8.1 and 6.4.8.3**). This suggests that Mn treatment in *slc39a14*^{U801} mutants rescues some of the transcriptomic changes observed in unexposed mutants. This is only possible if SLC39A14 deficiency leads to Mn deficiency in parallel to the observed Mn accumulation. Hence, it is likely that while SLC39A14 deficiency leads to systemic Mn accumulation it also causes deficiency of Mn in some parts of the cell or certain tissues due to its role as a Mn uptake transporter. This would suggest the following two disease mechanisms: firstly, impaired hepatic Mn uptake with subsequent Mn accumulation and toxicity in blood and brain as observed in SLC30A10 deficiency and environmental Mn overload, and secondly, subcellular and perhaps tissue specific Mn deficiency affecting Mn dependent signalling pathways, enzymatic reactions or transcription factors.

The latter would suggest that some features of SLC39A14 deficiency may overlap with the recently described disorder caused by deficiency of SLC39A8 (**Section 1.1**). Individuals with mutations in *SLC39A8* present with intellectual disability, developmental delay, hypotonia, epilepsy, strabismus, cerebellar atrophy and short stature[15,16]. However, patients with SLC39A14 deficiency did not develop short stature, epilepsy or strabismus, and intellectual ability appeared normal. Nevertheless, some patients did have signs of cerebellar atrophy. SLC39A8 deficiency is also associated with dysglycosylation corresponding to a type II CDG with impaired galactosylation[16]. Mn is an important cofactor for enzymes required for glycosylation in the Golgi[289-291], hence, Mn deficiency leads to an impairment of protein glycosylation. Patients with SLC39A8 deficiency show increased levels of trisialo, disialo, monosialo and asialo transferrin[16]. Transferrin glycosylation assessed in a patient with SLC39A14 deficiency (E-II-2) on the other hand was normal indicating that glycosylation is not affected in this disorder[65]. Hence, it seems that SLC39A14 deficiency does not share the characteristic features of SLC39A8 deficiency.

Should Mn deficiency play a role in the pathogenesis of SLC39A14 deficiency, this may have implications for Mn chelation treatment. Reducing Mn availability in parts of the cell or certain tissues may aggravate the neurological disease and lead to further decline. This may explain why the response of the two patients with SLC39A14 deficiency treated with $Na_2CaEDTA$ chelation was remarkably different. Patient C-II-2 who experienced a striking clinical recovery carries mutations solely affecting isoform 2 that is thought to facilitate Mn detoxification. Patient E-II-2 on the other hand continued to deteriorate despite treatment. It is possible that loss-of-function of all isoforms in this individual causes neurodegeneration through two mechanisms, Mn deficiency and Mn toxicity. However, the less favourable treatment response in this patient may as well be attributed to the advanced stage of neurological disease.

Differentially expressed genes identified in unexposed *slc39a14*^{U801} mutants compared to wild-types encode pre- and post-synaptic proteins involved in neurotransmitter signalling (**Section 6.4.8.1**). Some of them are part of the SNARE-synaptotagmin complex required for neurotransmitter release (**Figure 6.35**)[276]. Synaptic vesicle exocytosis occurs following the binding of Ca^{2+}. Interestingly, synaptotagmin I can bind Ca^{2+} and Mn^{2+} in the same manner[292]. Mn dyshomeostasis may therefore directly affect neurotransmitter release by replacing Ca^{2+} at its binding site. Other differentialy

expressed genes include some that encode glutamatergic and GABAergic receptor subunits (**Table 6.1**). Mn toxicity is known to disrupt glutamate and GABA signalling[128,137,293-296]. For instance, Mn neurotoxicity is associated with alterations in extracellular GABA levels which may be explained by altered receptor expression[297]. Mn also functions as a potent inhibitor of the NMDA receptor thereby affecting glutamate signalling[298]. These results strengthen the hypothesis that Mn dyshomeostasis affects neurotransmitter signalling. Further study of these candidate genes may shed new light on the specific neurotransmitter systems involved. Whether the changes in gene expression observed in *slc39a14*^{U801} mutants are due to Mn toxicity or partial deficiency has yet to be determined.

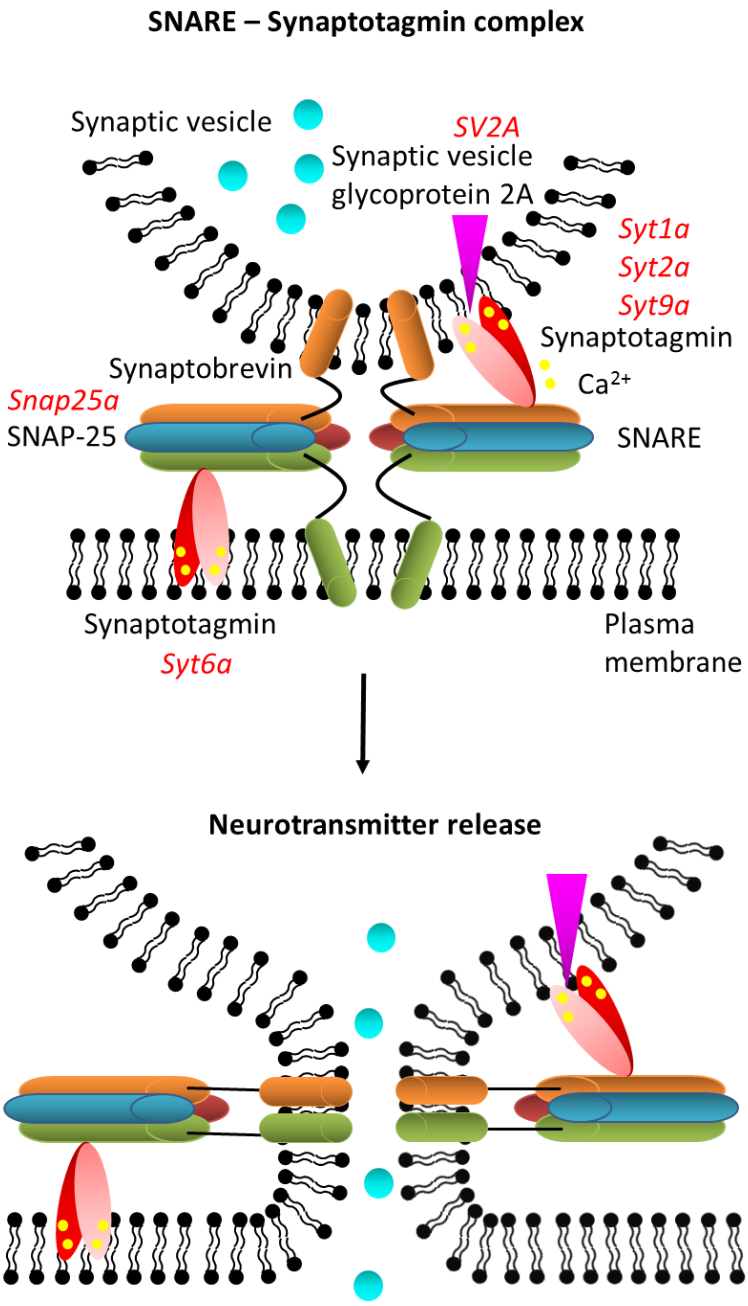

Figure 6.35 Differentially expressed genes in *slc39a14*^{U801} mutants are involved in the formation of the SNARE-synaptotagmin complex.

A schematic showing the components of the SNARE-synaptotagmin complex affected by loss of slc39a14 function at transcriptional level. DE genes in red. Binding of Ca^{2+} (yellow) to synaptotagmin facilitates fusion of the plasma membrane and the synaptic vesicle through conformational changes of proteins of the SNARE-synaptotagmin complex leading to pore formation and neurotransmitter release. Syt, synaptotagmin. SNAP, Synaptosomal-Associated Protein. SV, synaptic vesicle. Adapted from Rizo et al.[276]

Gene expression of *bdnf*, encoding the brain derived neurotrophic factor (BDNF), was also found to be downregulated in *slc39a14*^{U801} mutants. BDNF is an extracellular signalling molecule that inhibits the retrieval of synaptic vesicles from the plasma membrane with subsequent enhancement of neurotransmission[299]. Furthermore, BDNF has several trophic roles promoting neuronal cell survival, neurite growth and cell migration, particularly during glutamatergic synaptic development. BDNF signals through its receptor tyrosine kinase B (TrkB) activating MAPK, phosphoinositide 3-kinase (PI3K) or phospholipase C gamma (PLCγ) pathways regulating synaptic activity and plasticity, gene transcription, and protein translation and transport[300]. Interestingly, it has been shown previously that Mn exposure is associated with lower plasma BDNF levels in occupational manganism[301]. Also, Mn treated rats develop lower BDNF levels which is suggested to affect cAMP signalling in the hippocampus[302]. BDNF is therefore likely to play a crucial role in the disease mechanisms of SLC39A14 deficiency.

Transcriptome analysis of both Mn exposed wild-type and mutant larvae identified several differentially expressed genes involved in the regulation of the circadian clock (**Section 6.4.8.2**). These include cryptochrome genes, a period gene and genes of the nuclear receptor 1d family (**Table 6.3**) that are known to regulate the circadian clock feedback loops[303,304]. Mn has previously been shown to abolish circadian variation of beta-adrenceptor expression[305]. Furthermore, the observed diurnal locomotor behaviour changes upon Mn exposure in *slc39a14*^{U801} mutants (**Section 6.4.3**) would be consistent with Mn associated disruption of the circadian clock. Similar locomotor behaviour alterations have been reported in rats exposed to excess Mn previously[283]. These may occur secondary to changes in striatal dopamine, GABA and glutamate levels upon Mn exposure[284]. Indeed, Mn treatment of *slc39a14*^{U801} mutants lead to expression changes of genes involved in GABA and glutamatergic neurotransmitter signalling (**Table 6.5**).

Other noteworthy differentially expressed genes in Mn treated wild-type larvae include *hamp2* and *egln3*, genes previously linked with Mn metabolism. *Hamp2* encodes hepcidin, the main regulatory hormone of Fe homeostasis[101]. As Mn and Fe transport are closely interlinked[6,10,11,79,97,98] it is expected that Mn overload has consequences for mechanisms regulating Fe uptake. *Egln3* encodes one of three prolyl hydroxylases (phd3) involved in the regulation of the hif-pathway[279,306] (**Figure 1.1**). Mn exposed wild-type zebrafish show downregulation of *egln3* which may result in stabilisation of Hifα. This may help explain the mechanism leading to polycythaemia in patients with

SLC30A10 deficiency due to the high Mn load. Cell culture studies have previously shown that 24 hour exposure to Mn concentrations as low as 50 µM induce erythropoietin protein expression[307]. In *slc39a14*^{U801} mutants, Mn levels were raised at an average of 70 pg at 5 dpf. Assuming that the volume of a 5 dpf larva is similar to that of a freshly laid egg with a diameter of 0.7 mm and a volume of around 0.18 µL, the actual Mn concentration in mutant larvae equates to 7 µM. Although this Mn concentration has not been tested in cell culture it seems reasonable to assume that over a time period longer than 24 hours this concentration may well activate the hif pathway. From human patients we know that hepatic manganese concentrations are raised 2- to 9-fold which lead to increased erythropoietin blood levels[50, 210]. Similar to that, mutant fish manganese levels are raised 1.5-fold at 5 dpf and 4-fold at 14 dpf. This suggests that the observed Mn concentration is indeed in the range of that required for the activation of the hif pathway.

While it seems plausible that the hif pathway is affected by Mn toxicity which is corroborated by the finding of polycythaemia and increased erythropoietin expression in human patients, it is important to remember that the main hydroxylase responsible for hif inhibition is egln1 and not egln3. *Egln3* is highly upregulated in Vhl zebrafish loss-of-function mutants and acts as a reporter of hif function[306]. Gene downregulation of *egln3* may therefore paradoxically suggest a drop in hif signalling in mutant zebrafish. Further work is required to delineate the effect of Mn on the hif pathway.

Mn exposure of *slc39a14*^{U801} mutants revealed expression changes of numerous retinal genes that are involved in phototransduction (**Figure 6.36, Section 6.4.8.4**)[308-312]. These included genes required for the activation of phototransduction such as those encoding cone opsins, G-proteins, phosphodiesterase (PDE), guanylcyclase activating proteins (GCAPs), and cyclic nucleotide gated cation channels (CNGs). Also, genes involved in the deactivation of phototransduction including G-protein coupled receptor kinases, arrestin, recoverin and regulators of G-protein signalling were identified (**Table 6.5**). Mutations in the majority of these genes are known to cause retinal dystrophies in humans[313]. Further work is required to pinpoint the basis of the observed visual defect. The function of the outer retina can be assessed using electroretinography. The measured sum field potentials of the retina give a ready read-out of light perception of photoreceptor and subsequent synaptic transmission to bipolar cells[314]. Since light perception is not completely abolished as indicated by the optokinetic response result (**Section 6.4.5**), at least some photoreceptors are expected

to be functional. Ideally, future studies should involve the study of synaptic transmission using antibodies against proteins of the photoreceptor synapse such as the glutamate transporters, and transgenic constructs to establish which connections are abnormal.

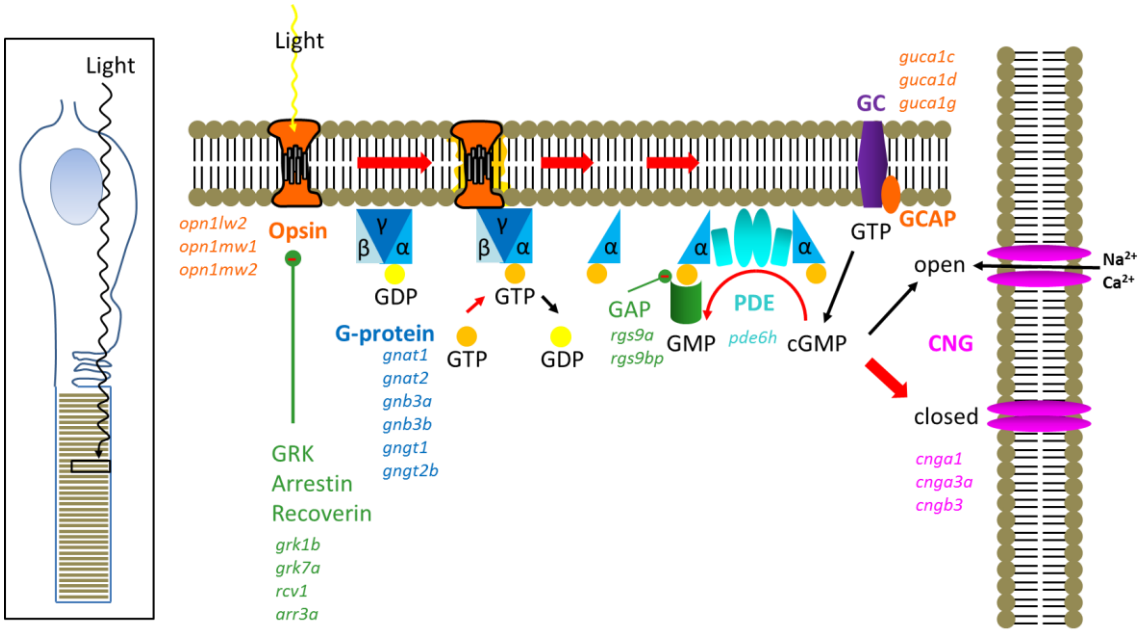

Figure 6.36 Mechanisms of visual phototransduction.

Schematic displaying the ciliary outer segment of a photoreceptor that contains the photopigments. In darkness cyclic guanosine monophosphate (cGMP) maintains the cyclic nucleotide gated non-selective cation channels (CNG) at the plasma membrane in an open state allowing a steady inward current and depolarisation (dark current). cGMP is steadily produced by a guanylyl cyclase (GC) that is activated by guanylate cyclase activating protein (GCAP). A light photon leads to photoactivation of the opsin through conformational change that activates a G-protein which subsequently stimulates a phosphodiesterase (PDE) resulting in hydrolysis of cGMP. The reduction of cGMP facilitates the closure of the CNGs and subsequent hyperpolarisation of the cell. Deactivation of phototransduction is facilitated by opsin phosphorylation through G-protein coupled receptor kinase (GRK) and binding of arrestin. GTPase activating protein (GAP) promotes deactivation of the G-protein through conversion of GTP to GDP. Red arrows indicate the pathway of activation of phototransduction, green errors the deactivation. DE genes of Mn exposed slc39a14^{U801} mutants in italics. Adapted from Kaup et al.[308]

Other differentially expressed genes indicated a stress response upon Mn exposure in *slc39a14*^{U801} mutants and included genes involved in the unfolded protein response (UPR) in the ER and apoptotic pathways (**Table 6.5**). ER stress occurs when misfolded proteins overload the protein folding capacity of the ER. This leads to activation of the UPR with subsequent increase of the ER folding capacity and reduction of misfolded protein through transcriptional and translational changes facilitating proteasomal degradation (**Figure 6.37**). Continuous ER stress activates the apoptotic cascade resulting in cell death[315]. Mn toxicity has been previously shown to activate UPR pathways similar to observations with other heavy metals[316-321]. Indeed, Mn exposure of *slc39a14*^{U801} mutants led to upregulation of genes encoding heat shock proteins (HSP) *hsp5* and *hsp90*[320,322]. Heat shock proteins are molecular chaperones required for protein folding[323]. *Hsp5* encoding glucose regulated protein 78 (GRP78) associates with the transmembrane ER stress sensors inositol-requiring kinase 1 (IRE1), activating transcription factor 6 (ATF6) and PKR-like eukaryotic initiation factor 2a kinase (PERK) (**Figure 6.36**). It suppresses the activity of the UPR and is required for the maintenance of ER integrity[324]. HSP90 stabilises key components of the UPR pathway such as IRE1[325,326]. Therefore, the identified transcriptomic changes suggest that Mn toxicity leads to ER stress and activation of the UPR.

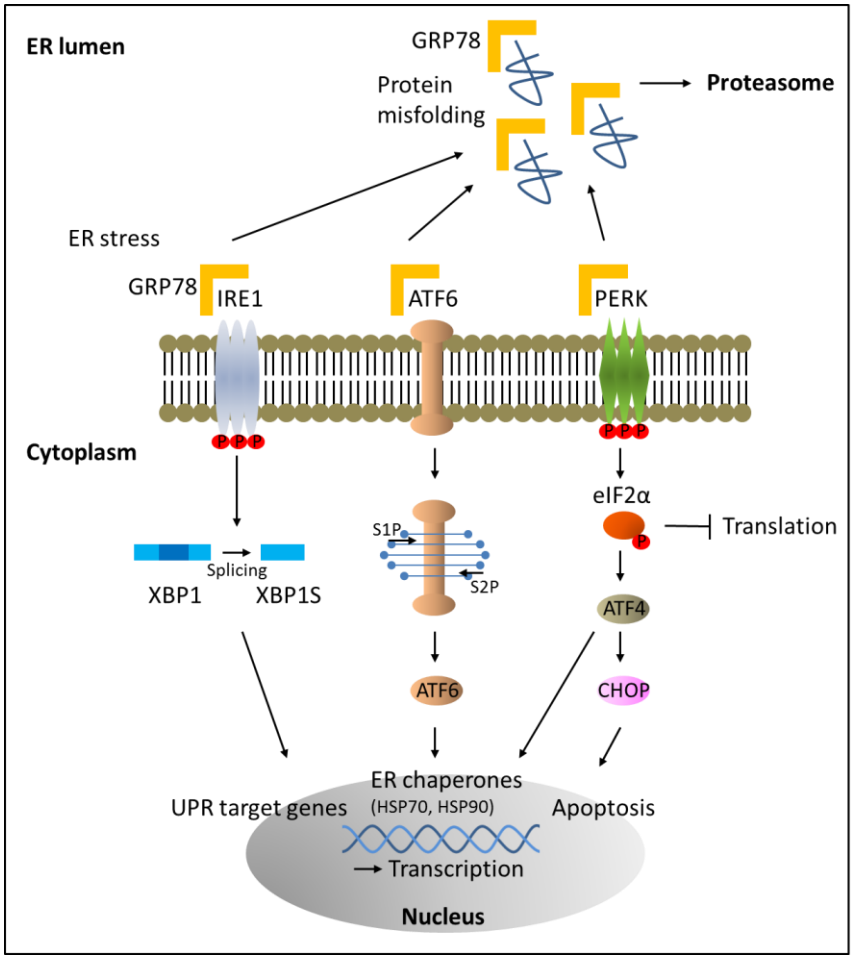

Figure 6.37 Unfolded protein response pathways.

Schematic illustrating the function of the three ER stress sensors IRE1, PERK and ATF6. Under physiological conditions IRE1, ATF6, and PERK are bound by GRP78 rendering them inactive. Upon accumulation of misfolded proteins in the ER lumen, GRP78 binds misfolded proteins and releases the ER stress sensors. IRE1 and PERK autophosphorylate and activate downstream signaling cascades. IRE1 splices XBP1 mRNA with subsequent translation of the transcription factor that upregulates UPR target genes. PERK phosphorylates eukaryotic initiation factor 2 alpha (eIF2α) leading to inhibition of translation and increased expression of ATF4, which then upregulates transcription of ER chaperones and activation of pro-apoptotic pathways that depend on the production of the CHOP transcription factor. Site-1 protease (S1P) and Site-2 protease (S2P) release the N-terminal domain of ATF6 that translocates to the nucleus to upregulate genes encoding ER chaperones such as HSP70 and HSP90. IRE1, inositol-requiring kinase 1; ATF6, activating transcription factor 6; PERK, PKR-like eukaryotic initiation factor 2a kinase; XBP1, X-box binding protein 1; ATF4, activating transcription factor 4. Adapted from Kaufman et al., Lajoie et al. and Marre et al.[327-329]

Some effects of Mn exposure on the expression levels of divalent cation transporters in *slc39a14*^{U801} mutants were identified by transcriptome analysis. RNA sequencing suggested that both *atp2b1b* and *tfr1a* were altered upon Mn exposure. *atp2b1b* encodes a plasma membrane calcium ATPase 1 (PMCA1) involved in Ca uptake that may well be capable of transporting Mn and hence undergoes downregulation upon Mn overload[330]. In zebrafish two *tfr1* paralogues are involved in Fe acquisition with different spatial tissue expression. *tfr1a* is mainly found in erythroid precursor cells where it is required for Hb production while *tfr1b* is primarily expressed in the brain[331]. Given that Fe and Mn homeostasis are closely interlinked, it is not surprising that transcript levels of this receptor are altered in *slc39a14*^{U801} mutants and upon Mn exposure. Perhaps surprisingly, RNA sequencing found gene expression of *slc30a10* not to be altered in *slc39a14*^{U801} mutants. However, it is possible that in *slc39a14*^{U801} mutants, Mn dyshomeostasis leads to altered protein expression or redistribution of the transporter rather than inducing transcriptional changes.

qPCR analysis showed a trend towards increased *tfr1a* expression in *slc39a14*^{U801} mutant larvae but the finding was not statistically significant (**Section 6.4.2**). On the other hand, qPCR analysis found downregulation of *slc39a8* and upregulation of *tfr1b* expression upon Mn overexposure in both wild-type and mutant larvae that was not identified by transcript counting. The observation that *slc39a8* expression is downregulated upon Mn overexposure is consistent with its recently identified function of the acquisition of Mn[15,16].

Chapter 7. Summary and Future Work

Until recently, very little was known about the regulation of Mn homeostasis *in vivo*. The identification of the inherited Mn transportopathies caused by mutations in *SLC30A10*[46,48], *SLC39A8*[15,16] and *SLC39A14*[65] has dramatically advanced our understanding how Mn is trafficked across the cell and throughout the organism. It has highlighted a novel group of transporters that has previously been thought to be important for Zn and Fe transfer but is crucial for Mn homeostasis. As with many other monogenic disorders, we have gained new insights into vertebrate gene function by studying human patients.

As discussed in **Chapter 1 and 3**, SLC30A10 is a pivotal Mn transporter expressed in liver and brain that is required for the detoxification of Mn from the cell and final hepatobiliary excretion. This work has shown that SLC39A14 is essential for Mn uptake into the liver for subsequent biliary excretion through SLC30A10 (**Chapter 4**). SLC39A14 may have further crucial roles in the uptake of Mn in certain tissues and cell organelles. SLC39A8 on the other hand facilitates Mn uptake into the organism and cell[15,16]. The established roles of these transporters explain the clinical features observed in individuals affected by the three inherited Mn transportopathies. SLC30A10 deficiency causes accumulation of Mn in the blood, brain and liver leading to hypermanganesaemia, dystonia-parkinsonism, polycythaemia and cirrhosis (**Chapter 3**). In SLC39A14 deficiency Mn accumulates in the blood and brain causing hypermanganesaemia and dystonia-parkinsonism but no cirrhosis or polycythaemia (**Chapter 4**). SLC39A8 deficiency causes a Mn depletion syndrome with resulting cerebellar atrophy, epilepsy, developmental delay, hypotonia, short-stature and severe dysglycosylation – the biochemical hallmark of this disorder[15,16]. Study of further patients with similar clinical features will allow an estimation of the population incidence, and a better delineation of the phenotypical spectrum and genotype-phenotype correlation. For SLC30A10 deficiency we know that a late-onset form exists that mimics Parkinson's disease[48]. Residual transporter protein function is likely to account for the delayed onset. It is also possible that individuals with mutations in *SLC39A14* that do not lead to complete loss of protein function present with late-onset parkinsonism. As clinicians' awareness of the characteristic MRI brain features of Mn deposition increase, it is expected that more patients with SLC30A10 and SLC39A14 deficiency will be diagnosed. $Na_2CaEDTA$ is extremely effective in mobilising Mn in

both SLC30A10 and SLC39A14 deficiency. Patients with SLC30A10 deficiency respond well to Mn chelation with improvement of neurological symptoms and stabilisation of liver disease. While one patient with SLC39A14 deficiency has shown dramatic improvement upon chelation treatment, a second patient had a less favourable response. The consequences of Mn chelation in SLC39A14 deficiency will need to be assessed further. As discussed in **Chapter 4 and 6**, while impaired SLC39A14 transporter function causes marked Mn neurotoxicity it may also lead to subcellular Mn deficiency that may be worsened by Mn chelation.

Ultimately, identification of effective oral Mn chelators is crucial to relieve the treatment burden of intravenous $Na_2CaEDTA$ application. As shown in **Chapter 6**, the generated zebrafish *slc3914*^{U801} loss-of-function mutant presents a promising animal model to assess the effect of Mn chelators on Mn levels and locomotor behaviour as well as other small molecules with potentially disease modifying effect. Several antioxidants have been shown to protect against Mn associated cytotoxicity and may therefore alleviate Mn neurotoxicity[143,282,332,333]. Recovery of neurological symptoms in SLC30A10 and SLC39A14 deficiency implies that in addition to neuronal death, circuit dysfunction must in part be caused by interference of Mn with some unknown aspects of neuronal function. The *slc3914*^{U801} zebrafish mutant mirrors the human phenotype of Mn accumulation in the brain and locomotor impairment. Additionally, visual phototransduction is affected by Mn toxicity in zebrafish. Study of the functional defects in retinal circuitry offers an excellent opportunity to discover the mechanisms underlying Mn dependent disruptions to circuit function in vertebrates.

As described in **Chapter 6**, RNA sequencing of *slc3914*^{U801} loss-of-function mutants has highlighted numerous brain expressed genes involved in neurotransmitter signalling and release, ER stress, HIF signalling and circadian rhythm to be affected by Mn dyshomeostasis. Confirmation of these findings and study of the involved pathways may shed new light on our understanding of how Mn is both essential and disruptive to neurological function. Identification of the mechanisms involved in Mn toxicity may ultimately ascertain novel treatment targets in other neurodegenerative disorders associated with Mn dyshomeostasis such as inherited forms of Parkinson's disease[334].

As discussed in **Chapter 5**, the *slc30a10*^{U800} zebrafish mutant unexpectedly did not recapitulate the human phenotype. While Mn accumulation appears to occur under

physiological husbandry conditions, *slc30a10*^{U800} mutants show an attenuated response to Mn toxicity. Further analysis is required to determine whether this result is a consequence of the analysed time point during zebrafish development or whether the function of Slc30a10 or response to loss of Slc30a10 function in zebrafish may be different to that in human.

While the functions of SLC30A10 and SLC39A14 have been substantively delineated, functional analysis of SLC39A8 with regard to its involvement in the regulation of Mn homeostasis has been minimal. Preliminary results show that a *slc39a8* loss-of-function zebrafish mutant presents a promising tool for the study of this transporter *in vivo* (see **Appendix 1**).

The applied TALEN and CRISPR/Cas9 genome editing methods present a powerful tool to generate loss-of-function mutants of single genes but also analyse the function of non-coding genes, gene clusters or regulatory sequences by deletion of large regions through simultaneous disruption at two different sites on a chromosome. TALENs were generated using the FLASH assembly method[188] (**Chapter 2**). The protocol to generate the TALEN mRNAs for injection into zebrafish embryos is time consuming and involves approximately one month of intensive lab work. Ligation of the DNA fragments encoding the TAL effector repeats was often incomplete. Therefore, a high number of clones required screening in order to identify those encoding the full length of the TALEN arrays. The costs for consumables is substantial. On the other hand, the cutting efficiency of the generated TALENs is high, in most cases affecting more than 90% of injected embryos, with efficient germline mutagenesis. Survival of injected embryos was high with a low number of deformed embryos at the concentration of TALEN mRNAs used. Generation of stable lines was unproblematic and the progeny of F0 injected fish looked healthy with good survival. In-cross of mutant fish had a low rate of deformed embryos suggesting a low genotoxicity through off-target effects.

The protocol to generate the CRISPR gRNAs and Cas9 nuclease on the other hand is extremely simple and quick with an average time from CRISPR design to mRNA injection of one week (**Chapter 2**). The modfication published by Gagnon *et al.*[335] which involves annealing a gene-specific and a constant oligonucleotide further simplifies the protocol. Cutting efficiency and germline mutagenesis was similarly high

as observed with TALENs. However, when propagating the F0 generation a high number of deformed embryos was obtained with poor survival. Furthermore, in-cross of mutant fish over several generations produced malformed embryos suggesting that off-target effects may indeed be present. gRNAs can tolerate mismatches leading to the high frequency of off-target effects[336,337]. The TALEN pair on the other hand requires binding to two opposite DNA sites separated by a spacer region. It appears that TALENs are therefore more specific by default[338]. However, for generation of loss-of-function zebrafish mutants the CRISPR/Cas9 system used here presents an extremely efficient and simple method to analyse gene function *in vivo* in a vertebrate organism.

As demonstrated in **Chapter 5 and 6**, zebrafish has proven a powerful animal model to study metal transporter function and model human disorders in a vertebrate organism. The generated *slc30a10*^{U800} and *slc39a14*^{U801} lines have the potential to illuminate the mechanisms of Mn toxicity and provide new avenues for drug discovery for both rare and common neurodegenerative disorders associated with Mn toxicity.

TALEN and CRISPR approaches to disrupt gene function can be applied to any other inherited metabolic disorder in order to study disease processes and gene function. This is of particular importance as with the emergence of next generation sequencing techniques a large number of novel candidate genes are being identified that require functional analysis. Genome engineering in zebrafish provides an excellent model to functionally assess those sequence variants *in vivo*.

Appendix

1. Combined TALEN/CRISPR injections generate large genomic deletions

1.1 Introduction

The TALEN and CRISPR methodology was also investigated to generate much larger genomic deletions. This could be useful for several reasons: (i) several exons can be deleted at once reducing the likelihood that an alternative transcript or start codon could compensate for loss of gene function, (ii) to study the function of regulatory sequences such as promoter regions. To achieve this a double injection approach of TALEN mRNAs and CRISPR gRNA/Cas9 mRNA was attempted.

1.2 Combined TALEN / CRISPR injections to generate large deletions in *slc30a10*

The TALEN mRNA pair targeting exon 1 of *slc30a10* (**Section 5.3.1**) was co-injected with the gRNA/Cas9 mRNA targeting exon 3 of *slc30a10* (**Section 5.3.2**) in one cell stage embryos (**Figure A1a**). DNA was extracted at 1 dpf and PCR amplified using a forward primer upstream of the TALEN binding site and a reverse primer downstream of the CRISPR target site. If deletion of the targeted region had occurred an amplicon of approximately 230 bp would be expected. Indeed, 13 out of 16 injected embryos had a visible band of 230 bp suggesting that a deletion had been introduced (**Figure A1b**). Positive gel bands were purified, cloned into the pCRII-TOPO vector and sequenced. Sequencing results confirmed the presence of genomic deletions spanning >2.1 kb (**Figure A1c**).

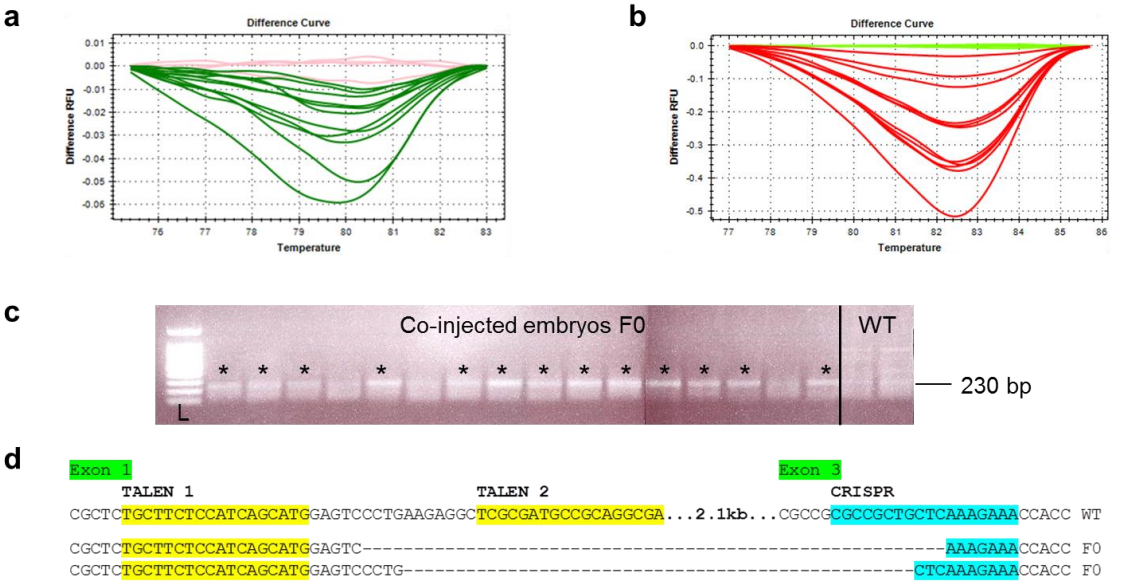

Figure A1 Targeting two loci within *slc30a10* by TALEN/CRISPR nucleases generates large genomic deletions.

*HRMA result confirming the mutagenic efficiency of the (**a**) TALEN pair, un-injected embryos in pink, injected embryos in green, and (**b**) CRISPR gRNA, un-injected embryos in green, injected embryos in red. (**c**) PCR result of co-injected embryos. * 13 out of 16 injected embryos show a 230 bp band indicating that deletion of the region spanning the two target sites had occurred. (**d**) Wild-type (WT) slc30a10 genomic sequence given on the top, introduced deletions displayed below. TALEN binding arms are marked in yellow, CRISPR target region in turquoise. The targeted loci are approximately 2.1 kb apart.*

1.3 Double CRISPR injections to generate large deletions in *slc39a14*

gRNAs with target sites in exon 5 and 8 (9 kb apart) or exon 5 and 9 (11.5 kb apart) were co-injected together with Cas9 mRNA into on cell stage embryos (**Figures A2a and A3a**). DNA was extracted from co-injected embryos at 1 dpf and PCR amplified using a forward primer upstream of the target site in exon 5 and a reverse primer downstream of the target site in exon 8 or 9. If deletion of the region spanning the two target sites had occurred an amplicon of approximately 290 bp and 280 bp would be expected. Indeed, 15 out 17 and 13 out of 17 embryos screened positive for large

deletions across exon 5 to 8 and exon 5 to 9, respectively (**Figures A2b and A3b**). Agarose gel bands of the correct size were purified, cloned into pCRII-TOPO vector and sequenced. The sequencing results confirmed that genomic deletions spanning >9 kb and >11.5 kb had been generated (**Figures A2c and A3c**).

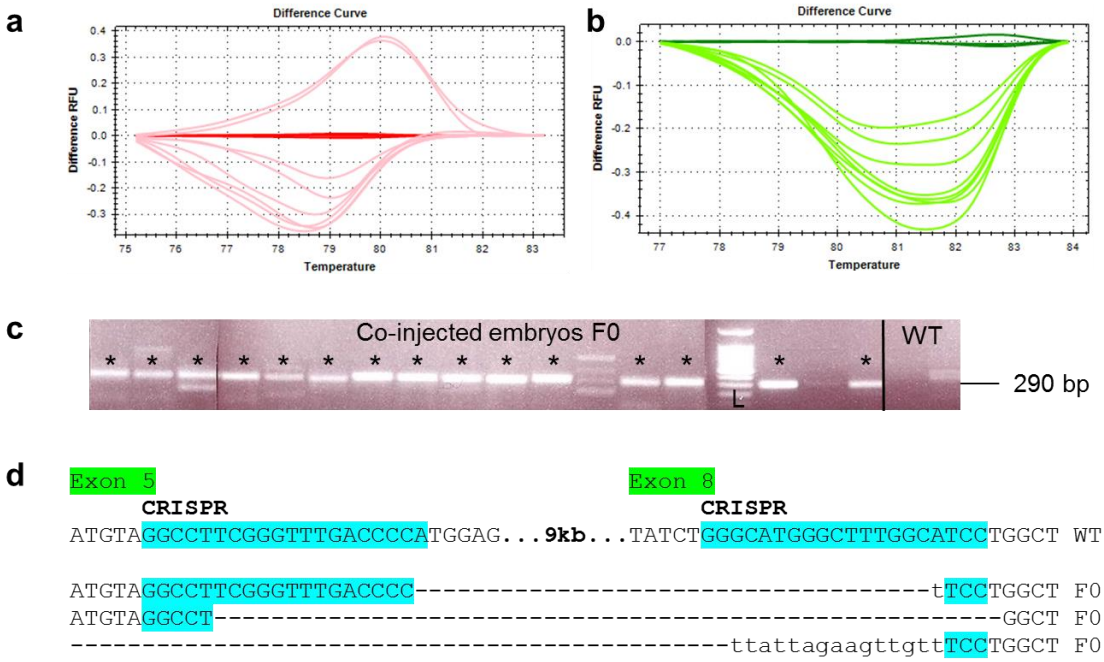

Figure A2 A "double CRISPR approach" targeting two loci within exon 5 and 8 of *slc39a14* introduces large genomic deletions spanning over 9 kb.

*HRMA result confirming the mutagenic efficiency of each individual gRNA/Cas9 to (**a**) exon 5 (un-injected embryos in red, injected embryos in pink) and (**b**) exon 8 (un-injected embryos in dark green, injected embryos in light green). (**c**) Gel electrophoresis image of PCR products amplified from DNA extracted from co-injected embryos using primers to exon 5 and 8. * 15 out of 17 injected embryos show the expected 290 bp band compared to un-injected embryos (WT) indicating that a deletion had occurred. (**d**) Wild-type (WT) sequence is given on the top, introduced deletions displayed below. The CRISPR target regions are highlighted in turquoise. The targeted loci are approximately 9 kb apart.*

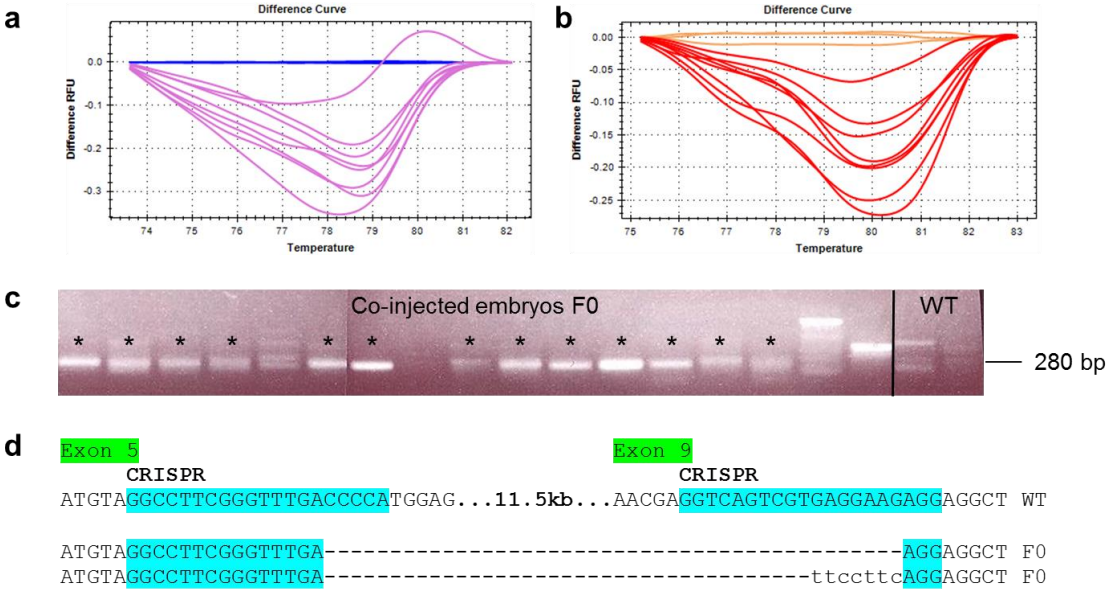

Figure A3 A "double CRISPR approach" targeting two loci within exon 5 and 9 of *slc39a14* can effectively introduce large genomic deletions spanning 11.5 kb.
*HRMA result confirming mutagenic efficiency of each individual gRNA/Cas9 to (**a**) exon 5 (un-injected embryos in blue, injected embryos in purple) and (**b**) exon 9 (un-injected embryos in orange, injected embryos in red). (**c**) Gel electrophoresis image of PCR products amplified from DNA extracted from co-injected embryos using primers to exon 5 and 9. * 13 out of 17 injected embryos show the expected band of 280 bp compared to un-injected (WT) embryos indicating that a deletion had occurred. (**d**) Wild-type (WT) sequence is given on the top, introduced deletions displayed below. CRISPR target regions are highlighted in turquoise.*

1.4 Discussion

The attempted double injection approach using the TALEN/CRISPR methodology to target two loci was shown to effectively generate genomic deletions of up to 11.5 kb. Screening for effective mutagenesis and to identify founders in the F1 generation can simply be performed by PCR using a forward primer upstream of the first and a reverse primer downstream of the second target site. This approach facilitates deletion of several exons ensuring that multiple transcripts are targeted at the same time and prevent compensation for loss of gene function through an alternative transcript or start codon. Additionally, large intronic regions as well as regulatory sequences can be deleted allowing for instance the study of promoter functions.

2. Preliminary results

2.1 Delineating the function of *slc39a8* in zebrafish

With the identification of SLC30A10 and SLC39A14 as pivotal Mn transporters involved in Mn clearance in vertebrates we have reached a better understanding of the mechanisms underlying Mn homeostasis. However, it remains unclear which is the primary Mn transporter facilitating Mn uptake in the gut, the main site of Mn uptake in humans. Recently, mutations in *SLC39A8* have been suggested to cause a novel autosomal recessive syndrome characterised by Mn deficiency, cerebellar atrophy, skeletal dysplasia, cognitive impairment and a defect of glycosylation[15,16]. *SLC39A8* shares close sequence homology with *SLC39A14*, is known to be expressed in the gut in humans and has been shown to transport Mn *in vitro*[69,72,73]. Therefore, SLC39A8 is likely to play an essential role in Mn homeostasis. In order to assess its function *in vivo* a similar CRISPR approach as described earlier was used to generate a *slc39a8* loss-of-function zebrafish mutant. The results presented here were obtained by Alaa Doubi, an MSc student under my supervision during 01/2015 to 08/2015.

2.2 Characterisation of *slc39a8* in zebrafish

Slc39a8 expression is present in zebrafish larvae as early as 12 hpf and remains expressed throughout embryonic and early larval development between 1 dpf and 5 dpf (**Figure A4**). The eight exons of zebrafish *slc39a8* encode a protein of 448 amino acids that shares 51 percent sequence homology with the human protein (**Figure A5**). Particularly high conservation is found around the TMDs and the metal binding motif EEFPHE[73]. A second transcript has recently been published as part of the latest Ensembl genome assembly for zebrafish (GRCz10). This second transcript consists only of three exons (exon 6-8) encoding a significantly shorter protein of 183 amino acids that lacks the first four TMDs.

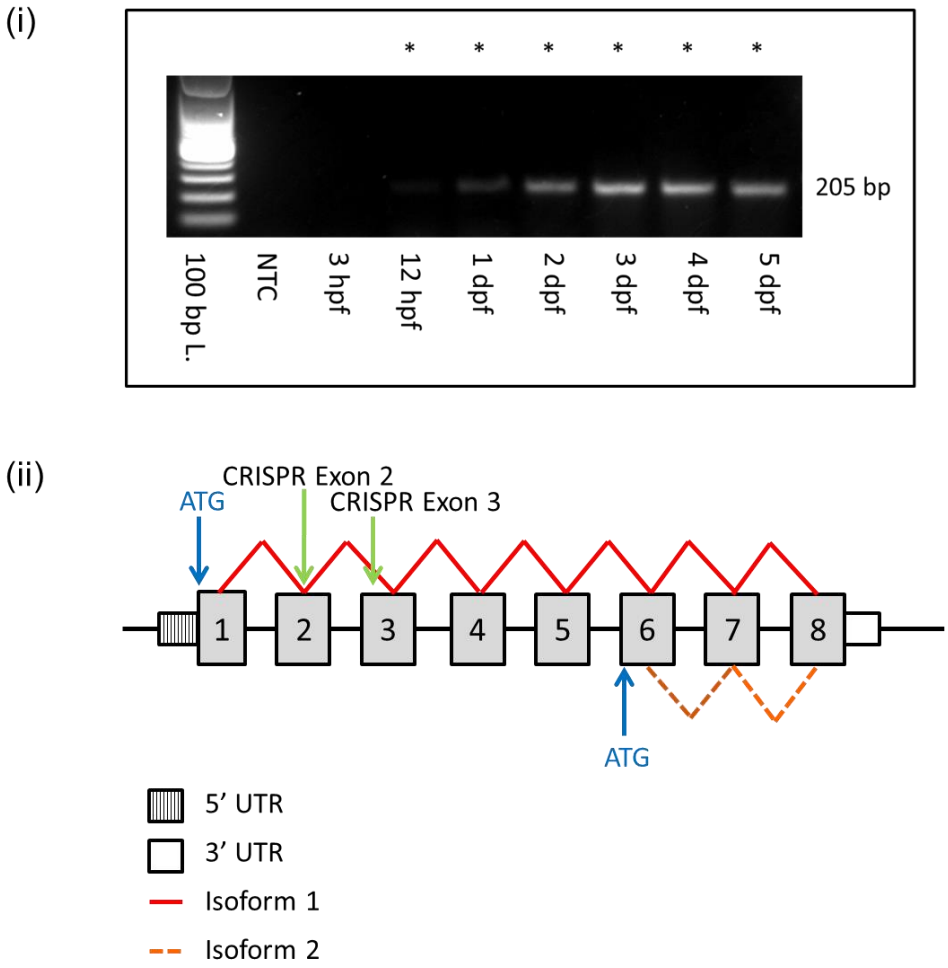

Figure A4 Zebrafish slc39a8 is expressed throughout embryonic and early larval development and has two alternative transcripts.

*(**i**) Gel electrophoresis image showing slc39a8 expression analysed by RT-PCR between 3 and 120 hpf using primers spanning 205 bp from the 2nd to 3rd exon. (*) indicates visible amplicon. (**ii**) Schematic overview of the slc39a8 gene. Exons are shaded in grey, encoded isoforms are marked in red/orange. Start codon is highlighted in blue, CRISPR target sites in green (not drawn to scale).*

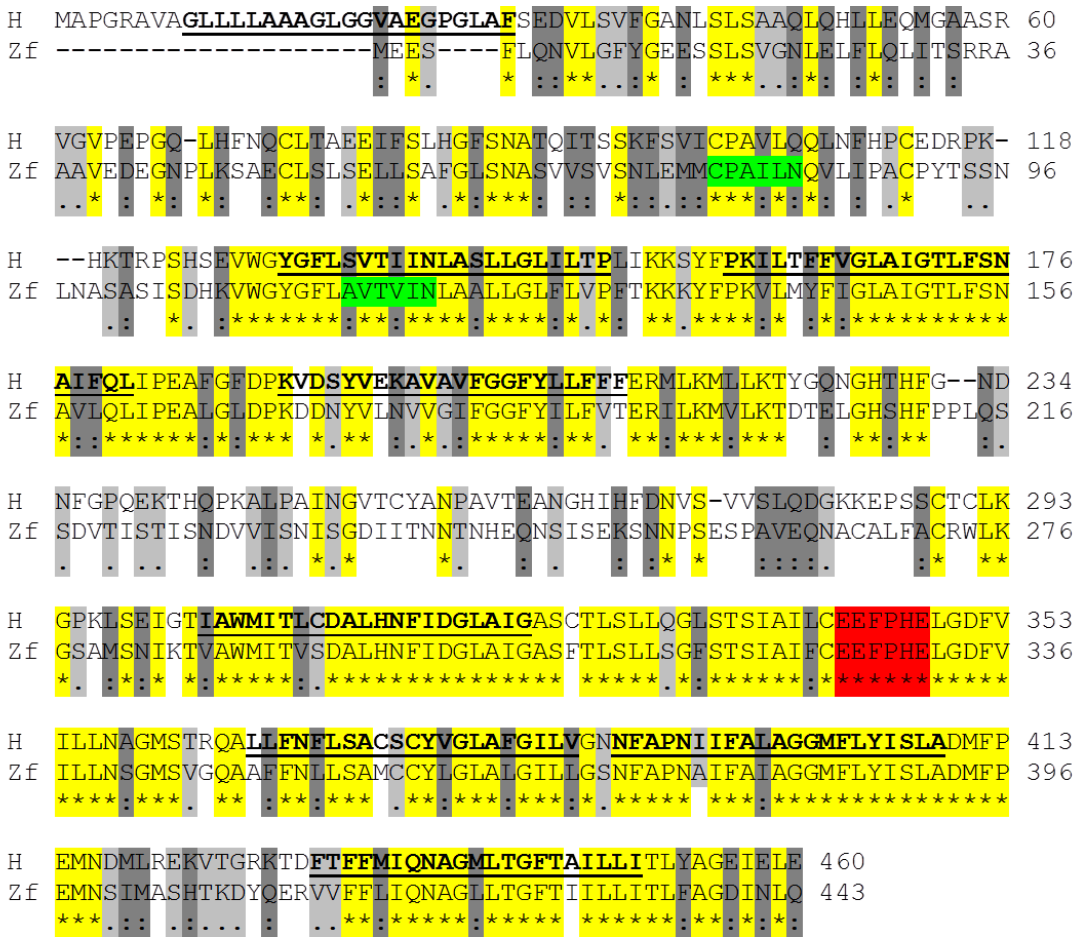

Figure A5 Protein sequence alignment of human and zebrafish Slc39a8.

Sequence alignment of human (top) and zebrafish (bottom) SLC39A8. Protein sequences of human isoform 1 (NP_001128618) and zebrafish isoform 1 (ENSDARP00000037866.6) were aligned using ClustalW2 (http://www.ebi.ac.uk/Tools/msa/clustalw2/). Residues identical to the human SLC39A8 sequence are marked in yellow with an asterisk (*). Conservation between amino acids of strongly and weakly similar properties is indicated by a colon (:, dark grey) and a period (. light grey), respectively. The putative TMDs are underlined. The LZT consensus motif required for metal binding is highlighted in red. The position of the CRISPR target sequences are indicated in green.

2.3 Generation of a *slc39a8* loss-of-function mutant using CRISPR/Cas9 targeting exon 2 or 3

Two gRNAs were designed to target a region within exon 2 and 3, respectively (**Figures A4 and A5, Section 2.3.18**). The rate of somatic mutagenesis was determined in healthy looking, gRNA/Cas9 mRNA injected embryos at 24 hpf using HRMA (**Figure A6**). All injected embryos showed a change in the melt curve shape confirming a high mutagenic efficiency of the generated gRNA/Cas9 complex. Amplicons with shifted melt peaks from injected embryos of the F0 generation were cloned into the pCRII-TOPO vector for sequencing. Amplicons with shifted melt peaks from embryos of the F1 generation were sequenced and analysed using PolyPeakParser software. Sequencing identified a range of frameshift causing indel mutations in the F0 and F1 generation that are expected to be deleterious for protein function (**Figure A7**).

(i)

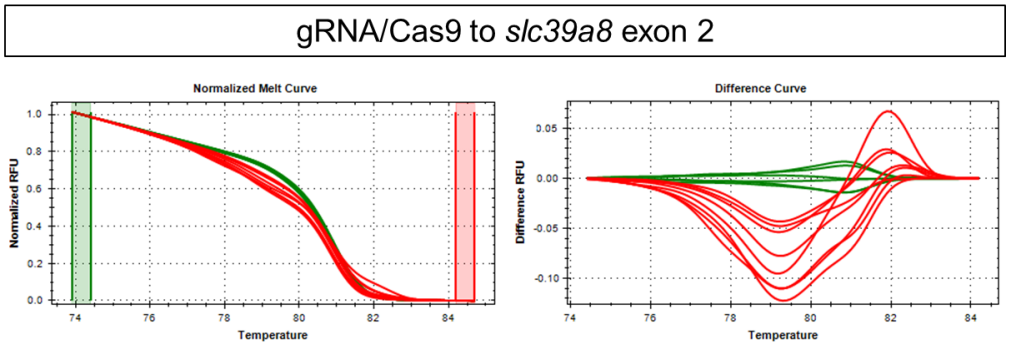

(ii)

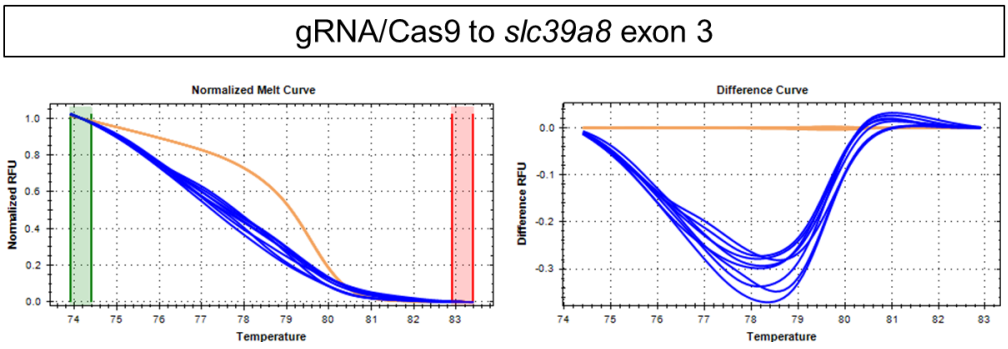

Figure A6 Mutagenesis induced by a gRNA/Cas9 to exon 2 and 3 of slc39a8.

*(**i**) HRMA result of injected (red) and un-injected (green) embryos showing a clear shift of the melt curve from injected embryos. Each melt curve represents a single embryo. Normalised melt curve (left) and difference plot (right) were generated using Biorad Precision Melt Analysis Software. (**ii**) HRMA result of injected (blue) and un-injected (orange) embryos showing a clear shift of the melt curve from injected embryos. Each melt curve represents a single embryo. Normalised melt curve (left) and difference plot (right) were generated using Biorad Precision Melt Analysis Software.*

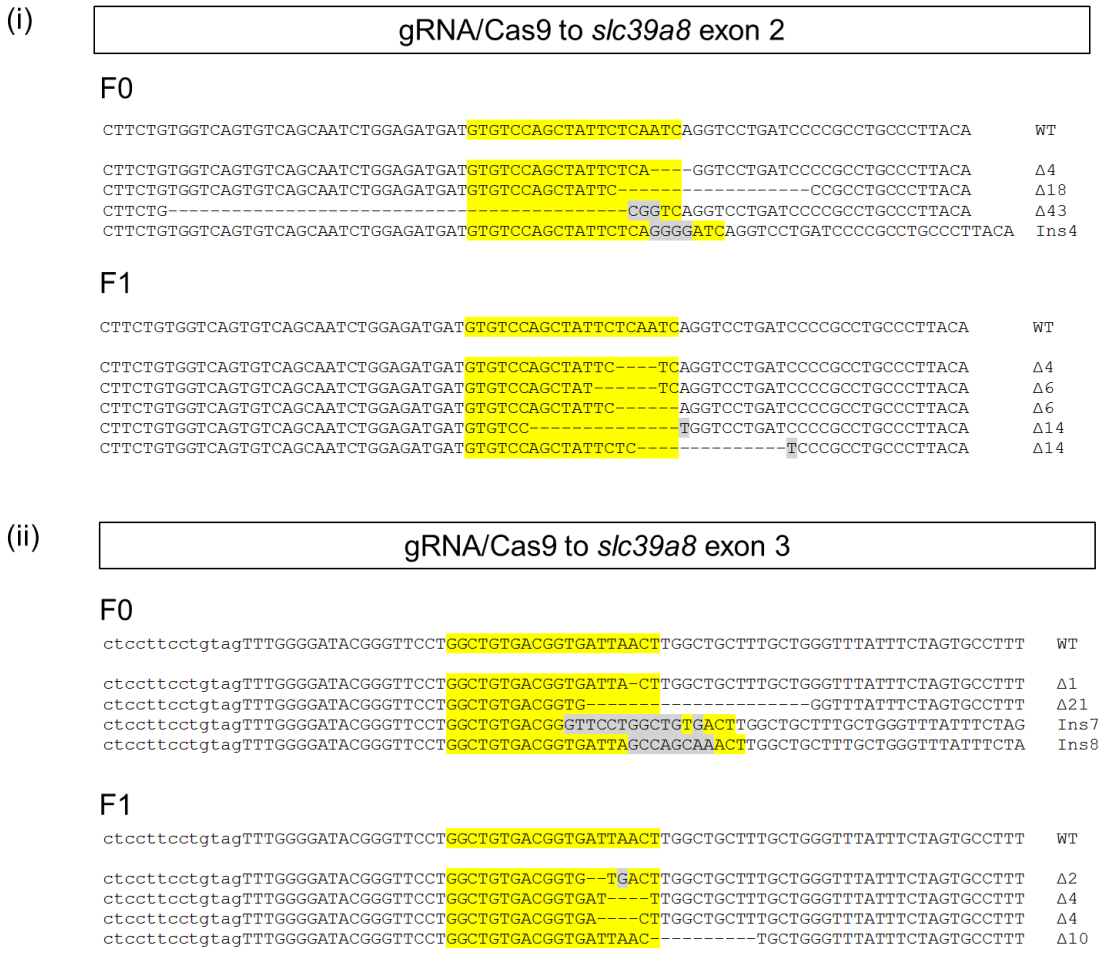

Figure A7 CRISPR induced indel mutations in exon 2 and 3 of slc39a8 in F0 and F1 embryos.

Wild-type (WT) sequence is given in the top row. The CRISPR target region is marked in yellow, (−) depicts a deleted nucleotide, insertions are marked in grey, (Δ) / (Ins) indicates the number of deleted / inserted nucleotides.

A stable mutant line harbouring a frameshift mutation will be generated that will allow the study of the function of *slc39a8* in zebrafish.

3. Protocols for the preparation of general laboratory reagents

1 x PBS	
10 tablets (Thermo Scientific)	MQ H_2O to 1L
0.5 M EDTA pH 8.0	
Disodium EDTA MQ H_2O	186.1 g 800 mL
	stir on hotplate and adjust pH to 8 with NaOH MQ H_2O to 1L
1M Tris-HCl pH 7.0 – 9.0	
Tris base MQ H_2O	121.1 g 800 mL
	Adjust pH with conc. HCl MQ H_2O to 1L
50 x TAE	
Tris Base Glacial acetic acid 0.5M EDTA pH 8.0	242 g 57.1 mL 100 mL
	MQ H_2O to 1L
4% PFA	
Paraformaldehyde	40 g
	1 x PBS to 1L (stir on hotplate in fumehood)
20 x SSC	
Sodium chloride Tri-sodium citrate dihydrate	175.3 g 88.2 g
	MQ H_2O to 1L, pH to 7.0
Hyb$^+$	
Formamide 20 x SSC RNA from torula yeast 50 mg/mL (Sigma R6875) Heparin 100 mg/mL in MQ H_2O (Sigma H3393) 20% Tween 20	250 mL 125 mL 5 mL 250 µL 2.5 mL

Citric acid 1M	4.6 mL
MQ H_2O	115.15 mL
Hyb$^-$	
20 x SSC	12.5 mL
Formamide	25 mL
20% Tween 20	250 µL
MQ H_2O	12.25 mL
Maleic acid buffer	
Maleic acid	11.61 g
NaCl	8.77 g
	MQ H_2O to 1L, pH to 7.5 with NaOH
MABlock	
Blocking reagent (Roche 11096176001)	2 g
Maleic acid buffer	100 mL
	Autoclave to dissolve
1000 x Proteinase K	
Proteinase K (Sigma P6556)	25 mg
	MQ H_2O to 2.5 mL
Stop solution	
PBS, pH 5.5	10 mL
1 mM EDTA	10 mL
20% Tween 20	1 mL
25 x Phenylthiourea (PTU)	
N-Phenylthiourea (Sigma P7629)	300 mg
	MQ H_2O to 400 mL, stir fast to dissolve
25 x Tricaine (MS-222)	
MS-222 (Sigma A5040)	0.8 g
1M Tris-HCl pH 9.0	4.2 mL
MQ H_2O	195.8 mL, pH to 7.0
20 x Pronase	
Pronase (Sigma P5147, Protease from Streptomyces griseus)	100 mg

Fishwater	5 mL
1 x TE buffer	
1M Tris-HCl pH 8.0 0.5M EDTA pH 8.0 MQ H_2O	10 mL 2 mL 988 mL
X-gal 2% (use 40 µL per plate)	
X-gal (Roche 745-740) Dimethylformamide	1 g 50 mL
	filter-sterilise (200 nm), store protected from light
IPTG 20 % (use 4 µL per plate)	
IPTG (VWR 437142L) MQ H_2O	2 g 10 mL
	filter-sterilise (200 nm)
LB agar plates	
LB Broth with agar (Miller) MQ H_2O	40 g 1 L
	autoclave at 121°C for 15 min
LB broth	
LB broth (Miller) MQ H_2O	25 g 1 L
	autoclave at 121°C for 15 min
Ampicillin	
Ampicillin MQ H_2O	50 mg 1 mL
	filter sterilise (200 nm), use at final concentration of 50 µg/mL
Kanamycin	
Kanamycin MQ H_2O	50 mg 1 mL
	filter sterilise (200 nm), use at final concentration of 50 µg/mL

4. FLASH assembly protocol

Adapted from Reyon et al.[188]

Reagents:

1. Forward and reverse primer for amplifying initial α one-mer unit:
5’ Biotin–TCTAGAGAAGACAAGAACCTGACC 3'
5’ GGATCCGGTCTCTTAAGGCCGTGG 3'
3. Digested βγδε four-mer units (for extension)
4. Digested βγδ three-mer units (for termination)
5. 2X B&W buffer (see below)
6. 1X B&W buffer with 0.005% Tween 20 (see below)
7. 100X Bovine Serum Albumin (BSA) (10 mg/mL) (NEB)
8. Dynabeads MyOne Streptavidin C1 magnetic beads (Life Technologies)
9. BsaI-HF (20 U/μL)
10. SalI-HF (20 U/μL)
11. XbaI (20 U/μL)
12. BamHI-HF (20 U/μL)
13. BbsI (5 U/μL)
14. BsmBI (10 U/μL)
15. NEBuffer 2
16. NEBuffer 4
17. T4 DNA Ligase (400 U/μL)
18. 2X Quick Ligase Buffer (QLB)(NEB)
19. QIAquick PCR Purification Kit (QIAGEN)
20. MinElute PCR Purification Kit (QIAGEN)
22. Herculase II Fusion DNA Polymerase (Agilent)
23. SOC medium (Invitrogen)
24. Chemically competent XL-10 Gold bacterial cells
25. SPRIplate 96-Ring magnet (Beckman Coulter Genomics)
26. DynaMagTM-96 Side magnet (Invitrogen)

Buffers:

1. 2X B&W Buffer:
    10.0 mM Tris-HCl (pH 7.5)
    1.0 mM EDTA
    2.0 M NaCl
2. 1X B&W Buffer with 0.005% Tween20:
    5.0 mM Tris-HCl (pH 7.5)
    0.5 mM EDTA
    1.0 M NaCl
    0.005% Tween 20
3. 1X BSA (diluted in H_2O)

Master Mixes:

1. α unit master mix (total volume of 31.5 µL):
    2 µL Purified and digested α one-mer fragment (prepared as described above)
    27 µL 2X QLB buffer
    2.5 µL T4 DNA Ligase (400 U/µL)
2. BsaI-HF master mix (50 µL):
    5 µL NEBuffer 4
    2 µL BsaI-HF (20 U/µL)
    43 µL H_2O
3. BbsI master mix (50 µL):
    40 µL water
    5 µL NEBuffer 2
    5 µL BbsI (5 U/µL)
4. Ligase master mix (27.5 µL):
    25 µL 2X QLB buffer
    2.5 µL T4 DNA ligase (400 U/µL)

Digestion of TALEN expression vector backbone:

1. Digest 5 µg of TALEN expression vector plasmid with BsmBI for 8 hours at 55°C using the following conditions:

    5 µL BsmBI (10 U/µL)

    5 µL NEBuffer 3

    20 µL DNA (5 µg)

    20 µL H_2O

2. Purify using the QIAquick PCR purification kit

3. Dilute purified digested plasmid from step 2 to a final concentration of 5 ng/µL in H_2O.

Preparation of DNA fragments encoding initial α one-mers:

1. Amplify biotinylated PCR product by setting up the following PCR reaction:

    10 µL 5X Herculase II reaction buffer

    0.5 µL dNTP mixture (25mM each)

    1.25 µL Fwd primer (10 µM)

    1.25 µL Rev primer (10 µM)

    0.5 µL DMSO (final concentration 1%)

    2 µL Initial α one-mer unit plasmid (1 ng/µL)

    34 µL Nuclease-Free Water

    0.5 µL Herculase II Fusion DNA Polymerase

    Thermocycling conditions:

Initial denaturation		95°C	2 min
35 cycles	Denaturation	95°C	20 sec
	Annealing	53°C	20 sec
	Extension	72°C	30 sec
Final extension		72°C	5 min

2. Purify PCR reaction from step 1 using the QIAquick PCR Purification Kit and elute in 40 µL 0.1 X EB buffer.

3. Digest the purified PCR product from step 2 with BsaI-HF enzymes by adding the following and incubating for 15 minutes at 50°C:

5 µL NEBuffer 4

5 µL BsaI-HF (20 U/µL)

4. Purify digested DNA from step 1 using the QIAquick PCR Purification Kit and elute in 50 µL 0.1X EB (final DNA concentration of ~15ng/µL).

Preparation of DNA fragments encoding one-, two-, three-, and four-mers (for extension or termination):

Extension fragment: βγδε four-mer units

Termination fragment: βγδ three-mer units

1. Perform initial digestion of plasmids encoding the one-, two-, three-, or four-mer for extension or termination using the following conditions for two hours at 37°C:

50 µL plasmid (~200 ng/µL)

10 µL NEBuffer 2

10 µL BbsI (5 U/µL)

30 µL H_2O

2. Add the following components to the digestion of step 1 and incubate for an additional 5 minutes at 37°C:

25 µL NEBuffer 4

2.5 µL 100X BSA

107.5 µL H_2O

5 µL XbaI (20 U/µL)

3. Add 5 µL of BamHI-HF enzyme (20 U/µL) to the digestion of step 2 and incubate for an additional 5 minutes at 37°C.

4. Add 5 µL SalI-HF enzyme (20 U/µL) to the digestion of step 3 and incubate for an additional 5 minutes at 37°C.

5. Purify the digestion of step 4 using a QIAquick PCR Purification Kit according to the manufacturer's instructions and elute in 50 µL of 0.1X EB buffer.

6. Quantify the purified DNA of step 5 using a Nanodrop spectrophotometer (typical concentration of 40 ng/µL).

FLASH assembly of DNA fragments encoding TALE repeat arrays: perform in 96 well plate

1. Set up initial ligations by mixing the following components and incubating for 15 minutes at room temperature:

    31.5 µL α unit master mix

    22.5 µL first extension fragment

2. Prepare magnetic beads by performing the following steps in a 96 well plate:

    a. Wash 5 µL beads in 50 µL of 1X B&W by pipetting up and down five times

    b. Place plate on the SPRIplate 96-Ring magnet for 3 minutes

    c. Aspirate supernatant

    d. Repeat steps a to c for a total of 3 washes

    e. Resuspend beads in 54 µL 2X B&W buffer

3. Bind initial ligation products of step 1 to magnetic beads prepared in step 2 by performing the following steps:

    a. Add 54 µL of initial ligation reaction from step 1 to 54 µL of washed beads from step 2

    b. Mix by pipetting up/down five times

    c. Incubate for 15 min at room temperature re-mixing every 5 minutes

    d. Place on magnet for 3 minutes

    e. Aspirate supernatant

4. Wash beads from step 3 by performing the following steps:

    a. Add 100 µL 1X B&W buffer

    b. Mix by placing into adjacent slots of the DynaMagTM-96 Side magnet for 31 times

    c. Place plate on the SPRIplate 96-Ring magnet for 1 minute

    d. Aspirate supernatant

    e. Add 100 µL 1X BSA

    f. Place into adjacent slots of the DynaMagTM-96 Side magnet for 31 times

    g. Place plate on the magnet for 3 minutes

    h. Aspirate supernatant

5. Perform BsaI-HF digestion to prepare 3’ end of bead-bound DNA fragment for next ligation:

    a. Re-suspend washed beads from step 4 in 50 µL of BsaI-HF Mix by mixing up and down 20 times

    b. Incubate at 50°C for 10 minutes

c. Add 50 µL 1X B&W buffer

d. Place plate on the SPRIplate 96-Ring magnet for 3 minutes

e. Aspirate supernatant

6. Wash beads from step 5 by performing the following steps:

a. Add 100 µL 1X B&W buffer

b. Mix by placing into adjacent slots of the DynaMagTM-96 Side magnet for 31 times

c. Place plate on the SPRIplate 96-Ring magnet for 1 minute

d. Aspirate supernatant

e. Add 100 µL 1X BSA

f. Place into adjacent slots of the DynaMagTM-96 Side magnet for 31 times

g. Place plate on the magnet for 3 minutes

h. Aspirate supernatant

7. Ligate next “extension fragment” or “termination fragment” by performing the following steps:

a. Add 22.5 µL of extension fragment or termination fragment to washed beads of step 6.

b. Add 27.5 µL of ligase master mix

c. Mix well by pipetting up and down 10 times

d. Incubate at room temperature for 15 minutes (mixing every 5 minutes)

e. Add 50 µL of 1X B&W buffer

f. Place on SPRIplate 96-Ring magnet for 3 minutes

g. Aspirate supernatant

8. Wash the beads from step 7 by performing the following steps:

a. Add 100 µL 1X B&W buffer

b. Mix by placing into adjacent slots of the DynaMagTM-96 Side magnet for 31 times

c. Place plate on the SPRIplate 96-Ring magnet for 1 minute

d. Aspirate supernatant

e. Add 100 µL 1X BSA

f. Place into adjacent slots of the DynaMagTM-96 Side magnet for 31 times

g. Place plate on the magnet for 3 minutes

h. Aspirate supernatant

9. Perform BsaI-HF digestion to prepare 3’ end of bead-bound DNA fragment

a. Re-suspend washed beads from step 4 in 50 µL of BsaI-HF Mix by mixing up and down 20 times

b. Incubate at 50°C for 10 minutes

c. Add 50 µL 1X B&W buffer

d. Place plate on the SPRIplate 96-Ring magnet for 3 minutes

e. Aspirate supernatant

10. Repeat steps 6 to 9 as needed to complete extension of the fragment

11. Wash the beads from step 10 by performing the following steps:

a. Add 100 µL 1X B&W buffer

b. Mix by placing into adjacent slots of the DynaMagTM-96 Side magnet for 31 times

c. Place plate on the SPRIplate 96-Ring magnet for 1 minute

d. Aspirate supernatant

e. Add 100 µL 1X BSA

f. Place into adjacent slots of the DynaMagTM-96 Side magnet for 31 times

g. Place plate on the magnet for 3 minutes

h. Aspirate supernatant

12. Release DNA fragments from magnetic beads by performing the following steps:

a. Resuspend beads in 50 µL BbsI mix

b. Incubate at 37°C for 2 hours with shaking at 1500 rpm

c. Place on SPRIplate 96-Ring magnet for 3 minutes

d. Aspirate and save supernatant with released DNA fragments

13. Purify DNA fragments from step 12 using a MinElute PCR Purification Kit with two additional buffer PE washes and elute in 15 µL 0.1 X EB buffer.

Ligation of DNA fragments encoding TALE repeat arrays into the TALEN expression vector:

Mix together the following components and incubate at 37°C for 15 minutes:

3 µL Purified DNA fragments from step 13

1 µL BsmBI-digested TALEN expression plasmid vector

1 µL T4 DNA Ligase (400 U/µL)

5 µL 2X QLB buffer

Transformation of chemically competent XL-10 Gold cells:

a. Mix 4 µL of ligation with 50 µL ice-cold chemically competent XL1 Blue cells

b. Incubate on ice for 10 minutes

c. Heat shock cells at 42°C for 30 seconds

d. Immediately return transformation to ice and incubate for 2 minutes

e. Add 446 µL of SOC medium

f. Recover for 1 hour at 37°C

g. Spin cells down at 300 x g for 3 minutes

h. Aspirate 470 µL of supernatant from each transformation

i. Re-suspend cell pellets in remaining medium

j. Plate entire resuspension onto LB agar plates containing 50 µg/mL of Ampicillin

k. Incubate plates overnight at 37°C

5. RNA sequencing raw data

i. Differentially expressed genes in homozygous *slc39a14*^{U801} mutants versus siblings

(genes are listed in order of their fold-change)

Chr	p-value	Distance to 3' end	e76 Ensembl Gene ID	Gene name	Fold change (mut/sib)
Upregulated					
16	0.02	-9	ENSDARG00000028367	sult2st3	2.96
23	0.04	0	ENSDARG00000058873	PTPDC1 (1 of 2)	2.94
5	0.04	2788	ENSDARG00000089770	5S_rRNA	2.90
5	0.00	-2	ENSDARG00000011168	anxa1c	2.89
6	0.05	1	ENSDARG00000078814	si:dkey-34m19.3	2.71
19	0.00	2615	ENSDARG00000089168	EXT1 (2 of 2)	2.70
5	0.04	2990	ENSDARG00000086530	SMAD4 (2 of 2)	2.70
5	0.01	375	ENSDARG00000086835	ostf1	2.49
5	0.04	3	ENSDARG00000003144	pxmp2	2.33
4	0.00	4008	ENSDARG00000002174	itfg2	2.20
20	0.02	0	ENSDARG00000032117	ddx1	2.03
5	0.01	1582	ENSDARG00000059817	mtmr12	1.97
25	0.02	4111	ENSDARG00000062375	lcat	1.93
20	0.04	-6	ENSDARG00000010276	ptgs2b	1.91
8	0.05	-3	ENSDARG00000089156	egr3	1.85
16	0.03	-2	ENSDARG00000021033	herpud2	1.82
6	0.03	0	ENSDARG00000044280	opn1mw2	1.82
2	0.04	-5	ENSDARG00000031426	csrnp1a	1.82
18	0.02	1567	ENSDARG00000073824	RASGRF1	1.77
21	0.02	1811	ENSDARG00000069501	abhd11	1.77
1	0.00	0	ENSDARG00000091609	SPINK4	1.76
14	0.01	-1	ENSDARG00000075014	sqstm1	1.73
11	0.00	-4	ENSDARG00000021059	alas1	1.70
20	0.00	-1	ENSDARG00000095767	dio3b	1.65
5	0.04	0	ENSDARG00000075326	mrps30	1.64
1	0.00	-2	ENSDARG00000006588	zgc:111983	1.64
5	0.00	0	ENSDARG00000060249	WDR44	1.63
10	0.05	3976	ENSDARG00000075747	zfyve16	1.62
20	0.04	1	ENSDARG00000034076	lrp11	1.62
16	0.03	1	ENSDARG00000009018	rhbg	1.62
18	0.01	6	ENSDARG00000041595	ces3	1.60
13	0.02	0	ENSDARG00000014031	abcc2	1.59

1	0.04	3318	ENSDARG00000029751	wbp1lb	1.59
5	0.05	1	ENSDARG00000003091	oclnb	1.57
5	0.03	-1	ENSDARG00000052851	golph3	1.56
5	0.04	0	ENSDARG00000016319	c9	1.56
3	0.03	0	ENSDARG00000004034	arhgdig	1.56
1	0.02	-6	ENSDARG00000017985	C1H4orf33	1.55
8	0.04	0	ENSDARG00000028071	bmp1a	1.55
5	0.05	0	ENSDARG00000045979	PTGDS (2 of 3)	1.53
20	0.03	1735	ENSDARG00000070584	clic5b	1.53
15	0.01	0	ENSDARG00000045408	tagln	1.53
14	0.03	1707	ENSDARG00000053668	stag2b	1.52
11	0.03	-2	ENSDARG00000020761	arrdc2	1.52
15	0.01	2138	ENSDARG00000062319	si:dkey-103g5.3	1.51
22	0.05	-1	ENSDARG00000094496	cfhl4	1.51
18	0.02	7	ENSDARG00000088030	rpl35a	1.50
13	0.01	0	ENSDARG00000079840	kcnma1a	1.49
3	0.01	1331	ENSDARG00000079544	si:ch1073-464p5.5	1.48
1	0.03	0	ENSDARG00000093494	si:ch211-217k17.9	1.47
6	0.04	160	ENSDARG00000036433	ERP27	1.47
19	0.02	-5	ENSDARG00000035909	mfsd2ab	1.46
25	0.02	-2	ENSDARG00000042874	phlda2	1.45
15	0.03	-1	ENSDARG00000097205	ulk2	1.45
16	0.04	-1	ENSDARG00000092158	cbx3b	1.45
15	0.04	0	ENSDARG00000043102	lxn	1.44
16	0.01	0	ENSDARG00000008363	mcl1b	1.44
7	0.03	1	ENSDARG00000016260	fxr2	1.43
Zv9_ NA991	0.01	0	ENSDARG00000077566	CZv9_NA991H1orf52	1.43
23	0.01	4	ENSDARG00000007216	abce1	1.42
11	0.04	0	ENSDARG00000070171	errfi1	1.42
5	0.05	2852	ENSDARG00000079624	amer1	1.41
21	0.04	190	ENSDARG00000068589	CABZ01079764.1	1.41
17	0.01	-9	ENSDARG00000016651	znf106a	1.41
23	0.04	0	ENSDARG00000089429	si:dkey-205h13.2	1.39
9	0.04	-1	ENSDARG00000006220	ugt1a7	1.39
9	0.04	3246	ENSDARG00000055009	col4a1	1.39
6	0.03	1003	ENSDARG00000044528	slc15a1b	1.37
19	0.01	-95	ENSDARG00000094041	krt17	1.37
5	0.01	2188	ENSDARG00000035188	rab14l	1.37
5	0.04	0	ENSDARG00000039929	ckmt2b	1.37
23	0.05	-6	ENSDARG00000074201	flna	1.37

11	0.03	-3	ENSDARG00000018146	gpx1a	1.36
10	0.02	0	ENSDARG00000087243	zgc:100918	1.36
16	0.02	-1	ENSDARG00000037998	flot1b	1.36
6	0.01	-2	ENSDARG00000013561	pgm1	1.36
24	0.02	-1	ENSDARG00000038559	h1f0	1.36
8	0.03	-4	ENSDARG00000059646	nt5dc2	1.36
23	0.02	-6	ENSDARG00000037539	tnnc1b	1.34
12	0.01	-3	ENSDARG00000071445	myoz1b	1.32
23	0.00	-1	ENSDARG00000036754	hmgn3	1.32
8	0.00	-3	ENSDARG00000094310	si:ch211-255g12.6	1.32
15	0.01	0	ENSDARG00000041169	hif1al	1.32
3	0.04	0	ENSDARG00000054849	bcat2	1.32
24	0.02	0	ENSDARG00000000069	dap	1.32
16	0.03	-4	ENSDARG00000056856	tax1bp1b	1.32
11	0.03	7	ENSDARG00000042777	ndufa11	1.32
21	0.03	3490	ENSDARG00000022682	add1	1.31
7	0.05	-1	ENSDARG00000015392	dhx15	1.31
2	0.01	-6	ENSDARG00000003016	eef2b	1.30
10	0.05	0	ENSDARG00000033088	ubl3a	1.30
23	0.00	-4	ENSDARG00000018404	krt18	1.30
1	0.05	-8	ENSDARG00000094133	si:dkey-9i23.11	1.30
8	0.01	-1	ENSDARG00000079745	-	1.30
19	0.04	-2	ENSDARG00000005162	tpm3	1.29
1	0.01	-6	ENSDARG00000015490	rpl24	1.29
24	0.03	-3	ENSDARG00000018285	pdpk1b	1.29
3	0.05	0	ENSDARG00000038068	ddx5	1.28
18	0.02	-2	ENSDARG00000054272	caprin1b	1.28
19	0.01	0	ENSDARG00000076892	nme2b.2	1.28
9	0.01	8	ENSDARG00000086917	crygm2d2	1.28
8	0.02	0	ENSDARG00000089418	wu:fk66f10	1.27
21	0.04	0	ENSDARG00000074057	calm1a	1.27
13	0.05	-1	ENSDARG00000090228	gstal	1.27
5	0.04	0	ENSDARG00000067995	myhz1.2	1.27
11	0.01	0	ENSDARG00000033609	map1lc3a	1.27
9	0.05	-3	ENSDARG00000069792	crygm2d5	1.27
14	0.01	0	ENSDARG00000061764	ahnak	1.26
16	0.02	-5	ENSDARG00000019902	rcv1	1.26
21	0.04	0	ENSDARG00000013430	bhmt	1.26
18	0.01	3705	ENSDARG00000061338	ddx6	1.26
15	0.04	-2	ENSDARG00000040565	ckmb	1.25
9	0.05	-3	ENSDARG00000086912	crygm2d18	1.25

9	0.00	-5	ENSDARG00000028213	ttna	1.25
2	0.01	0	ENSDARG00000035860	rps28	1.25
16	0.01	-3	ENSDARG00000039914	gapdhs	1.25
10	0.04	14	ENSDARG00000043493	cltca	1.24
5	0.02	2	ENSDARG00000035400	btf3	1.23
5	0.03	-1	ENSDARG00000003032	eif4a1b	1.23
18	0.02	0	ENSDARG00000042931	mibp2	1.22
5	0.04	0	ENSDARG00000035136	sepw1	1.22
10	0.02	0	ENSDARG00000062592	myl10	1.21
14	0.01	1	ENSDARG00000039641	rpl26	1.21
11	0.03	2	ENSDARG00000021838	rps23	1.20
12	0.02	-2	ENSDARG00000002768	pvalb2	1.20
3	0.04	20	ENSDARG00000014420	elavl3	1.20
25	0.05	0	ENSDARG00000046157	RPS17L	1.19
13	0.01	-22	ENSDARG00000012972	cfl1l	1.19
13	0.03	0	ENSDARG00000013968	psap	1.18
16	0.05	0	ENSDARG00000011405	rps9	1.18
19	0.04	-35	ENSDARG00000023290	fabp3	1.16
3	0.05	244	ENSDARG00000088371	junbb	1.15
Downregulated					
5	0.00	1814	ENSDARG00000010108	bri3bp	-8.59
25	0.00	2444	ENSDARG00000001127	slc17a6a	-4.88
5	0.00	3978	ENSDARG00000079757	SCARF2	-4.67
11	0.02	1436	ENSDARG00000055620	acad9	-4.04
19	0.00	2754	ENSDARG00000093300	si:dkey-18f7.2	-3.93
18	0.00	2735	ENSDARG00000068421	ttc9b	-3.89
5	0.00	1429	ENSDARG00000076611	fbxo21	-3.73
5	0.00	1866	ENSDARG00000068820	h2afva	-3.68
15	0.00	3512	ENSDARG00000006585	CABZ01113899.1	-3.59
16	0.00	4953	ENSDARG00000070620	grin2db	-3.48
11	0.00	2568	ENSDARG00000075456	PIK3CA (1 of 2)	-3.47
5	0.04	1694	ENSDARG00000011065	camk2b1	-3.31
7	0.00	4392	ENSDARG00000025797	abhd2a	-3.22
11	0.00	1770	ENSDARG00000025699	mbd1	-3.12
1	0.03	-30	ENSDARG00000023678	ercc5	-2.94
5	0.00	1968	ENSDARG00000062646	tet3	-2.91
1	0.00	1026	ENSDARG00000024785	ctnna2	-2.91
13	0.03	3899	ENSDARG00000092473	apopt1	-2.85
5	0.00	338	ENSDARG00000059789	parp8	-2.83
24	0.01	1187	ENSDARG00000008275	klhl24b	-2.81
7	0.05	4108	ENSDARG00000034434	igf1rb	-2.78

23	0.02	24	ENSDARG00000028894	mrgbp	-2.78
5	0.00	2920	ENSDARG00000033498	rorb	-2.72
7	0.04	4748	ENSDARG00000085920	5S_rRNA	-2.71
5	0.00	1289	ENSDARG00000081232	dre-mir-454b	-2.70
5	0.00	0	ENSDARG00000012468	aacs	-2.66
7	0.04	3	ENSDARG00000036036	mdka	-2.65
23	0.02	3342	ENSDARG00000007751	lmnl3	-2.64
5	0.00	4689	ENSDARG00000075347	chfr	-2.62
5	0.00	2790	ENSDARG00000059719	fam169aa	-2.61
21	0.01	7	ENSDARG00000058630	BDP1 (2 of 2)	-2.59
6	0.01	1013	ENSDARG00000079491	KCNA3	-2.58
18	0.02	1204	ENSDARG00000054864	aplp2	-2.57
16	0.00	2352	ENSDARG00000059945	SV2A	-2.51
23	0.04	1860	ENSDARG00000076730	syt6a	-2.49
1	0.02	2050	ENSDARG00000088676	CT573191.1	-2.47
10	0.03	4018	ENSDARG00000020913	ddx56	-2.35
16	0.03	1794	ENSDARG00000062244	setd2	-2.33
3	0.00	3582	ENSDARG00000004597	lrrc4ba	-2.33
3	0.00	1777	ENSDARG00000075461	suv420h2	-2.32
14	0.03	882	ENSDARG00000028740	msnb	-2.29
7	0.00	259	ENSDARG00000063035	ntrk3b	-2.28
4	0.01	2220	ENSDARG00000006747	tmem178b	-2.28
4	0.00	14	ENSDARG00000061089	KIF21A (1 of 3)	-2.25
11	0.00	1	ENSDARG00000070545	top1l	-2.25
13	0.01	1958	ENSDARG00000069044	agpat4	-2.23
25	0.04	3094	ENSDARG00000020718	SLC25A22 (1 of 2)	-2.23
1	0.00	6	ENSDARG00000061661	igf2bp2b	-2.21
5	0.02	758	ENSDARG00000019549	cds1	-2.21
8	0.00	1329	ENSDARG00000017365	slc23a2	-2.20
4	0.00	1495	ENSDARG00000015053	grip1	-2.19
14	0.03	1073	ENSDARG00000037423	SMIM19	-2.17
7	0.00	4219	ENSDARG00000077782	ACER2	-2.15
14	0.00	25	ENSDARG00000079586	gabrb2	-2.13
16	0.01	1284	ENSDARG00000080201	5S_rRNA	-2.12
14	0.01	1205	ENSDARG00000026651	APBB2 (1 of 2)	-2.11
18	0.01	1685	ENSDARG00000026664	uri1	-2.11
10	0.00	2366	ENSDARG00000032083	dpysl2b	-2.09
14	0.00	1887	ENSDARG00000056563	ppargc1b	-2.09
10	0.00	1235	ENSDARG00000090124	alcama	-2.08
6	0.00	-5	ENSDARG00000020301	os9	-2.07
23	0.00	3461	ENSDARG00000086856	stk35	-2.04

12	0.00	-49	ENSDARG00000012094	prkar1ab	-2.03
25	0.03	2927	ENSDARG00000015502	adam10b	-2.02
21	0.02	360	ENSDARG00000001857	aff4	-1.99
19	0.04	1985	ENSDARG00000079899	FAM135B	-1.96
17	0.00	1512	ENSDARG00000044462	qkia	-1.96
11	0.02	1109	ENSDARG00000042458	rfc4	-1.95
1	0.00	643	ENSDARG00000060148	sh3pxd2aa	-1.94
24	0.00	561	ENSDARG00000079312	kmt2ca	-1.93
3	0.00	135	ENSDARG00000027357	cd2bp2	-1.92
7	0.05	3168	ENSDARG00000069430	tp53i11a	-1.92
22	0.03	2628	ENSDARG00000033589	EPHB3 (2 of 2)	-1.92
5	0.00	99	ENSDARG00000041926	DLG4 (2 of 2)	-1.91
5	0.00	6	ENSDARG00000007034	hnrpkl	-1.91
9	0.00	573	ENSDARG00000055543	appb	-1.91
20	0.02	-5	ENSDARG00000008209	myt1la	-1.90
8	0.00	4406	ENSDARG00000037904	cacna1db	-1.89
3	0.01	-98	ENSDARG00000060348	map3k3	-1.86
10	0.00	2163	ENSDARG00000093503	RSF1 (3 of 3)	-1.86
5	0.01	-48	ENSDARG00000002771	SLC4A5 (1 of 2)	-1.85
9	0.00	2019	ENSDARG00000001676	gpm6bb	-1.85
5	0.00	2735	ENSDARG00000035256	eef2l2	-1.84
23	0.02	-5	ENSDARG00000053857	-	-1.84
8	0.01	-72	ENSDARG00000043474	atp2b3a	-1.84
6	0.00	3815	ENSDARG00000052142	ACVR1B (2 of 2)	-1.81
25	0.00	1599	ENSDARG00000051748	ccnd2a	-1.81
2	0.00	-67	ENSDARG00000068745	MAP4 (1 of 3)	-1.80
1	0.00	0	ENSDARG00000043226	nfixa	-1.80
14	0.00	2898	ENSDARG00000055792	FOXO4	-1.80
13	0.00	2898	ENSDARG00000070242	ENDOD1 (5 of 13)	-1.80
15	0.00	531	ENSDARG00000033845	igsf9ba	-1.80
7	0.00	639	ENSDARG00000021442	cdh11	-1.80
12	0.01	-5	ENSDARG00000054154	bms1l	-1.79
9	0.00	1404	ENSDARG00000000563	ttnb	-1.79
11	0.04	-31	ENSDARG00000030791	mafgb	-1.78
10	0.00	2417	ENSDARG00000018856	dclk1a	-1.78
23	0.02	-3	ENSDARG00000025206	syt2a	-1.78
17	0.00	1515	ENSDARG00000097478	qkia	-1.78
9	0.01	2563	ENSDARG00000037203	insig2	-1.75
5	0.00	3	ENSDARG00000046090	dhrs11a	-1.75
20	0.00	861	ENSDARG00000090703	pdgfra	-1.75
16	0.03	0	ENSDARG00000073784	FEZ2 (2 of 2)	-1.73

14	0.00	3331	ENSDARG00000033556	PCDH11Y	-1.73
21	0.01	40	ENSDARG00000078317	si:dkey-175m17.7	-1.73
7	0.04	4005	ENSDARG00000087397	TEAD1 (2 of 2)	-1.73
21	0.00	2485	ENSDARG00000056181	ncam1a	-1.71
9	0.00	4246	ENSDARG00000029497	tfcp2l1	-1.70
11	0.05	2067	ENSDARG00000085035	5S_rRNA	-1.69
7	0.01	661	ENSDARG00000024877	ptgr1	-1.69
11	0.00	2087	ENSDARG00000016918	ace2	-1.68
13	0.00	4151	ENSDARG00000074759	ccar1	-1.68
8	0.00	4565	ENSDARG00000038300	rnf34a	-1.68
8	0.04	2139	ENSDARG00000074126	ttc39a	-1.67
2	0.00	861	ENSDARG00000054290	acin1a	-1.67
2	0.01	2033	ENSDARG00000032317	tox	-1.67
6	0.03	2507	ENSDARG00000018032	scn8ab	-1.66
25	0.00	3033	ENSDARG00000022045	map1ab	-1.65
12	0.04	-1	ENSDARG00000012094	prkar1ab	-1.65
23	0.02	1809	ENSDARG00000056554	rap1gap	-1.65
18	0.02	268	ENSDARG00000003994	syt9a	-1.64
16	0.01	2765	ENSDARG00000056642	hdac9b	-1.63
1	0.03	140	ENSDARG00000054274	pcdh10a	-1.63
3	0.03	4130	ENSDARG00000085512	5S_rRNA	-1.62
5	0.01	3913	ENSDARG00000089770	5S_rRNA	-1.61
5	0.00	2819	ENSDARG00000032039	mxd1	-1.61
2	0.00	-1	ENSDARG00000052419	ankrd12	-1.61
19	0.00	2848	ENSDARG00000033804	snx27a	-1.60
7	0.05	1782	ENSDARG00000051852	kcnc1a	-1.59
21	0.04	4682	ENSDARG00000002600	pcsk1	-1.59
23	0.01	281	ENSDARG00000024895	fam50a	-1.58
16	0.00	-79	ENSDARG00000017220	otud7b	-1.58
23	0.03	4425	ENSDARG00000078011	NAV1 (2 of 3)	-1.57
21	0.01	15	ENSDARG00000078581	crebrf	-1.57
5	0.00	0	ENSDARG00000009336	aif1l	-1.56
13	0.00	1895	ENSDARG00000056322	ldb3a	-1.56
21	0.05	1243	ENSDARG00000019693	CLCN5 (1 of 2)	-1.56
19	0.00	4818	ENSDARG00000063690	nrm	-1.56
2	0.02	70	ENSDARG00000038855	chmp5a	-1.55
1	0.05	-88	ENSDARG00000069438	neurl1aa	-1.55
6	0.01	-88	ENSDARG00000094792	twf2a	-1.55
7	0.00	0	ENSDARG00000006487	anp32a	-1.53
21	0.04	1189	ENSDARG00000026035	ube2b	-1.53
3	0.00	-79	ENSDARG00000029394	ilf3b	-1.53

23	0.00	1040	ENSDARG00000052604	CPEB2	-1.53
11	0.02	911	ENSDARG00000085592	5S_rRNA	-1.53
3	0.03	435	ENSDARG00000055855	kcnc3a	-1.52
20	0.04	47	ENSDARG00000046106	rab10	-1.52
12	0.00	74	ENSDARG00000005567	map2k6	-1.52
7	0.00	185	ENSDARG00000056722	cd99l2	-1.51
10	0.04	3203	ENSDARG00000079251	nlgn2b	-1.51
21	0.02	2932	ENSDARG00000010524	si:ch211-282j22.3	-1.51
13	0.02	424	ENSDARG00000028148	pax2a	-1.50
4	0.00	-1	ENSDARG00000017841	cand1	-1.49
6	0.01	96	ENSDARG00000071113	xirp2a	-1.49
23	0.00	84	ENSDARG00000012777	nucks1b	-1.49
11	0.00	-19	ENSDARG00000009754	zc3h11a	-1.49
21	0.00	25	ENSDARG00000053665	gabrg2	-1.49
7	0.04	305	ENSDARG00000078078	lrfn4b	-1.48
2	0.00	866	ENSDARG00000052419	ankrd12	-1.47
5	0.00	1039	ENSDARG00000089271	si:dkey-114c15.7	-1.47
12	0.00	-51	ENSDARG00000061647	nrxn1a	-1.47
7	0.03	792	ENSDARG00000022251	znf536	-1.46
8	0.00	76	ENSDARG00000068123	gkap1	-1.46
7	0.03	-78	ENSDARG00000068457	tnnt3b	-1.46
5	0.01	3454	ENSDARG00000078302	BRINP1	-1.46
7	0.04	409	ENSDARG00000035750	ccnd1	-1.46
5	0.04	4136	ENSDARG00000035158	MCAM (2 of 3)	-1.46
10	0.02	0	ENSDARG00000097170	pcdh1a3	-1.45
12	0.01	5	ENSDARG00000020521	exoc6	-1.45
3	0.03	3615	ENSDARG00000035952	cdr2a	-1.45
16	0.02	302	ENSDARG00000043304	nop2	-1.45
8	0.02	281	ENSDARG00000043474	atp2b3a	-1.44
10	0.04	14	ENSDARG00000013005	opcml	-1.44
14	0.00	-2	ENSDARG00000068582	rnf44	-1.44
18	0.01	66	ENSDARG00000061635	myo5aa	-1.43
21	0.00	2854	ENSDARG00000075546	CABZ01109624.1	-1.43
21	0.00	3537	ENSDARG00000032188	lrrc8a	-1.42
21	0.04	4556	ENSDARG00000056244	-	-1.42
19	0.05	463	ENSDARG00000070981	ash1l	-1.42
25	0.01	0	ENSDARG00000021378	phf21ab	-1.42
18	0.00	140	ENSDARG00000062020	gse1	-1.42
16	0.05	39	ENSDARG00000094933	si:dkey-165g20.5	-1.41
11	0.01	3817	ENSDARG00000043835	rab3ab	-1.41
20	0.01	0	ENSDARG00000034187	calm2a	-1.41

6	0.05	699	ENSDARG00000079540	CACNA2D2 (3 of 3)	-1.41
18	0.00	2002	ENSDARG00000062138	ranbp10	-1.41
1	0.01	-3	ENSDARG00000010791	dla	-1.41
21	0.00	0	ENSDARG00000068214	ccni	-1.40
21	0.05	-3	ENSDARG00000015221	nsrp1	-1.40
7	0.01	-1	ENSDARG00000018817	bdnf	-1.39
20	0.01	-1	ENSDARG00000014013	lbr	-1.39
11	0.04	0	ENSDARG00000007824	CR847998.1	-1.39
9	0.01	1610	ENSDARG00000020164	efnb2a	-1.38
19	0.02	173	ENSDARG00000059674	lrp12	-1.38
16	0.03	543	ENSDARG00000005867	gon4l	-1.37
2	0.00	584	ENSDARG00000056490	SSBP4 (2 of 2)	-1.37
25	0.00	58	ENSDARG00000051748	ccnd2a	-1.37
20	0.02	-27	ENSDARG00000021753	ccdc25	-1.37
24	0.00	865	ENSDARG00000076559	RB1CC1	-1.37
14	0.00	638	ENSDARG00000019213	CTBP1	-1.36
3	0.01	2642	ENSDARG00000028521	c1ql3b	-1.36
18	0.01	2830	ENSDARG00000038121	ELL3	-1.36
9	0.05	433	ENSDARG00000020834	CEP250	-1.36
4	0.00	5	ENSDARG00000030614	syt1a	-1.36
5	0.00	194	ENSDARG00000035126	brd3b	-1.35
1	0.01	217	ENSDARG00000069619	atf7ip	-1.35
25	0.00	876	ENSDARG00000022045	map1ab	-1.35
1	0.00	-1	ENSDARG00000024702	parn	-1.34
11	0.01	-2	ENSDARG00000057940	dido1	-1.34
17	0.02	23	ENSDARG00000001129	dicer1	-1.34
11	0.02	734	ENSDARG00000008034	skib	-1.33
8	0.03	523	ENSDARG00000060081	crb2b	-1.33
16	0.02	0	ENSDARG00000093482	dedd1	-1.32
24	0.02	-51	ENSDARG00000038814	myrip	-1.32
25	0.01	1741	ENSDARG00000010844	kras	-1.32
9	0.00	0	ENSDARG00000001220	mycbp2	-1.32
17	0.00	0	ENSDARG00000071018	ptena	-1.32
8	0.00	3794	ENSDARG00000090454	gnb1a	-1.31
20	0.00	83	ENSDARG00000029150	hsp90ab1	-1.31
2	0.00	-5	ENSDARG00000057013	cadm3	-1.31
7	0.04	551	ENSDARG00000052091	rbpjb	-1.31
3	0.01	-1	ENSDARG00000040657	wipi1	-1.31
9	0.03	0	ENSDARG00000010437	fam46c	-1.30
19	0.03	2526	ENSDARG00000033367	rrm2b	-1.30
12	0.04	0	ENSDARG00000055930	zc3h7b	-1.30

15	0.00	-3	ENSDARG00000042837	atp1b3b	-1.30
19	0.00	-1	ENSDARG00000021140	pabpc1b	-1.29
6	0.01	-1	ENSDARG00000063538	kalrnb	-1.29
3	0.01	2115	ENSDARG00000006031	abat	-1.29
7	0.00	3043	ENSDARG00000044635	ptprda	-1.27
5	0.05	488	ENSDARG00000013730	slc4a4a	-1.27
6	0.02	-77	ENSDARG00000057782	baz2ba	-1.27
20	0.01	-1	ENSDARG00000042539	ywhaqa	-1.27
11	0.05	0	ENSDARG00000057940	dido1	-1.26
7	0.01	1787	ENSDARG00000091371	vgf	-1.25
24	0.01	1663	ENSDARG00000062154	dip2c	-1.24
5	0.03	-1	ENSDARG00000020008	vcp	-1.24
8	0.04	0	ENSDARG00000000966	ncor2	-1.23
19	0.00	1215	ENSDARG00000035994	rims2b	-1.20
8	0.00	2984	ENSDARG00000045639	elavl4	-1.19
20	0.02	-2	ENSDARG00000020609	snap25a	-1.13

ii. Differentially expressed genes in $MnCl_2$ treated wild-type and heterozygous *slc39a14*^{U801} siblings

(genes are listed in order of their fold-change)

Chr	p-value	Distance to 3' end	e76 Ensembl Gene ID	Gene name	Fold change (wt/wt_$MnCl_2$)
Upregulated					
3	0.04	3547	ENSDARG00000094901	ABCC6 (3 of 3)	3.38
8	0.01	2019	ENSDARG00000095866	fabp1b.2	2.62
1	0.04	2515	ENSDARG00000088020	cdkn1d	2.42
13	0.02	2491	ENSDARG00000079230	sorbs1	2.28
16	0.01	3764	ENSDARG00000054814	PTP4A3 (2 of 2)	2.27
11	0.00	0	ENSDARG00000059370	nr1d4b	2.10
3	0.01	3582	ENSDARG00000004597	lrrc4ba	2.08
10	0.01	2417	ENSDARG00000018856	dclk1a	1.93
16	0.01	2765	ENSDARG00000056642	hdac9b	1.89
23	0.02	-13	ENSDARG00000037607	NOL4L (1 of 2)	1.84
23	0.01	326	ENSDARG00000031161	nr1d4a	1.81
1	0.00	98	ENSDARG00000019945	ptprdb	1.80
18	0.01	4510	ENSDARG00000038121	ELL3	1.80
1	0.04	2089	ENSDARG00000052012	rtn4rl2a	1.78
22	0.03	2628	ENSDARG00000033589	EPHB3 (2 of 2)	1.73
18	0.04	169	ENSDARG00000086034	pvrl1b	1.72

16	0.03	2352	ENSDARG00000059945	SV2A	1.69
3	0.01	2011	ENSDARG00000043237	nfil3-2	1.67
18	0.03	4899	ENSDARG00000069122	si:ch211-216l23.2	1.66
1	0.00	3420	ENSDARG00000088020	cdkn1d	1.66
16	0.03	1572	ENSDARG00000056719	slc6a19b	1.64
17	0.01	1829	ENSDARG00000075397	si:dkey-204k5.2	1.63
12	0.02	1326	ENSDARG00000084694	SNORD27	1.60
20	0.03	861	ENSDARG00000090703	pdgfra	1.60
19	0.01	2	ENSDARG00000030215	matn1	1.58
7	0.00	-1	ENSDARG00000018817	bdnf	1.57
16	0.00	662	ENSDARG00000003820	nr1d2a	1.56
15	0.01	531	ENSDARG00000033845	igsf9ba	1.55
18	0.00	38	ENSDARG00000061328	cdon	1.48
17	0.02	3952	ENSDARG00000040135	-	1.47
2	0.05	0	ENSDARG00000071219	pik3r3a	1.47
9	0.04	140	ENSDARG00000077192	slc15a1a	1.44
9	0.01	5	ENSDARG00000030012	lrrfip1a	1.44
17	0.04	258	ENSDARG00000043932	stmn4l	1.36
Downregulated					
10	0.00	-73	ENSDARG00000019498	cry5	-9.56
24	0.00	-7	ENSDARG00000093044	si:ch211-161h7.5	-5.11
2	0.00	0	ENSDARG00000034503	per2	-4.69
8	0.02	-2	ENSDARG00000090130	LRIF1 (2 of 2)	-4.43
24	0.00	0	ENSDARG00000012388	CU855779.1	-4.16
25	0.00	234	ENSDARG00000019532	fads2	-3.82
8	0.03	744	ENSDARG00000041848	rh50	-3.73
16	0.00	259	ENSDARG00000091334	BX511252.1	-3.72
17	0.02	54	ENSDARG00000032553	egln3	-3.41
15	0.01	433	ENSDARG00000040628	CLDN17	-3.39
24	0.02	298	ENSDARG00000089881	BX547934.1	-3.10
8	0.00	874	ENSDARG00000078567	lonrf1l	-2.96
22	0.00	-2	ENSDARG00000091131	cry2b	-2.84
23	0.00	0	ENSDARG00000036864	slc34a2b	-2.80
6	0.00	1	ENSDARG00000087873	si:ch211-170n20.3	-2.73
11	0.00	2295	ENSDARG00000097499	si:ch211-268b10.2	-2.66
13	0.04	4767	ENSDARG00000046133	b3galnt2	-2.62
14	0.00	2710	ENSDARG00000075048	lonrf1	-2.59
16	0.00	-6	ENSDARG00000014496	trpv6	-2.58
20	0.00	0	ENSDARG00000042630	hebp2	-2.56
24	0.00	246	ENSDARG00000088190	si:dkeyp-88h4.2	-2.48
24	0.00	-11	ENSDARG00000027088	ptgdsb	-2.44

8	0.01	0	ENSDARG00000039754	xpc	-2.43
3	0.01	2530	ENSDARG00000038009	si:ch73-233k15.1	-2.39
15	0.03	-3	ENSDARG00000074526	zbtb16b	-2.37
2	0.00	286	ENSDARG00000015564	dhcr7	-2.33
18	0.00	-1	ENSDARG00000041140	ddb2	-2.31
24	0.00	0	ENSDARG00000002396	cry-dash	-2.29
24	0.03	2916	ENSDARG00000085208	5S_rRNA	-2.27
7	0.00	0	ENSDARG00000029446	bcmo1l	-2.26
19	0.00	4919	ENSDARG00000061752	fam65b	-2.25
12	0.04	3511	ENSDARG00000096505	si:ch73-103l1.2	-2.22
16	0.01	93	ENSDARG00000094929	APOA4 (4 of 4)	-2.22
9	0.02	1172	ENSDARG00000089651	CR936465.1	-2.20
4	0.01	1787	ENSDARG00000021647	gnai1	-2.19
1	0.00	-2	ENSDARG00000055876	msmo1	-2.17
9	0.00	2308	ENSDARG00000011770	dhrs12	-2.16
25	0.01	1093	ENSDARG00000011636	si:ch211-93f2.1	-2.12
19	0.01	0	ENSDARG00000086281	APOA4 (3 of 4)	-2.10
23	0.03	3865	ENSDARG00000076292	tenc1a	-2.09
19	0.00	2	ENSDARG00000070972	si:ch211-81a5.8	-2.08
16	0.00	0	ENSDARG00000053227	hamp2	-2.08
16	0.04	1308	ENSDARG00000040277	fbxo32	-2.07
3	0.00	9	ENSDARG00000075015	soul5	-2.06
5	0.05	2066	ENSDARG00000074581	add2	-2.01
12	0.00	2659	ENSDARG00000079166	ace	-2.00
4	0.00	0	ENSDARG00000045768	cry1a	-1.98
25	0.00	0	ENSDARG00000011636	si:ch211-93f2.1	-1.96
19	0.00	2	ENSDARG00000086370	apoea	-1.95
1	0.02	0	ENSDARG00000091609	SPINK4	-1.91
16	0.00	-3	ENSDARG00000020866	APOA4 (1 of 4)	-1.91
5	0.03	20	ENSDARG00000026964	hk2	-1.90
12	0.00	-1	ENSDARG00000039117	tefa	-1.89
11	0.02	516	ENSDARG00000010978	trmt1	-1.88
20	0.00	-1	ENSDARG00000095767	dio3b	-1.88
11	0.04	2	ENSDARG00000071211	C11H1orf50	-1.87
8	0.01	-1	ENSDARG00000088116	gstm3	-1.87
15	0.01	1	ENSDARG00000077236	hspb6	-1.86
6	0.00	0	ENSDARG00000031647	stat2	-1.86
18	0.01	-1	ENSDARG00000017675	cirh1a	-1.83
6	0.00	138	ENSDARG00000044356	tp63	-1.83
13	0.00	-5	ENSDARG00000033285	gsto2	-1.82
3	0.04	732	ENSDARG00000044852	wbp2nl	-1.79

5	0.00	0	ENSDARG00000007276	ela3l	-1.77
10	0.05	3819	ENSDARG00000068714	KSR1 (2 of 2)	-1.77
2	0.00	-2	ENSDARG00000095362	si:ch211-77g15.32	-1.76
1	0.03	1678	ENSDARG00000089138	LONRF2	-1.76
19	0.02	4603	ENSDARG00000055206	dtnbp1b	-1.74
16	0.04	-69	ENSDARG00000030602	rps19	-1.71
12	0.00	-3	ENSDARG00000089885	slc16a12b	-1.71
7	0.01	2111	ENSDARG00000025797	abhd2a	-1.70
2	0.02	-2	ENSDARG00000030896	foxq1a	-1.70
16	0.05	2732	ENSDARG00000021787	abcb5	-1.66
3	0.04	-2	ENSDARG00000038196	zgc:112146	-1.66
20	0.03	-2	ENSDARG00000042980	cyp2p7	-1.66
3	0.01	-1	ENSDARG00000022232	ppan	-1.66
5	0.01	348	ENSDARG00000061017	spns2	-1.65
6	0.01	1	ENSDARG00000052638	fam210b	-1.63
15	0.01	0	ENSDARG00000043102	lxn	-1.63
15	0.04	2225	ENSDARG00000077396	tlcd2	-1.62
4	0.00	12	ENSDARG00000006029	lta4h	-1.62
9	0.05	0	ENSDARG00000060504	PFKL (2 of 2)	-1.60
18	0.00	260	ENSDARG00000016080	nob1	-1.60
21	0.02	-8	ENSDARG00000017490	cel.1	-1.59
25	0.00	-73	ENSDARG00000016598	ckmt1	-1.59
12	0.01	-2	ENSDARG00000006413	rpl38	-1.59
18	0.02	0	ENSDARG00000069630	tat	-1.59
13	0.03	4	ENSDARG00000090337	pprc1	-1.59
16	0.02	-5	ENSDARG00000089399	tmem176l.2	-1.59
5	0.00	2015	ENSDARG00000060319	scn4bb	-1.58
13	0.00	0	ENSDARG00000039347	rps24	-1.58
23	0.00	4	ENSDARG00000007216	abce1	-1.57
14	0.01	2961	ENSDARG00000056563	ppargc1b	-1.57
16	0.00	2396	ENSDARG00000063540	foxo1a	-1.57
2	0.00	-1	ENSDARG00000007320	rpl7	-1.56
14	0.00	-1	ENSDARG00000037421	egr1	-1.56
20	0.03	-5	ENSDARG00000003751	lats1	-1.55
25	0.03	-3	ENSDARG00000021339	cpa5	-1.55
14	0.00	0	ENSDARG00000036121	pcdh10b	-1.54
6	0.01	0	ENSDARG00000058337	nop58	-1.54
16	0.02	-1	ENSDARG00000095863	zgc:161979	-1.54
23	0.00	1	ENSDARG00000025850	rps21	-1.54
23	0.03	0	ENSDARG00000060288	prosc	-1.52
10	0.01	-1	ENSDARG00000013871	slc5a1	-1.52

13	0.01	-1	ENSDARG00000090228	gstal	-1.52
15	0.01	3524	ENSDARG00000089170	CABZ01087568.1	-1.51
18	0.00	0	ENSDARG00000046119	rps3	-1.50
11	0.03	-4	ENSDARG00000021059	alas1	-1.50
9	0.03	4246	ENSDARG00000029497	tfcp2l1	-1.50
1	0.02	-6	ENSDARG00000077533	eif3f	-1.50
1	0.04	1	ENSDARG00000014313	atp5j	-1.50
13	0.05	0	ENSDARG00000090656	tomm20a	-1.49
22	0.02	1396	ENSDARG00000058440	slc6a6b	-1.49
15	0.00	34	ENSDARG00000090386	cd3eap	-1.47
20	0.05	3	ENSDARG00000041787	cx32.3	-1.47
22	0.03	1543	ENSDARG00000070907	lcor	-1.47
12	0.03	-40	ENSDARG00000071426	lrrc59	-1.47
15	0.01	2918	ENSDARG00000016465	slc1a5	-1.47
19	0.00	0	ENSDARG00000043509	rpl11	-1.46
17	0.03	3	ENSDARG00000086789	bahd1	-1.46
22	0.01	-3	ENSDARG00000074332	SPEN (2 of 2)	-1.46
6	0.05	-3	ENSDARG00000061923	amotl2a	-1.45
16	0.00	1	ENSDARG00000017219	pabpc1a	-1.45
18	0.03	797	ENSDARG00000075118	CABZ01079192.1	-1.43
16	0.01	-5	ENSDARG00000010411	epn1	-1.43
15	0.03	0	ENSDARG00000026821	tmem106ba	-1.43
25	0.03	2	ENSDARG00000090186	rps27.2	-1.43
20	0.05	0	ENSDARG00000053097	hsf2	-1.42
23	0.04	-1	ENSDARG00000036875	rps12	-1.41
2	0.00	0	ENSDARG00000035860	rps28	-1.41
14	0.02	-7	ENSDARG00000053262	atp1b4	-1.41
3	0.02	-2	ENSDARG00000053058	rps11	-1.40
9	0.01	0	ENSDARG00000055389	si:dkey-67c22.2	-1.40
6	0.01	0	ENSDARG00000030408	rps26l	-1.40
17	0.05	0	ENSDARG00000044395	ZFP36	-1.39
6	0.01	-4	ENSDARG00000015862	rpl5b	-1.39
7	0.03	-1	ENSDARG00000036298	rps13	-1.39
1	0.02	-59	ENSDARG00000006427	fabp2	-1.38
18	0.02	0	ENSDARG00000068374	si:ch211-132b12.7	-1.38
9	0.05	-11	ENSDARG00000040466	vil1	-1.38
7	0.00	6	ENSDARG00000011201	rplp2l	-1.38
15	0.05	-1	ENSDARG00000059035	POR (2 of 2)	-1.37
22	0.00	2	ENSDARG00000013012	rpl36	-1.37
6	0.03	-2	ENSDARG00000013561	pgm1	-1.37
13	0.00	19	ENSDARG00000057890	TTC31	-1.37

19	0.04	-3	ENSDARG00000016623	si:ch211-195b13.1	-1.36
3	0.00	1	ENSDARG00000020574	atp2a1	-1.36
1	0.02	0	ENSDARG00000045627	cyp3a65	-1.35
9	0.01	3246	ENSDARG00000060521	rbm27	-1.35
10	0.00	3951	ENSDARG00000056877	vamp2	-1.35
21	0.03	0	ENSDARG00000054191	pgk1	-1.35
10	0.03	-13	ENSDARG00000043154	ucp2	-1.33
1	0.03	2294	ENSDARG00000075141	gprc5bb	-1.32
3	0.03	0	ENSDARG00000053457	rpl23	-1.32
14	0.01	0	ENSDARG00000041619	gnb2l1	-1.31
12	0.04	41	ENSDARG00000077505	rbp4	-1.31
1	0.03	0	ENSDARG00000076833	atp1b1b	-1.30
24	0.05	-3	ENSDARG00000010516	rpl21	-1.29
2	0.04	3	ENSDARG00000008109	eef1da	-1.29
2	0.04	3176	ENSDARG00000018534	slc6a9	-1.26
3	0.03	146	ENSDARG00000037919	rbbp6	-1.23
6	0.01	4290	ENSDARG00000018032	scn8ab	-1.22
2	0.01	1047	ENSDARG00000061048	ranbp9	-1.21

iii. Differentially expressed genes only in untreated homozygous *slc39a14*^{U801} mutants which normalised upon $MnCl_2$ treatment

(genes are listed in order of their fold-change)

Chr	p-value	Distance to 3' end	e76 Ensembl Gene ID	Gene name	Fold change (mut/sib)
Upregulated					
13	0.00	2385	ENSDARG00000078272	CABP7 (2 of 2)	4.51
2	0.01	-9	ENSDARG00000028367	sult2st3	2.95
1	0.00	0	ENSDARG00000058873	PTPDC1 (1 of 2)	2.93
3	0.02	2990	ENSDARG00000086530	SMAD4 (2 of 2)	2.69
21	0.02	375	ENSDARG00000086835	ostf1	2.48
3	0.02	668	ENSDARG00000063126	GUSB (1 of 2)	2.35
25	0.00	3	ENSDARG00000003144	pxmp2	2.32
16	0.01	1553	ENSDARG00000076789	cx32.2	2.25
23	0.01	4008	ENSDARG00000002174	itfg2	2.19
8	0.01	0	ENSDARG00000070399	alg2	2.03
20	0.03	0	ENSDARG00000032117	ddx1	2.02
11	0.05	-3	ENSDARG00000035579	-	2.00
18	0.01	1582	ENSDARG00000059817	mtmr12	1.97
24	0.01	385	ENSDARG00000083837	CU467832.1	1.96

19	0.04	605	ENSDARG00000020994	wu:fb63a08	1.95
3	0.04	239	ENSDARG00000086947	-	1.94
25	0.05	3907	ENSDARG00000062134	KCNAB2 (1 of 2)	1.93
14	0.04	4111	ENSDARG00000062375	lcat	1.92
19	0.05	-6	ENSDARG00000070542	mafbb	1.92
7	0.01	-6	ENSDARG00000010276	ptgs2b	1.91
17	0.05	4690	ENSDARG00000078227	cspg4	1.83
13	0.04	-2	ENSDARG00000021033	herpud2	1.82
17	0.03	0	ENSDARG00000038894	tmx3	1.80
8	0.04	-1	ENSDARG00000054610	coro1a	1.77
23	0.03	1567	ENSDARG00000073824	RASGRF1	1.77
3	0.04	1811	ENSDARG00000069501	abhd11	1.76
7	0.04	4165	ENSDARG00000035595	ficd	1.74
2	0.00	-1	ENSDARG00000075014	sqstm1	1.72
7	0.00	-4	ENSDARG00000021059	alas1	1.69
9	0.00	-1	ENSDARG00000095767	dio3b	1.65
23	0.03	0	ENSDARG00000075326	mrps30	1.63
8	0.00	-2	ENSDARG00000006588	zgc:111983	1.63
6	0.01	6	ENSDARG00000041595	ces3	1.59
8	0.03	0	ENSDARG00000014031	abcc2	1.58
22	0.05	3318	ENSDARG00000029751	wbp1lb	1.58
10	0.02	-1	ENSDARG00000052851	golph3	1.56
15	0.03	0	ENSDARG00000004034	arhgdig	1.55
25	0.04	0	ENSDARG00000028071	bmp1a	1.54
8	0.00	-2	ENSDARG00000011168	anxa1c	1.53
19	0.04	0	ENSDARG00000045979	PTGDS (2 of 3)	1.53
11	0.03	1735	ENSDARG00000070584	clic5b	1.53
6	0.01	0	ENSDARG00000045408	tagln	1.52
23	0.01	1707	ENSDARG00000053668	stag2b	1.52
23	0.05	-2	ENSDARG00000020761	arrdc2	1.51
3	0.04	-3	ENSDARG00000079497	C5H8orf4 (2 of 2)	1.51
16	0.02	2138	ENSDARG00000062319	si:dkey-103g5.3	1.50
12	0.05	-1	ENSDARG00000094496	cfhl4	1.50
14	0.01	0	ENSDARG00000079840	kcnma1a	1.48
20	0.02	1331	ENSDARG00000079544	si:ch1073-464p5.5	1.48
21	0.05	-1	ENSDARG00000009544	cldnb	1.48
11	0.05	0	ENSDARG00000093494	si:ch211-217k17.9	1.46
23	0.05	0	ENSDARG00000042444	ankrd13c	1.46
11	0.05	-2	ENSDARG00000042874	phlda2	1.45
20	0.03	-1	ENSDARG00000097205	ulk2	1.44
12	0.02	-1	ENSDARG00000092158	cbx3b	1.44

7	0.04	0	ENSDARG00000008363	mcl1b	1.44
24	0.03	0	ENSDARG00000077566	CZv9_NA991H1orf52	1.42
4	0.01	4	ENSDARG00000007216	abce1	1.41
16	0.04	-9	ENSDARG00000016651	znf106a	1.40
6	0.03	1838	ENSDARG00000000861	scrib	1.39
7	0.05	1386	ENSDARG00000001710	flot1a	1.39
22	0.03	0	ENSDARG00000089429	si:dkey-205h13.2	1.39
7	0.04	3246	ENSDARG00000055009	col4a1	1.38
19	0.04	-95	ENSDARG00000094041	krt17	1.37
23	0.01	0	ENSDARG00000087243	zgc:100918	1.36
16	0.02	-1	ENSDARG00000038559	h1f0	1.35
8	0.05	-4	ENSDARG00000059646	nt5dc2	1.35
21	0.03	-6	ENSDARG00000037539	tnnc1b	1.34
9	0.04	-1	ENSDARG00000036073	cebpg	1.33
23	0.04	-3	ENSDARG00000071445	myoz1b	1.32
3	0.01	-1	ENSDARG00000036754	hmgn3	1.32
10	0.01	-3	ENSDARG00000094310	si:ch211-255g12.6	1.32
14	0.01	0	ENSDARG00000041169	hif1al	1.32
21	0.04	0	ENSDARG00000054849	bcat2	1.32
23	0.03	-4	ENSDARG00000056856	tax1bp1b	1.31
18	0.03	3490	ENSDARG00000022682	add1	1.31
6	0.04	-3	ENSDARG00000018285	pdpk1b	1.29
15	0.04	0	ENSDARG00000038068	ddx5	1.28
9	0.04	0	ENSDARG00000076892	nme2b.2	1.27
15	0.04	8	ENSDARG00000086917	crygm2d2	1.27
8	0.05	0	ENSDARG00000074057	calm1a	1.27
25	0.02	3705	ENSDARG00000061338	ddx6	1.25
11	0.00	-5	ENSDARG00000028213	ttna	1.25
10	0.02	-3	ENSDARG00000039914	gapdhs	1.24
3	0.05	2	ENSDARG00000035400	btf3	1.23
17	0.04	0	ENSDARG00000035136	sepw1	1.21
21	0.04	1	ENSDARG00000039641	rpl26	1.20
Downregulated					
1	0.00	1814	ENSDARG00000010108	bri3bp	-8.62
15	0.01	1514	ENSDARG00000088962	sdc3	-7.47
1	0.00	4998	ENSDARG00000012196	fer	-6.31
20	0.01	1436	ENSDARG00000055620	acad9	-4.06
3	0.01	2754	ENSDARG00000093300	si:dkey-18f7.2	-3.95
12	0.00	1429	ENSDARG00000076611	fbxo21	-3.75
18	0.00	4953	ENSDARG00000070620	grin2db	-3.49
4	0.00	2568	ENSDARG00000075456	PIK3CA (1 of 2)	-3.48

13	0.00	1694	ENSDARG00000011065	camk2b1	-3.32
20	0.00	4392	ENSDARG00000025797	abhd2a	-3.24
2	0.02	-30	ENSDARG00000023678	ercc5	-2.95
7	0.00	1968	ENSDARG00000062646	tet3	-2.92
11	0.00	1026	ENSDARG00000024785	ctnna2	-2.92
21	0.03	3899	ENSDARG00000092473	apopt1	-2.86
2	0.00	338	ENSDARG00000059789	parp8	-2.84
9	0.00	2920	ENSDARG00000033498	rorb	-2.73
11	0.04	4748	ENSDARG00000085920	5S_rRNA	-2.72
1	0.00	1289	ENSDARG00000081232	dre-mir-454b	-2.71
4	0.00	0	ENSDARG00000012468	aacs	-2.67
20	0.03	3342	ENSDARG00000007751	lmnl3	-2.65
2	0.00	4689	ENSDARG00000075347	chfr	-2.64
10	0.00	2790	ENSDARG00000059719	fam169aa	-2.62
25	0.01	7	ENSDARG00000058630	BDP1 (2 of 2)	-2.60
25	0.04	1204	ENSDARG00000054864	aplp2	-2.58
15	0.00	2352	ENSDARG00000059945	SV2A	-2.52
17	0.04	3076	ENSDARG00000076030	cacnb3b	-2.37
21	0.01	3582	ENSDARG00000004597	lrrc4ba	-2.34
6	0.02	1777	ENSDARG00000075461	suv420h2	-2.32
14	0.00	2220	ENSDARG00000006747	tmem178b	-2.29
19	0.00	259	ENSDARG00000063035	ntrk3b	-2.29
11	0.00	14	ENSDARG00000061089	KIF21A (1 of 3)	-2.26
16	0.01	1958	ENSDARG00000069044	agpat4	-2.24
24	0.01	758	ENSDARG00000019549	cds1	-2.22
10	0.00	1329	ENSDARG00000017365	slc23a2	-2.21
1	0.00	1495	ENSDARG00000015053	grip1	-2.20
9	0.00	1073	ENSDARG00000037423	SMIM19	-2.19
20	0.01	1284	ENSDARG00000080201	5S_rRNA	-2.13
17	0.04	1205	ENSDARG00000026651	APBB2 (1 of 2)	-2.12
8	0.01	1685	ENSDARG00000026664	uri1	-2.12
25	0.00	2366	ENSDARG00000032083	dpysl2b	-2.10
19	0.01	1887	ENSDARG00000056563	ppargc1b	-2.10
13	0.00	1235	ENSDARG00000090124	alcama	-2.08
13	0.01	-5	ENSDARG00000020301	os9	-2.07
13	0.03	20	ENSDARG00000026964	hk2	-2.06
23	0.00	3461	ENSDARG00000086856	stk35	-2.04
7	0.00	-49	ENSDARG00000012094	prkar1ab	-2.04
9	0.04	2927	ENSDARG00000015502	adam10b	-2.03
8	0.04	606	ENSDARG00000053724	ADCYAP1R1 (2 of 2)	-1.99
23	0.01	561	ENSDARG00000079312	kmt2ca	-1.94

8	0.01	135	ENSDARG00000027357	cd2bp2	-1.93
18	0.04	3168	ENSDARG00000069430	tp53i11a	-1.93
3	0.02	2628	ENSDARG00000033589	EPHB3 (2 of 2)	-1.92
11	0.00	99	ENSDARG00000041926	DLG4 (2 of 2)	-1.92
20	0.02	573	ENSDARG00000055543	appb	-1.91
15	0.02	-5	ENSDARG00000008209	myt1la	-1.91
23	0.00	4406	ENSDARG00000037904	cacna1db	-1.90
3	0.01	-98	ENSDARG00000060348	map3k3	-1.87
11	0.00	2163	ENSDARG00000093503	RSF1 (3 of 3)	-1.86
14	0.00	-48	ENSDARG00000002771	SLC4A5 (1 of 2)	-1.86
3	0.03	2019	ENSDARG00000001676	gpm6bb	-1.85
17	0.00	2735	ENSDARG00000035256	eef2l2	-1.85
15	0.01	-5	ENSDARG00000053857	-	-1.85
3	0.01	-72	ENSDARG00000043474	atp2b3a	-1.84
7	0.03	13	ENSDARG00000012274	eif4e1c	-1.82
2	0.00	3815	ENSDARG00000052142	ACVR1B (2 of 2)	-1.82
7	0.00	1599	ENSDARG00000051748	ccnd2a	-1.81
11	0.00	-67	ENSDARG00000068745	MAP4 (1 of 3)	-1.81
16	0.00	0	ENSDARG00000043226	nfixa	-1.81
7	0.00	2898	ENSDARG00000070242	ENDOD1 (5 of 13)	-1.80
2	0.00	531	ENSDARG00000033845	igsf9ba	-1.80
20	0.00	639	ENSDARG00000021442	cdh11	-1.80
14	0.00	1404	ENSDARG00000000563	ttnb	-1.79
18	0.02	2417	ENSDARG00000018856	dclk1a	-1.79
16	0.02	-3	ENSDARG00000025206	syt2a	-1.78
1	0.00	1515	ENSDARG00000097478	qkia	-1.78
17	0.01	2563	ENSDARG00000037203	insig2	-1.76
4	0.00	3	ENSDARG00000046090	dhrs11a	-1.76
14	0.00	861	ENSDARG00000090703	pdgfra	-1.75
1	0.02	40	ENSDARG00000078317	si:dkey-175m17.7	-1.73
8	0.01	661	ENSDARG00000024877	ptgr1	-1.70
21	0.00	2087	ENSDARG00000016918	ace2	-1.69
4	0.00	4151	ENSDARG00000074759	ccar1	-1.69
19	0.01	4565	ENSDARG00000038300	rnf34a	-1.69
14	0.01	2139	ENSDARG00000074126	ttc39a	-1.68
2	0.04	-13	ENSDARG00000037607	NOL4L (1 of 2)	-1.68
23	0.01	861	ENSDARG00000054290	acin1a	-1.67
20	0.01	2033	ENSDARG00000032317	tox	-1.67
12	0.04	2507	ENSDARG00000018032	scn8ab	-1.67
6	0.00	3033	ENSDARG00000022045	map1ab	-1.66
10	0.01	1809	ENSDARG00000056554	rap1gap	-1.66

21	0.00	3913	ENSDARG00000089770	5S_rRNA	-1.62
25	0.02	2819	ENSDARG00000032039	mxd1	-1.62
7	0.00	2848	ENSDARG00000033804	snx27a	-1.61
18	0.01	-79	ENSDARG00000017220	otud7b	-1.58
24	0.01	281	ENSDARG00000024895	fam50a	-1.58
1	0.05	4425	ENSDARG00000078011	NAV1 (2 of 3)	-1.58
21	0.04	15	ENSDARG00000078581	crebrf	-1.58
13	0.03	70	ENSDARG00000038855	chmp5a	-1.56
3	0.04	9	ENSDARG00000017673	nova2	-1.55
2	0.01	1189	ENSDARG00000026035	ube2b	-1.54
16	0.01	-79	ENSDARG00000029394	ilf3b	-1.54
9	0.01	1040	ENSDARG00000052604	CPEB2	-1.54
19	0.04	911	ENSDARG00000085592	5S_rRNA	-1.53
12	0.00	74	ENSDARG00000005567	map2k6	-1.52
15	0.00	185	ENSDARG00000056722	cd99l2	-1.52
19	0.01	3203	ENSDARG00000079251	nlgn2b	-1.52
10	0.04	2932	ENSDARG00000010524	si:ch211-282j22.3	-1.51
10	0.00	-1	ENSDARG00000017841	cand1	-1.50
14	0.01	84	ENSDARG00000012777	nucks1b	-1.49
23	0.03	96	ENSDARG00000071113	xirp2a	-1.49
16	0.01	25	ENSDARG00000053665	gabrg2	-1.49
9	0.03	68	ENSDARG00000019258	elmo1	-1.49
6	0.00	866	ENSDARG00000052419	ankrd12	-1.48
1	0.00	1039	ENSDARG00000089271	si:dkey-114c15.7	-1.48
24	0.02	-51	ENSDARG00000061647	nrxn1a	-1.47
16	0.01	76	ENSDARG00000068123	gkap1	-1.47
23	0.04	3454	ENSDARG00000078302	BRINP1	-1.46
19	0.02	4136	ENSDARG00000035158	MCAM (2 of 3)	-1.46
12	0.04	0	ENSDARG00000097170	pcdh1a3	-1.46
22	0.02	5	ENSDARG00000020521	exoc6	-1.46
16	0.04	3615	ENSDARG00000035952	cdr2a	-1.46
24	0.04	302	ENSDARG00000043304	nop2	-1.45
21	0.01	-2	ENSDARG00000068582	rnf44	-1.45
4	0.05	470	ENSDARG00000052150	pbx4	-1.44
6	0.04	66	ENSDARG00000061635	myo5aa	-1.44
16	0.03	4556	ENSDARG00000056244	-	-1.42
9	0.02	463	ENSDARG00000070981	ash1l	-1.42
18	0.01	0	ENSDARG00000021378	phf21ab	-1.42
25	0.05	140	ENSDARG00000062020	gse1	-1.42
2	0.03	699	ENSDARG00000079540	CACNA2D2 (3 of 3)	-1.42
8	0.00	2002	ENSDARG00000062138	ranbp10	-1.42

19	0.00	-3	ENSDARG00000010791	dla	-1.41
23	0.00	0	ENSDARG00000068214	ccni	-1.41
17	0.00	-1	ENSDARG00000018817	bdnf	-1.40
13	0.01	-1	ENSDARG00000014013	lbr	-1.40
20	0.05	-62	ENSDARG00000097699	si:ch211-9f20.5	-1.40
11	0.04	1610	ENSDARG00000020164	efnb2a	-1.38
8	0.01	173	ENSDARG00000059674	lrp12	-1.38
19	0.02	58	ENSDARG00000051748	ccnd2a	-1.37
20	0.01	865	ENSDARG00000076559	RB1CC1	-1.37
6	0.04	-9	ENSDARG00000059973	fbxo11a	-1.37
8	0.00	638	ENSDARG00000019213	CTBP1	-1.37
19	0.03	2830	ENSDARG00000038121	ELL3	-1.37
25	0.00	5	ENSDARG00000030614	syt1a	-1.37
16	0.00	194	ENSDARG00000035126	brd3b	-1.36
21	0.00	876	ENSDARG00000022045	map1ab	-1.36
3	0.05	1732	ENSDARG00000077582	ank3b	-1.35
3	0.00	-1	ENSDARG00000024702	parn	-1.34
11	0.01	23	ENSDARG00000001129	dicer1	-1.34
18	0.04	-1	ENSDARG00000074581	add2	-1.34
18	0.03	734	ENSDARG00000008034	skib	-1.33
8	0.01	523	ENSDARG00000060081	crb2b	-1.33
23	0.01	0	ENSDARG00000093482	dedd1	-1.33
6	0.03	-51	ENSDARG00000038814	myrip	-1.32
23	0.02	1741	ENSDARG00000010844	kras	-1.32
2	0.03	0	ENSDARG00000071018	ptena	-1.32
14	0.00	3794	ENSDARG00000090454	gnb1a	-1.32
4	0.00	-5	ENSDARG00000057013	cadm3	-1.32
14	0.04	1985	ENSDARG00000062510	bcl11ba	-1.31
10	0.04	0	ENSDARG00000055930	zc3h7b	-1.31
21	0.00	-3	ENSDARG00000042837	atp1b3b	-1.30
25	0.04	2716	ENSDARG00000078416	zeb2b	-1.30
12	0.02	-1	ENSDARG00000021140	pabpc1b	-1.30
6	0.03	-1	ENSDARG00000063538	kalrnb	-1.29
14	0.00	3043	ENSDARG00000044635	ptprda	-1.28
18	0.05	488	ENSDARG00000013730	slc4a4a	-1.28
21	0.01	-1	ENSDARG00000042539	ywhaqa	-1.27
23	0.01	1663	ENSDARG00000062154	dip2c	-1.25
7	0.03	-1	ENSDARG00000020008	vcp	-1.24
1	0.05	-2	ENSDARG00000023323	ywhaqb	-1.24
13	0.03	0	ENSDARG00000000966	ncor2	-1.23
16	0.04	1215	ENSDARG00000035994	rims2b	-1.20

9	0.00	2984	ENSDARG00000045639	elavl4	-1.20
21	0.05	-2	ENSDARG00000020609	snap25a	-1.14
8	0.02	-3	ENSDARG00000011701	ctsll	-1.13

iv. Genes differentially expressed in $MnCl_2$ treated homozygous *slc39a14*^{U801} mutants

(genes are listed in order of their fold-change)

Chr	p-value	Distance to 3' end	e76 Ensembl Gene ID	Gene name	Fold change (mut/sib)
Upregulated					
13	0.00	0	ENSDARG00000011862	inaa	6.49
22	0.01	686	ENSDARG00000044526	camk1ga	5.44
6	0.00	3109	ENSDARG00000070726	cnga3a	5.24
19	0.00	4818	ENSDARG00000063690	nrm	3.80
16	0.00	-1	ENSDARG00000038439	fabp10a	3.19
6	0.00	-1	ENSDARG00000097008	opn1mw1	3.09
2	0.00	1640	ENSDARG00000020602	grk7a	2.83
19	0.00	2197	ENSDARG00000063014	dbpa	2.72
8	0.00	-8	ENSDARG00000078917	zgc:195245	2.59
1	0.00	0	ENSDARG00000042988	SLC24A2 (1 of 2)	2.57
17	0.02	1985	ENSDARG00000062510	bcl11ba	2.44
16	0.05	-2	ENSDARG00000037860	cox6b2	2.39
3	0.00	-4	ENSDARG00000037925	rgs9a	2.39
22	0.04	-6	ENSDARG00000070918	FETUB (2 of 2)	2.37
21	0.00	2	ENSDARG00000094217	si:dkey-17e16.15	2.34
1	0.02	-8	ENSDARG00000094133	si:dkey-9i23.11	2.31
13	0.00	0	ENSDARG00000014840	prph2b	2.29
14	0.00	125	ENSDARG00000039963	fgfbp1	2.28
8	0.00	-3	ENSDARG00000012848	arih2	2.26
19	0.00	-5	ENSDARG00000035909	mfsd2ab	2.21
25	0.00	-3	ENSDARG00000018566	flnca	2.03
18	0.01	-16	ENSDARG00000018119	cox5ab	2.03
4	0.01	-31	ENSDARG00000045490	NDUFB2	2.01
16	0.04	0	ENSDARG00000070399	alg2	1.99
3	0.04	1882	ENSDARG00000061836	nfixb	1.95
3	0.04	-2	ENSDARG00000059610	gpr146	1.94
1	0.02	-1	ENSDARG00000031164	tuba8l2	1.91
3	0.01	5	ENSDARG00000037941	syt5a	1.90
21	0.02	8	ENSDARG00000057571	pgam2	1.88
18	0.02	0	ENSDARG00000068374	si:ch211-132b12.7	1.88
22	0.01	2852	ENSDARG00000071375	celf5a	1.87

2	0.00	-10	ENSDARG00000055595	clul1	1.87
8	0.00	4257	ENSDARG00000077112	sc:d0413	1.84
16	0.02	4249	ENSDARG00000062374	leng9	1.84
6	0.05	1	ENSDARG00000044199	gnat1	1.83
19	0.01	0	ENSDARG00000011146	uqcrb	1.82
22	0.00	11	ENSDARG00000022968	fxr1	1.81
14	0.04	2	ENSDARG00000056874	lygl1	1.81
12	0.02	-6	ENSDARG00000096721	si:rp71-1c10.11	1.76
1	0.00	-75	ENSDARG00000029898	CNGA1 (2 of 2)	1.71
18	0.00	3062	ENSDARG00000086756	RGS9BP	1.65
4	0.03	12	ENSDARG00000006029	lta4h	1.64
16	0.01	-1	ENSDARG00000040251	ctsk	1.64
15	0.00	223	ENSDARG00000063475	abcg1	1.63
15	0.04	1143	ENSDARG00000077785	atf5b	1.60
19	0.00	12	ENSDARG00000011334	ncaldb	1.60
6	0.02	0	ENSDARG00000038153	lgals2b	1.55
12	0.00	-7	ENSDARG00000056605	wbp2	1.55
4	0.01	1637	ENSDARG00000045798	ptn	1.53
12	0.02	-1	ENSDARG00000078461	pde6c	1.52
3	0.00	-2	ENSDARG00000038196	zgc:112146	1.51
11	0.05	235	ENSDARG00000028066	diras1a	1.51
14	0.04	1	ENSDARG00000032929	cryba1l1	1.50
6	0.01	-23	ENSDARG00000015531	SLC4A8	1.49
15	0.04	0	ENSDARG00000079414	sez6b	1.49
17	0.04	1053	ENSDARG00000057790	ankrd6a	1.46
19	0.03	-1	ENSDARG00000070012	sesn2	1.46
3	0.00	-2	ENSDARG00000053058	rps11	1.45
10	0.04	-13	ENSDARG00000030498	il6st	1.45
19	0.00	1215	ENSDARG00000035994	rims2b	1.44
4	0.04	-58	ENSDARG00000001953	pfkfb3	1.43
13	0.03	1151	ENSDARG00000004702	irf2bp2a	1.43
20	0.00	47	ENSDARG00000046106	rab10	1.43
9	0.01	1435	ENSDARG00000057768	RBMS1 (1 of 2)	1.40
6	0.01	0	ENSDARG00000009505	slmo2	1.37
8	0.00	-1	ENSDARG00000042529	gnat2	1.37
21	0.00	1040	ENSDARG00000059978	cplx4a	1.37
3	0.01	0	ENSDARG00000053457	rpl23	1.35
25	0.03	-6	ENSDARG00000062477	kiaa1549la	1.34
8	0.01	-12	ENSDARG00000056090	capza1b	1.34
15	0.02	-1	ENSDARG00000069361	spa17	1.34
15	0.01	0	ENSDARG00000010764	flj13639	1.33
4	0.03	3	ENSDARG00000092677	COA6	1.30
16	0.00	-5	ENSDARG00000019902	rcv1	1.29
9	0.04	-2	ENSDARG00000040674	ctdsp1	1.23

Downregulated					
6	0.00	-2	ENSDARG00000070439	pde6h	-6.19
25	0.00	0	ENSDARG00000011636	si:ch211-93f2.1	-5.27
1	0.01	27	ENSDARG00000094910	si:dkey-22i16.7	-4.61
23	0.00	1153	ENSDARG00000031161	nr1d4a	-4.36
25	0.00	657	ENSDARG00000045737	guca1g	-3.96
15	0.02	-10	ENSDARG00000088885	si:ch1073-340i21.3	-3.66
6	0.02	0	ENSDARG00000052099	agxta	-3.66
19	0.00	0	ENSDARG00000011334	ncaldb	-3.45
19	0.00	-1	ENSDARG00000002696	gnb3b	-3.31
3	0.05	-2	ENSDARG00000038141	atf4b2	-3.24
8	0.04	-3	ENSDARG00000056765	ela2l	-3.24
9	0.00	0	ENSDARG00000013708	usp9	-3.23
6	0.00	-2	ENSDARG00000097445	si:dkey-195m11.8	-3.18
6	0.03	-3	ENSDARG00000096398	si:ch211-276a17.5	-3.12
9	0.04	444	ENSDARG00000069440	dachd	-3.07
16	0.00	-6	ENSDARG00000043457	gapdh	-3.04
17	0.01	111	ENSDARG00000082907	dre-mir-124-4	-2.85
8	0.02	0	ENSDARG00000076873	C8H9orf172 (2 of 2)	-2.84
23	0.00	33	ENSDARG00000055638	ankrd33aa	-2.81
11	0.02	3817	ENSDARG00000043835	rab3ab	-2.79
24	0.03	-2	ENSDARG00000015567	zic1	-2.75
11	0.01	815	ENSDARG00000082495	dre-mir-726	-2.61
21	0.00	3140	ENSDARG00000044629	guca1d	-2.60
22	0.01	-1	ENSDARG00000057598	s100b	-2.59
8	0.02	-23	ENSDARG00000010933	CACNA1F (1 of 2)	-2.57
21	0.01	-3	ENSDARG00000089716	FP085391.3	-2.56
2	0.03	2	ENSDARG00000053358	basp1	-2.54
24	0.03	2	ENSDARG00000004274	zgc:112496	-2.54
23	0.00	326	ENSDARG00000031161	nr1d4a	-2.49
15	0.02	2109	ENSDARG00000088513	si:dkey-95o3.4	-2.49
6	0.00	2402	ENSDARG00000070726	cnga3a	-2.45
1	0.02	1831	ENSDARG00000089742	FAM161A	-2.43
6	0.04	0	ENSDARG00000005526	igfn1.1	-2.41
25	0.01	3984	ENSDARG00000090595	5S_rRNA	-2.39
3	0.00	1	ENSDARG00000096849	si:dkey-16p21.8	-2.38
12	0.00	2	ENSDARG00000038018	prph2a	-2.38
7	0.01	0	ENSDARG00000009466	rgs9bp	-2.34
16	0.05	662	ENSDARG00000003820	nr1d2a	-2.32
18	0.01	4899	ENSDARG00000069122	si:ch211-216l23.2	-2.29
1	0.00	-73	ENSDARG00000052035	NXNL1 (1 of 2)	-2.20
7	0.00	1767	ENSDARG00000052138	slc1a2a	-2.19
20	0.00	0	ENSDARG00000010434	clu	-2.17
21	0.00	3	ENSDARG00000053875	cryba1b	-2.13

10	0.00	0	ENSDARG00000011422	ryr1a	-2.11
20	0.00	0	ENSDARG00000069305	si:ch211-203k16.3	-2.10
15	0.00	0	ENSDARG00000030758	guca1c	-2.09
7	0.01	647	ENSDARG00000035732	arntl1b	-2.09
8	0.01	0	ENSDARG00000019417	gadd45g	-2.03
6	0.04	-4	ENSDARG00000015862	rpl5b	-2.02
20	0.00	-3	ENSDARG00000070781	cx35b	-2.00
7	0.00	4746	ENSDARG00000079738	ZNF219	-1.98
10	0.01	108	ENSDARG00000063614	SKOR2	-1.97
3	0.05	639	ENSDARG00000054320	ap2a1	-1.97
16	0.04	0	ENSDARG00000019622	rims2a	-1.96
17	0.00	0	ENSDARG00000060494	eprs	-1.95
8	0.04	-1	ENSDARG00000055294	atoh1a	-1.91
8	0.03	2337	ENSDARG00000069484	dab2ipa	-1.91
16	0.00	0	ENSDARG00000057652	dbpb	-1.90
2	0.02	0	ENSDARG00000007663	amph	-1.89
23	0.04	561	ENSDARG00000094280	USP21	-1.89
21	0.00	1748	ENSDARG00000079286	bcr	-1.87
15	0.05	3746	ENSDARG00000043483	otx5	-1.87
19	0.01	-3	ENSDARG00000078529	bai1b	-1.86
8	0.02	2507	ENSDARG00000036820	mgll	-1.83
13	0.02	4770	ENSDARG00000004695	six4a	-1.83
12	0.00	-2	ENSDARG00000096616	si:ch211-255p10.3	-1.83
24	0.00	225	ENSDARG00000087082	CNGB3 (2 of 2)	-1.82
12	0.03	2	ENSDARG00000061844	ARHGEF15 (2 of 2)	-1.82
13	0.00	-1	ENSDARG00000090228	gstal	-1.81
13	0.00	97	ENSDARG00000007382	ubtd1a	-1.80
10	0.01	-9	ENSDARG00000070080	nbeaa	-1.80
11	0.00	10	ENSDARG00000074221	ABCA7	-1.78
3	0.05	-3	ENSDARG00000037790	pvalb8	-1.78
23	0.00	-3	ENSDARG00000013963	mipb	-1.78
22	0.01	-3	ENSDARG00000000212	zgc:92061	-1.77
21	0.00	-8	ENSDARG00000017490	cel.1	-1.76
3	0.01	0	ENSDARG00000056791	zgc:112320	-1.76
9	0.02	65	ENSDARG00000034677	scel	-1.74
2	0.01	-5	ENSDARG00000063218	ppm1la	-1.74
21	0.03	2072	ENSDARG00000077650	tnks	-1.73
22	0.00	1396	ENSDARG00000058440	slc6a6b	-1.73
4	0.00	185	ENSDARG00000045574	lrmp	-1.72
1	0.01	0	ENSDARG00000045627	cyp3a65	-1.72
16	0.02	0	ENSDARG00000044719	nrsn1	-1.72
11	0.00	0	ENSDARG00000087981	CABZ01088330.1	-1.71
3	0.04	0	ENSDARG00000074752	hlfa	-1.71
19	0.02	219	ENSDARG00000071015	pbxip1a	-1.69

18	0.00	-5	ENSDARG00000041691	bhlhe41	-1.68
19	0.00	2	ENSDARG00000070972	si:ch211-81a5.8	-1.67
23	0.00	1	ENSDARG00000025850	rps21	-1.67
15	0.00	2019	ENSDARG00000063475	abcg1	-1.67
25	0.00	-2	ENSDARG00000009563	slc1a2b	-1.67
17	0.00	258	ENSDARG00000043932	stmn4l	-1.66
15	0.01	-1	ENSDARG00000096909	GUCA1C (3 of 3)	-1.65
8	0.05	-60	ENSDARG00000011521	upb1	-1.65
6	0.00	-6	ENSDARG00000077004	aldh1l1	-1.65
11	0.01	3457	ENSDARG00000005966	slc4a5	-1.64
13	0.00	-2	ENSDARG00000033364	zgc:158387	-1.64
16	0.00	-5	ENSDARG00000089399	tmem176l.2	-1.64
6	0.00	-3	ENSDARG00000096324	si:ch211-155d24.7	-1.64
24	0.01	-2	ENSDARG00000071626	PTGDS (3 of 3)	-1.63
14	0.02	1260	ENSDARG00000040198	fstl5	-1.63
18	0.01	1459	ENSDARG00000062821	slc6a15	-1.63
20	0.03	0	ENSDARG00000011602	si:dkeyp-117h8.2	-1.63
3	0.00	1068	ENSDARG00000052223	rcvrna	-1.62
1	0.03	184	ENSDARG00000070452	tmem66	-1.60
15	0.05	4270	ENSDARG00000028793	nlk2	-1.60
10	0.01	3562	ENSDARG00000018065	ntm	-1.60
16	0.00	-2	ENSDARG00000033655	stmn1b	-1.60
25	0.04	-1	ENSDARG00000045904	nr2e3	-1.59
12	0.01	-3	ENSDARG00000037618	ddit4	-1.58
17	0.00	-2	ENSDARG00000053485	aldh6a1	-1.58
14	0.02	-1	ENSDARG00000080010	adh5	-1.57
19	0.00	0,0	ENSDARG00000036830, ENSDARG00000092947	zgc:92533,yt1	-1.57
7	0.01	6	ENSDARG00000011201	rplp2l	-1.57
10	0.05	2	ENSDARG00000015978	COX5B (2 of 3)	-1.56
16	0.00	-8	ENSDARG00000055514	icn2	-1.56
2	0.01	0	ENSDARG00000038894	tmx3	-1.55
20	0.00	-1	ENSDARG00000007823	atf3	-1.55
20	0.02	0	ENSDARG00000090722	C20H6orf58 (1 of 2)	-1.54
8	0.00	523	ENSDARG00000060081	crb2b	-1.54
21	0.00	-1	ENSDARG00000009553	gng3	-1.53
16	0.04	-5	ENSDARG00000010420	ndrg1b	-1.53
8	0.02	0	ENSDARG00000093606	RPS11 (2 of 2)	-1.53
2	0.04	1	ENSDARG00000076223	SERP1 (2 of 2)	-1.53
20	0.00	59	ENSDARG00000007823	atf3	-1.52
12	0.00	0	ENSDARG00000052896	lrit1b	-1.52
7	0.03	3203	ENSDARG00000067829	ppargc1a	-1.52
19	0.04	0	ENSDARG00000042620	zgc:162356	-1.52
8	0.00	-6	ENSDARG00000005776	guk1b	-1.52
16	0.00	-2	ENSDARG00000009978	icn	-1.51

12	0.00	0	ENSDARG00000089997	gngt2b	-1.50
10	0.00	-1	ENSDARG00000056511	arr3a	-1.50
2	0.00	3207	ENSDARG00000077722	ppp2r3a	-1.50
13	0.00	0	ENSDARG00000039347	rps24	-1.49
23	0.03	-1	ENSDARG00000004836	dnajc5ab	-1.49
20	0.02	-8	ENSDARG00000095743	sox11b	-1.49
16	0.04	0	ENSDARG00000040159	wnt4b	-1.49
25	0.05	6	ENSDARG00000007788	atp2b1b	-1.48
19	0.00	0	ENSDARG00000036832	cyt1l	-1.48
19	0.02	0	ENSDARG00000076892	nme2b.2	-1.48
25	0.00	0	ENSDARG00000043722	cpa4	-1.47
12	0.03	0	ENSDARG00000045051	slc16a3	-1.47
3	0.01	470	ENSDARG00000052150	pbx4	-1.47
6	0.01	-2	ENSDARG00000013561	pgm1	-1.47
9	0.00	-3	ENSDARG00000005470	kif5aa	-1.47
16	0.04	-6	ENSDARG00000004358	gnb3a	-1.47
22	0.00	-1	ENSDARG00000007421	ftcd	-1.47
17	0.00	3	ENSDARG00000086789	bahd1	-1.46
20	0.04	0	ENSDARG00000012656	atf6	-1.46
12	0.00	0	ENSDARG00000074001	crygmxl2	-1.46
24	0.01	509	ENSDARG00000042751	riok3	-1.45
17	0.03	-3	ENSDARG00000097369	si:ch1073-358o18.3	-1.45
21	0.03	-6	ENSDARG00000055523	slc22a6l	-1.45
16	0.00	-7	ENSDARG00000002311	fabp11b	-1.45
12	0.04	0	ENSDARG00000022820	pde6g	-1.44
13	0.01	2990	ENSDARG00000028228	zbtb18	-1.44
4	0.02	4	ENSDARG00000019396	rergla	-1.44
18	0.00	0	ENSDARG00000088839	BX248120.1	-1.44
9	0.00	-6	ENSDARG00000019856	atp1a1b	-1.44
22	0.05	2	ENSDARG00000013012	rpl36	-1.44
17	0.00	0	ENSDARG00000007697	fabp7a	-1.43
12	0.02	-1	ENSDARG00000021806	zfp36l2	-1.43
17	0.05	-2	ENSDARG00000021811	calm1a	-1.43
13	0.00	-5	ENSDARG00000033285	gsto2	-1.43
9	0.03	-4	ENSDARG00000055052	map2	-1.42
7	0.04	662	ENSDARG00000052082	GABARAP (2 of 2)	-1.42
21	0.04	-1	ENSDARG00000010385	sept4a	-1.41
12	0.04	3822	ENSDARG00000076434	ARHGAP22 (2 of 2)	-1.41
23	0.01	-86	ENSDARG00000037559	uba1	-1.41
14	0.00	-1	ENSDARG00000037488	canx	-1.40
13	0.02	0	ENSDARG00000074919	CU929052.1	-1.40
22	0.03	0	ENSDARG00000043180	gpd1b	-1.40
19	0.00	2	ENSDARG00000035694	stm	-1.39
7	0.00	-1	ENSDARG00000015536	sox6	-1.39

17	0.00	3302	ENSDARG00000055158	prox1a	-1.39
25	0.00	-73	ENSDARG00000016598	ckmt1	-1.39
8	0.03	-1	ENSDARG00000079745	-	-1.38
23	0.00	-8	ENSDARG00000039007	eno3	-1.38
7	0.03	-4	ENSDARG00000039730	zgc:112160	-1.38
6	0.00	5	ENSDARG00000059775	slc32a1	-1.38
23	0.00	1	ENSDARG00000088091	pfn1	-1.38
11	0.00	-16	ENSDARG00000044861	opn1lw2	-1.38
16	0.03	-1	ENSDARG00000042993	try	-1.37
17	0.01	-1	ENSDARG00000014106	cfl2	-1.37
21	0.00	9	ENSDARG00000024831	crhbp	-1.37
1	0.01	0	ENSDARG00000093494	si:ch211-217k17.9	-1.37
3	0.00	0	ENSDARG00000038401	tefb	-1.37
1	0.04	0	ENSDARG00000076833	atp1b1b	-1.37
2	0.05	0	ENSDARG00000020103	calrl	-1.37
4	0.01	-51	ENSDARG00000085168	AL935186.3	-1.36
11	0.05	0	ENSDARG00000004060	bhlhe40	-1.36
6	0.00	0	ENSDARG00000017624	krt4	-1.36
6	0.01	0	ENSDARG00000031647	stat2	-1.36
20	0.05	-3	ENSDARG00000016528	C20H2orf44	-1.36
22	0.00	0	ENSDARG00000059738	ptprsa	-1.36
10	0.02	-1	ENSDARG00000029764	mef2ca	-1.36
3	0.00	-1	ENSDARG00000053467	gtpbp1	-1.35
20	0.05	1553	ENSDARG00000076789	cx32.2	-1.35
7	0.01	2	ENSDARG00000044125	txn	-1.35
3	0.05	0	ENSDARG00000052642	shisa9b	-1.35
1	0.00	157	ENSDARG00000052713	lrrtm1	-1.35
24	0.00	659	ENSDARG00000005332	lipi	-1.35
18	0.03	0	ENSDARG00000034753	tspan3a	-1.35
3	0.00	3	ENSDARG00000033160	nr1d1	-1.35
24	0.01	0	ENSDARG00000012388	CU855779.1	-1.34
25	0.04	1975	ENSDARG00000070734	dyrk4	-1.34
20	0.02	0	ENSDARG00000054723	PDE4DIP	-1.34
14	0.02	-5	ENSDARG00000004261	tmed9	-1.34
16	0.03	0	ENSDARG00000021808	nmt2	-1.34
2	0.04	0	ENSDARG00000089534	CU693369.1	-1.34
19	0.04	-2	ENSDARG00000071026	mllt11	-1.34
18	0.00	1	ENSDARG00000056745	necab2	-1.33
2	0.01	6	ENSDARG00000087277	selj	-1.33
9	0.02	-11	ENSDARG00000040466	vil1	-1.33
6	0.02	4830	ENSDARG00000096252	artna	-1.33
7	0.00	0	ENSDARG00000059571	dennd4c	-1.33
11	0.00	0	ENSDARG00000039444	FAIM2	-1.33
15	0.01	4553	ENSDARG00000088898	CALN1	-1.32

24	0.04	-2	ENSDARG00000014556	serpinb1l3	-1.32
6	0.02	-2	ENSDARG00000030349	cryba2a	-1.32
19	0.01	-7	ENSDARG00000035798	gngt1	-1.32
1	0.05	-3	ENSDARG00000027355	slc25a4	-1.31
13	0.02	0	ENSDARG00000078102	PSD (2 of 3)	-1.31
6	0.05	0	ENSDARG00000070951	hmga1b	-1.31
19	0.01	0	ENSDARG00000020850	eef1a1l1	-1.31
15	0.00	1072	ENSDARG00000026784	robo1	-1.31
15	0.03	-6	ENSDARG00000070019	taf15	-1.31
11	0.00	82	ENSDARG00000003165	nr2f6b	-1.30
19	0.00	0	ENSDARG00000036830	zgc:92533	-1.30
20	0.05	0	ENSDARG00000077187	impg1a	-1.30
14	0.00	385	ENSDARG00000083837	CU467832.1	-1.30
21	0.05	76	ENSDARG00000002587	dpysl3	-1.30
18	0.02	797	ENSDARG00000075118	CABZ01079192.1	-1.30
13	0.00	-1	ENSDARG00000062139	eif2ak3	-1.29
24	0.00	1	ENSDARG00000045442	cpb1	-1.29
11	0.00	675	ENSDARG00000016551	IQSEC1	-1.28
14	0.00	-7	ENSDARG00000053262	atp1b4	-1.28
18	0.00	2244	ENSDARG00000039232	DUSP8 (2 of 2)	-1.28
21	0.05	4721	ENSDARG00000090617	CTIF	-1.28
14	0.03	20	ENSDARG00000037393	slc43a1a	-1.28
23	0.02	0	ENSDARG00000074790	C23H20orf24	-1.28
21	0.01	1374	ENSDARG00000041562	CABZ01079427.1	-1.27
22	0.00	-1	ENSDARG00000044526	camk1ga	-1.27
4	0.00	-1	ENSDARG00000003570	hsp90b1	-1.27
17	0.05	3	ENSDARG00000037840	actc1b	-1.27
25	0.04	3603	ENSDARG00000061368	klf13	-1.27
24	0.02	3	ENSDARG00000058005	hgd	-1.27
3	0.01	3861	ENSDARG00000014134	prkacaa	-1.27
1	0.03	1013	ENSDARG00000023600	sh3gl2	-1.26
2	0.01	1869	ENSDARG00000058784	tfr1a	-1.26
6	0.00	-2	ENSDARG00000078842	TNS1 (2 of 2)	-1.26
10	0.01	-13	ENSDARG00000023174	fez1	-1.26
23	0.00	0	ENSDARG00000088040	MDP1	-1.26
6	0.05	-2	ENSDARG00000038076	ROMO1	-1.25
10	0.02	9	ENSDARG00000029764	mef2ca	-1.25
19	0.00	-2	ENSDARG00000036834	zgc:109868	-1.24
22	0.03	-1	ENSDARG00000019307	dusp5	-1.24
10	0.00	3951	ENSDARG00000056877	vamp2	-1.24
6	0.00	4290	ENSDARG00000018032	scn8ab	-1.23
4	0.05	19	ENSDARG00000073963	C4H12orf56	-1.23
3	0.00	2760	ENSDARG00000014420	elavl3	-1.23
7	0.01	-1	ENSDARG00000008100	slc7a10a	-1.22

22	0.04	0	ENSDARG00000053973	fetub	-1.22
17	0.01	3459	ENSDARG00000079068	adam12	-1.22
22	0.00	-5	ENSDARG00000022372	kng1	-1.21
1	0.05	3574	ENSDARG00000059036	appa	-1.21
6	0.00	0	ENSDARG00000044280	opn1mw2	-1.21
23	0.00	0	ENSDARG00000058873	PTPDC1 (1 of 2)	-1.21
11	0.00	0	ENSDARG00000059370	nr1d4b	-1.20
7	0.00	623	ENSDARG00000091111	TIFA	-1.19

5. Copyright clearance

ELSEVIER LICENSE
TERMS AND CONDITIONS

Jun 16, 2016

This Agreement between Karin Tuschl ("You") and Elsevier ("Elsevier") consists of your license details and the terms and conditions provided by Elsevier and Copyright Clearance Center.

License Number	3842990970550
License date	Apr 06, 2016
Licensed Content Publisher	Elsevier
Licensed Content Publication	Elsevier Books
Licensed Content Title	International Review of Neurobiology
Licensed Content Author	Karin Tuschl,Philippa B. Mills,Peter T. Clayton
Licensed Content Date	2013
Start Page	277
End Page	312
Type of Use	reuse in a thesis/dissertation
Portion	excerpt
Number of excerpts	10
Format	both print and electronic
Are you the author of this Elsevier chapter?	Yes
How many pages did you author in this Elsevier book?	35
Will you be translating?	No
Order reference number	
Title of your thesis/dissertation	Zebrafish disease models to study the pathogenesis of inherited manganese transporter defects and provide a route for drug discovery
Expected completion date	Sep 2016

Estimated size (number of pages)	400
Elsevier VAT number	GB 494 6272 12
Requestor Location	Karin Tuschl 30 Guilford Street UCL Institute of Child Health Clinical and Molecular Genetics Unit London, WC1N 1EH United Kingdom Attn: Karin Tuschl
Billing Type	Invoice
Billing Address	Karin Tuschl 30 Guilford Street UCL Institute of Child Health Clinical and Molecular Genetics Unit London, United Kingdom WC1N 1EH Attn: Karin Tuschl
Total	0.00 GBP
Total	0.00 GBP

Nature communications

- **Order detail ID:**69870782
- **Order License Id:**3890820432711
- **ISSN:**2041-1723
- **Publication Type:**e-Journal
- **Volume:**
- **Issue:**
- **Start page:**
- **Publisher:**Nature Publishing Group
- **Permission Status:** **Granted**
- **Permission type:**Republish or display content
- **Type of use:**Republish in a thesis/dissertation

Requestor type	Author of requested content
Format	Print, Electronic
Portion	chart/graph/table/figure
Number of charts/graphs/tables/figures	8
Title or numeric reference of the portion(s)	Figure 1-8, Table 1-2
Title of the article or chapter the portion is from	Mutations in SLC39A14 disrupt manganese homeostasis and cause childhood-onset parkinsonism–dystonia
Editor of portion(s)	Min Cho
Author of portion(s)	Karin Tuschl
Volume of serial or monograph	11601
Page range of portion	1-16
Publication date of portion	27 May 2016
Rights for	Main product
Duration of use	Life of current edition
Creation of copies for the disabled	no

With minor editing privileges	yes
For distribution to	U.K. and Commonwealth (excluding Canada)
In the following language(s)	Original language of publication
With incidental promotional use	no
Lifetime unit quantity of new product	Up to 499
Made available in the following markets	education
The requesting person/organization	Karin Tuschl
Order reference number	
Author/Editor	Karin Tuschl
The standard identifier of New Work	Thesis
The proposed price	0
Title of New Work	Zebrafish disease models to study the pathogenesis of inherited manganese transporter defects and provide a route for drug discovery
Publisher of New Work	Karin Tuschl
Expected publication date	Sep 2016
Estimated size (pages)	318

Note: This item will be invoiced or charged separately through CCC's **RightsLink** service. More info**$ 0.00**

Reference List

1. Aschner, J.L. & Aschner, M. Nutritional aspects of manganese homeostasis. *Mol. Aspects Med* **26**, 353-362 (2005).
2. Aschner, M., Erikson, K.M. & Dorman, D.C. Manganese dosimetry: species differences and implications for neurotoxicity. *Crit Rev. Toxicol* **35**, 1-32 (2005).
3. Roth, J.A. Homeostatic and toxic mechanisms regulating manganese uptake, retention, and elimination. *Biol. Res* **39**, 45-57 (2006).
4. Abrams, E. *et al.* Absorption as a factor in manganese homeostasis. *J. Anim Sci* **42**, 630-636 (1976).
5. Britton, A.A. & Cotzias, G.C. Dependence of manganese turnover on intake. *Am. J. Physiol* **211**, 203-206 (1966).
6. Davis, C.D., Wolf, T.L. & Greger, J.L. Varying levels of manganese and iron affect absorption and gut endogenous losses of manganese by rats. *J. Nutr* **122**, 1300-1308 (1992).
7. Malecki, E.A., Radzanowski, G.M., Radzanowski, T.J., Gallaher, D.D. & Greger, J.L. Biliary manganese excretion in conscious rats is affected by acute and chronic manganese intake but not by dietary fat. *J. Nutr* **126**, 489-498 (1996).
8. Davidsson, L., Cederblad, A., Lonnerdal, B. & Sandstrom, B. The effect of individual dietary components on manganese absorption in humans. *Am. J. Clin. Nutr* **54**, 1065-1070 (1991).
9. Alsulimani, H.H., Ye, Q. & Kim, J. Effect of Hfe deficiency on memory capacity and motor coordination after manganese exposure by drinking water in mice. *Toxicol Res* **31**, 347-54 (2015).
10. Fitsanakis, V.A. *et al.* Changes in dietary iron exacerbate regional brain manganese accumulation as determined by magnetic resonance imaging. *Toxicol. Sci* **120**, 146-153 (2011).
11. Fitsanakis, V.A., Zhang, N., Garcia, S. & Aschner, M. Manganese (Mn) and iron (Fe): interdependency of transport and regulation. *Neurotox. Res* **18**, 124-131 (2010).
12. Keen, C.L. *et al.* Nutritional aspects of manganese from experimental studies. *Neurotoxicology* **20**, 213-223 (1999).
13. Friedman, B.J. *et al.* Manganese balance and clinical observations in young men fed a manganese-deficient diet. *J. Nutr* **117**, 133-143 (1987).
14. Penland, J.G. & Johnson, P.E. Dietary calcium and manganese effects on menstrual cycle symptoms. *Am. J. Obstet. Gynecol* **168**, 1417-1423 (1993).
15. Boycott, K.M. *et al.* Autosomal-recessive intellectual disability with cerebellar atrophy syndrome caused by mutation of the manganese and zinc transporter gene SLC39A8. *Am J Hum Genet* **97**, 886-93 (2015).
16. Park, J.H. *et al.* SLC39A8 Deficiency: A disorder of manganese transport and glycosylation. *Am J Hum Genet* **97**, 894-903 (2015).
17. Couper, J. On the effects of black oxide of manganese when inhaled into the lungs. *Brit Ann Med Pharm* **1**, 41-42 (1837).
18. Rodier, J. Manganese poisoning in Maroccan miners. *Br J Ind Med* **12**, 21-35 (1955).
19. Huang, C.C., Chu, N.S., Lu, C.S. & Calne, D.B. Cock gait in manganese intoxication. *Mov Disord* **12**, 807-808 (1997).
20. Roth, J.A. Are there common biochemical and molecular mechanisms controlling manganism and parkisonism. *Neuromolecular. Med* **11**, 281-296 (2009).
21. Calne, D.B., Chu, N.S., Huang, C.C., Lu, C.S. & Olanow, W. Manganism and idiopathic parkinsonism: similarities and differences. *Neurology* **44**, 1583-1586 (1994).

22. Kwakye, G.F., Paoliello, M.M., Mukhopadhyay, S., Bowman, A.B. & Aschner, M. Manganese-induced parkinsonism and parkinson's disease: shared and distinguishable features. *Int J Environ Res Public Health* **12**, 7519-40 (2015).
23. Heilig, E.A. *et al.* Manganese and iron transport across pulmonary epithelium. *Am. J. Physiol Lung Cell Mol. Physiol* **290**, L1247-L1259 (2006).
24. Leavens, T.L., Rao, D., Andersen, M.E. & Dorman, D.C. Evaluating transport of manganese from olfactory mucosa to striatum by pharmacokinetic modeling. *Toxicol. Sci* **97**, 265-278 (2007).
25. Sanders, A.P., Miller, S.K., Nguyen, V., Kotch, J.B. & Fry, R.C. Toxic metal levels in children residing in a smelting craft village in Vietnam: a pilot biomonitoring study. *BMC Public Health* **14**, 114 (2014).
26. Bouchard, M.F. *et al.* Intellectual impairment in school-age children exposed to manganese from drinking water. *Environ. Health Perspect* **119**, 138-143 (2011).
27. Khan, K. *et al.* Manganese exposure from drinking water and children's academic achievement. *Neurotoxicology* **33**, 91-97 (2012).
28. Chalela, J.A., Bonillha, L., Neyens, R. & Hays, A. Manganese encephalopathy: an under-recognized condition in the intensive care unit. *Neurocrit. Care* **14**, 456-458 (2011).
29. Baker, B., Ali, A. & Isenring, L. Recommendations for manganese supplementation to adult patients receiving long-term home parenteral nutrition: an analysis of the supporting evidence. *Nutr Clin Pract* **31**, 180-5 (2016).
30. Dastych, M., Dastych, M., Jr. & Senkyrik, M. Manganese in whole blood and hair in patients with long-term home parenteral nutrition. *Clin Lab* **62**, 173-7 (2016).
31. Janocha-Litwin, J., Marianska, K., Serafinska, S. & Simon, K. Manganese encephalopathy among ephedron abusers. *J Neuroimaging* **25**, 832-5 (2015).
32. Poniatowska, R. *et al.* MRI brain findings in ephedrone encephalopathy associated with manganese abuse: Single-center perspective. *Pol J Radiol* **79**, 150-5 (2014).
33. Sikk, K. & Taba, P. Methcathinone "kitchen chemistry" and permanent neurological damage. *Int Rev Neurobiol* **120**, 257-71 (2015).
34. Stepens, A. *et al.* A Parkinsonian syndrome in methcathinone users and the role of manganese. *N. Engl. J. Med* **358**, 1009-1017 (2008).
35. Butterworth, R.F. Parkinsonism in cirrhosis: pathogenesis and current therapeutic options. *Metab Brain Dis* (2012).
36. Chen, P., Parmalee, N. & Aschner, M. Genetic factors and manganese-induced neurotoxicity. *Front Genet* **5**, 265 (2014).
37. Roth, J.A. Correlation between the biochemical pathways altered by mutated parkinson-related genes and chronic exposure to manganese. *Neurotoxicology* **44C**, 314-325 (2014).
38. Gitler, A.D. *et al.* Alpha-synuclein is part of a diverse and highly conserved interaction network that includes PARK9 and manganese toxicity. *Nat. Genet* **41**, 308-315 (2009).
39. Higashi, Y. *et al.* Parkin attenuates manganese-induced dopaminergic cell death. *J. Neurochem* **89**, 1490-1497 (2004).
40. Tan, J. *et al.* Regulation of intracellular manganese homeostasis by Kufor-Rakeb syndrome-associated ATP13A2 protein. *J. Biol. Chem* **286**, 29654-29662 (2011).
41. Rentschler, G. *et al.* ATP13A2 (PARK9) polymorphisms influence the neurotoxic effects of manganese. *Neurotoxicology* **33**, 697-702 (2012).
42. Ducic, T. *et al.* Alpha-synuclein regulates neuronal levels of manganese and calcium. *ACS Chem Neurosci* **6**, 1769-79 (2015).
43. Bates, C.A., Fu, S., Ysselstein, D., Rochet, J.C. & Zheng, W. Expression and transport of alpha-synuclein at the blood-cerebrospinal fluid barrier and effects of manganese exposure. *ADMET DMPK* **3**, 15-33 (2015).

44. Carboni, E. & Lingor, P. Insights on the interaction of alpha-synuclein and metals in the pathophysiology of Parkinson's disease. *Metallomics* **7**, 395-404 (2015).
45. Xu, B. *et al.* Inhibition of calpain prevents manganese-induced cell injury and alpha-synuclein oligomerization in organotypic brain slice cultures. *PLoS One* **10**, e0119205 (2015).
46. Tuschl, K. *et al.* Syndrome of hepatic cirrhosis, dystonia, polycythemia, and hypermanganesemia caused by mutations in SLC30A10, a manganese transporter in man. *Am. J. Hum. Genet* **90**, 457-466 (2012).
47. Leyva-Illades, D. *et al.* SLC30A10 is a cell surface-localized manganese efflux transporter, and parkinsonism-causing mutations block its intracellular trafficking and efflux activity. *J Neurosci* **34**, 14079-14095 (2014).
48. Quadri, M. *et al.* Mutations in SLC30A10 cause parkinsonism and dystonia with hypermanganesemia, polycythemia, and chronic liver disease. *Am. J. Hum. Genet* **90**, 467-477 (2012).
49. Quadri, M. *et al.* Manganese transport disorder: Novel SLC30A10 mutations and early phenotypes. *Mov Disord* (2015).
50. Tuschl, K. *et al.* Hepatic cirrhosis, dystonia, polycythaemia and hypermanganesaemia--a new metabolic disorder. *J. Inherit. Metab Dis* **31**, 151-163 (2008).
51. Stamelou, M. *et al.* Dystonia with brain manganese accumulation resulting from SLC30A10 mutations: a new treatable disorder. *Mov Disord* **27**, 1317-1322 (2012).
52. Li, S.J. *et al.* Pallidal index as biomarker of manganese brain accumulation and associated with manganese levels in blood: a meta-analysis. *PLoS. One* **9**, e93900 (2014).
53. Huang, P. *et al.* Manganese effects in the liver following subacute or subchronic manganese chloride exposure in rats. *Ecotoxicol. Environ. Saf* **74**, 615-622 (2011).
54. Witzleben, C.L., Pitlick, P., Bergmeyer, J. & Benoit, R. Ccute manganese overload. A new experimental model of intrahepatic cholestasis. *Am. J. Pathol* **53**, 409-422 (1968).
55. Sanchez, B. *et al.* Fatal manganese intoxication due to an error in the elaboration of Epsom salts for a liver cleansing diet. *Forensic Sci. Int* **223**, e1-e4 (2012).
56. Borchers, A., Epstein, S.E., Gindiciosi, B., Cartoceti, A. & Puschner, B. Acute enteral manganese intoxication with hepatic failure due to ingestion of a joint supplement overdose. *J Vet Diagn Invest* **26**, 658-63 (2014).
57. Tuschl, K., Clayton, P.T., Gospe, S.M. & Mills, P.B. Dystonia/Parkinsonism, hypermanganesemia, polycythemia, and chronic liver disease. (1993).
58. Delnooz, C.C. *et al.* Phenotypic variability in a dystonia family with mutations in the manganese transporter gene. *Mov Disord* (2013).
59. Gospe, S.M., Jr. *et al.* Paraparesis, hypermanganesaemia, and polycythaemia: a novel presentation of cirrhosis. *Arch. Dis. Child* **83**, 439-442 (2000).
60. Ebert, B.L. & Bunn, H.F. Regulation of the erythropoietin gene. *Blood* **94**, 1864-1877 (1999).
61. Kaczmarek, M. *et al.* Metal ions-stimulated iron oxidation in hydroxylases facilitates stabilization of HIF-1 alpha protein. *Toxicol Sci* **107**, 394-403 (2009).
62. Haase, V.H. Regulation of erythropoiesis by hypoxia-inducible factors. *Blood Rev* **27**, 41-53 (2013).
63. Lieb, M.E., Menzies, K., Moschella, M.C., Ni, R. & Taubman, M.B. Mammalian EGLN genes have distinct patterns of mRNA expression and regulation. *Biochem Cell Biol* **80**, 421-6 (2002).
64. Bunn, H.F. Erythropoietin. *Cold Spring Harb. Perspect. Med* **3**, a011619 (2013).

65. Tuschl, K. *et al.* Mutations in SLC39A14 disrupt manganese homeostasis and cause childhood-onset parkinsonism-dystonia. *Nat Commun* **7**, 11601 (2016).
66. Bradberry, S. & Vale, A. A comparison of sodium calcium edetate (edetate calcium disodium) and succimer (DMSA) in the treatment of inorganic lead poisoning. *Clin. Toxicol. (Phila)* **47**, 841-858 (2009).
67. Ribeiro, R.T., Dos Santos-Neto, D., Braga-Neto, P. & Barsottini, O.G. Inherited manganism. *Clin. Neurol. Neurosurg* (2013).
68. Brna, P., Gordon, K., Dooley, J.M. & Price, V. Manganese toxicity in a child with iron deficiency and polycythemia. *J. Child Neurol* **26**, 891-894 (2011).
69. Fujishiro, H., Yano, Y., Takada, Y., Tanihara, M. & Himeno, S. Roles of ZIP8, ZIP14, and DMT1 in transport of cadmium and manganese in mouse kidney proximal tubule cells. *Metallomics* **4**, 700-708 (2012).
70. Girijashanker, K. *et al.* Slc39a14 gene encodes ZIP14, a metal/bicarbonate symporter: similarities to the ZIP8 transporter. *Mol. Pharmacol* **73**, 1413-1423 (2008).
71. Jenkitkasemwong, S., Wang, C.Y., Mackenzie, B. & Knutson, M.D. Physiologic implications of metal-ion transport by ZIP14 and ZIP8. *Biometals* **25**, 643-655 (2012).
72. Nebert, D.W. *et al.* ZIP14 and ZIP8 zinc/bicarbonate symporters in Xenopus oocytes: characterization of metal uptake and inhibition. *Metallomics* **4**, 1218-1225 (2012).
73. He, L. *et al.* ZIP8, member of the solute-carrier-39 (SLC39) metal-transporter family: characterization of transporter properties. *Mol. Pharmacol* **70**, 171-180 (2006).
74. Wang, C.Y. *et al.* ZIP8 is an iron and zinc transporter whose cell-surface expression is up-regulated by cellular iron loading. *J. Biol. Chem* **287**, 34032-34043 (2012).
75. Sacher, A., Cohen, A. & Nelson, N. Properties of the mammalian and yeast metal-ion transporters DCT1 and Smf1p expressed in Xenopus laevis oocytes. *J. Exp. Biol* **204**, 1053-1061 (2001).
76. Gunshin, H. *et al.* Cloning and characterization of a mammalian proton-coupled metal-ion transporter. *Nature* **388**, 482-488 (1997).
77. Garcia, S.J., Gellein, K., Syversen, T. & Aschner, M. Iron deficient and manganese supplemented diets alter metals and transporters in the developing rat brain. *Toxicol. Sci* **95**, 205-214 (2007).
78. Burdo, J.R. *et al.* Distribution of divalent metal transporter 1 and metal transport protein 1 in the normal and Belgrade rat. *J. Neurosci. Res* **66**, 1198-1207 (2001).
79. Chua, A.C. & Morgan, E.H. Manganese metabolism is impaired in the Belgrade laboratory rat. *J. Comp Physiol B* **167**, 361-369 (1997).
80. Knopfel, M., Zhao, L. & Garrick, M.D. Transport of divalent transition-metal ions is lost in small-intestinal tissue of b/b Belgrade rats. *Biochemistry* **44**, 3454-3465 (2005).
81. Wang, X.S., Ong, W.Y. & Connor, J.R. A light and electron microscopic study of the iron transporter protein DMT-1 in the monkey cerebral neocortex and hippocampus. *J. Neurocytol* **30**, 353-360 (2001).
82. Yokel, R.A. & Crossgrove, J.S. Manganese toxicokinetics at the blood-brain barrier. *Res. Rep. Health Eff. Inst*, 7-58 (2004).
83. Huang, E., Ong, W.Y. & Connor, J.R. Distribution of divalent metal transporter-1 in the monkey basal ganglia. *Neuroscience* **128**, 487-496 (2004).
84. Sriram, K. *et al.* Dopaminergic neurotoxicity following pulmonary exposure to manganese-containing welding fumes. *Arch. Toxicol* **84**, 521-540 (2010).

85. Gruenheid, S. *et al.* The iron transport protein NRAMP2 is an integral membrane glycoprotein that colocalizes with transferrin in recycling endosomes. *J. Exp. Med* **189**, 831-841 (1999).
86. Au, C., Benedetto, A. & Aschner, M. Manganese transport in eukaryotes: the role of DMT1. *Neurotoxicology* **29**, 569-576 (2008).
87. Gunter, T.E. *et al.* Manganese transport via the transferrin mechanism. *Neurotoxicology* **34C**, 118-127 (2012).
88. Crossgrove, J.S. & Yokel, R.A. Manganese distribution across the blood-brain barrier. IV. Evidence for brain influx through store-operated calcium channels. *Neurotoxicology* **26**, 297-307 (2005).
89. Lucaciu, C.M., Dragu, C., Copaescu, L. & Morariu, V.V. Manganese transport through human erythrocyte membranes. An EPR study. *Biochim. Biophys. Acta* **1328**, 90-98 (1997).
90. Kannurpatti, S.S., Joshi, P.G. & Joshi, N.B. Calcium sequestering ability of mitochondria modulates influx of calcium through glutamate receptor channel. *Neurochem. Res* **25**, 1527-1536 (2000).
91. Crossgrove, J.S., Allen, D.D., Bukaveckas, B.L., Rhineheimer, S.S. & Yokel, R.A. Manganese distribution across the blood-brain barrier. I. Evidence for carrier-mediated influx of managanese citrate as well as manganese and manganese transferrin. *Neurotoxicology* **24**, 3-13 (2003).
92. Sreedharan, S., Stephansson, O., Schioth, H.B. & Fredriksson, R. Long evolutionary conservation and considerable tissue specificity of several atypical solute carrier transporters. *Gene* **478**, 11-18 (2011).
93. Seve, M., Chimienti, F., Devergnas, S. & Favier, A. In silico identification and expression of SLC30 family genes: an expressed sequence tag data mining strategy for the characterization of zinc transporters' tissue expression. *BMC. Genomics* **5**, 32 (2004).
94. Lin, H. *et al.* A single amino acid change in the yeast vacuolar metal transporters ZRC1 and COT1 alters their substrate specificity. *J. Biol. Chem* **283**, 33865-33873 (2008).
95. Bosomworth, H.J., Thornton, J.K., Coneyworth, L.J., Ford, D. & Valentine, R.A. Efflux function, tissue-specific expression and intracellular trafficking of the Zn transporter ZnT10 indicate roles in adult Zn homeostasis. *Metallomics* **4**, 771-779 (2012).
96. Aschner, M., Guilarte, T.R., Schneider, J.S. & Zheng, W. Manganese: recent advances in understanding its transport and neurotoxicity. *Toxicol. Appl. Pharmacol* **221**, 131-147 (2007).
97. Madejczyk, M.S. & Ballatori, N. The iron transporter ferroportin can also function as a manganese exporter. *Biochim. Biophys. Acta* **1818**, 651-657 (2012).
98. Yin, Z. *et al.* Ferroportin is a manganese-responsive protein that decreases manganese cytotoxicity and accumulation. *J. Neurochem* **112**, 1190-1198 (2010).
99. Santos, P.C. *et al.* Non-HFE hemochromatosis. *Rev. Bras. Hematol. Hemoter* **34**, 311-316 (2012).
100. Seo, Y.A. & Wessling-Resnick, M. Ferroportin deficiency impairs manganese metabolism in flatiron mice. *FASEB J* **29**, 2726-33 (2015).
101. Tussing-Humphreys, L., Pusatcioglu, C., Nemeth, E. & Braunschweig, C. Rethinking iron regulation and assessment in iron deficiency, anemia of chronic disease, and obesity: introducing hepcidin. *J. Acad. Nutr. Diet* **112**, 391-400 (2012).
102. Bartnikas, T.B. Known and potential roles of transferrin in iron biology. *Biometals* **25**, 677-686 (2012).

103. Mukhopadhyay, S. & Linstedt, A.D. Identification of a gain-of-function mutation in a Golgi P-type ATPase that enhances Mn2+ efflux and protects against toxicity. *Proc. Natl. Acad. Sci. U. S. A* **108**, 858-863 (2011).
104. Vanoevelen, J. *et al.* The secretory pathway Ca2+/Mn2+-ATPase 2 is a Golgi-localized pump with high affinity for Ca2+ ions. *J. Biol. Chem* **280**, 22800-22808 (2005).
105. Xiang, M., Mohamalawari, D. & Rao, R. A novel isoform of the secretory pathway Ca2+,Mn(2+)-ATPase, hSPCA2, has unusual properties and is expressed in the brain. *J. Biol. Chem* **280**, 11608-11614 (2005).
106. Sepulveda, M.R., Berrocal, M., Marcos, D., Wuytack, F. & Mata, A.M. Functional and immunocytochemical evidence for the expression and localization of the secretory pathway Ca2+-ATPase isoform 1 (SPCA1) in cerebellum relative to other Ca2+ pumps. *J. Neurochem* **103**, 1009-1018 (2007).
107. Leitch, S. *et al.* Vesicular distribution of Secretory Pathway Ca(2)+-ATPase isoform 1 and a role in manganese detoxification in liver-derived polarized cells. *Biometals* **24**, 159-170 (2011).
108. Chiesi, M. & Inesi, G. Adenosine 5'-triphosphate dependent fluxes of manganese and and hydrogen ions in sarcoplasmic reticulum vesicles. *Biochemistry* **19**, 2912-2918 (1980).
109. Gomes da, C.A. & Madeira, V.M. Magnesium and manganese ions modulate Ca2+ uptake and its energetic coupling in sarcoplasmic reticulum. *Arch. Biochem. Biophys* **249**, 199-206 (1986).
110. Van, B.K. *et al.* The Ca2+/Mn2+ pumps in the Golgi apparatus. *Biochim. Biophys. Acta* **1742**, 103-112 (2004).
111. Behrens, M.I. *et al.* Clinical spectrum of Kufor-Rakeb syndrome in the Chilean kindred with ATP13A2 mutations. *Mov Disord* **25**, 1929-1937 (2010).
112. Schmidt, K., Wolfe, D.M., Stiller, B. & Pearce, D.A. Cd2+, Mn2+, Ni2+ and Se2+ toxicity to Saccharomyces cerevisiae lacking YPK9p the orthologue of human ATP13A2. *Biochem. Biophys. Res. Commun* **383**, 198-202 (2009).
113. Chen, P., Culbreth, M. & Aschner, M. Exposure, epidemiology, and mechanism of the environmental toxicant manganese. *Environ Sci Pollut Res Int* (2016).
114. Guilarte, T.R. & Gonzales, K.K. Manganese-induced parkinsonism is not idiopathic Parkinson's Disease: environmental and genetic evidence. *Toxicol Sci* **146**, 204-12 (2015).
115. Guilarte, T.R. Manganese and Parkinson's disease: a critical review and new findings. *Cien. Saude Colet* **16**, 4549-4566 (2011).
116. Chen, P. *et al.* Manganese homeostasis in the nervous system. *J Neurochem* (2015).
117. Yamada, M. *et al.* Chronic manganese poisoning: a neuropathological study with determination of manganese distribution in the brain. *Acta Neuropathol* **70**, 273-278 (1986).
118. Deng, Y. *et al.* Melatonin inhibits manganese-induced motor dysfunction and neuronal loss in mice: involvement of oxidative stress and dopaminergic neurodegeneration. *Mol Neurobiol* **51**, 68-88 (2015).
119. Guilarte, T.R. *et al.* Impairment of nigrostriatal dopamine neurotransmission by manganese is mediated by pre-synaptic mechanism(s): implications to manganese-induced parkinsonism. *J. Neurochem* **107**, 1236-1247 (2008).
120. Roth, J.A., Li, Z., Sridhar, S. & Khoshbouei, H. The effect of manganese on dopamine toxicity and dopamine transporter (DAT) in control and DAT transfected HEK cells. *Neurotoxicology* **35**, 121-128 (2013).
121. Huang, C.Y. *et al.* Chronic manganism: A long-term follow-up study with a new dopamine terminal biomarker of 18F-FP-(+)-DTBZ (18F-AV-133) brain PET scan. *J Neurol Sci* **353**, 102-6 (2015).

122. McDougall, S.A. *et al.* Postnatal manganese exposure alters dopamine transporter function in adult rats: Potential impact on nonassociative and associative processes. *Neuroscience* **154**, 848-860 (2008).
123. Butterworth, R.F., Spahr, L., Fontaine, S. & Layrargues, G.P. Manganese toxicity, dopaminergic dysfunction and hepatic encephalopathy. *Metab Brain Dis* **10**, 259-267 (1995).
124. Mousseau, D.D., Perney, P., Layrargues, G.P. & Butterworth, R.F. Selective loss of pallidal dopamine D2 receptor density in hepatic encephalopathy. *Neurosci. Lett* **162**, 192-196 (1993).
125. Brouillet, E.P., Shinobu, L., McGarvey, U., Hochberg, F. & Beal, M.F. Manganese injection into the rat striatum produces excitotoxic lesions by impairing energy metabolism. *Exp. Neurol* **120**, 89-94 (1993).
126. Benedetto, A., Au, C., Avila, D.S., Milatovic, D. & Aschner, M. Extracellular dopamine potentiates mn-induced oxidative stress, lifespan reduction, and dopaminergic neurodegeneration in a BLI-3-dependent manner in Caenorhabditis elegans. *PLoS. Genet* **6**(2010).
127. Chakraborty, S. & Aschner, M. Altered manganese homeostasis: implications for BLI-3-dependent dopaminergic neurodegeneration and SKN-1 protection in C. elegans. *J. Trace Elem. Med Biol* **26**, 183-187 (2012).
128. Sidoryk-Wegrzynowicz, M., Lee, E., Albrecht, J. & Aschner, M. Manganese disrupts astrocyte glutamine transporter expression and function. *J. Neurochem* **110**, 822-830 (2009).
129. Aschner, M., Gannon, M. & Kimelberg, H.K. Manganese uptake and efflux in cultured rat astrocytes. *J. Neurochem* **58**, 730-735 (1992).
130. Farina, M., Avila, D.S., da Rocha, J.B. & Aschner, M. Metals, oxidative stress and neurodegeneration: A focus on iron, manganese and mercury. *Neurochem. Int* (2012).
131. Rao, K.V. & Norenberg, M.D. Manganese induces the mitochondrial permeability transition in cultured astrocytes. *J. Biol. Chem* **279**, 32333-32338 (2004).
132. Wedler, F.C. *et al.* Effects of Ca(II) ions on Mn(II) dynamics in chick glia and rat astrocytes: potential regulation of glutamine synthetase. *Neurochem. Res* **19**, 145-151 (1994).
133. Sidoryk-Wegrzynowicz, M., Lee, E., Mingwei, N. & Aschner, M. Disruption of astrocytic glutamine turnover by manganese is mediated by the protein kinase C pathway. *Glia* **59**, 1732-1743 (2011).
134. Erikson, K.M., Suber, R.L. & Aschner, M. Glutamate/aspartate transporter (GLAST), taurine transporter and metallothionein mRNA levels are differentially altered in astrocytes exposed to manganese chloride, manganese phosphate or manganese sulfate. *Neurotoxicology* **23**, 281-288 (2002).
135. Roth, J.A., Ganapathy, B. & Ghio, A.J. Manganese-induced toxicity in normal and human B lymphocyte cell lines containing a homozygous mutation in parkin. *Toxicol. In Vitro* **26**, 1143-1149 (2012).
136. Anderson, J.G. *et al.* Manganese exposure alters extracellular GABA, GABA receptor and transporter protein and mRNA levels in the developing rat brain. *Neurotoxicology* **29**, 1044-1053 (2008).
137. Fordahl, S.C. *et al.* Manganese exposure inhibits the clearance of extracellular GABA and influences taurine homeostasis in the striatum of developing rats. *Neurotoxicology* **31**, 639-646 (2010).
138. Racette, B.A. *et al.* Increased risk of parkinsonism associated with welding exposure. *Neurotoxicology* **33**, 1356-1361 (2012).
139. Martinez-Finley, E.J., Gavin, C.E., Aschner, M. & Gunter, T.E. Manganese neurotoxicity and the role of reactive oxygen species. *Free Radic. Biol. Med* (2013).

140. Balasz, M. *et al.* Perinatal manganese exposure and hydroxyl radical formation in rat brain. *Neurotox Res* **27**, 1-14 (2015).
141. Bonke, E., Zwicker, K. & Drose, S. Manganese ions induce H2O2 generation at the ubiquinone binding site of mitochondrial complex II. *Arch Biochem Biophys* **580**, 75-83 (2015).
142. Gavin, C.E., Gunter, K.K. & Gunter, T.E. Mn2+ sequestration by mitochondria and inhibition of oxidative phosphorylation. *Toxicol. Appl. Pharmacol* **115**, 1-5 (1992).
143. Cordova, F.M. *et al.* Manganese-exposed developing rats display motor deficits and striatal oxidative stress that are reversed by Trolox. *Arch. Toxicol* (2013).
144. HaMai, D. & Bondy, S.C. Oxidative basis of manganese neurotoxicity. *Ann N. Y. Acad. Sci* **1012**, 129-141 (2004).
145. Settivari, R., Levora, J. & Nass, R. The divalent metal transporter homologues SMF-1/2 mediate dopamine neuron sensitivity in caenorhabditis elegans models of manganism and parkinson disease. *J. Biol. Chem* **284**, 35758-35768 (2009).
146. Yoon, H. *et al.* Apoptosis induced by manganese on neuronal SK-N-MC Cell line: Endoplasmic reticulum (ER) stress and mitochondria dysfunction. *Environ. Health Toxicol* **26**, e2011017 (2011).
147. Prabhakaran, K., Ghosh, D., Chapman, G.D. & Gunasekar, P.G. Molecular mechanism of manganese exposure-induced dopaminergic toxicity. *Brain Res. Bull* **76**, 361-367 (2008).
148. Stephenson, A.P. *et al.* Manganese-induced oxidative DNA damage in neuronal SH-SY5Y cells: Attenuation of thymine base lesions by glutathione and N-acetylcysteine. *Toxicol. Lett* (2013).
149. Donaldson, J., McGregor, D. & LaBella, F. Manganese neurotoxicity: a model for free radical mediated neurodegeneration? *Can. J. Physiol Pharmacol* **60**, 1398-1405 (1982).
150. van Muiswinkel, F.L. *et al.* Expression of NAD(P)H:quinone oxidoreductase in the normal and Parkinsonian substantia nigra. *Neurobiol. Aging* **25**, 1253-1262 (2004).
151. Goldstein, S., Meyerstein, D. & Czapski, G. The Fenton reagents. *Free Radic. Biol. Med* **15**, 435-445 (1993).
152. Apaydin, M., Erbas, O. & Taskiran, D. Protection by Edaravone, a radical scavenger, against manganese-induced neurotoxicity in rats. *J Biochem Mol Toxicol* (2016).
153. Filipov, N.M. & Dodd, C.A. Role of glial cells in manganese neurotoxicity. *J. Appl. Toxicol* **32**, 310-317 (2012).
154. Hazell, A.S., Normandin, L., Norenberg, M.D., Kennedy, G. & Yi, J.H. Alzheimer type II astrocytic changes following sub-acute exposure to manganese and its prevention by antioxidant treatment. *Neurosci. Lett* **396**, 167-171 (2006).
155. Spranger, M. *et al.* Manganese augments nitric oxide synthesis in murine astrocytes: a new pathogenetic mechanism in manganism? *Exp. Neurol* **149**, 277-283 (1998).
156. Moreno, J.A., Sullivan, K.A., Carbone, D.L., Hanneman, W.H. & Tjalkens, R.B. Manganese potentiates nuclear factor-kappaB-dependent expression of nitric oxide synthase 2 in astrocytes by activating soluble guanylate cyclase and extracellular responsive kinase signaling pathways. *J. Neurosci. Res* **86**, 2028-2038 (2008).
157. Seth, A., Stemple, D.L. & Barroso, I. The emerging use of zebrafish to model metabolic disease. *Dis. Model. Mech* **6**, 1080-1088 (2013).
158. Phillips, J.B. & Westerfield, M. Zebrafish models in translational research: tipping the scales toward advancements in human health. *Dis Model Mech* **7**, 739-43 (2014).

159. Schlegel, A. & Gut, P. Metabolic insights from zebrafish genetics, physiology, and chemical biology. *Cell Mol Life Sci* **72**, 2249-60 (2015).
160. Chu, J. *et al.* A zebrafish model of congenital disorders of glycosylation with phosphomannose isomerase deficiency reveals an early opportunity for corrective mannose supplementation. *Dis. Model. Mech* **6**, 95-105 (2013).
161. Friedrich, T., Lambert, A.M., Masino, M.A. & Downes, G.B. Mutation of zebrafish dihydrolipoamide branched-chain transacylase E2 results in motor dysfunction and models maple syrup urine disease. *Dis. Model. Mech* **5**, 248-258 (2012).
162. Kim, S.H. *et al.* Multi-organ abnormalities and mTORC1 activation in zebrafish model of multiple acyl-CoA dehydrogenase deficiency. *PLoS. Genet* **9**, e1003563 (2013).
163. Louwette, S. *et al.* NPC1 defect results in abnormal platelet formation and function: studies in Niemann-Pick disease type C1 patients and zebrafish. *Hum. Mol. Genet* **22**, 61-73 (2013).
164. Mahmood, F. *et al.* A zebrafish model of CLN2 disease is deficient in tripeptidyl peptidase 1 and displays progressive neurodegeneration accompanied by a reduction in proliferation. *Brain* **136**, 1488-1507 (2013).
165. Shih, D.F. *et al.* Aromatic L-Amino Acid Decarboxylase (AADC) is crucial for brain development and motor functions. *PLoS. One* **8**, e71741 (2013).
166. McGown, A. *et al.* Early interneuron dysfunction in ALS: insights from a mutant sod1 zebrafish model. *Ann Neurol* **73**, 246-258 (2013).
167. Santana, S., Rico, E.P. & Burgos, J.S. Can zebrafish be used as animal model to study Alzheimer's disease? *Am. J. Neurodegener. Dis* **1**, 32-48 (2012).
168. Schmid, B. & Haass, C. Genomic editing opens new avenues for zebrafish as a model for neurodegeneration. *J. Neurochem* (2013).
169. Donovan, A. *et al.* The zebrafish mutant gene chardonnay (cdy) encodes divalent metal transporter 1 (DMT1). *Blood* **100**, 4655-4659 (2002).
170. Hernandez, P.P. & Allende, M.L. Zebrafish (Danio rerio) as a model for studying the genetic basis of copper toxicity, deficiency, and metabolism. *Am. J Clin. Nutr* **88**, 835S-839S (2008).
171. Zhao, L., Xia, Z. & Wang, F. Zebrafish in the sea of mineral (iron, zinc, and copper) metabolism. *Front Pharmacol* **5**, 33 (2014).
172. Rinkwitz, S., Mourrain, P. & Becker, T.S. Zebrafish: an integrative system for neurogenomics and neurosciences. *Prog. Neurobiol* **93**, 231-243 (2011).
173. Lessman, C.A. The developing zebrafish (Danio rerio): a vertebrate model for high-throughput screening of chemical libraries. *Birth Defects Res. C. Embryo. Today* **93**, 268-280 (2011).
174. Peal, D.S., Peterson, R.T. & Milan, D. Small molecule screening in zebrafish. *J. Cardiovasc. Transl. Res* **3**, 454-460 (2010).
175. Leite, C.E. *et al.* Involvement of purinergic system in inflammation and toxicity induced by copper in zebrafish larvae. *Toxicol. Appl. Pharmacol* (2013).
176. Howe, K. *et al.* The zebrafish reference genome sequence and its relationship to the human genome. *Nature* **496**, 498-503 (2013).
177. Hwang, W.Y. *et al.* Heritable and precise zebrafish genome editing using a CRISPR-Cas system. *PLoS. One* **8**, e68708 (2013).
178. Hwang, W.Y. *et al.* Efficient genome editing in zebrafish using a CRISPR-Cas system. *Nat. Biotechnol* **31**, 227-229 (2013).
179. Xiao, A. *et al.* Chromosomal deletions and inversions mediated by TALENs and CRISPR/Cas in zebrafish. *Nucleic Acids Res* **41**, e141 (2013).
180. Zu, Y. *et al.* TALEN-mediated precise genome modification by homologous recombination in zebrafish. *Nat. Methods* **10**, 329-331 (2013).

181. Dahlem, T.J. *et al.* Simple methods for generating and detecting locus-specific mutations induced with TALENs in the zebrafish genome. *PLoS. Genet* **8**, e1002861 (2012).
182. Shah, A.N., Davey, C.F., Whitebirch, A.C., Miller, A.C. & Moens, C.B. Rapid reverse genetic screening using CRISPR in zebrafish. *Zebrafish* **13**, 152-3 (2016).
183. Cade, L. *et al.* Highly efficient generation of heritable zebrafish gene mutations using homo- and heterodimeric TALENs. *Nucleic Acids Res* **40**, 8001-8010 (2012).
184. Cermak, T. *et al.* Efficient design and assembly of custom TALEN and other TAL effector-based constructs for DNA targeting. *Nucleic Acids Res* **39**, e82 (2011).
185. Gaj, T., Gersbach, C.A. & Barbas, C.F., III. ZFN, TALEN, and CRISPR/Cas-based methods for genome engineering. *Trends Biotechnol* **31**, 397-405 (2013).
186. Moore, F.E. *et al.* Improved somatic mutagenesis in zebrafish using transcription activator-like effector nucleases (TALENs). *PLoS. One* **7**, e37877 (2012).
187. Reyon, D. *et al.* Engineering customized TALE nucleases (TALENs) and TALE transcription factors by fast ligation-based automatable solid-phase high-throughput (FLASH) assembly. *Curr Protoc Mol Biol* **Chapter 12**, Unit 12 16 (2013).
188. Reyon, D. *et al.* FLASH assembly of TALENs for high-throughput genome editing. *Nat. Biotechnol* **30**, 460-465 (2012).
189. Li, T. *et al.* Modularly assembled designer TAL effector nucleases for targeted gene knockout and gene replacement in eukaryotes. *Nucleic Acids Res* **39**, 6315-6325 (2011).
190. Wei, C. *et al.* TALEN or Cas9 - rapid, efficient and specific choices for genome modifications. *J. Genet. Genomics* **40**, 281-289 (2013).
191. Jao, L.E., Wente, S.R. & Chen, W. Efficient multiplex biallelic zebrafish genome editing using a CRISPR nuclease system. *Proc. Natl. Acad. Sci. U. S. A* **110**, 13904-13909 (2013).
192. Tuschl, K., Mills, P.B. & Clayton, P.T. Manganese and the brain. *Int. Rev. Neurobiol* **110**, 277-312 (2013).
193. Truett, G.E. *et al.* Preparation of PCR-quality mouse genomic DNA with hot sodium hydroxide and tris (HotSHOT). *Biotechniques* **29**, 52, 54 (2000).
194. Sherry, S.T. *et al.* dbSNP: the NCBI database of genetic variation. *Nucleic Acids Res* **29**, 308-311 (2001).
195. Hill, J.T. *et al.* Poly peak parser: Method and software for identification of unknown indels using sanger sequencing of polymerase chain reaction products. *Dev Dyn* **243**, 1632-6 (2014).
196. Gonzalez, M.A. *et al.* GEnomes Management Application (GEM.app): a new software tool for large-scale collaborative genome analysis. *Hum. Mutat* **34**, 842-846 (2013).
197. Livak, K.J. & Schmittgen, T.D. Analysis of relative gene expression data using real-time quantitative PCR and the 2(-Delta Delta C(T)) Method. *Methods* **25**, 402-408 (2001).
198. Thisse, C. & Thisse, B. High-resolution in situ hybridization to whole-mount zebrafish embryos. *Nat. Protoc* **3**, 59-69 (2008).
199. He, C., Holme, J. & Anthony, J. SNP genotyping: the KASP assay. *Methods Mol Biol* **1145**, 75-86 (2014).
200. Kimmel, C.B., Ballard, W.W., Kimmel, S.R., Ullmann, B. & Schilling, T.F. Stages of embryonic development of the zebrafish. *Dev. Dyn* **203**, 253-310 (1995).
201. Migheli, A., Attanasio, A. & Schiffer, D. Ultrastructural detection of DNA strand breaks in apoptotic neural cells by in situ end-labelling techniques. *J Pathol* **176**, 27-35 (1995).

202. Rihel, J., Prober, D.A. & Schier, A.F. Monitoring sleep and arousal in zebrafish. *Methods Cell Biol* **100**, 281-294 (2010).
203. Quaghebeur, G. *et al.* MRI in children receiving total parenteral nutrition. *Neuroradiology* **38**, 680-683 (1996).
204. Avelino, M.A. *et al.* Inherited manganism: the "cock-walk" gait and typical neuroimaging features. *J Neurol. Sci* **341**, 150-152 (2014).
205. Mukhtiar, K., Ibrahim, S., Tuschl, K. & Mills, P. Hypermanganesemia with Dystonia, Polycythemia and Cirrhosis (HMDPC) due to mutation in the SLC30A10 gene. *Brain Dev* (2016).
206. Ke, Q. & Costa, M. Hypoxia-inducible factor-1 (HIF-1). *Mol Pharmacol* **70**, 1469-80 (2006).
207. Grinfeld, J. & Godfrey, A.L. After 10years of JAK2V617F: Disease biology and current management strategies in polycythaemia vera. *Blood Rev* (2016).
208. Scott, L.M. *et al.* JAK2 exon 12 mutations in polycythemia vera and idiopathic erythrocytosis. *N Engl J Med* **356**, 459-68 (2007).
209. Tefferi, A. & Barbui, T. Polycythemia vera and essential thrombocythemia: 2015 update on diagnosis, risk-stratification and management. *Am J Hematol* **90**, 162-73 (2015).
210. Lechpammer, M. *et al.* Pathology of inherited manganese transporter deficiency. *Ann Neurol* **75**, 608-612 (2014).
211. Zhu, H., Jackson, T. & Bunn, H.F. Detecting and responding to hypoxia. *Nephrol Dial Transplant* **17 Suppl 1**, 3-7 (2002).
212. Taylor, M. *et al.* Hypoxia-inducible factor-2alpha mediates the adaptive increase of intestinal ferroportin during iron deficiency in mice. *Gastroenterology* **140**, 2044-55 (2011).
213. Chabanova, E. *et al.* Effect of new manganese contrast agent on tissue intensities in human volunteers: comparison of 0.23, 0.6 and 1.5 T MRI, a part of a phase I trial. *MAGMA* **17**, 28-35 (2004).
214. Janocha-Litwin, J., Marianska, K., Serafinska, S. & Simon, K. Manganese encephalopathy among ephedron abusers-case reports. *J Neuroimaging* (2014).
215. Nelson, K., Golnick, J., Korn, T. & Angle, C. Manganese encephalopathy: utility of early magnetic resonance imaging. *Br. J. Ind. Med* **50**, 510-513 (1993).
216. EASL Clinical Practice Guidelines: Wilson's disease. *J Hepatol* **56**, 671-685 (2012).
217. Blanusa, M., Varnai, V.M., Piasek, M. & Kostial, K. Chelators as antidotes of metal toxicity: therapeutic and experimental aspects. *Curr Med Chem* **12**, 2771-94 (2005).
218. Jiang, Y.M. *et al.* Effective treatment of manganese-induced occupational Parkinsonism with p-aminosalicylic acid: a case of 17-year follow-up study. *J. Occup. Environ. Med* **48**, 644-649 (2006).
219. Zheng, W. *et al.* Chelation therapy of manganese intoxication with para-aminosalicylic acid (PAS) in Sprague-Dawley rats. *Neurotoxicology* **30**, 240-8 (2009).
220. Angle, C.R. Dimercaptosuccinic acid (DMSA): negligible effect on manganese in urine and blood. *Occup Environ Med* **52**, 846 (1995).
221. Blaurock-Busch, E., Friedle, A., Godfrey, M. & Schulte-Uebbing, C.E. Metal exposure in the physically and mentally challenged children of Punjab, India. *Maedica (Buchar)* **5**, 102-10 (2010).
222. Zhao, Y., Feresin, R.G., Falcon-Perez, J.M. & Salazar, G. Differential targeting of SLC30A10/ZnT10 heterodimers to endolysosomal compartments modulates EGF-induced MEK/ERK1/2 activity. *Traffic* **17**, 267-88 (2016).
223. Cooper, D.N., Krawczak, M., Polychronakos, C., Tyler-Smith, C. & Kehrer-Sawatzki, H. Where genotype is not predictive of phenotype: towards an

understanding of the molecular basis of reduced penetrance in human inherited disease. *Hum Genet* **132**, 1077-130 (2013).
224. Gross, L. The case of XPD: sometimes two different mutant genes are better than one. *PLoS Biol* **4**, e347 (2006).
225. Itoh, H. *et al.* Long QT syndrome with compound mutations is associated with a more severe phenotype: a Japanese multicenter study. *Heart Rhythm* **7**, 1411-8 (2010).
226. Ng, E. *et al.* Genome-wide association study of toxic metals and trace elements reveals novel associations. *Hum Mol Genet* **24**, 4739-45 (2015).
227. Wahlberg, K. *et al.* Common polymorphisms in the solute carrier SLC30A10 are associated with blood manganese and neurological function. *Toxicol Sci* **149**, 473-83 (2016).
228. Taylor, K.M., Morgan, H.E., Johnson, A. & Nicholson, R.I. Structure-function analysis of a novel member of the LIV-1 subfamily of zinc transporters, ZIP14. *FEBS Lett* **579**, 427-432 (2005).
229. Taylor, K.M. *et al.* The emerging role of the LIV-1 subfamily of zinc transporters in breast cancer. *Mol. Med* **13**, 396-406 (2007).
230. Tominaga, K. *et al.* SLC39A14, a LZT protein, is induced in adipogenesis and transports zinc. *FEBS J* **272**, 1590-1599 (2005).
231. Liuzzi, J.P., Aydemir, F., Nam, H., Knutson, M.D. & Cousins, R.J. Zip14 (Slc39a14) mediates non-transferrin-bound iron uptake into cells. *Proc. Natl. Acad. Sci. U. S. A* **103**, 13612-13617 (2006).
232. Min, K.S., Takano, M., Amako, K., Ueda, H. & Tanaka, K. Involvement of the essential metal transporter Zip14 in hepatic Cd accumulation during inflammation. *Toxicol. Lett* **218**, 91-96 (2013).
233. Beker, A.T. *et al.* Zinc transporter ZIP14 functions in hepatic zinc, iron and glucose homeostasis during the innate immune response (endotoxemia). *PLoS. One* **7**, e48679 (2012).
234. Guthrie, G.J. *et al.* Influence of ZIP14 (slc39A14) on intestinal zinc processing and barrier function. *Am. J Physiol Gastrointest. Liver Physiol* **308**, G171-G178 (2015).
235. Nam, H. *et al.* ZIP14 and DMT1 in the liver, pancreas, and heart are differentially regulated by iron deficiency and overload: implications for tissue iron uptake in iron-related disorders. *Haematologica* **98**, 1049-1057 (2013).
236. Pinilla-Tenas, J.J. *et al.* Zip14 is a complex broad-scope metal-ion transporter whose functional properties support roles in the cellular uptake of zinc and nontransferrin-bound iron. *Am. J Physiol Cell Physiol* **301**, C862-C871 (2011).
237. Zhao, N., Zhang, A.S., Worthen, C., Knutson, M.D. & Enns, C.A. An iron-regulated and glycosylation-dependent proteasomal degradation pathway for the plasma membrane metal transporter ZIP14. *Proc. Natl. Acad. Sci. U. S. A* **111**, 9175-9180 (2014).
238. Goulle, J.P. *et al.* Metal and metalloid multi-elementary ICP-MS validation in whole blood, plasma, urine and hair. Reference values. *Forensic Sci. Int* **153**, 39-44 (2005).
239. Harrington, J.M., Young, D.J., Essader, A.S., Sumner, S.J. & Levine, K.E. Analysis of human serum and whole blood for mineral content by ICP-MS and ICP-OES: development of a mineralomics method. *Biol. Trace Elem. Res* **160**, 132-142 (2014).
240. Kruer, M.C. The neuropathology of neurodegeneration with brain iron accumulation. *Int. Rev. Neurobiol* **110**, 165-194 (2013).
241. Zhao, N., Gao, J., Enns, C.A. & Knutson, M.D. ZRT/IRT-like protein 14 (ZIP14) promotes the cellular assimilation of iron from transferrin. *J Biol. Chem* **285**, 32141-32150 (2010).

242. Guerinot, M.L. The ZIP family of metal transporters. *Biochim. Biophys. Acta* **1465**, 190-198 (2000).
243. Rutherford, J.C. & Bird, A.J. Metal-responsive transcription factors that regulate iron, zinc, and copper homeostasis in eukaryotic cells. *Eukaryot. Cell* **3**, 1-13 (2004).
244. Fujishiro, H., Yoshida, M., Nakano, Y. & Himeno, S. Interleukin-6 enhances manganese accumulation in SH-SY5Y cells: implications of the up-regulation of ZIP14 and the down-regulation of ZnT10. *Metallomics* **6**, 944-9 (2014).
245. Kobayashi, K. *et al.* Induction of metallothionein by manganese is completely dependent on interleukin-6 production. *J Pharmacol. Exp. Ther* **320**, 721-727 (2007).
246. Crossgrove, J.S. & Yokel, R.A. Manganese distribution across the blood-brain barrier III. The divalent metal transporter-1 is not the major mechanism mediating brain manganese uptake. *Neurotoxicology* **25**, 451-460 (2004).
247. Yokel, R.A. Manganese flux across the blood-brain barrier. *Neuromolecular. Med* **11**, 297-310 (2009).
248. Maxel, T. *et al.* Gene expression of the zinc transporter ZIP14 (SLC39a14) is affected by weight loss and metabolic status and associates with PPARgamma in human adipose tissue and 3T3-L1 pre-adipocytes. *BMC Obes* **2**, 46 (2015).
249. Suzuki, T., Katsumata, S.I., Matsuzaki, H. & Suzuki, K. A short-term zinc-deficient diet decreases bone formation through down-regulated BMP2 in rat bone. *Biosci Biotechnol Biochem*, 1-3 (2016).
250. Troche, C., Aydemir, T.B. & Cousins, R.J. Zinc transporter Slc39a14 regulates inflammatory signaling associated with hypertrophic adiposity. *Am J Physiol Endocrinol Metab* **310**, E258-68 (2016).
251. Wessels, I. & Cousins, R.J. Zinc dyshomeostasis during polymicrobial sepsis in mice involves zinc transporter Zip14 and can be overcome by zinc supplementation. *Am J Physiol Gastrointest Liver Physiol* **309**, G768-78 (2015).
252. Aydemir, T.B. *et al.* Zinc transporter ZIP14 functions in hepatic zinc, iron and glucose homeostasis during the innate immune response (endotoxemia). *PLoS One* **7**, e48679 (2012).
253. Hojyo, S. *et al.* The zinc transporter SLC39A14/ZIP14 controls G-protein coupled receptor-mediated signaling required for systemic growth. *PLoS. One* **6**, e18059 (2011).
254. Geisse, S. & Voedisch, B. Transient expression technologies: past, present, and future. *Methods Mol Biol* **899**, 203-19 (2012).
255. Burgess, D.J. Genomics: New zebrafish genome resources. *Nat. Rev. Genet* **14**, 368-369 (2013).
256. Glasauer, S.M. & Neuhauss, S.C. Whole-genome duplication in teleost fishes and its evolutionary consequences. *Mol Genet Genomics* **289**, 1045-60 (2014).
257. Langdon, Y.G. & Mullins, M.C. Maternal and zygotic control of zebrafish dorsoventral axial patterning. *Annu. Rev. Genet* **45**, 357-377 (2011).
258. Dhillon, S.S. *et al.* Optimisation of embryonic and larval ECG measurement in zebrafish for quantifying the effect of QT prolonging drugs. *PLoS. One* **8**, e60552 (2013).
259. Bakthavatsalam, S., Das, S.S., Sonawane, M., Thirumalai, V. & Datta, A. A zebrafish model of manganism reveals reversible and treatable symptoms that are independent of neurotoxicity. *Dis. Model. Mech* **7**, 1239-1251 (2014).
260. Coneyworth, L.J. *et al.* Identification of the human zinc transcriptional regulatory element (ZTRE): a palindromic protein-binding DNA sequence responsible for zinc-induced transcriptional repression. *J. Biol. Chem* **287**, 36567-36581 (2012).
261. Guh, Y.J., Lin, C.H. & Hwang, P.P. Osmoregulation in zebrafish: ion transport mechanisms and functional regulation. *EXCLI J* **14**, 627-59 (2015).

262. Brinkhaus, S.G. *et al.* Elemental bioimaging of manganese uptake in C. elegans. *Metallomics* **6**, 617-21 (2014).
263. Norris, F.C. *et al.* Enhanced tissue differentiation in the developing mouse brain using magnetic resonance micro-histology. *Magn Reson Med* **70**, 1380-8 (2013).
264. Kumar, K.K., Aboud, A.A., Patel, D.K., Aschner, M. & Bowman, A.B. Optimization of fluorescence assay of cellular manganese status for high throughput screening. *J Biochem Mol Toxicol* **27**, 42-9 (2013).
265. Schweitzer, J., Lohr, H., Filippi, A. & Driever, W. Dopaminergic and noradrenergic circuit development in zebrafish. *Dev. Neurobiol* **72**, 256-268 (2012).
266. Schweitzer, J. & Driever, W. Development of the dopamine systems in zebrafish. *Adv Exp Med Biol* **651**, 1-14 (2009).
267. Semenova, S.A., Chen, Y.C., Zhao, X., Rauvala, H. & Panula, P. The tyrosine hydroxylase 2 (TH2) system in zebrafish brain and stress activation of hypothalamic cells. *Histochem Cell Biol* **142**, 619-33 (2014).
268. Filippi, A., Mahler, J., Schweitzer, J. & Driever, W. Expression of the paralogous tyrosine hydroxylase encoding genes th1 and th2 reveals the full complement of dopaminergic and noradrenergic neurons in zebrafish larval and juvenile brain. *J Comp Neurol* **518**, 423-38 (2010).
269. Xi, Y. *et al.* Transgenic zebrafish expressing green fluorescent protein in dopaminergic neurons of the ventral diencephalon. *Dev. Dyn* **240**, 2539-2547 (2011).
270. Kim, D.S. *et al.* p73 gene in dopaminergic neurons is highly susceptible to manganese neurotoxicity. *Neurotoxicology* (2016).
271. Ma, X. *et al.* Involvement of dysregulated Wip1 in manganese-induced p53 signaling and neuronal apoptosis. *Toxicol Lett* **235**, 17-27 (2015).
272. Hatamoto, K. & Shingyoji, C. Cyclical training enhances the melanophore responses of zebrafish to background colours. *Pigment Cell Melanoma Res* **21**, 397-406 (2008).
273. Neuhauss, S.C. Behavioral genetic approaches to visual system development and function in zebrafish. *J Neurobiol* **54**, 148-160 (2003).
274. Haug, M.F., Biehlmaier, O., Mueller, K.P. & Neuhauss, S.C. Visual acuity in larval zebrafish: behavior and histology. *Front Zool* **7**, 8 (2010).
275. Bowman, A.B., Kwakye, G.F., Hernandez, E.H. & Aschner, M. Role of manganese in neurodegenerative diseases. *J. Trace Elem. Med. Biol* **25**, 191-203 (2011).
276. Rizo, J. & Xu, J. The synaptic vesicle release machinery. *Annu Rev Biophys* **44**, 339-67 (2015).
277. Vatine, G., Vallone, D., Gothilf, Y. & Foulkes, N.S. It's time to swim! Zebrafish and the circadian clock. *FEBS Lett* **585**, 1485-94 (2011).
278. Casalino, E., Sblano, C., Landriscina, V., Calzaretti, G. & Landriscina, C. Rat liver glutathione S-transferase activity stimulation following acute cadmium or manganese intoxication. *Toxicology* **200**, 29-38 (2004).
279. Cavadas, M.A., Nguyen, L.K. & Cheong, A. Hypoxia-inducible factor (HIF) network: insights from mathematical models. *Cell Commun. Signal* **11**, 42 (2013).
280. Hernandez, R.B., Nishita, M.I., Esposito, B.P., Scholz, S. & Michalke, B. The role of chemical speciation, chemical fractionation and calcium disruption in manganese-induced developmental toxicity in zebrafish (Danio rerio) embryos. *J Trace Elem Med Biol* **32**, 209-17 (2015).
281. Bouabid, S., Delaville, C., De Deurwaerdere, P., Lakhdar-Ghazal, N. & Benazzouz, A. Manganese-induced atypical parkinsonism is associated with altered Basal Ganglia activity and changes in tissue levels of monoamines in the rat. *PLoS One* **9**, e98952 (2014).

282. Adedara, I.A., Abolaji, A.O., Rocha, J.B. & Farombi, E.O. Diphenyl diselenide protects against mortality, locomotor deficits and oxidative stress in drosophila melanogaster model of manganese-induced neurotoxicity. *Neurochem Res* (2016).
283. Fordahl, S. *et al.* Waterborne manganese exposure alters plasma, brain, and liver metabolites accompanied by changes in stereotypic behaviors. *Neurotoxicol Teratol* **34**, 27-36 (2012).
284. Fitsanakis, V.A., Au, C., Erikson, K.M. & Aschner, M. The effects of manganese on glutamate, dopamine and gamma-aminobutyric acid regulation. *Neurochem Int* **48**, 426-33 (2006).
285. Das, S. & Choudhury, S.S. Analysis of heavy metals from water, sediment, and tissues of Labeo angra (Hamilton, 1822), from an Ox-box lake- an wetland site from Assam, India. *J Environ Sci Health A Tox Hazard Subst Environ Eng* **51**, 21-33 (2016).
286. Hwang, P.P., Lee, T.H. & Lin, L.Y. Ion regulation in fish gills: recent progress in the cellular and molecular mechanisms. *Am J Physiol Regul Integr Comp Physiol* **301**, R28-47 (2011).
287. Chow, E.S., Hui, M.N., Cheng, C.W. & Cheng, S.H. Cadmium affects retinogenesis during zebrafish embryonic development. *Toxicol Appl Pharmacol* **235**, 68-76 (2009).
288. Jorge-Nebert, L.F. *et al.* Comparing gene expression during cadmium uptake and distribution: untreated versus oral Cd-treated wild-type and ZIP14 knockout mice. *Toxicol Sci* **143**, 26-35 (2015).
289. Jiao, Y., Shashkina, E., Shashkin, P., Hansson, A. & Katz, A. Manganese sulfate-dependent glycosylation of endogenous glycoproteins in human skeletal muscle is catalyzed by a nonglucose 6-P-dependent glycogen synthase and not glycogenin. *Biochim Biophys Acta* **1427**, 1-12 (1999).
290. Kaufman, R.J., Swaroop, M. & Murtha-Riel, P. Depletion of manganese within the secretory pathway inhibits O-linked glycosylation in mammalian cells. *Biochemistry* **33**, 9813-9 (1994).
291. Potelle, S. *et al.* Glycosylation abnormalities in Gdt1p/TMEM165 deficient cells result from a defect in Golgi manganese homeostasis. *Hum Mol Genet* **25**, 1489-500 (2016).
292. Ubach, J., Zhang, X., Shao, X., Sudhof, T.C. & Rizo, J. Ca2+ binding to synaptotagmin: how many Ca2+ ions bind to the tip of a C2-domain? *EMBO J* **17**, 3921-30 (1998).
293. Sidoryk-Wegrzynowicz, M. Impairment of glutamine/glutamate-gamma-aminobutyric acid cycle in manganese toxicity in the central nervous system. *Folia Neuropathol* **52**, 377-82 (2014).
294. Sidoryk-Wegrzynowicz, M. & Aschner, M. Manganese toxicity in the CNS: the glutamine/glutamate-gamma-aminobutyric acid cycle. *J. Intern. Med* (2013).
295. Sidoryk-Wegrzynowicz, M., Lee, E. & Aschner, M. Mechanism of Mn(II)-mediated dysregulation of glutamine-glutamate cycle: focus on glutamate turnover. *J. Neurochem* **122**, 856-867 (2012).
296. Dydak, U. *et al.* In vivo measurement of brain GABA concentrations by magnetic resonance spectroscopy in smelters occupationally exposed to manganese. *Environ. Health Perspect* **119**, 219-224 (2011).
297. Anderson, J.G. *et al.* Manganese exposure alters extracellular GABA, GABA receptor and transporter protein and mRNA levels in the developing rat brain. *Neurotoxicology* **29**, 1044-53 (2008).
298. Guilarte, T.R. & Chen, M.K. Manganese inhibits NMDA receptor channel function: implications to psychiatric and cognitive effects. *Neurotoxicology* **28**, 1147-52 (2007).

299. Smillie, K.J., Pawson, J., Perkins, E.M., Jackson, M. & Cousin, M.A. Control of synaptic vesicle endocytosis by an extracellular signalling molecule. *Nat Commun* **4**, 2394 (2013).
300. Yoshii, A. & Constantine-Paton, M. Postsynaptic BDNF-TrkB signaling in synapse maturation, plasticity, and disease. *Dev Neurobiol* **70**, 304-22 (2010).
301. Zou, Y. *et al.* Cognitive function and plasma BDNF levels among manganese-exposed smelters. *Occup Environ Med* **71**, 189-94 (2014).
302. Liang, G. *et al.* Effects of chronic manganese exposure on the learning and memory of rats by observing the changes in the hippocampal cAMP signaling pathway. *Food Chem Toxicol* **83**, 261-7 (2015).
303. Idda, M.L. *et al.* Circadian clocks: lessons from fish. *Prog Brain Res* **199**, 41-57 (2012).
304. Ramakrishnan, S.N. & Muscat, G.E. The orphan Rev-erb nuclear receptors: a link between metabolism, circadian rhythm and inflammation? *Nucl Recept Signal* **4**, e009 (2006).
305. Witte, K., Parsa-Parsi, R., Vobig, M. & Lemmer, B. Mechanisms of the circadian regulation of beta-adrenoceptor density and adenylyl cyclase activity in cardiac tissue from normotensive and spontaneously hypertensive rats. *J Mol Cell Cardiol* **27**, 1195-202 (1995).
306. Elks, P.M., Renshaw, S.A., Meijer, A.H., Walmsley, S.R. & van Eeden, F.J. Exploring the HIFs, buts and maybes of hypoxia signalling in disease: lessons from zebrafish models. *Dis Model Mech* **8**, 1349-60 (2015).
307. Goldberg, M.A., Dunning, S.P. & Bunn, H.F. Regulation of the erythropoietin gene: evidence that the oxygen sensor is a heme protein. *Science* **242**, 1412-5 (1988).
308. Kaupp, U.B. & Seifert, R. Cyclic nucleotide-gated ion channels. *Physiol Rev* **82**, 769-824 (2002).
309. Nguyen, O.N. *et al.* Peripherin-2 differentially interacts with cone opsins in outer segments of cone photoreceptors. *Hum Mol Genet* (2016).
310. Nickle, B. & Robinson, P.R. The opsins of the vertebrate retina: insights from structural, biochemical, and evolutionary studies. *Cell Mol Life Sci* **64**, 2917-32 (2007).
311. Schon, C., Biel, M. & Michalakis, S. Gene replacement therapy for retinal CNG channelopathies. *Mol Genet Genomics* **288**, 459-67 (2013).
312. Zang, J., Keim, J., Kastenhuber, E., Gesemann, M. & Neuhauss, S.C. Recoverin depletion accelerates cone photoresponse recovery. *Open Biol* **5**(2015).
313. Nash, B.M., Wright, D.C., Grigg, J.R., Bennetts, B. & Jamieson, R.V. Retinal dystrophies, genomic applications in diagnosis and prospects for therapy. *Transl Pediatr* **4**, 139-63 (2015).
314. Makhankov, Y.V., Rinner, O. & Neuhauss, S.C. An inexpensive device for non-invasive electroretinography in small aquatic vertebrates. *J Neurosci Methods* **135**, 205-10 (2004).
315. Freeman, O.J. & Mallucci, G.R. The UPR and synaptic dysfunction in neurodegeneration. *Brain Res* (2016).
316. Angeli, S. *et al.* Manganese disturbs metal and protein homeostasis in Caenorhabditis elegans. *Metallomics* **6**, 1816-23 (2014).
317. Poynton, H.C., Robinson, W.E., Blalock, B.J. & Hannigan, R.E. Correlation of transcriptomic responses and metal bioaccumulation in Mytilus edulis L. reveals early indicators of stress. *Aquat Toxicol* **155**, 129-41 (2014).
318. Xu, B. *et al.* Endoplasmic reticulum stress signaling involvement in manganese-induced nerve cell damage in organotypic brain slice cultures. *Toxicol Lett* **222**, 239-46 (2013).

319. Kato, H., Katoh, R. & Kitamura, M. Dual regulation of cadmium-induced apoptosis by mTORC1 through selective induction of IRE1 branches in unfolded protein response. *PLoS One* **8**, e64344 (2013).
320. Permenter, M.G., Lewis, J.A. & Jackson, D.A. Exposure to nickel, chromium, or cadmium causes distinct changes in the gene expression patterns of a rat liver derived cell line. *PLoS One* **6**, e27730 (2011).
321. Wang, T. *et al.* ER stress and ER stress-mediated apoptosis are involved in manganese-induced neurotoxicity in the rat striatum in vivo. *Neurotoxicology* **48**, 109-19 (2015).
322. Zhu, Y. *et al.* The effect of manganese-induced cytotoxicity on mRNA expressions of HSP27, HSP40, HSP60, HSP70 and HSP90 in chicken spleen lymphocytes in vitro. *Biol Trace Elem Res* **156**, 144-52 (2013).
323. Li, Z. & Srivastava, P. Heat-shock proteins. *Curr Protoc Immunol* **Appendix 1**, Appendix 1T (2004).
324. Zhu, G. & Lee, A.S. Role of the unfolded protein response, GRP78 and GRP94 in organ homeostasis. *J Cell Physiol* **230**, 1413-20 (2015).
325. Davenport, E.L., Morgan, G.J. & Davies, F.E. Untangling the unfolded protein response. *Cell Cycle* **7**, 865-9 (2008).
326. Marcu, M.G. *et al.* Heat shock protein 90 modulates the unfolded protein response by stabilizing IRE1alpha. *Mol Cell Biol* **22**, 8506-13 (2002).
327. Lajoie, P., Fazio, E.N. & Snapp, E.L. Approaches to imaging unfolded secretory protein stress in living cells. *Endoplasmic Reticulum Stress Dis* **1**, 27-39 (2014).
328. Kaufman, R.J., Back, S.H., Song, B., Han, J. & Hassler, J. The unfolded protein response is required to maintain the integrity of the endoplasmic reticulum, prevent oxidative stress and preserve differentiation in beta-cells. *Diabetes Obes Metab* **12 Suppl 2**, 99-107 (2010).
329. Marre, M.L., James, E.A. & Piganelli, J.D. beta cell ER stress and the implications for immunogenicity in type 1 diabetes. *Front Cell Dev Biol* **3**, 67 (2015).
330. Tempel, B.L. & Shilling, D.J. The plasma membrane calcium ATPase and disease. *Subcell Biochem* **45**, 365-83 (2007).
331. Wingert, R.A. *et al.* The chianti zebrafish mutant provides a model for erythroid-specific disruption of transferrin receptor 1. *Development* **131**, 6225-35 (2004).
332. da Silva Santos, V. *et al.* Anthocyanin-rich acai (Euterpe oleracea Mart.) extract attenuates manganese-induced oxidative stress in rat primary astrocyte cultures. *J Toxicol Environ Health A* **77**, 390-404 (2014).
333. Maddirala, Y., Tobwala, S. & Ercal, N. N-acetylcysteineamide protects against manganese-induced toxicity in SHSY5Y cell line. *Brain Res* **1608**, 157-66 (2015).
334. Harischandra, D.S., Jin, H., Anantharam, V., Kanthasamy, A. & Kanthasamy, A.G. alpha-Synuclein protects against manganese neurotoxic insult during the early stages of exposure in a dopaminergic cell model of Parkinson's disease. *Toxicol Sci* **143**, 454-68 (2015).
335. Gagnon, J.A. *et al.* Efficient mutagenesis by Cas9 protein-mediated oligonucleotide insertion and large-scale assessment of single-guide RNAs. *PLoS One* **9**, e98186 (2014).
336. Fu, Y. *et al.* High-frequency off-target mutagenesis induced by CRISPR-Cas nucleases in human cells. *Nat Biotechnol* **31**, 822-6 (2013).
337. Kuscu, C., Arslan, S., Singh, R., Thorpe, J. & Adli, M. Genome-wide analysis reveals characteristics of off-target sites bound by the Cas9 endonuclease. *Nat Biotechnol* **32**, 677-83 (2014).
338. Mussolino, C. *et al.* TALENs facilitate targeted genome editing in human cells with high specificity and low cytotoxicity. *Nucleic Acids Res* **42**, 6762-73 (2014).